The Dissertation Committee for Chalence Timber Safranek-Shrader
certifies that this is the approved version of the following dissertation:

Star Formation in the First Galaxies

Committee:

Volker Bromm, Co-Supervisor

Miloš Milosavljević, Co-Supervisor

Karl Gebhardt

Neal J. Evans II

Steve Finkelstein

Abraham Loeb

Star Formation in the First Galaxies

by

Chalence Timber Safranek-Shrader, B.S.

DISSERTATION

Presented to the Faculty of the Graduate School of
The University of Texas at Austin
in Partial Fulfillment
of the Requirements
for the Degree of

DOCTOR OF PHILOSOPHY

THE UNIVERSITY OF TEXAS AT AUSTIN
August 2014

Dedicated to my parents.

Acknowledgments

Newton observed, *"if I have seen further it is by standing on the shoulders of giants."* I believe he was, and still is, correct — scientific progress is incremental and is based on past research achievements. The research presented in this dissertation is no exception and thus many others deserve acknowledgement.

I have been formally co-advised by two individuals, Volker Bromm and Milos Milosavljevic, and I must thank both of them for their unique skill set and guidance. Volker is a leader in his field, creative, and has a true gift for teaching. Milos Milosavljevic is hands-on, unselfishly caring, and scientifically energetic. Both are brilliant. Together, they made a potent advising team and I am privileged to have been their student. I also extend thanks to my Ph.D committee, Karl, Steve, Avi, and Neal, for their input and support.

Most of the major research projects I have spearheaded have been performed using the hydrodynamics code FLASH. This extremely powerful and well engineered piece of software was developed over many years by numerous people and I am thankful for the time and effort they have dedicated to FLASH. Additionally, most of this work has been completed using the computational resources of the Texas Advanced Computing Center (TACC) whose powerful machines and helpful staff deserve serious recognition.

I extend thanks to my graduate class here at UT. I remember sitting in a room with these individuals for departmental orientation, not realizing at the time the integral role they would play in my life. Erik Brugamyer, Manos Chatzopoulos, Michael Gully-Santiago, JJ Hermes, John Jardel, Julie Krugler, Chris Lindner, Manual Merello, and Paul Robertson. Thank you all for being the best graduate class anyone could hope to be part of.

Finally, and most importantly, I thank my parents, Penelope Safranek and Ray Shrader. They instilled within me the value of education — growing up, the only acceptable grade was an ‘A’. I would not be the person I was without their unconditional encouragement, love, and support.

Star Formation in the First Galaxies

Chalence Timber Safranek-Shrader, Ph.D.
The University of Texas at Austin, 2014

Supervisors: Volker Bromm
Miloš Milosavljević

The ignition of the first sources of light marked the end of the cosmic dark ages, an era when the Universe transitioned from the relatively simple conditions following the Big Bang to the complex tapestry of dark matter, baryons, and pervasive cosmic radiation fields we see today. To better understand this uncharted cosmic epoch, we primarily utilize hydrodynamical, N-body simulations to model the assembly of the first galaxies at redshifts $z \gtrsim 10$ and the stars that form within them. These simulations begin from cosmological initial conditions, employ a robust, non-equilibrium chemo-thermodynamic model, and take advantage of adaptive-grid-refinement to probe the multi-scale, complex process of star formation from *ab initio* principles. We explore the consequences that metal enrichment has on the process of star formation, confirming the presence of a *critical metallicity* for low-mass star formation. To assess the observational prospects of these primeval stellar populations with next-generation telescopes, like the *James Webb Space Telescope*, we constrain the star formation efficiency of both metal-enriched and metal-free star formation in a typical first galaxy. We also resolve the formation of individual

metal-enriched stars in simulations that ultimately began from cosmological scales, allowing meaningful comparisons between our simulations and the recently discovered ultra-faint dwarf satellite galaxies, the suspected analogs of the first galaxies in the local Universe.

Table of Contents

List of Tables

List of Figures

Chapter 1

Introduction

Look up to the sky on a dark night. There will be many bright points against the dark — planets, artificial satellites, airplanes, meteoroids, perhaps the Moon. Mostly, though, there are stars. These objects are nothing more than massive balls of gas that have collapsed under their own gravity. Their centers become so hot that nuclei smash together and fuse, producing the energy that makes stars shine. Either directly or indirectly, all sources of energy on Earth come from stars.

Stars evolve over time. The Sun formed roughly 5 billion years ago and will remain mostly unchanged for another 5 billion. When the Sun, and other stars of similar mass, exhaust their nuclear fuel they enter a new phase and become idle white dwarfs. More massive stars may only live for a few million years before ending their lives with a cataclysmic supernovae explosion, spewing newly synthesized chemical elements into their galactic neighborhood. New stars will form in part from this ejecta and the stellar life cycle repeats.

Stars are the key drivers of cosmic evolution. In particular, the earliest stellar generations illuminated the cosmos with ultraviolet light, beginning the gradual process of reionization and ending the cosmic dark ages. Heavy chemical elements produced in these stars and ejected in their supernovae seeded the cosmos with the building blocks of planets and life. These stars also seeded supermassive black holes, the power source of high-redshift quasars. The central goal of the following chapters is to better understand how these earliest stellar generations formed, the effect they had on their surroundings, and how observations, both direct and indirect, can be used to probe the nature of the first galaxies and the role that the earliest stellar generations played in early cosmic evolution.

1.1 From Cosmology...

To properly understand star formation in the first galaxies, we must work within a broader cosmological framework. In the successful Lambda Cold Dark Mater (ΛCDM) cosmological model, collisionless dark matter assembles hierarchically, with smaller 'halos' merging to form progressively larger ones. Baryons fall into the gravitational potential well of the dark matter where they are able to cool, fragment, and ultimately form galaxies, stars, planets, and ultimately, life. While the first stars formed ~ 100 million years after the Big Bang in $\sim 10^6\,M_\odot$ dark matter 'minihalos', the 'first galaxies' are generally believed to have been hosted in $\sim 10^8\,M_\odot$ dark matter halos that formed roughly 500 million years after the Big Bang. Unlike minihalos, these systems had the ability to harbor self-sustained, self-regulated star formation and contained a multi-phase interstellar medium (ISM), traits that are arguably necessary for the title of 'galaxy.'

1.2 ...to Star Formation

Star formation is one of the most poorly understood astrophysical phenomena. In it, a wide range of complex, multidimensional physical processes all play a role in regulating the conversion of gas into stars. While supersonic turbulence and self-gravity are believed to be the two main ingredients that control the process of star formation, there are a number of other factors such as non-ideal magnetohydrodyanmics, ionizing and non-ionizing radiative feedback, and chemical processes, that can not be neglected. Even in the Galaxy, where direct observations are available, there is not an agreed upon, predictive model for the formation of stars. Extending the theory of star formation to the first galaxies presents its own unique set of challenges, such as a lack of direct observations and markedly different physical conditions.

1.3 Outline

In this thesis, we aim to better understand the process, outcome, and consequences of star formation in the earliest galaxies. We attack this problem numerically, primarily using hydrodynamical simulations. Specifically, we focus on how the interplay of thermodynamics, self-gravity, and supersonically turbulent gas motions moderates the process of gas fragmentation, and thus star formation, all within a realistic cosmological environment.

Chapters 2 and 4 primary focus is the thermodynamic role that metals play in regulating the transition from Population III to Population II star formation. In Chapter 2 we present a idealized, one-zone model for the fragmentation of 'cold-accretion' streams in the first galaxies. By considering isobaric post-shock gas evolution and the expected baryonic growth rate of high-redshift halos, we show that there are two regimes of fragmentation, high- and low-mass, in the first galaxies demarcated by metallicity and external radiation field strength. In Chapter 4 we present a cosmological simulation where gas around an atomic cooling halo is endowed with a non-zero metallicity. We show that the increased cooling rate that accompanies metal enrichment plays a significant role in how star forming gas evolves, with significant fragmentation occurring above $Z = 10^{-4}\,Z_{\odot}$ and none below.

If an atomic cooling halo can avoid being polluted with heavy elements, it has been suggested that clustered, metal-free star formation is possible. We explore this idea in Chapter 3, where we present results from a cosmological simulation in which an atomic cooling halo forms without being polluted with metals due to the complete suppression of minihalo star formation via a strong Lyman-Werner radiation background. Only when molecular hydrogen in the atomic cooling halo begins to self-shield does collapse, and thus star formation, become possible. We are able to place upper-limits on the star formation efficiency of such 'Lyman-Werner delayed' systems, and argue that if a cluster of metal-free stars does form under optimum conditions, that it should be marginally detectable with the *James Webb Space Telescope* (JWST).

In Chapters 5 we extend the simulations presented in Chapter 4 to much higher densities and smaller length scales, now resolving the formation of individual stars. We augment our thermodynamical model to include dust processes, significantly dust grain thermal emission and protostellar radiative heating of dust, both of which become significant at high densities. These are the first studies that have resolved the formation of individual metal-enriched stars in a simulation that ultimately began from cosmological initial conditions. We are able to measure a stellar initial mass function (IMF) and show tentative evidence that high-mass ($> 0.1\,M_\odot$) slope is shallower (i.e., more top-heavy) than the standard Salpeter slope observed in the Galaxy.

Chapter 2

Fragmentation of Cold Accretion Streams in the First Galaxies[1]

2.1 Introduction

An important open question in cosmology is to identify the conditions under which the first Population II (Pop II) stars could have formed. It has been argued that clusters of predominantly low-mass stars could have arisen in the first galaxies at $z \approx 10$ (e.g., Bromm & Clarke 2002, Greif & Bromm 2006). Their emergence straddles the end of the so-called cosmic dark ages, arguably the most uncharted time in the history of the universe (Barkana & Loeb 2001, Miralda-Escudé 2003). Between the release of the cosmic microwave background (CMB) at $z \simeq 1,100$ and the highest redshift gamma ray burst (GRB) at $z \simeq 8.2$ (Salvaterra et al. 2009, Tanvir et al. 2009), no direct observations have been made yet, thus rendering theoretical models our best tools for exploring this formative cosmic epoch.

The standard ΛCDM cosmological model predicts the first stars (Pop III) formed at redshifts $z \simeq 20-30$ in $\sim 10^6\,M_\odot$ dark matter 'minihalos' (e.g., Couchman & Rees 1986, Haiman et al. 1996, Tegmark et al. 1997) bringing about an end to the cosmic dark ages. The cooling properties of H_2, the most effective primordial gas coolant at temperatures below 10^4 K, set a characteristic mass scale of $\sim 100\,M_\odot$ for Pop III stars (Abel et al. 2000, Bromm et al. 2002). The primordial initial mass

---

[1] This chapter has been published as Safranek-Shrader, C., Bromm, V., Milosavljevic, M., 2010, ApJ, 723, 1568. V. Bromm and M. Milosavljevic supervised the project.

function (IMF) would then have been top-heavy, a result that has been confirmed by subsequent studies (e.g., Omukai & Palla 2003, O'Shea & Norman 2007, Yoshida et al. 2006). Further investigations were directed at elucidating the properties and key implications of massive Pop III stars, such as the chemical signature (Heger & Woosley 2002, Iwamoto et al. 2005), the detailed IMF (Nakamura & Umemura 2001), the effect on reionization (Wyithe & Loeb 2003, Sokasian et al. 2004), the formation rate (Trenti et al. 2009), and the tendency toward binarity (Turk et al. 2009, Stacy et al. 2010). These massive Pop III stars had extremely hot photospheres ($T_{\rm eff} \sim 10^5\,{\rm K}$, see Bromm et al. 2001, Schaerer 2002), and very short lifetimes of $\sim$ 3 Myr (for the case against this standard picture see Tumlinson et al. 2004, Silk & Langer 2006, Clark et al. 2011a).

It is still not known with any certainty when and how the universe shifted its star formation mode from the top-heavy IMF for Pop III to the roughly Salpeter distribution seen today. Bromm et al. (2001) suggested it is the chemical input from Pop III stars that allowed gas in minihalos to cool more efficiently and thus fragment at a smaller mass scale. They found that when molecular cooling is excluded by a soft ultraviolet (UV) photodissociating background, gas enriched above $Z_{\rm crit} \simeq 10^{-3.5}\,Z_{\odot}$, the so-called critical metallicity, fragments into smaller mass clumps. The idea of metallicity being the main driver of the mode transition was advanced by many other studies. Santoro & Shull (2006) found individual critical metallicities for carbon, iron, silicon, and oxygen and suggested that for densities and temperatures conducive to Pop III star formation, these species contribute more to the cooling rate than atomic hydrogen or $\rm H_2$. Smith et al. (2009) found that there exists a critical metallicity window, due in part to the CMB temperature floor, which regulates the transition. Other studies (Omukai et al. 2005, Schneider et al. 2006) showed that dust may have a significant impact on the Pop

III/II transition. Specifically, the inclusion of lowers the critical metallicity derived from pure metal-line cooling by several orders of magnitude due to its efficient radiative properties. However, the effect of dust generally becomes important late in the pre-stellar gas contraction phase at high densities. Schneider & Omukai (2010) argued that the interplay of dust and metal cooling is the key driver, together with the CMB temperature floor. A different view was developed in a series of studies (Jappsen et al. 2007, 2009b,a) who argued metallicity plays an insignificant role in the fragmentation of collapsing clouds while initial conditions, set by the details of galaxy formation, the CMB temperature, turbulence, and rotation, dominate the Pop III/II transition. This star formation mode transition is clearly a complex, gradual process, regulated in part by all of these factors.

Most studies of the critical metallicity to date have focused on $\sim 10^6\,M_\odot$ dark matter halos, or minihalos, as the primordial star formation environment. However, the majority of the first Pop II stars likely formed in deeper potential wells, possibly in halos that can cool via atomic hydrogen cooling (e.g., Bromm et al. 2009). Whereas the quasi-hydrostatic, roughly spherical nature of baryonic collapse inside of minihalos admits modeling of low metallicity cooling in a rather straightforward fashion, the hydrodynamics inside the first galaxies is much more complex. Simulations with realistic cosmological initial conditions have recently demonstrated how cold accretion streams feed dense, turbulent gas to the center of the galaxy, where second generation star formation will take place (e.g., Greif et al. 2008, Wise & Abel 2007a, 2008). Since detailed simulations of the fragmentation properties in such a cloud with different levels of pre-enrichment are still lacking, it is timely to carry out an exploratory survey of the crucial physics involved in the fragmentation of such shocked, stream-fed gas.

These cosmic filaments play a pivotal role in galaxy formation by adding a third accretion mode to the two processes that have traditionally been thought to partake in galaxy formation. Spheroidal galaxy components were thought to have been built by gas channeling in galactic mergers (Toomre 1977, White & Rees 1978) and disk components by accretion from a shock-heated intergalactic medium (IGM) during virialization (Rees & Ostriker 1977, Silk 1997). Hot accretion occurs when gas is shock heated to approximately the virial temperature close to the virial radius of the dark matter halo; the gas then cools, falls inward, and circularizes in the galactic disk. Recently, however, a new mode of accretion has been found to dominate in high-σ cosmological peak halos at high redshift (Dekel & Birnboim 2006, Dekel et al. 2009). This mode, coined 'cold flow accretion,' occurs along cosmic filaments that feed gas directly to the inner parts of a galaxy, leading to shocks at radii much smaller than the halo virial radius (see, also, Wise & Abel 2007a, Binney 2004). This differs qualitatively from hot accretion in that the infalling gas passes through the virial shock unaffected, has a much higher density, and is deposited much closer to the center of the galaxy. Cold accretion is theoretically very appealing. It presents a solution to the observed blue-red galaxy bimodality (Baldry et al. 2004). It provides a natural explanation for high redshift galaxies with large star formation rates but no evidence of a major merger (e.g., Genzel et al. 2006). Also, cold accretion naturally arises in many simulations of galaxy formation (Kereš et al. 2005, Dekel & Birnboim 2006, Wise & Abel 2007a, Greif et al. 2008, Harford et al. 2008, Regan & Haehnelt 2009), suggesting this type of accretion is natural to high-σ peak halos at high redshifts within ΛCDM models.

Dark matter halos with masses $\sim 10^8\,M_\odot$ around $z \approx 10$ represent the smallest structures that can be classified as 'first galaxies' (Kitayama & Yoshida 2005, Read et al. 2006, Wise & Abel 2007a, Greif et al. 2008, Bromm et al. 2009). Halos of this mass have virial temperatures $T_{\rm vir} > 10^4$ K which allows efficient cooling via excitation of atomic hydrogen (e.g., Haiman et al. 1997, Miralda-Escude & Rees 1998, Barkana & Loeb 1999, Oh & Haiman 2002). This is the halo mass scale where we first expect to see sustained, possibly self-regulated, star formation, similar to the present-day case. Finally, in $10^8\,M_\odot$ halos, gas accreting along cosmic filaments will drive supersonic turbulence (Wise & Abel 2007a, Greif et al. 2008, Regan & Haehnelt 2009, Klessen & Hennebelle 2010), fundamentally changing the star formation dynamics (Padoan & Nordlund 2002, Mac Low & Klessen 2004, McKee & Ostriker 2007). In this work, as in many others, we define a first galaxy to be one of the first dark matter halos to form with mass $\geq 5 \times 10^7\,M_\odot$, thus meeting the requirement that gas heated to the virial temperature is able to cool through atomic hydrogen excitation (or $\mathrm{Ly}\alpha$) emission.

A further motivation for this work is understanding the formation of low-luminosity dwarf spheriodal satellite galaixes (dSph) and globular clusters (GCs). These structures have similar luminosities, stellar masses, generally no gas nor recent star formation, and contain metal-poor, old stellar populations. However, GCs are small ($\sim 1 - 10\,\mathrm{pc}$) and do not seem to contain much dark matter while dSph galaxies are much larger ($> 100\,\mathrm{pc}$) and are heavily dominated by dark matter as indicated by their large mass-to-light ratios (Mateo 1998, Strigari et al. 2008). It is clear these are two structurally distinct populations (e.g., Kormendy 1985, Belokurov et al. 2007), but it is necessary to understand the cosmological circumstances of their formation. To answer whether the first galaxies are progenitors to dSph galaxies, GCs, or both requires an understanding of star formation in these objects.

With this in mind, we investigate the fragmentation properties of the metal-pre-enriched cold flow accretion in protogalaxies at high redshift, and explore implications for star formation in these objects. Dense, metal-enriched baryonic streams flow along the filaments of the cosmic web and penetrate deep into a protogalaxy. Multiple streams collide with each other, or collide with a turbulently-supported gas accumulation that has already collected in the center of the protogalaxy. Since the stream inflow is supersonic, the colliding gas must pass a strong shock, but then cools rapidly under approximate isobaric conditions. We identify the characteristic fragmentation mass scale in the shocked, isobarically cooling gas. We find that if a strong photodissociating Lyman-Werner (LW) background has significantly suppressed molecule formation, the characteristic mass scale depends strongly on the metallicity content of the gas.

The outline of this work is as follows. In Section 2.2 we describe our methodology for the cooling of shocked, metal-enriched gas. Section 2.3 motivates the initial conditions for our model, including metal abundances and the physics of cold accretion. In Section 2.4 we discuss our fragmentation criteria and the results from our numerical integrations, and summarize our findings and broader implications in Section 2.5. Throughout the paper we assume the ΛCDM cosmological parameters: $\Omega_{\mathrm{m}} = 0.27$, $\Omega_\Lambda = 0.73$, and $h = 0.70$, consistent with the 5 year Wilkinson Microwave Anisotropy Probe results (Komatsu et al. 2009).

2.2 Cooling of Shocked, Metal-Enriched Gas

A cold accretion stream penetrates deep inside the protogalactic halo until it encounters an accretion shock. Subsequently, the shocked gas layer grows in size while cooling isobarically (Shapiro & Kang 1987, Clarke & Bromm 2003), until it becomes gravitationally unstable and fragments into Jeans-mass-sized clumps. Our objective is to calculate the initial masses of these fragments; we do not follow their evolution past the point of initial fragmentation. To this end, we model the evolution of the shocked, cooling gas accurately within the one-zone approximation. We utilize a comprehensive chemical network to track the time evolution of the abundances of all primordial species (H, H^+, H^-, H_2, H_2^+, e^-, He, He^+, D, D^+, and HD) and the most important metal coolants expected at high redshifts: neutral and singly ionized O, Si, C, and Fe (Bromm & Loeb 2003b, Santoro & Shull 2006, Maio et al. 2007, Glover & Jappsen 2007). The cooling gas is subject to compression by the ram pressure of the accretion shock which suggests isobaric conditions are approximately valid in the post-shock region. In Sections 2.2.1 and 2.2.2 we proceed to discuss cooling and heating processes in the shocked gas. In Section 2.2.3 we discuss the relevant chemical processes in the post-shock gas. Finally, in Section 2.2.4 we describe the time evolution of the shock-compressed gas under isobaric conditions.

2.2.1 Cooling Processes

We calculate all relevant cooling and heating processes in low-density, shock heated gas at high redshift. The cooling of gas with primordial abundances set by big bang nucleosynthesis has been extensively studied (e.g., Shapiro & Kang 1987, Oh & Haiman 2002). Above $10^4\,\mathrm{K}$, hydrogen and helium excitation are the dominant cooling channels. Between $200\,\mathrm{K} \lesssim T \lesssim 10^4\,\mathrm{K}$, if molecular hydrogen forms, the cooling that it facilitates is dominant. If present, HD can continue to cool the gas below $200\,\mathrm{K}$ due to its permanent dipole moment and smaller rotational energy level spacing, although an elevated electron fraction is necessary for its efficient formation (Uehara & Inutsuka 2000, Nakamura & Umemura 2002, Johnson & Bromm 2006, Yoshida et al. 2007). Metals, supplied from previous star formation, can be a significant coolant at $T < 10^4\,\mathrm{K}$ due to forbidden, fine structure photon emission from low-lying electronic radiative transitions (Sutherland & Dopita 1993, Gnat & Sternberg 2007) and can substantially change the gas dynamics (Omukai 2000, Bromm & Loeb 2003b). Below 10^4 K, our cooling rate as a function of metallicity closely matches the cooling rates calculated by other authors in gas of similar temperatures and densities (e.g., Santoro & Shull 2006, Maio et al. 2007, Smith et al. 2008). We consider fine structure emission from O, Si, Fe, and C—the species that dominate metal cooling in a low-density, low-metallicity gas (e.g., Santoro & Shull 2006). We find that in the shocked gas in an atomic cooling halo, Si, Fe, and C are, to a large extent, singly ionized (see Section 2.3.3), but O remains mostly neutral. Above 10^4 K, our cooling rate is not accurate at high metallicities (especially for $Z \gtrsim Z_\odot$) as we do not include any multiply ionized species, but since we restrict ourselves to $Z < 10^{-2} Z_\odot$ (see Section 2.3), this assumption does not affect our results (see Figure 4 in Gnat & Sternberg 2007).

Due to NLTE conditions in the low-density IGM, Boltzmann statistics does not describe the state of an atom or molecule, but instead, level populations must be calculated from the principle of detailed balance (see Glover & Jappsen 2007), where electronic collisional excitations and de-excitations are balanced by spontaneous downward transitions. Excitation and de-excitation rates, energy level spacings, and spontaneous emission coefficients for C, C^+ Si, Si^+, Fe, Fe^+, O, and O^+ are the parameters needed to determine the fine structure cooling rate. We refer the reader to other sources, such as Hollenbach & McKee (1989) (hereafter HM89), Santoro & Shull (2006), and Glover & Jappsen (2007), for detailed discussion of the individual cooling rates. We here only provide the references from which we compiled our data: C – HM89 and Johnson et al. (1987); C^+ – HM89 and Wilson & Bell (2002); O – Glover & Jappsen (2007) and Bell et al. (1998); Si – HM89; Si^+ – HM89; Roueff (1990); Fe, Fe^+ – HM89.

The simplest model of fine structure cooling from an atom is one in which the electron has only one excited state to occupy, the so-called two level system. In this system, the excited state level population is given by (e.g., Maio et al. 2007)

$$n_2 = \frac{\gamma_{12}^{\mathrm{H}} + \gamma_{12}^{\mathrm{e}} n_{\mathrm{e}}/n_{\mathrm{H}}}{\gamma_{12}^{\mathrm{H}} + \gamma_{21}^{\mathrm{H}} + (\gamma_{12}^{\mathrm{e}} + \gamma_{21}^{\mathrm{e}}) n_{\mathrm{e}}/n_{\mathrm{H}} + A_{21}/n_{\mathrm{H}}} n_{\mathrm{tot}} \,, \tag{2.1}$$

where n_2 is the number density of particles in the second excited state, n_{tot} the total number density of the species, while $\gamma_{12}^{\{\mathrm{H},e\}}$ and $\gamma_{21}^{\{\mathrm{H},e\}}$ are, respectively, the excitation and de-excitation rates due to collisions with neutral hydrogen and free electrons (collisions with hydrogen ions, H_2, and other species are subdominant). The corresponding volumetric cooling rate for fine structure line emission is given by $\Lambda_{\mathrm{line}} = n_2 A_{21} \Delta E_{21}$, where A_{21} is the spontaneous emission coefficient and ΔE_{21} is the energy difference between states. For n level systems, n coupled equations are solved to determine the level populations. The CMB temperature sets a thermodynamic lower limit on the gas temperature (see Larson 1998); we incorporate this limit by replacing the cooling rates with the effective rate: $\Lambda_{\mathrm{eff}}(T) = \Lambda(T) - \Lambda(T_{\mathrm{CMB}})$.

For illustration, in Figure 2.1 we show the non-equilibrium cooling rate as a function of metallicity, evaluated at every step during the evolution of the post-shock gas in our fiducial model with a $10^8\,M_\odot$ halo at $z = 10$, solar distributions of metals, and with a high LW radiation background ($J_{21,\mathrm{LW}} = 10^4$, see Section 2.3.3). The latter significantly photodissociates H_2, and will keep metallic species singly ionized (see Section 2.3.3). The wide peak at $T \sim 200\,\mathrm{K}$ is due to the isobaric increase in density towards lower temperatures. The initial values for density and temperature are $4 \times 10^3\,\mathrm{cm}^{-3}$ and $1.1 \times 10^4\,\mathrm{K}$, respectively, and the initial chemical abundances are set to the values corresponding to thermal and statistical equilibrium at this temperature. Below $T \sim 10^4\,\mathrm{K}$, the cooling rate is a strong function of metallicity. Figure 2.2 shows the individual elemental contributions to the nonequilibrium cooling curve for a solar abundance pattern. Metal cooling, particularly from O, Fe^+, and Si^+, dominates below $800\,\mathrm{K}$;

H_2 dominates between 800 and $8,000\,\mathrm{K}$ .The critical density for the C$^+$ fine structure transition is $n_{\mathrm{cr,C^+}} = A_{10}/\gamma_{10} \simeq 3 \times 10^3\,\mathrm{cm}^{-3}$. Thus, at the densities sampled by our isobarically cooling gas, $n = 10^3 - 10^6\,\mathrm{cm}^{-3}$, the C$^+$ line is in LTE, which makes it a weaker coolant compared to Fe$^+$, Si$^+$, and O, whose critical densities are $\sim 10^5 - 10^6\,\mathrm{cm}^{-3}$, so thermalization occurs at a later evolutionary stage (Santoro & Shull 2006). In this regime, HD is always an ineffective coolant. If, however, metallicity is $Z < 10^{-5}\,Z_\odot$, and molecules are permitted to form, the gas is able to reach T_{CMB} by HD cooling.

2.2.2 Heating Processes

Since we here ignore the effect of dust, the predominant source of heating is UV pumping of H_2, particularly at higher densities. To compute the rate, we assume a pumping rate 8.5 times that of the photodissociation of H_2 (Draine & Bertoldi 1996, Glover & Jappsen 2007). If each pumping produces $\sim 2\,(1 + n_{\mathrm{cr}}/n)^{-1}\,\mathrm{eV}$ of heat (Burton et al. 1990), where n_{cr} is the critical density for H_2 (which we always take to be $6000\,\mathrm{cm}^{-3}$), the corresponding heating rate is: $\Gamma = 2.7 \times 10^{-11} R_{\mathrm{diss}} n_{\mathrm{H_2}} (1 + n_{\mathrm{cr}}/n)^{-1}\,\mathrm{erg\,s^{-1}\,cm^{-3}}$; the computation of R_{diss} is discussed in Section 2.3.3 below.

Other significant sources of heating are the photoionization of metallic species and the radiative coupling to the CMB. It is safe to assume that at $z \sim 10$, prior to complete reionization, the mean free path of H ionizing photons is very short compared to photons below the Lyman limit, thus rendering heating from H and He ionization unimportant. However, photons below the Lyman limit should be $1/f_{\mathrm{esc}} \sim 10^2$ times more abundant than H-ionizing ones (Bromm & Loeb 2003b), making photoionization heating of metallic species with first ionization potentials below 13.6 eV (C, Si, and Fe) dominant. This also has consequences for the pho-

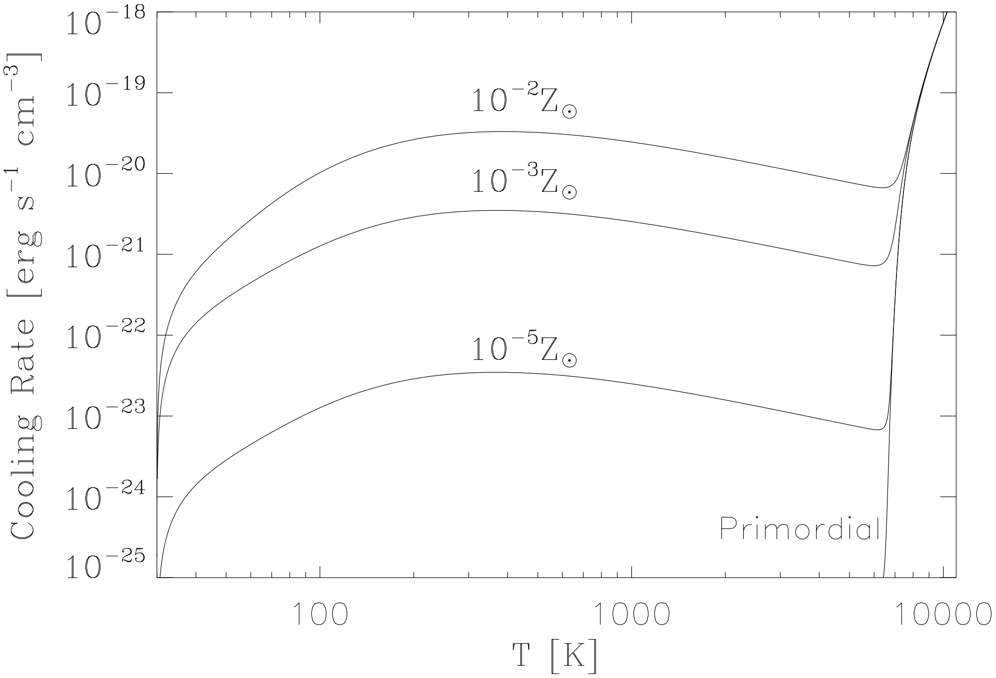

Figure 2.1 Post-shock non-equilibrium cooling rate for differing metallicites for a $10^8\,M_\odot$ at $z = 10$, using a solar pattern of metals. This figure only includes cooling from hydrogen excitation and metallic fine structure emission - molecules are ignored. The bump at $T \sim 200\,\mathrm{K}$ is due to the density increase towards lower temperatures due to our isobaric density evolution. The initial density is $n \sim 4 \times 10^3\,\mathrm{cm}^{-3}$. Towards $30\,\mathrm{K}$ the cooling rate drops off as we approach T_{CMB}. Below $T \sim 10^4\,\mathrm{K}$ the cooling rate is a strong function of metallicity.

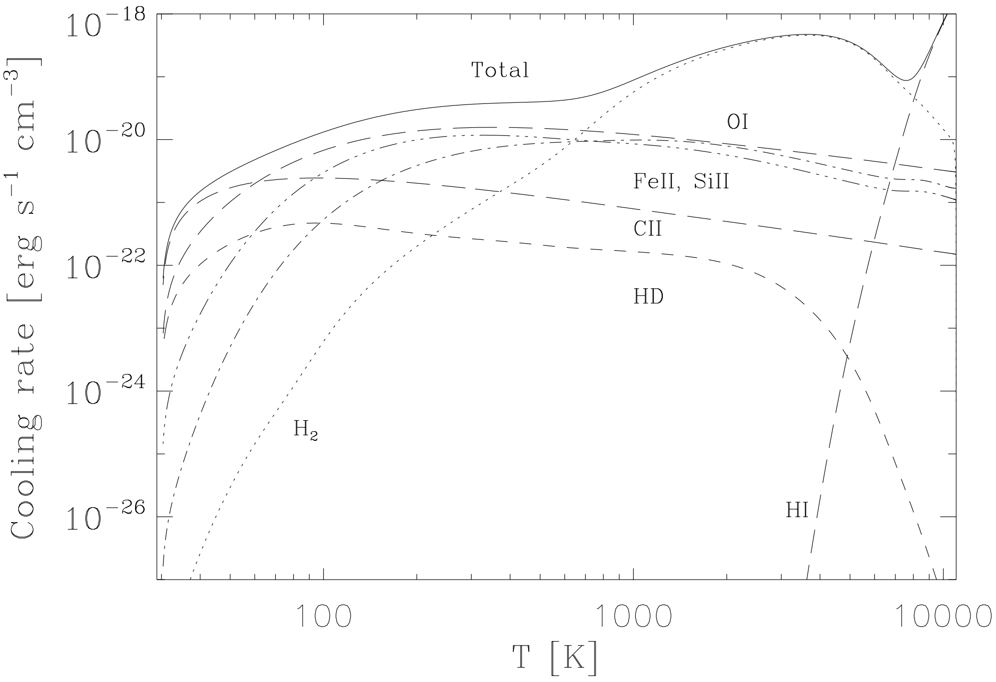

Figure 2.2 Post-shock non-equilibrium cooling rate showing the contributing components for an accretion shock in a $10^8\,M_\odot$ dark matter halo at $z = 10$ with $J_{21} = 10$ and metallicity $Z = 10^{-2}\,Z_\odot$ with a solar pattern of metals. It is evident that fine structure emission from Fe^+, Si^+ and O are the dominant metal coolants. C^+ is not effective as the density is above its critical density, $n_{\mathrm{cr,C^+}} \simeq 3 \times 10^3\,\mathrm{cm}^{-3}$. H_2 cooling dominates from $1000 - 6000\,\mathrm{K}$ while metals dominate below 1000 K. HD is always an insignificant coolant at $10^{-2}\,Z_\odot$.

todissociation of H_2, which occurs in the LW bands just below 13.6 eV (see Section 2.3.3). As discussed in Section 2.2.1, CMB heating is achieved by modifying the effective cooling rate. Overall, heating of the gas is generally not a significant effect for the evolution considered here.

2.2.3 Chemistry

Our chemical model includes all relevant primordial chemical species: H, H^+, H^-, H_2, H_2^+, e^-, He, He^+, He^{++}, D, D^+, and HD (e.g., Galli & Palla 2002). We also include the most important metal coolants — neutral and singly ionized C, Si, O, and Fe. Collisional ionization, recombination, and charge exchange reactions for C, Si, and O are taken from the compilation in Jappsen et al. (2009b). The reactions for Fe were taken from HM89 and Woods et al. (1981).

Chemically, the formation and destruction of H_2 and HD has the strongest impact on our results as they can be very effective low-temperature coolants. In the absence of dust, molecular hydrogen can form through two channels (e.g., Galli & Palla 1998). In the H^- channel, H^- and H combine to form H_2 and e^-, whereas in the H_2^+ channel, H_2^+ and H participate in a charge exchange reaction producing H_2 and H^+. The efficiency of these formation channels strongly depends on the abundance of free electrons that are required for H^- and H_2^+ synthesis (Oh & Haiman 2002). In all our calculations, the H^- channel dominates. Destruction of H_2 is mainly from UV photons in the LW bands and will be discussed in Section 2.3.3. HD may be an important coolant below $200\mathrm{K}$ (Johnson & Bromm 2006). Its formation proceeds by a charge exchange reaction between D^+ and H_2. In our physical scenario, HD will only be a significant coolant in a low metallicity environment.

2.2.4 Isobaric Cooling and Time Evolution

If the post-shock cooling is thermally stable and if the shocked gas is in approximate pressure balance, the thermodynamic evolution of a gas packet that has passed the shock obeys conservation of energy, as expressed by (see, e.g., Shapiro & Kang 1987):

$$\frac{d(\rho\epsilon)}{dt} = \left(\epsilon + \frac{p}{\rho}\right)\frac{d\rho}{dt} - \Lambda + \Gamma, \tag{2.2}$$

where ρ, ϵ, p, Λ, and Γ, are, respectively, the gas density, specific internal energy, pressure, volumetric cooling and heating rate. We can write the pressure as

$$P = (\gamma - 1)\rho\epsilon = \rho k_{\mathrm{B}} T/\mu \tag{2.3}$$

where μ is the mean molecular weight (in grams) and γ is the adiabatic index. In our regime, γ can approximated as

$$\gamma = \frac{5 + 5x_{\mathrm{He}} + 5x_{\mathrm{e}} - 3x_{\mathrm{H_2}}}{3 + 3x_{\mathrm{He}} + 3x_{\mathrm{e}} - x_{\mathrm{H_2}}}, \tag{2.4}$$

where x_i is the abundance of species i with respect to the number density of hydrogen nuclei. Isobaricity can be expressed as

$$\frac{d\ \ln\ \rho}{dt} + \frac{d\ \ln\ T}{dt} - \frac{d\ \ln\ \mu}{dt} = 0. \tag{2.5}$$

By combining Equations (2.2), (2.3), and (2.5) we find that the gas temperature evolves according to (e.g., Glover & Abel 2008)

$$\frac{dT}{dt} = \frac{T}{\mu}\frac{d\mu}{dt} + \frac{T}{\gamma(\gamma-1)}\frac{d\gamma}{dt} - \frac{\gamma-1}{\gamma}\frac{\mu}{k_{\mathrm{B}}}\frac{\Lambda-\Gamma}{\rho}, \tag{2.6}$$

for an isobaric gas.

Equations (2.6) and N_{species} additional differential equations following the abundances of each chemical species are solved and we integrate the $N_{\mathrm{species}}+1$ differential equations implicitly using the Bulirsch-Stoer-type, semi-implicit extrapolation mid-point method. The coarsest Bulirsch-Stoer time step is set to $\Delta t = \min\{n_i/|\dot{n}_i|\}$.

Isobaricity, i.e., pressure equilibrium, is a valid approximation if the sound crossing time of the post shock region is shorter than the cooling time, $t_{\rm sound} < t_{\rm cool}$. In Figure 2.3, we confirm that this condition is satisfied throughout the evolution of the gas leading to gravitational instability and fragmentation, except for the highest metallicity case, $Z = 10^{-2}\,Z_\odot$, when the cooling time becomes shorter than the sound crossing time at $\sim 2 \times 10^4\,{\rm cm}^{-3}$. We thus conclude that for high metallicity, thermal instabilities may play a dynamically significant role. It is interesting that these instabilities only occur in the presence of efficient metal cooling. Thermal instabilities (e.g., Field 1965, Balbus 1986) are one proposed mechanism for the formation of molecular clouds and the origin of turbulence. Niklaus et al. (2009) performed two-dimensional adapative mesh refinement (AMR) simulations of colliding flows with non-zero metallicity and found turbulent, clumpy structures formed from thermal instabilities triggered by a supersonic collision. It is tempting to suggest that the thermal instabilities we anticipate here at substantial metallicities could lead to clumpiness and turbulence like that seen in Niklaus et al. (2009).

2.3 Model Parameters

The choice of parameters for our modeling of the accretion flow into the protogalaxy will govern the resulting fragmentation mass scale. This section focuses on the three most important model ingredients. In Section 2.3.1, we discuss the properties of the cold flows into high redshift galaxies. In Section 2.3.2, we describe the possible abundance patterns of accreting gas and place an upper limit on the metallicity content of the gas. Finally, in Section 2.3.3, we discuss the effect of a LW radiation background on the dissociation of molecular hydrogen and the ionization of metallic species.

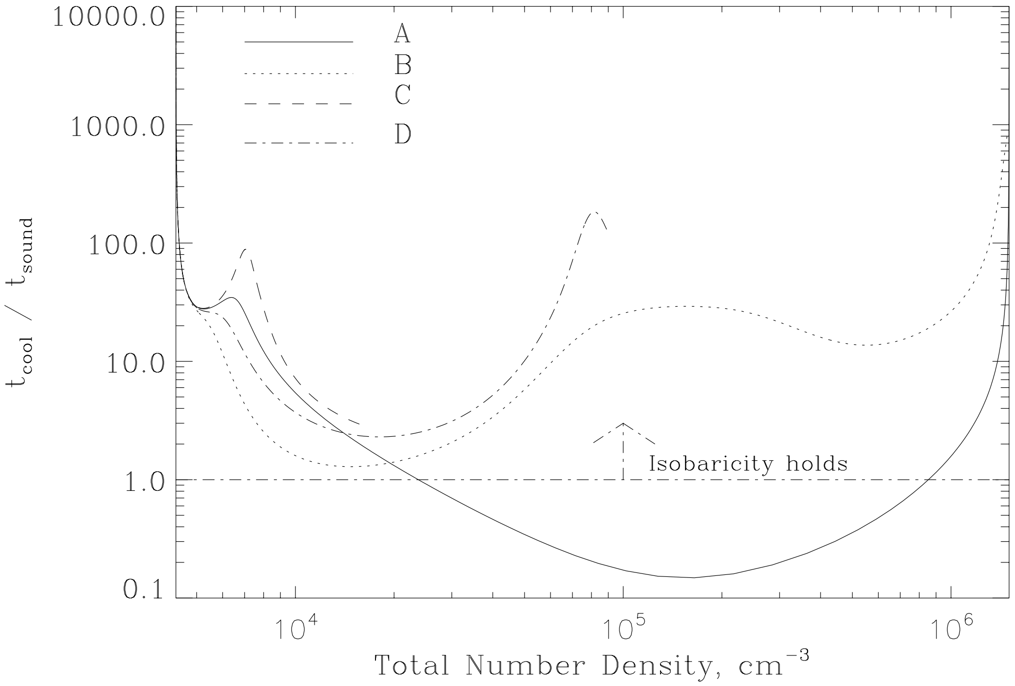

Figure 2.3 Test of the validity of our isobaric density evolution assumption. The four lines correspond as shown to the four cases of Table 2.2. As shown, isobaricity holds except in case A (strong metal cooling), where it is violated for densities above $\sim 10^4\,\mathrm{cm}^{-3}$. This will likely lead to runaway cooling collapse in the density regime where $t_{\mathrm{cool}}/t_{\mathrm{sound}} < 1$. In the other cases, where H_2 cooling dominates, we conclude that pressure support acts on a smaller timescale than radiative cooling. This effectively allows the ram pressure of the cold flow to keep the shocked region at approximately constant pressure throughout the evolution, at least until fragmentation occurs. Runs C and D undergo fragmentation before being able to reach high densities, and we do not follow their evolution past this point.

2.3.1 Cold Flow Accretion

Birnboim & Dekel (2003) consider accretion of non-virialized gas from the IGM into a dark matter halo and find that, at redshifts $z > 2$, under the assumptions of spherical symmetry, a stable virial accretion shock does not exist in halos smaller than $10^{11}\,M_\odot$ due to the rapid cooling of the post-shock gas. Our model halos are well within this regime. Instead, the accreting gas continues on supersonic infall trajectories until it reaches much closer to the center of the halo. Kereš et al. (2005) find, using smoothed particle hydrodynamics (SPH) simulations, that in halos with masses $< 10^{11.4}\,M_\odot$ at $z = 3$, almost none of the gas that enters the galaxy has been heated to the virial temperature, further supporting the conclusion that cold accretion is the main feeder of baryonic material into galaxies at high redshift.

Wise & Abel (2007a) simulated the cosmological formation of a $\sim 10^8\,M_\odot$ cosmological object and find that the virialization of shocked accretion streams creates a nearly isothermal ($\sim r^{-12/5}$) density profile containing supersonically turbulent gas. Greif et al. (2008) carried out a similar simulation and found filamentary accretion dominates the buildup of the baryonic component of a similar mass galaxy and high redshift. In their simulation, the density of cold accretion streams just prior to impact with the central turbulent mass concentration was $\sim 10^3\,\mathrm{cm}^{-3}$ with a temperature of $\sim 200\,\mathrm{K}$. The pre-shock number density in cold streams can be estimated by considering infall in a halo with mass $M = 10^8\,M_8\,M_\odot$ and virial radius $R_{\mathrm{vir}} = 1.5\,M_8^{1/3}\,[(1+z)/10]^{-1}$ kpc, where in the latter we define as the radius within which the mean density of a halo equals 200 times the critical density of the universe. If the density of the infalling baryons scales as $\propto r^{-2}$, the hydrogen number density extrapolated to the innermost 10 pc, the approximate radius of cold-stream collisions and shock formation (Wise & Abel 2008), is $\sim 10^3\ \mathrm{cm}^{-3}$, consistent with the numerical result.

2.3.2 Abundances from Early Enrichment

We restrict ourselves to an upper metallicity limit of $10^{-2}\,Z_{\odot}$. This follows from the work of Greif et al. (2008) who find that a $10^{8}\,M_{\odot}$ halo will be assembled out of material that has experienced a maximum of ~ 10 Pop III supernovar. Bromm et al. (2003) showed that in a Pop III supernova explosion, $\sim 90\%$ of the metallic yield will be ejected into the IGM. Greif et al. (2010) find that accretion inflows return roughly 50% of the metallic enrichment to the central halo by the time it grows to $\sim 10^{8}\,M_{\odot}$. Assuming a homogeneous density distribution of metals over the halo, roughly 1 proper kpc in size, gives a metallicity fraction of $\sim 10^{-3}\,Z_{\odot}$, suggesting that $10^{-2}\,Z_{\odot}$ is a conservative upper limit for the metallicity. We explore the effect of metallicity that varies from a primordial composition, effectively described by $Z \leq 10^{-8}\,Z_{\odot}$, to this upper limit, using both pair-instability supernova (PISN) and solar abundance patterns.

There have been assertions that a LW background from Pop III stars could inhibit further star formation by destroying H_2 and H^{-}, which would keep the first galaxies starless and thus metal free or metal deficient (e.g., Haiman & Bryan 2006, Dijkstra et al. 2008). Other studies have shown that an ionizing background enhances metal enrichment as a high rate of ionization encourages molecule formation and enhanced cooling (e.g., Johnson et al. 2008) . Ahn & Shapiro (2007) revisited the question of radiative feedback from Pop III stars using detailed radiation-hydrodynamical simulations and found radiative feedback to be neutral for Pop III.2 star formation (stars still forming from pure H/He gas but influenced radiatively by previous star formation), suggesting there will be a metal abundance of at least $10^{-4}\,Z_{\odot}$ in these protogalaxies, depending on the halo capture fraction of supernovae nucleosynthetic products. The metal abundance pattern is also not known with any certainty. Umeda & Nomoto (2002, 2003) suggest that the abundance pattern reflects enrichment from hypernovae, produced by stars in the $20 - 120\,M_\odot$ mass range, while other authors argue that Pop III stars end their lives as PISNe, producing a very different metallicity pattern (Heger & Woosley 2002). Therefore, it is crucial to explore a range of abundance patterns in our modeling.

Finally, the mixing of heavy elements within the protogalaxy after they get incorporated through cold accretion streams, or following a SN explosion inside the galaxy itself, remains poorly understood. Heavy elements produced from Pop III stars may never return to the galaxy and may reside in the IGM indefinitely. Another possibility is that metals may leave the host galaxy after a supernova and return at a later time. Once the galaxy is assembled, will there be a region of high metallicity contained around supernovae, or will metallicity quickly diffuse throughout the protogalaxy? Inhomogeneous mixing may create pockets of enhanced enrichment, with a metallicity much greater than $Z_\odot$. The degree of mixing or clumpiness of the metal distribution inside the protogalaxy will be investigated in greater detail in later work.

Our numerical integrations are run for both standard solar (see Grevesse & Sauval 1998) and PISN metal abundance patterns. PISN patterns are from Heger & Woosley (2002) for a 150 and $250\,M_\odot$ progenitor stars (corresponding to a 75 and $125\,M_\odot$ helium core, respectively). Table 2.1 represents the number density (in cm^{-3}) of metallic species given a hydrogen number density of $1\,\mathrm{cm}^{-3}$. The PISN values are computed with the same overall mass fraction in metals, but differing elemental proportions compared to the Sun.

Table 2.1. Metal abundance patterns in the Solar photosphere, from a 150, and from a $250\,M_\odot$ PISN, all normalized to the Solar mass fraction of metals (i.e., $Z = Z_\odot$).

Pattern	$x_{\rm C}$	$x_{\rm Fe}$	$x_{\rm O}$	$x_{\rm Si}$	Ref.
Solar	2.5×10^{-4}	2.8×10^{-5}	4.6×10^{-4}	3.2×10^{-5}	1
$150\,M_\odot$ PISN	5.0×10^{-5}	1.2×10^{-6}	5.1×10^{-4}	1.4×10^{-4}	2
$250\,M_\odot$ PISN	1.4×10^{-5}	1.3×10^{-4}	1.5×10^{-4}	1.0×10^{-4}	2

References. — (1) Grevesse & Sauval (1998); (2) Heger & Woosley (2002)

2.3.3 Radiation Field

The rate of photoionization of a species ($R_{\rm photo}$) for an optically thin gas is given by (e.g., Osterbrock & Ferland 2006)

$$R_{\rm photo} = \int_{\nu_{\rm th}}^{\infty} \frac{4\pi J_\nu}{h\nu} \sigma(\nu)\, d\nu, \tag{2.7}$$

where $J_\nu = 10^{-21}\, J_{21}\, {\rm ergs\, s^{-1}\, cm^{-2}\, Hz^{-1}\, sr^{-1}}$ is the mean intensity, $\sigma(\nu)$ is the frequency dependent photoionization cross section, and the integration runs from the threshold photoionization frequency, $\nu_{\rm th}$, to infinity. In the case of metallic photoionizations which are dominant (see Section 2.2.2), we run this integration to $\nu_{\rm H}$, the ionization threshold of hydrogen, as hydrogen ionizing photons are effectively shielded by the IGM prior to reionization. Photoionization cross-sections for C, Si, Fe, and O are taken from the fits of Verner et al. (1996). For our incident spectrum, we use thermal Planck spectra with $T_* = 10^4$ and 10^5 K and a power law spectrum, $J_\nu \propto \nu^{-1}$. As in Bromm & Loeb (2003a), we normalize these spectra at the Lyman limit by J_{21}. The photodissociation of H_2 is a more complicated process occuring through the two-step Solomon process (Stecher & Williams 1967) by photons in the LW bands, $11.2 - 13.6\,\mathrm{eV}$. A commonly used approximation for this rate of dissociation, $R_{\mathrm{diss,H_2}}$, is given by $\sim 1.38 \times 10^9 J_{\bar{\nu}}$ where $J_{\bar{\nu}}$ is the mean intensity at 12.4 eV, the mean energy of a LW band photon (see Abel et al. 1997). We assume the photodissociation rate of HD equals that of $\mathrm{H_2}$.

At high column densities, $\mathrm{H_2}$ can be particularly effective at shielding itself from LW radiation which can significantly alter its photodissociation rate (e.g., Oh & Haiman 2002). Draine & Bertoldi (1996) provide an approximation for the shielding factor such that $R_{\mathrm{diss}} \propto f_{\mathrm{shield}}$, where $f_{\mathrm{shield}} \simeq \min[1.0, (N_{\mathrm{H_2}}/10^{14}\mathrm{cm}^{-2})^{-0.75}]$ with $N_{\mathrm{H_2}}$ being the column density of $\mathrm{H_2}$. However, this applies to a static, cold medium. If the LW bands are Doppler shifted by large thermal or bulk motions, the shielding rate will be much lower. In in accreting protogalaxy, where large-scale velocity gradients reach ~ 20 km s^{-1}, self-shielding will certainly be overestimated within this prescription. Taking thermal broadening into consideration, Draine & Bertoldi (1996) provide another fit to the shielding factor as

$$f_{\mathrm{shield}} = \frac{0.965}{(1 + x/b_5)^2} + \frac{0.035}{(1 + x)^{0.5}} \exp[-8.5 \times 10^{-4}(1 + x)^{0.5}], \tag{2.8}$$

where $x = N_{\mathrm{H_2}}$ and $b_5 = b/10^5$ cm s^{-1}. We follow Ahn & Shapiro (2007) in setting $b = 9.12$ km s^{-1}, as their physical system is approximately similar to ours. Although this will still overestimate the amount of self-shielding when bulk motions dominate, it is an improvement over the previous fit and will be used in computing our value of $\mathrm{H_2}$ self-shielding.

The radiation field present in these high redshift protogalaxies is uncertain, owing to the contribution from the external, global IGM field, and the local field produced by internal Pop III/II stars. One can estimate, at $z = 10$, that the intensity just above the Lyman limit, J_{21}^{+}, necessary to reionize the universe is ~ 40

(Bromm & Loeb 2003a). However, photons with energies below the Lyman limit are virtually free to escape their host halo, so that the corresponding intensity, J_{21}^{-}, which includes the H_2 dissociating LW bands, could potentially be $f_{\rm esc}^{-1} \sim 100$ times higher, where $f_{\rm esc}$ is the escape fraction of H-ionizing photons (Wood & Loeb 2000). Other recent estimates (Razoumov & Sommer-Larsen 2010, Wise & Cen 2009) have found $f_{\rm esc} \sim 0.25 - 1$ in dwarf galaxies at high redshift. Finally, the LW background can be elevated orders of magnitude above the global average LW field in clustered halos (Dijkstra et al. 2008, Whalen et al. 2008, Johnson et al. 2008, Ahn et al. 2009, Shang et al. 2010) . For this study, we take $J_{21} = 10$ and $J_{21} = 10^4$, representing small and large radiation fields which could be realistically present at this epoch.

2.4 Thermal Evolution and Fragmentation

We now consider the case of a cold accretion stream which is shock heated in the center of a primordial protogalaxy. In Section 2.4.1 we derive a simple criterion for when the post-shock region will fragment based on the free-fall and sound crossing times. Section 2.4.2 describes the thermal evolution of the post-shock region, and presents the fragmentation mass scale for different parameter choices, whereas Section 2.4.3 outlines a simple analytical model for the critical metallicity in molecule-free regime.

2.4.1 Fragmentation Criterion and Mass Scale

To derive a rough estimate of when fragmentation will occur, we consider the growth of the shocked gas region within our one-zone model. Following the shock that terminates the accretion stream near the center of the protogalaxy, the gas begins to cool off isobarically (see Shapiro & Kang 1987, Clarke & Bromm 2003) from the virial temperature of the halo, $T_{\rm vir} = \frac{1}{2}\mu m_p v_{\rm vir}^2/k_{\rm B} \simeq 2 \times 10^4 \mu_{0.6} M_8^{2/3}[(1+$

$z)/10]\,\mathrm{K}$, where $\mu = 0.6\,\mu_{0.6}$ is the mean molecular weight in the immediate post-shock gas. Applying the standard Jeans analysis for gravitational instability, we take it that fragmentation occurs when the ever-increasing sound crossing time equals the decreasing free fall time of the post-shock region. Specifically, we examine three time scales: the cooling time, $t_{\mathrm{cool}} \simeq \frac{3}{2} k_{\mathrm{B}} T n_{\mathrm{tot}} / \Lambda(n, T)$, the free-fall time, $t_{\mathrm{ff}} = (3\pi/32G\rho)^{1/2}$, and the sound-crossing time, $t_{\mathrm{s}} \simeq L/c_{\mathrm{s}}$, where L is the length of the shocked slab, $\Lambda(n, T)$ the volumetric cooling rate, and $c_{\mathrm{s}} = (\gamma k_{\mathrm{B}} T/\mu m_p)^{1/2}$ the adiabatic sound speed. The pre-shock density ρ_0 is related to the instantaneous post-shock density ρ_1 via $\rho_0(v_{\mathrm{infall}} + v_{\mathrm{shock}}) = \rho_1 v_{\mathrm{shock}}$. Since the shock is strong, $\rho_1 \sim 4\rho_0$. If the post shock gas further cools and isobarically compresses to $\rho(t)$, then the shock velocity in the frame of the gas will be further reduced by a factor of $\sim \rho_1/\rho(t)$, or $v_{\mathrm{shock}}/v_{\mathrm{infall}} \sim \rho_0\rho_1/[\rho(t)(\rho_1 - \rho_0)] \sim \frac{4}{3}\rho_0/\rho(t)$, and thus the length of the post shock region is (ignoring numerical factors order unity),

$$L(t) \sim v_{\mathrm{shock}} t \sim \frac{\rho_0}{\rho(t)}\, v_{\mathrm{vir}}\, t, \tag{2.9}$$

where $v_{\mathrm{infall}} = v_{\mathrm{vir}} = (GM/R_{\mathrm{vir}})^{1/2} \simeq 23\, M_8^{1/3} [(1+z)/10]^{1/2}\,\mathrm{km\ s^{-1}}$ the virial (or infall) velocity. Isobaric cooling requires $t_{\mathrm{cool}} > t_{\mathrm{s}}$, while gravitational (Jeans) instability and the onset of fragmentation requires $t_{\mathrm{s}} > t_{\mathrm{ff}}$. It is possible that gravitational instability does not set in before the gas cools to the CMB temperature. In this case, isobaricity is guaranteed and the fragmentation mass scale is entirely set by the CMB temperature and the initial conditions of the accretion flow.

We assume that following the initial gravitational instability, the gas fragments into clumps with masses given by the local Bonnor-Ebert (BE) mass,

$$M_{\mathrm{BE}} \simeq 150\, M_{\odot}\, (T/200\,\mathrm{K})^2, \tag{2.10}$$

assuming isobaric density evolution with $T_i = T_{\mathrm{vir}} = 1.1 \times 10^4\,\mathrm{K}$ and $n_i = 4.0 \times 10^3\,\mathrm{cm^{-3}}$. The resulting clump size sets an upper limit to the masses of the star

Table 2.2. Parameters for the Different Runs

Run	Metallicity	J_{21}	T_*	$M_{\rm BE}$ Final
A.........	$10^{-2}\,Z_\odot$	10^4 K	10^4	$\sim 3\,M_\odot$
B.........	$10^{-6}\,Z_\odot$	10 K	10^4	$\sim 10\,M_\odot$
C.........	$10^{-6}\,Z_\odot$	10^3 K	10^4	$\sim 10^5\,M_\odot$
D.........	$10^{-6}\,Z_\odot$	10^3 K	10^5	$\sim 10^4\,M_\odot$

in the aftermath of the fragmentation. Due to subtle processes affecting post-fragmentation accretion, the final stellar masses could be a fraction of the fragmentation scale: $M_\star \simeq \alpha M_{\rm BE}$, where $\alpha < 0.5$ in star formation in the local universe (e.g., McKee & Tan 2002).

2.4.2 Case Studies

For our case studies, we consider a high and low metallicity case (10^{-2} and $10^{-6}\,Z_\odot$), a high and low LW radiation fields ($J_{21} = 10, 10^3$, and 10^4), and source temperatures of $T_* = 10^4$ and 10^5 K. We do not present a run with high metallicity and efficient molecular cooling, but we do comment on the outcome of such a run at the end of this section. In Table 2.2 we provide the parameters of our four representative runs. We present the results for each case in succession. See Figures 2.4–2.7 for the temperature history, cooling rate, H_2 fraction, and ionization degree (defined such that ionization degree $\equiv n_{e^-\rm free}/n_{p^+\rm any\ form}$), respectively, for each run..

Run A represents a relatively high metallicity environment with a strong LW background that photodissociates H_2, rendering metals the predominant coolant at $T < 10^4$ K. As in all our runs, we assume that the baryons in dark matter filaments penetrate deeply into the center of a protogalaxy where they undergo a strong shock with $\mathcal{M} = v_{\rm vir}/c_{\rm s} \sim 10$. Calibrating to the gas density in Greif et al. (2008) as explained in Section 2.3.1 above, the post-shock number density is $4n_0 \sim 4 \times 10^3\,{\rm cm}^{-3}$. The shock raises the gas temperature to $T_{\rm vir} \sim 1.1 \times 10^4\,{\rm K}$. At this temperature, the gas cools effectively via atomic hydrogen line excitation, while the size of the post-shock region begins to increase in size according to equation (2.9). After $\sim 10^5\,{\rm yr}$ the gas has cooled to $\sim 35\,{\rm K}$, which is slightly above $T_{\rm CMB}(z = 10) \simeq 30\,{\rm K}$ due to UV pumping of H_2, and after $\sim 1.5 \times 10^6\,{\rm yr}$ the post-shock region has reached the fragmentation criterion ($t_{\rm ff} < t_{\rm sound}$). We do not follow the evolution past this point. The radiation background ($J_{21} = 10^4$) has prevented an appreciable amount of H_2 from building up, with $f_{\rm H_2} \equiv n_{\rm H_2}/n_{\rm H}$ never exceeding 10^{-7}. The BE mass at the point of fragmentation is $\sim 3M_\odot$. Using a fit to the baryonic growth rate of halos of $\dot{M} \simeq 6.6\, M_{12}^{1.15}(1+z)^{2.25} f_{.165}\, M_\odot\,{\rm yr}^{-1}$ (Dekel et al. 2009), where $M_{12} = M_{\rm vir}/10^{12}\,M_\odot$ and $f_{.165}$ is the halo baryonic fraction in units of the cosmological value $\Omega_{\rm b}/\Omega_{\rm m} \simeq 0.165$, we find that the protogalaxy accreted $\sim 5 \times 10^4\,M_\odot$ of baryons before the onset of fragmentation. If all these baryons experienced fragmentation, this would represent a region with $\sim 10^4$ separate fragments, possibly the precursor to a stellar or globular cluster (see Bromm et al. 2002). For more realistic star formation efficiencies, of order ~ 0.1, we would still expect a sizable cluster of Pop II stars to arise.

Run B explores a low metallicity environment together with a feeble LW background which allows for H_2/HD formation and cooling. Starting from the same initial density and temperature as Run A, molecular hydrogen, now able to form more effectively, reaches an abundance $f_{\rm H_2} \sim 10^{-3}$ only $10^3\,{\rm yr}$ after the shock passage; H_2 and HD dominate the cooling from $8,000$ to $30\,{\rm K}$ (see Fig. 2.5). Like in Run A, the post-shock region fragments after $\sim 10^6\,{\rm yr}$ at a temperature of $\sim 50\,{\rm K}$. The final BE mass is $\sim 10\,M_\odot$. Overall, this run is very similar to case A, but cooling is now dominated by $\mathrm{H_2}$ and HD instead of metallic fine structure lines. The likely end product is a collection $\sim 10^{3-4}$ fragments.

Run C is intended to illustrate the result for a post-shock region with little metal enrichment and a large enough LW background to keep $\mathrm{H_2}$ cooling suppressed, similar to the case examined in Bromm & Loeb (2003a). Initially, the gas is still able to cool via atomic hydrogen excitation to $\sim\ 6,000\,\mathrm{K}$, when the cooling time becomes similar to the Hubble time. The gas thus stalls at $6,000\,\mathrm{K}$, at a density of $6 \times 10^3\,\mathrm{cm^{-3}}$, until it fragments $10^6\,\mathrm{yr}$ after the shock. The final BE mass is $10^4\,\mathrm{M_\odot}$ while the total accreted mass is also of this order. This accretion episode, with no effective low temperature coolant, produced one large fragment, possibly indicative of an object which will not fragment further and become a super massive black hole (SMBH) precursor (Omukai 2001, Bromm & Loeb 2003a, Shang et al. 2010). Because of our overestimation of $\mathrm{H_2}$ self-shielding (see Section 2.3.3), this value reflects a lower limit on the fragmentation mass scale, which is most likely higher, possibly large enough to facilitate one large $10^5\,M_\odot$ fragment capable of direct collapse to a SMBH.

Run D has the same initial conditions as Run C, except that the blackbody source temperature is now $T_* = 10^5\,\mathrm{K}$ instead of $10^4\,\mathrm{K}$, more representative of the type of sources associated with Pop III stars (Bromm et al. 2001). Because of the normalization at 13.6 eV, a blackbody of $T_* = 10^5\,\mathrm{K}$ is much less effective at destroying $\mathrm{H^-}$, so that $\mathrm{H_2}$ formation is inhibited much less than for a $T = 10^4\,\mathrm{K}$ blackbody (see Fig. 2.6). The slightly more effective $\mathrm{H_2}$ cooling leads to a final fragmentation mass scale of $10^3\,M_\odot$. Like in case C, overestimation of $\mathrm{H_2}$ self shielding sets this as a lower limit on the fragmentation mass scale.

Our results indicate that if there is a low temperature coolant available, either metals or molecules, the gas will fragment with a characteristic mass of

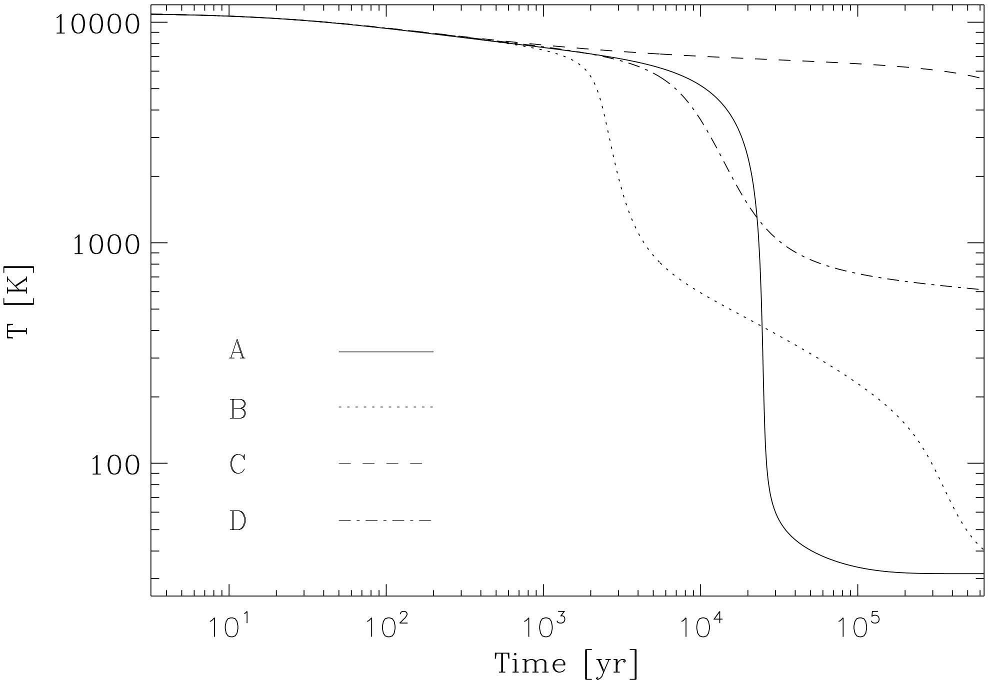

Figure 2.4 Post-shock temperature history of four different runs, all performed with a solar abundance pattern. See Table 2.2 for a description of the run parameters. All runs start at $T = 1.1 \times 10^4\,\mathrm{K} \sim T_{\mathrm{vir}}$. The addition of molecules (H_2 predominantly) produces additional cooling at high temperatures ($T \sim 10^3\,\mathrm{K}$) and thus the temperature falls off from $T \sim 6500\,\mathrm{K}$ first. Metals, which are effective low temperature coolants, allow the gas to reach the T_{CMB} quickly, as shown in case A. Case C initially has no effective coolant below $T \sim 10^4\,\mathrm{K}$, but as H_2 self-shielding builds up the gas is able to cool a small amount before fragmentation. Case D, with a blackbody source temperature of $T = 10^5\,\mathrm{K}$, is able to build up a small H_2 fraction and cool to $\sim 500\,\mathrm{K}$ before becoming gravitationally unstable. Fragmentation occurs for each run at $\sim 10^6$ yr.

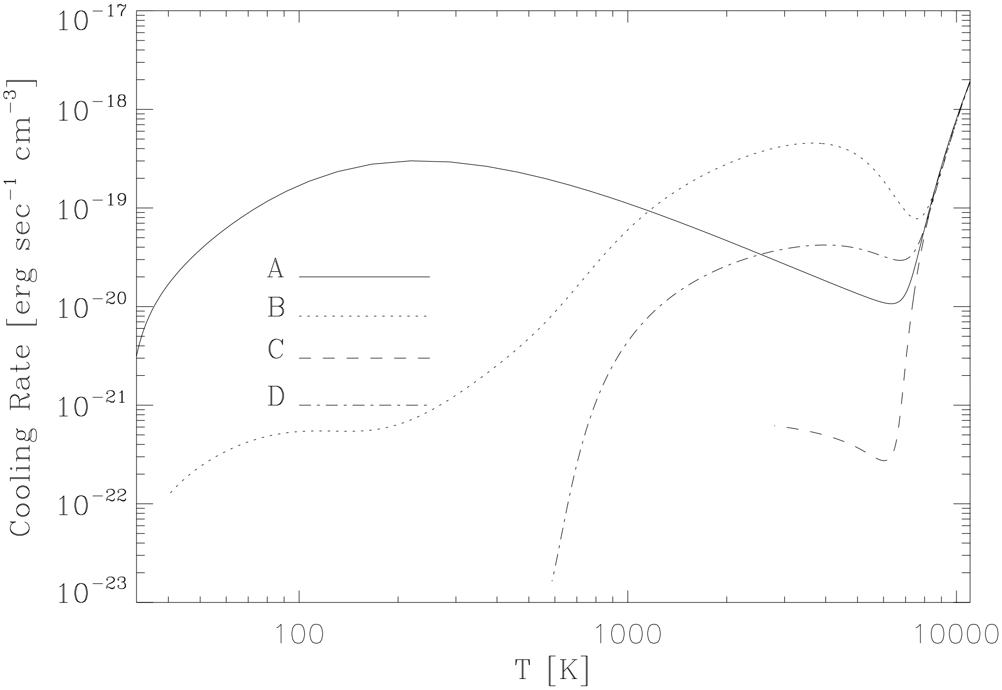

Figure 2.5 Total cooling rate as a function of temperature for the four representative runs. For Cases C and D, which fragment before reaching close to $T_{\rm CMB}$, only the pre-fragmentation cooling curve is shown. Metals dominate the cooling in case A at $T \sim 200\,$K while H_2 is a very effective coolant at $T \sim 3000\,$K.

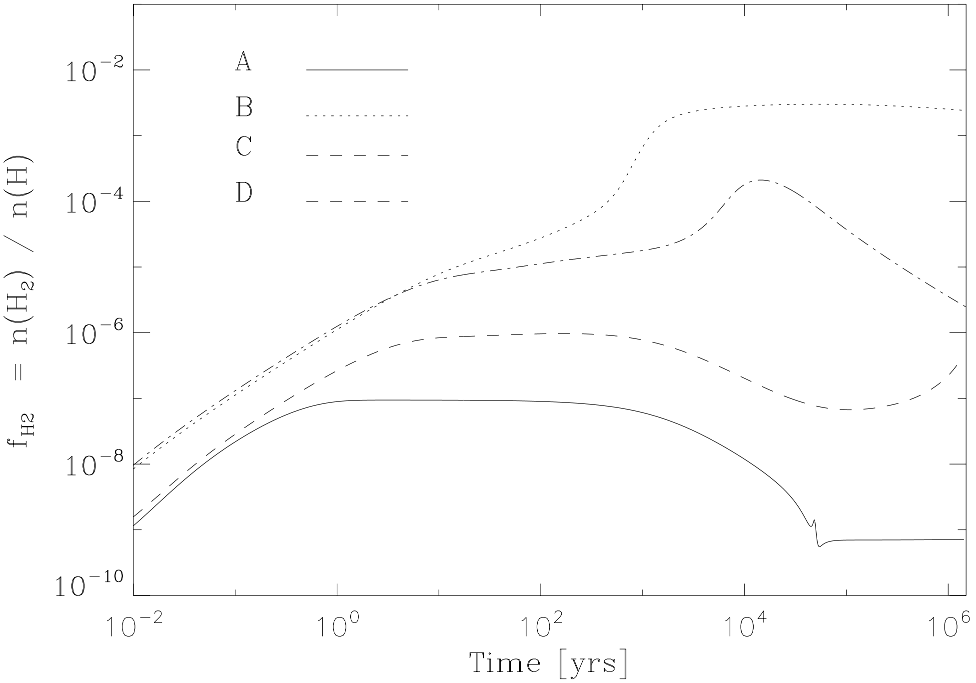

Figure 2.6 Time evolution of H_2, f_{H_2}, in the four representative runs. The strong photobackground in case A prevents any appreciable H_2 fraction from forming, while a LW background of $J_{21} = 10$ allows the H_2 fraction, $n(H_2)/n(H)$, to exceed 10^{-3}.

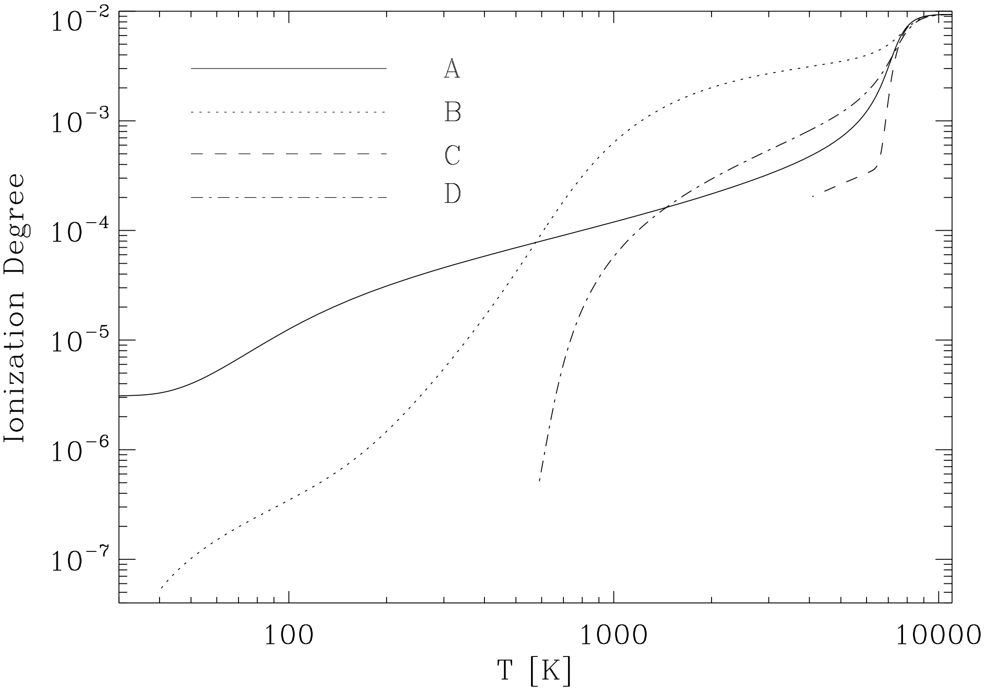

Figure 2.7 Ionization degree of the gas in the four runs. We define the ionization degree to be the number density of free electrons divided by the number density of protons in any form, $n_{e^-\mathrm{free}}/n_{p^+}$.

$1 - 10\, M_\odot$ (cases A and B); a fragment in this mass range has a very good chance of producing a solar mass star. Gas with both efficient molecular cooling and high metallicity ($J_{21} = 10$ and $Z = 10^{-2}\, Z_\odot$) will behave similarly to case A and produce a $\sim 1\ M_\odot$ fragment. If, however, no low-temperature coolant is available as a result of a high LW background and little chemical feedback from early supernovae, there will likely be only one large fragment, $\sim\ 10^{4-5} M_\odot$. The critical LW background where H_2 is no longer an effective coolant is approximately $J_{21} = 10^{3-4}$ for a blackbody spectrum of $T_* = 10^4\,\mathrm{K}$, close to the value found by Bromm & Loeb (2003a) for similar initial conditions. Shang et al. (2010) find a much smaller critical J_{21}, most likely due to the higher H_2 self-shielding experienced in these relatively high density accretion flows, although as discussed, we do consistently overestimate the degree of self-shielding. Schleicher et al. (2010) find cooling suppression for $J_{21} \sim 1 - 10^4$, depending on the gas density. Another point of interest is the appearance of a critical metallicity in the absence of molecular coolants. In case A, the final fragmentation mass is a strong function of metallicity (see Fig. 2.8). At low metallicities ($Z \lesssim 10^{-4}\, Z_\odot$) one large fragment is produced. Conversely, high metallicities ($Z \gtrsim 10^{-4}\, Z_\odot$) produce $\sim\ 10^3 - 10^4$ solar mass fragments, lending support to metallicity being the driver of the Pop III-II star formation transition protogalactic accretion flows. This behavior can be understood by comparing the cooling time from metals and a characteristic fragmentation time, as we explain in Section 2.4.3 below. We note that in runs with PISN abundances, a given metallicity will produce fragments nearly one order of magnitude smaller. Yields from PISNe are thus more effective at reducing the fragmentation mass scale.

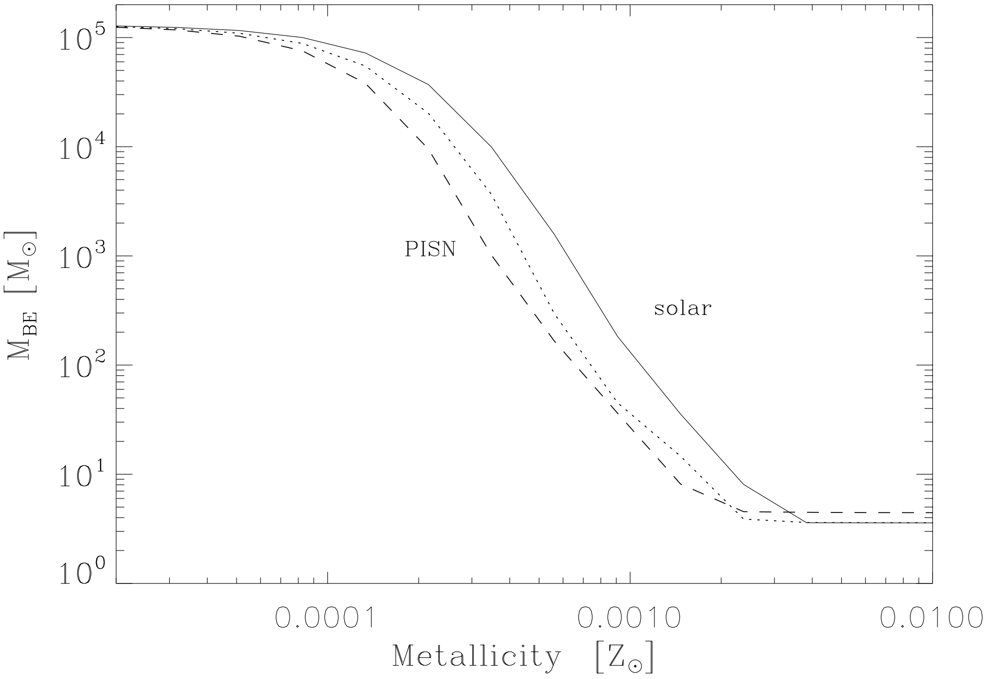

Figure 2.8 Characteristic fragmentation mass as function of metallicity for three different metallicity abundance patterns. The masses represent the Bonnor-Ebert mass at the point of fragmentation, when $t_{\rm sound} = t_{\rm ff}$. These represent the physical scenario in case A ($J_{21} = 10^4$) but with varying levels of metallicity. The two curves labeled PISN (overlaid) are for a 150 and $250\,M_\odot$ PISN metallicity yield pattern. The critical metallicity (the metallicity where the fragmentation mass scale drops appreciably) occurs at slighly lower metallicity for the two runs performed with PISN abundance patterns, due to the higher proportion of oxygen and silicon produced in PISNe as compared to the solar abundance pattern, the shift is small however. The upper mass scale of $\sim 10^5\,M_\odot$ reflects the initial conditions of the accretion flow while the lower mass limit of $\sim 3\,M_\odot$ is set by the CMB temperature floor. As discussed in Section 2.4.3, the critical metallicity can be understood by considering the three relevant timescales, $t_{\rm cool}$, $t_{\rm sound}$, and $t_{\rm ff}$; it is dependant on the gas being able to cool appreciably before the fragmentation criteria is reached (determined by $t_{\rm sound}$ and $t_{\rm ff}$).

2.4.2.1 The Impact of Dust

The presence of dust, which may accompany metals (e.g., Cazaux & Tielens 2002), could have a significant impact on the thermal evolution of the gas in that it radiates thermally and also catalyzes molecular hydrogen formation. Dust grains should be produced in primordial supernovae (Todini & Ferrara 2001, Nozawa et al. 2003, Schneider et al. 2004), but uncertainty still exists as to how much dust ultimately enriches the interstellar medium (Nozawa et al. 2007, Cherchneff & Dwek 2010). We do not include dust thermal emission nor grain surface molecule formation in our chemical model. Dust thermal emission is always a sub-dominant coolant at metallicities up to $10^{-2}\,Z_\odot$ and densities below $10^6\,\mathrm{cm}^{-3}$ (Omukai et al. 2005). To assess the catalytic impact of dust grains in our model, we compare the H_2 formation rate on dust grains with the H_2 formation rate through the H^- channel and the LW H_2 photo-dissociation rate. The formation rate of H_2 on dust grains is (Cazaux & Spaans 2004)

$$\begin{aligned} R_{\mathrm{d}} &= 3.025\times10^{-17}\,\epsilon_{\mathrm{H}_2} n_{\mathrm{H}} n(\mathrm{H})\,S_{\mathrm{H}}(T)\,f_{\mathrm{a}}(T) \\ &\quad\times\left(\frac{T_{\mathrm{g}}}{100}\right)^{1/2}\left(\frac{\xi_{\mathrm{d}}}{0.01}\right)\,\mathrm{cm}^{-3}\,\mathrm{s}^{-1}, \end{aligned} \tag{2.11}$$

where ϵ_{H_2} is the H_2 formation efficiency (Cazaux & Spaans 2009), $S_{\mathrm{H}}(T)$ is the temperature dependent sticking factor of hydrogen onto dust grains (Cazaux & Spaans 2004), n_{H} is the number density of neutral hydrogen, $n(\mathrm{H})$ is the number density of hydrogen nuclei, and $f_{\mathrm{a}}(T)$ is a temperature dependent factor accounting for thermal evaporation of hydrogen from the grain surface (Tielens & Hollenbach 1985). We assume a typical dust grain has a mass of $1.2\times10^{-14}\,\mathrm{g}$, such that $n_{\mathrm{d}} = 1.3\times10^{-10}\xi_d n_{\mathrm{H}}$. Equation (2.11) is normalized for a standard Galactic dust-to-gas mass ratio of $\xi_{\mathrm{d}} = 0.01$ at around solar metallicity. We can scale this for lower metallicity by writing $R_{\mathrm{d}}(Z) = (Z/Z_\odot)\,R_{\mathrm{d}}(Z_\odot)$ where $R_{\mathrm{d}}(Z_\odot)$ is equation (2.11) evaluated for $\xi_{\mathrm{d}} = 0.01$.

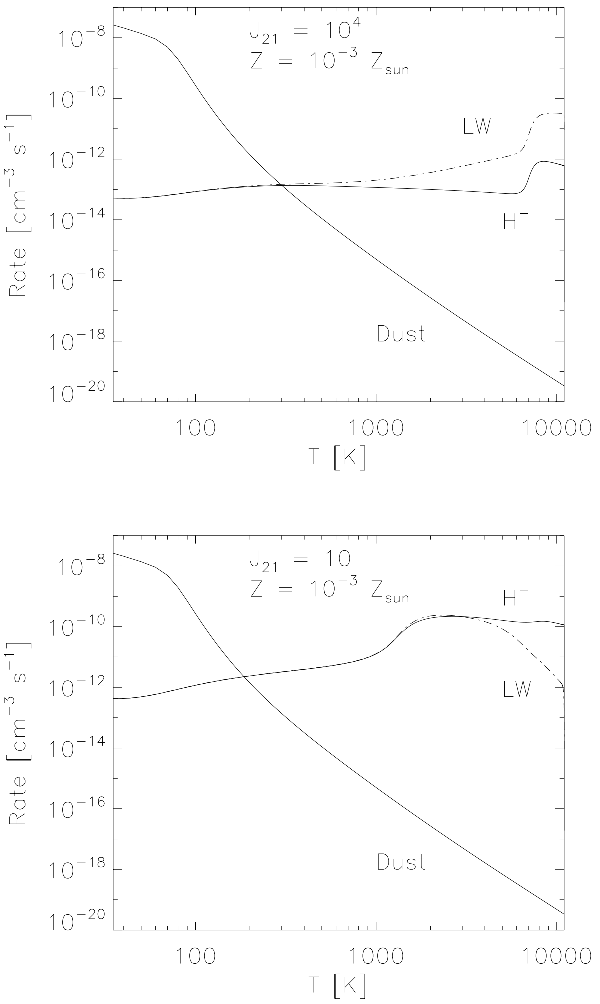

Figure 2.9 The volumetric chemical rates for the LW H_2 destruction rate (labeled LW), the formation rate of H_2 through the H^- channel (H^-), and the grain H_2 formation channel rate (Dust) for two different values of the intensity in the LW bands (see Section 2.3.3); $J_{21} = 10^4$ (top) and $J_{21} = 10$ (bottom). The dust formation rate drops off rapidly at high temperatures due to the steep temperature dependences of the H sticking coefficient $S_{\rm H}(T)$ and the H evaporation coefficient $f_{\rm a}(T)$. In the high LW intensity run, LW destruction initially dominates the chemistry of H_2 while dust formation is negligible. At 600 K, H_2 is in equilibrium with the radiation field and at 300 K dust H_2 formation becomes the primary formation channel. Gas which reaches roughly $T \sim 250\,{\rm K}$ will experience rapid H_2/HD formation, allowing the gas to cool rapidly to $T_{\rm CMB}$.

In Figure 2.9 we compare these three volumetric chemical rates—the LW H_2 destruction rate, the H_2 formation rate through the H^- channel, and the H_2 formation rate on dust grains for two different values of J_{21}. The grain H_2 formation rate is computed with equation (2.11) using the isobaric density evolution scheme while the other two rates are extracted from our chemical model. In the run with $J_{21} = 10^4$, LW photon destruction of H_2 dominates over dust grain H_2 formation at temperatures $T > 250\,\mathrm{K}$. Below this temperature, H_2 formation on dust grains is extremely efficient. We also repeat this run for $J_{21} = 10$ and find similar behavior. We chose these two values of J_{21} as they bracket the critical J_{21} for H_2 formation through the H^- channel (see Section 2.4.2). We do not consider dust opacity and its effect on the LW photon flux, as understanding the interplay between photodissociation and dust requires complicated multidimensional modeling of PDRs (e.g., Krumholz et al. 2008). We also do not consider H_2 formation heating in this work, but as is shown in Omukai et al. (2005), at metallicities up to $10^{-2}\,Z_\odot$ and densities below $10^6\,\mathrm{cm}^{-}3$, this heating mechanism is subdominant compared to H_2, metal line cooling, and adiabatic heating.

Examining Figure 2.8 and using equation (2.10), $T \sim 250\,\mathrm{K}$ corresponds to a BE mass of $\sim 230\,M_\odot$ which is the initial fragmentation mass scale of a gas with metallicity $Z \sim 10^{-3}\,Z_\odot$. Molecular hydrogen, however, is not able to cool gas below $T \sim 200\,\mathrm{K}$ due to its lack of a permanent dipole moment, thus further cooling depends on the formation rate of HD and other molecules (e.g., CO) which can cool the gas to even lower temperatures — these molecules will most likely also be formed on dust grains in significant number around this temperature as well. We can expect then, because of dust's impact on molecule formation, that the fragmentation mass scale will be sharply lowered at around $10^{-3}\,Z_\odot$. At higher metallicity, $\sim 10^{-2}\,Z_\odot$, the formation rate of H_2 on dust grains will increase. However, gas with a metallicity of $10^{-2}\,Z_{\odot}$ will reach $T_{\rm CMB}$ through metal cooling alone (see Figure 2.8); the addition of molecular cooling will only decrease the cooling time. Thus, while the formation rate of H_2 on dust grains will become increasingly larger at higher metallicity, it will not affect the end product, namely the initial fragmentation mass scale, of the gas in our model. Increased molecule formation brought about by dust may also allow thermal instabilities to develop more easily — see Section 2.2.4. We conclude that molecule formation on dust grains will alter the behavior of the gas below some critical temperature ($T \sim 250\,\mathrm{K}$) making the transition from high mass fragments to low mass fragments occur more abruptly, but while retaining the general picture which we present here.

These findings are complementary to those of Omukai et al. (2008) who also use a one-zone model to study the thermal evolution of gas in halos with $T_{\rm vir} \sim 10^4\,\mathrm{K}$. They find, with the inclusion of dust, that the gas will fragment vigorously with a metallicity as low as $Z \sim 10^{-6}\,Z_{\odot}$. This episode of dust-facilitated secondary fragmentation occurs at densities $n_{\rm H} \sim 10^{10}\,\mathrm{cm}^{-3}$, higher than the densities, $n \sim 10^{5-6}\,\mathrm{cm}^{-3}$, at which we first encounter fragmentation. For the densities which our models overlap there is excellent agreement – -see Figures 5a and 5b in Omukai et al. (2008).

2.4.2.2 Initial Density

These results depend sensitively on the choice of initial post-shock density, due to the dependence of the cooling rate and the BE mass on density. Motivated by Greif et al. (2008), we chose a pre-shock density of $n = 10^3\,\mathrm{cm}^{-3}$ as this is the density right before the cold stream gas experiences a shock near the center of the galaxy. If the pre-shock number density is smaller, $10^2\,\mathrm{cm}^{-3}$, the initial BE mass is $\sim 5\times10^5\,M_{\odot}$. The critical metallicity for the gas to reach $T_{\rm CMB}$ is also correspondingly shifted to higher metallicity, roughly $10^{-2.5}\,Z_\odot$, and even at this metallicity, the gas fragments with $M_{\rm BE} \sim 10\,M_\odot$. For a pre-shock density of $10\,{\rm cm}^{-3}$, the initial BE mass is $\sim 2 \times 10^6\,M_\odot$ and the gas temperature is not able to reach $T_{\rm CMB}$ at any reasonable metallicity.

2.4.2.3 Hot Accretion Mode

We proceed to comment on the implications of an even lower pre-shock density encountered in quasi-spherical baryonic accretion from the IGM onto the halo. As has been shown in simulations (Wise & Abel 2007a, Greif et al. 2008), accompanying the cold accretion mode is a hot mode where gas is accreted at the virial radius directly from the IGM residing between the (cold) filaments of the cosmic web. The fate of gas accreted in this mode will differ substantially from the case of cold accretion, mainly in the location of the shock and the subsequent cooling rate. As gas is accreted directly from the IGM, its post-shock density is $\sim 0.4\,{\rm cm}^{-3}$ (Wise & Abel 2007a), much lower than the initial density adopted for this study ($10^3\,{\rm cm}^{-3}$). Initially, the gas is not self gravitating as indicated by its large BE mass. None of the cooling processes discussed here will allow the gas to cool appreciably below $T \sim 7000\,{\rm K}$. At this point, $t_{\rm cool} \sim 10^9\,{\rm yr}$ while $t_{\rm ff} \sim 3 \times 10^7\,{\rm yr}$; this suggests a stable virial shock may develop, even with a high degree of metallicity in the gas. It seems likely that only the gas which enters the galaxy through a dense, cold accretion filament is able to immediately fragment with a small characteristic fragmentation mass.

2.4.3 Analytical Toy Model for Critical Metallicity

As shown in Section 2.4.2, runs with a large LW radiation background ($J_{21} > 10^4$) exhibit a strong dependance on metallicity of the final fragment mass scale. Here, we discuss the physical basis behind this critical metallicity, utilizing a simple toy model. As demonstrated, our critical metallicity is a result of cosmological initial conditions via the virial velocity and accretion density, cooling physics, and the Jeans analysis for gravitational fragmentation.

Let $t_{\rm frag}$ be the time it takes the expanding shocked region to reach the fragmentation criterion: $t_{\rm sound} > t_{\rm ff}$, where $t_{\rm sound} \sim L/c_{\rm s}$, the ratio of the length of the shocked region, given by equation (2.9), and the sound crossing time. In the absence of metals and molecular cooling, atomic cooling quickly brings the temperature from its post-shock value of $T \sim 10^4$ K to the asymptotic $T \sim 6500$ K, resulting in $L_{Z=0}(t) \sim \frac{1}{5}\, v_{\rm vir} t$, where the factor of $1/5$ is from equation (2.9) considering adiabatic and isobaric density enhancement at $T = 6,500\,{\rm K}$. In metal- and molecule-free gas fragmentation consequently sets in at $t_{{\rm frag},Z=0} \sim 10^6\,{\rm yr}$. Interestingly, due to the competing temperature dependence of the free-fall and sound crossing time, $t_{\rm frag}$ is roughly constant for any value of metallicity. To determine the level of metals needed to allow the gas to fragment at a small mass scale, we evaluate $t_{\rm frag} \sim t_{\rm cool}$, where $t_{\rm cool}$ is the cooling time due to metal transitions. Equating the timescales yields

$$t_{{\rm cool},i}(Z) \sim \frac{k_{\rm B}T}{X_i} A_{10}\Delta E_{10} \sim 10^6\,{\rm yrs}, \tag{2.12}$$

where A_{10} is the spontaneous emission coefficient of a transition, ΔE_{10} is the corresponding energy difference between states, and $X_{\rm i} \equiv n_{\rm i}/n_{\rm tot}$ is the number density fraction of the metal coolant. For the solar abundance pattern, O is the dominant coolant over a wide range of temperatures (see Fig. 2.2). For the two lower states of O, $A_{10} = 8.9 \times 10^{-5}\,{\rm s}^{-1}$ and $\Delta E_{10} = 3.14 \times 10^{-14}\,{\rm ergs}$. The critical O abundance therefore is

$$X_{\rm O} \sim \frac{k_{\rm B}T}{10^6\,{\rm yrs}\ A_{10}\Delta E_{10}} \sim 10^{-8}\ , \tag{2.13}$$

where $T = 6,500\,\mathrm{K}$. This fraction corresponds to an oxygen mass fraction $Z_{\mathrm{O}} \sim 10^{-4.8}\, Z_{\mathrm{O},\odot}$, agreeing with the critical metallicity demonstrated by Figure 2.8. The same analysis could be performed with the cooling rate of silicon (as it is the most effective coolant for runs with a PISN abundance pattern) — the conclusion would remain the same. Previous studies on the role played by metallicity in the star formation mode transition (Bromm et al. 2001, Omukai et al. 2005, Santoro & Shull 2006) have defined the critical metallicity as the metal fraction that alters the characteristic mass of stars formed from the standard Pop III initial conditions where cooling by H_2 and metals competes with the compressional heating due to self-gravity. Our physical scenario is very different; instead of a self-gravitating, adiabatic collapse in $10^6\, M_\odot$ dark matter minihalo, we consider an isobarically cooling gas that was shocked to $10^4\,\mathrm{K}$ in $10^8\, M_\odot$ halos. Direct comparison between critical metallicity values obtained in these two contexts is not entirely justified. Nonetheless, we do find a critical metallicity comparable to some of the minihalo results (Bromm et al. 2001). It is not clear why a hot, isobarically cooling shock should behave so similarly to the adiabatic collapse experienced in a minihalo.

2.5 Discussion and Conclusions

In this work, we have examined the fate of metal-enriched, cold, dense, and dust-free accretion streams into dark matter halos of mass $10^8\, M_\odot$ at redshift $z = 10$; we regard these objects as the first galaxies. From simulations, we know these cold streams penetrate very close to the center of the protogalaxy, where they shock and fragment. Our goal was to determine the fragmentation properties of these cold streams and to identify the key physical parameters governing this first step in the high redshift star formation process. We find that metallicity (due to metals being an effective low temperature coolant) and LW background strength (as it is capable of destroying H_2 and HD) are the dominant factors in determining the final fate of the post-shock region. Using a fit to the baryonic growth rate of halos, and assuming, as recent studies suggest, that these galaxies are fed entirely by cold streams and that their star formation rate closely matches the mass accretion rate, we can estimate the number of fragments produced by these flows. We either see one large ($\sim 10^4 M_\odot$) fragment being produced, or roughly 10^4 solar-mass fragments, depending on the initial conditions of the flow. The CMB temperature floor is also a key factor in determining the mass of fragments, as it represents a strict temperature lower limit of radiatively cooling gas. Roughly speaking, this scenario occuring at higher redshifts would still demonstrate similar behavior in terms of a critical metallicity, but would produce fragments of slightly higher mass. Overall, this effect is of little importance as even low-redshift star forming molecular clouds do not generally cool below $10\,\mathrm{K}$, wheres as the CMB temperature at $z = 10$ is $\sim 30\,\mathrm{K}$. Any observational effects from this temperature floor wold be difficult to extract from our simulations. Bailin et al. (2010a) studied CMB regulated star formation in some detail (at lower redshifts than we examine) and find that observations currently cannot confirm or refute CMB regulation on star formation.

We did not include dust grain physics in our chemical model, even though it can have a major impact in that it allows very efficent H_2 formation on grain surfaces and acts as an effective cooling source. We argue that its presence will not significantly alter our findings. The presence of dust and its effect on cooling has been discussed as a possible catalyst for the star formation mode transition. Schneider et al. (2006), Schneider & Omukai (2010) found that dust induced fragmentation can decrease the Pop II fragmentation mass scale by about four orders of magnitude over that accessible with metal fine structure lines only. Jappsen et al. (2009b) suggested that metallicity does not affect the fragmentation of gas with hot initial conditions, similar to the environment probed in this study. We attribute the difference in our conclusions to our examination of a slightly different physical regime and to our inclusion of a soft UV background that stifles H_2 cooling (as supported, e.g., by Shang et al. 2010). Taking guidance from galaxy formation simulations, we follow isobarically evolving gas in an expanding shocked slab to study its thermal evolution and fragmentation. Our model is designed to reflect the filament-dominated inflow topology of cold accretion flows, whereas Jappsen et al. (2009b) examine the collapse into a spherically-symmetric, centrally concentrated halo potential. In our isobarically evolving case, the tight coupling between density and temperature will increase the importance of the role of the cooling rate in determining the final outcome of fragmentation. This aside, if we include molecule formation and molecular cooling (H_2 and HD) by setting $J_{21} = 10$, our results agree with Jappsen et al. (2009a) in that metal line cooling does not affect the fragmentation properties of the evolving gas. This emphasizes the importance of a LW soft UV background in modeling the formation of Pop II stars in the first galaxies.

The first galaxies are suspected to be the first structures where turbulence begins to play a major role, driven by high Mach-number cold streams penetrating to the protogalactic core (Greif et al. 2008, Wise & Abel 2007a). It is the interplay of turbulence and self gravity which is suspected to be responsible for the shape of the present-day IMF, especially the high mass power law extension (Padoan & Nordlund 2002, Mac Low & Klessen 2004, McKee & Ostriker 2007) .Thus, it is likely that star formation inside the first galaxies will be characterized by a stellar mass distribution that for the first time in the history of the universe resembles the present-day IMF. Specifically, we can expect turbulence to introduce density perturbations on the order of $\mathcal{M}^2$, suggesting within our above model that fragments as low as

$\sim 0.3\,M_\odot$ might form. Such stars, below the mass limit of $0.8\,M_\odot$ required to survive for the age of the universe, would still exist today, and could be probed by Stellar Archaeology (Frebel et al. 2009, and references therein). To predict the detailed shape of the Pop II IMF inside the first galaxies, the source and impact of the turbulence needs to be studied with realistic numerical simulations.

Here, we have constrained some of the key physical processes that govern star formation in high-redshift protogalaxies within an idealized analytical framework that allowed us to explore the relevant parameter space. This work needs to be followed up by detailed simulations, including a number of ingredients ignored here, such as high optical depth effects, H and He ionizing radiation (Ricotti et al. 2002), turbulence, feedback effects (AGN, stellar outflows, etc.), and possibly cosmic rays from the first SNe (Jasche et al. 2007, Stacy & Bromm 2007). It needs to be emphasized that the estimates presented in this paper are derived with the Bonnor-Ebert mass and a simplified treatment of the post-shock dynamics. To truly probe the fragmentation mass scale in the first galaxies one must use multidimensional numerical simulations. The goal of understanding the complex first stages of galaxy formation seems now within reach, using state-of-the-art three dimensional radiation-hydrodynamical simulations, together with realistic cosmological initial conditions. Such calculations are crucial to make useful predictions for the *James Webb Space Telescope (JWST)*.

Chapter 3

Delayed Star Formation by Lyman-Werner Radiation within the First Galaxies[1]

3.1 Introduction

Theoretical studies have suggested that the first stars, Population III (Pop III), formed in $\sim 10^6\, M_\odot$ dark matter 'minihalos' at redshifts $z \sim 15-40$ (Couchman & Rees 1986, Haiman et al. 1996, Tegmark et al. 1997). Due to a lack of efficient coolants in metal-free gas, Pop III stars are thought to have been more massive than typical stars forming today. The details of their formation process, especially the shape of the Pop III initial mass function (IMF), are still a subject of intense study. Early works suggested these stars were extremely massive, exceeding $100\, M_\odot$, and formed one per minihalo (Abel et al. 2000, Bromm et al. 2002, Yoshida et al. 2006). More recent studies, exploring fragmentation at higher densities (Turk et al. 2009, Stacy et al. 2010, Clark et al. 2011a,b, Greif et al. 2011, 2012), or modeling the effects of protostellar feedback (Stacy et al. 2012, Hosokawa et al. 2011), have begun to suggest an IMF extending to lower masses. Detailed simulations that will further constrain the Pop III IMF are needed to assess the role that these stars played in early cosmic milestones, such as chemical enrichment of the intergalactic medium (IGM), reionzation, and the formation of supermassive black hole seeds (e.g., Barkana &

---

[1] This chapter has been published as Safranek-Shrader, C., Agarwal, M., Federrath, C., Dubey, A., Milosavljevic, M., Bromm, V., 2012, MNRAS, 426, 1159. M. Agarwal provided the implementation for the non-local column density calculation, the sink particle algorithm was originally written by C. Federrath, and A. Dubey provided the algorithm for delegate particle dark matter smoothing. V. Bromm and M. Milosavljevic supervised the project.

Loeb 2001, Bromm & Larson 2004, Ciardi & Ferrara 2005, Bromm & Yoshida 2011). Furthermore, determining the properties of Pop III stars is necessary for interpreting increasingly detailed observations of high-redshift sources (e.g., Dunlop 2013) and stellar relics in the local Universe (e.g., Frebel et al. 2005, Beers & Christlieb 2005, Frebel 2010, Karlsson et al. 2013).

Directly observing a chemically pristine stellar population would represent a significant step towards understanding the formation and properties of Pop III stars. However, the chances of detecting individual, high-redshift Pop III stars with the upcoming *James Webb Space Telescope* (JWST) are very low (e.g., Gardner et al. 2006, Greif et al. 2009, Rydberg et al. 2010). While a single pair-instability supernova (PISN) from a massive Pop III star may be detectable (e.g., Wise & Abel 2005, Hummel et al. 2012, Pan et al. 2012, Tanaka et al. 2012), clusters of Pop III stars, if they exist, would present the best opportunity for directly observing a metal-free, high-redshift stellar population (Inoue 2011, Zackrisson et al. 2011). It would seem that the halos capable of hosting these clusters, with virial masses $\sim 10^7 - 10^8\, M_\odot$ and often dubbed to be the first galaxies (Bromm et al. 2009), would have formed in high-density, biased regions, chemically pre-enriched with Pop III supernova ejecta (Trenti et al. 2009, Greif et al. 2010, Wise et al. 2012), precluding the possibility of Pop III star formation. There are scenarios, however, in which these halos reach the conditions necessary for atomic cooling while still metal-free. For example, if a strong hydrogen molecule dissociating 'Lyman-Werner' (LW) radiation background was set up sufficiently early (e.g., Haiman et al. 1997, Machacek et al. 2001, Johnson et al. 2008) or if Pop III stars ended their lives by collapsing directly to form black holes (Heger et al. 2003), the onset of local metal enrichment would have been substantially delayed. Additionally, pockets of metal-free gas could have remained until very low redshifts owing to inhomogeneous metal dispersal (Scannapieco et al. 2002, Furlanetto & Loeb 2005, Tornatore et al. 2007, Trenti et al. 2009, Stiavelli & Trenti 2010, Maio et al. 2010). Recently, the detection of metal-free gas clouds at $z \sim 3$ (Fumagalli et al. 2011) has confirmed that regions of space can remain chemically pristine long after reionization.

It has been suggested that two different modes of metal-free star formation occurred in the early Universe. First generation Pop III stars (Pop III.1) formed from initial conditions completely unaffected by previous star formation. Second generation Pop III stars (Pop III.2) formed from gas significantly influenced by the radiative output of previous star formation, but still containing no stellar nucleosynthetic products (O'Shea & Norman 2008, McKee & Tan 2008, Bromm et al. 2009). Cooling by the hydrogen deuteride (HD) molecule is generally thought to differentiate Pop III.1 and Pop III.2 star formation. Unlike H_2, which cannot cool gas below $\sim 200\,\mathrm{K}$, HD possesses an intrinsic electric dipole moment and can thus act as an effective cooling agent below $200\,\mathrm{K}$, possibly resulting in stars with lower characteristic masses. The abundance of HD can be enhanced in regions with an elevated free electron fraction. These regions can be produced from virialization shocks in halos with virial temperatures $T_{\mathrm{vir}} > 10^4\,\mathrm{K}$ (e.g., Oh & Haiman 2002, Greif & Bromm 2006) or in the collapse of relic HII regions produced around Pop III.1 stars (Ferrara 1998, Oh & Haiman 2003, O'Shea et al. 2005, Yoshida et al. 2007). For reference, T_{vir} is related to the virial mass of a halo as (e.g., Barkana & Loeb 2001)

$$T_{\mathrm{vir}} \approx 2 \times 10^4\,\mathrm{K} \left(\frac{\mu}{1.2}\right) \left(\frac{M_{\mathrm{vir}}}{10^8\,M_\odot}\right)^{2/3} \left(\frac{1+z}{10}\right) \tag{3.1}$$

where μ is the mean molecular weight ($\mu = 1.2$ for neutral atomic primordial gas), m_{H} is the mass of a hydrogen atom, k_{B} is Boltzmann's constant, and M_{vir} is the total mass contained within the radius in which the average matter density is $18\pi^2 \approx 178$ times the critical density. Theoretical investigations examining the chemistry, cooling, and dynamics of these regions have shown that gas is able to cool to the temperature of the cosmic microwave background ($T_{\rm CMB}$) as a result of HD cooling. This may result in lower characteristic fragmentation masses (e.g., Johnson & Bromm 2006).

One effect that can suppress gaseous collapse, star formation, and metal enrichment in small cosmic halos is a pervasive UV background. Photons with energies in the range $11.2\,{\rm eV} < h\nu < 13.6\,{\rm eV}$, the LW bands, are capable of photodissociating $\rm H_2$, the key cooling agent in metal-free gas below $10^4\,{\rm K}$, and have a very small optical depth in a neutral IGM. Additionally, the photodestruction of $\rm H^-$, an intermediary in the gas-phase formation of $\rm H_2$, can also limit the $\rm H_2$ abundance. Many studies have explored the effect of an UV background on early structure formation (Haiman et al. 1997, Ciardi et al. 2000, Machacek et al. 2001, Ricotti et al. 2001, Mesinger et al. 2006, Wise & Abel 2007b, Yoshida et al. 2007, O'Shea & Norman 2008). It is accepted that above a certain radiation intensity, $J_{\rm LW,21} \approx 10^{-1}$, LW radiation delays the collapse and cooling of metal-free gas until the assembly of more massive halos.[1]. Higher UV background intensities, $J_{\rm LW,21} \gtrsim 10$, completely suppress baryonic collapse and cooling in halos which allow only $\rm H_2$ cooling. In this regime, significant cooling will not occur until the assembly of larger mass halos with virial temperatures $T_{\rm vir} > 10^4\,{\rm K}$, the atomic cooling threshold. In these halos, Lyα emission will allow the gas to radiate its internal energy and collapse, effectively independent of the radiation background longward of $13.6\,{\rm eV}$.

Studies that have explored the thermodynamical evolution of metal-free gas exposed to a strong UV background (Omukai 2001, Omukai et al. 2008, Safranek-

---

[1] Here, $J_{\rm LW,21}$ denotes the radiation intensity at the centre of the LW bands, $12.4\,{\rm eV}$, in units of $10^{-21}\,{\rm erg\,s^{-1}\,cm^{-2}\,Hz^{-1}\,sr^{-1}}$. This is not to be confused with J_{21}, the radiation intensity at the Lyman limit, $13.6\,{\rm eV}$, in the same units. In general, $J_{\rm LW,21} = \beta\, J_{21}$, where $\beta = 3$ for a 10^4 K blackbody spectrum and 0.9 for a 10^5 K spectrum (e.g., Wolcott-Green et al. 2011)

Shrader et al. 2010, Wolcott-Green et al. 2011, Latif et al. 2011a) have similarly found that the evolution of metal-free gas undergoing free-fall or isobaric collapse is determined in large part by the background intensity, with the onset of effective $\mathrm{H_2}$ cooling delayed with an increasing $J_{\mathrm{LW},21}$. Gas that reaches the atomic cooling threshold is able to collapse isothermally while remaining at $T \sim 8000\,\mathrm{K}$ until $\mathrm{H_2}$ forms in sufficient abundance for its cooling rate to exceed the adiabatic heating rate, though this picture depends on the role played by $\mathrm{Ly}\alpha$ radiation trapping (see Latif et al. 2011b). Additionally, there exists a spectrum-dependent critical LW radiation intensity (e.g., Omukai 2001, Shang et al. 2010), $J_{\mathrm{LW},21}^{\mathrm{crit}}$, above which $\mathrm{H_2}$ never becomes an effective coolant. In this regime, LW irradiated gas collapses to high density via $\mathrm{Ly}\alpha$ and $\mathrm{H^-}$ free-bound emission. This evolutionary track has been suggested as a potential mechanism for the formation of supermassive black hole seeds via direct gaseous collapse (e.g., Bromm & Loeb 2003a, Begelman et al. 2006, Regan & Haehnelt 2009, Shang et al. 2010).

The atomic cooling threshold is an appealing criterion for classifying objects as the first galaxies (for a recent review see Bromm & Yoshida 2011). These halos, with virial masses $\gtrsim 5 \times 10^7\,M_\odot$ at $z \sim 10$, distinguish themselves from minihalos in that in them, metal-free gas can cool and collapse even in the presence of a strong UV radiation field. Additionally, supersonic turbulent gas flows, typically not present in minihalos, should potentially develop during the assembly of the more massive halos (Wise & Abel 2007a, Greif et al. 2008, Prieto et al. 2011). This turbulence may have influenced the process of star formation in Pop III.2 star forming halos.

To understand star formation in the first galaxies, it is instructive to take guidance from the better understood case of star formation in the nearby Universe. Overall, the formation of stars is observed to be extremely slow, in the sense that molecular clouds undergoing free-fall collapse should have star formation rates ~ 100 times higher than the observed rate (e.g., Zuckerman & Evans 1974, Krumholz et al. 2007, Evans et al. 2009, Kennicutt & Evans 2012). Observational and theoretical work has suggested this inefficiency stems from a number of effects, including supersonic turbulence, protostellar outflows, magnetic fields, and radiative feedback from massive stars. State-of-the-art radiative transfer simulations of star formation including these effects are able to reproduce the IMF and star formation rate in Orion-type Galactic star forming regions (e.g., Krumholz et al. 2012). While there are undoubtedly many effects which influence star formation, it is becoming accepted that the interplay of supersonic turbulence, gas self-gravity, and protostellar feedback are the key players (e.g., Mac Low & Klessen 2004, Elmegreen & Scalo 2004, McKee & Ostriker 2007), setting both the rate of star formation (e.g., Krumholz & McKee 2005), and establishing the shape of the stellar IMF (e.g., Padoan & Nordlund 2002, Padoan et al. 2007, Hennebelle & Chabrier 2008). With this in mind, we are particularly interested in whether supersonic turbulence plays a role in regulating star formation in the first, metal-free galaxies.

In this work, we present the results of a high-resolution cosmological simulation that follows the assembly of a metal-free, atomically cooling $3 \times 10^7 \, M_\odot$ dark matter halo in an environment exposed to strong LW radiation. We accurately compute the column density of H_2 to properly model the transition where H_2 starts shielding itself from LW radiation, as is necessary for the formation of a cool, dense, baryonic core where star formation can take place. We utilize a spatially adaptive grid to resolve densities up to $n = 10^8 \, \mathrm{cm}^{-3}$ and length scales down to $\sim 1000 \, \mathrm{AU}$. Then, we employ sink particles to study the long-term fragmentation tendencies of the gas. Similar studies that focused on LW suppression of H_2 explored smaller values of the radiation intensity, $J_{\mathrm{LW},21} \lesssim 1$, than we consider here and argued that $\mathrm{H_2}$ self-shielding was not an important effect in the small mass halos they considered (e.g., Machacek et al. 2001, O'Shea & Norman 2008). Other studies that explored much higher values of $J_{\mathrm{LW},21}$, relevant for the theoretical scenario where supermassive black hole seeds form by direct gaseous collapse, only included $\mathrm{H_2}$ self-shielding in an approximate fashion based on purely local estimates of the $\mathrm{H_2}$ column density (e.g., Bromm & Loeb 2003a, Shang et al. 2010). This work bridges the gap between these two extremes, exploring the scenario in which collapse in metal-free gas is delayed by LW radiation until the halo reaches the atomic cooling threshold, but with $J_{\mathrm{LW},21}$ remaining below $J_{\mathrm{LW},21}^{\mathrm{crit}}$ and thus permitting $\mathrm{H_2}$ cooling to play a major thermodynamic role.

We will address two primary questions in this study. First, what is the nature of the fragmentation which occurs in the cold, self-shielding gas? Utilizing sink particles, we can evolve the gas long past the initial gravitational collapse to times when a significant mass has been accreted by these particles. We can also identify any additional collapsing regions which would represent other potential star forming clumps. In addressing this question, we will comment on the importance of HD cooling which is thought to give rise to enhanced fragmentation, thus producing a distinct population of metal-free stars with lower characteristic stellar masses. Second, is it possible that LW radiation delayed collapse in metal-free atomic cooling halos can produce clusters of Pop III stars that have luminosities high enough to be detectable and identifiable with the JWST? Zackrisson et al. (2011) showed that clusters of Pop III stars with total stellar masses as low as $\sim 10^5\,M_\odot$ should be detectable at $z \approx 10$ in deep JWST exposures and that their primordial composition can be ascertained based on simple colour criteria. In a similar study, Inoue (2011) suggested that a star formation rate of a few solar masses per year at $z \sim 10$ will be needed for JWST detection. We provide rough estimates for the star formation efficiencies and mass spectra of high-redshift, metal-free stellar populations in atomic cooling halos and comment on the feasibility of detection.

The outline of the paper is as follows. In Section 3.2 we describe the initial conditions of the simulation and our numerical methodology. In Section 3.3 we present results of the simulation. In Section 3.4 we comment on the nature of supersonic turbulence. In Section 3.5, we discuss the trends towards gravitational fragmentation of gas and attempt to predict the properties of the expected starburst. In Section 3.6 we discuss the role of HD cooling. In Section 3.7 we provide further comments on our results, including a discussion on the expected intensity of the LW background, the effect of internal radiative feedback, and the detection prospects of metal-free stellar clusters with the JWST. And finally, we summarize our results and conclude in Section 3.8.

Throughout this paper we assume cosmological parameters consistent with the *Wilkinson Microwave Anisotropy Probe* (WMAP) 7 year results (Komatsu et al. 2011): $\Omega_\Lambda = 0.725$, $\Omega_{\rm b} = 0.0458$, $\Omega_{\rm m} = 0.275$, $h = 0.704$, $\sigma_8 = 0.810$, and $n_s = 0.967$. Additionally, all quantities will be expressed in physical rather than comoving units unless explicitly stated otherwise.

3.2 Numerical Setup

3.2.1 Algorithms and Initial Conditions

We use the publicly available adaptive mesh refinement (AMR) code FLASH (Fryxell et al. 2000, Dubey et al. 2009), version 3.3, which solves the equations of Eulerian hydrodynamics with the directionally split, piecewise parabolic method of Colella & Woodward (1984). Baryons are represented by a multispecies fluid and dark matter by collisionless, massive particles. The gravitational potential of gas and dark matter is computed with the iterative multigrid Poisson solver of Ricker (2008).

We initialize the simulation at $z = 146$ in a $1\ \mathrm{Mpc}^3$ (comoving) box. Cosmological initial conditions were generated with MPGRAFIC (Prunet et al. 2008), a parallel version of the multiscale Gaussian random field generator GRAFIC (Bertschinger 2001). We first run a 128^3 dark matter only simulation and use the halo finder HOP of Eisenstein & Hut (1998) to locate the site of the first $10^8\,M_\odot$ dark matter halo in the simulation volume. We then carry out a hierarchical zoom-in procedure to increase the mass resolution around this halo using three separate levels of dark matter refinement to reach a maximum effective resolution of 512^3 and an effective dark matter particle mass of $230\,M_\odot$ in the target halo itself. We choose the volume of the highest resolution region such that the total mass contained within it is $10^9\,M_\odot$, 10 times the mass of our target halo. We have verified that only the highest resolution dark matter particles are found in our target halo. Given our box size, the expected number of $10^8\,M_\odot$ dark matter halos at $z = 10$ is of order 10 (e.g., Greif et al. 2008).

3.2.2 Resolution and Adaptive Refinement Strategy

In order to capture gaseous collapse to progressively higher densities, we utilize AMR which creates more finely spaced grids (refines) in localized regions. To trigger refinement, we use two separate criteria that are based on local gas properties. We employ a criterion very similar to that used in Wise & Abel (2007a) which refines based on baryonic overdensity. In this scheme, the threshold comoving density for refinement is

$$\rho_{\mathrm{th}} = 3\rho_{\mathrm{b}}2^{3(l-l_i)(1+\phi)}\ , \qquad (3.2)$$

where $\rho_{\rm b} = 3H_0^2\Omega_{\rm b}/8\pi G$ is the comoving baryonic density, l is the current level of refinement, l_i is the initial level of refinement (given our grid resolution, $l_i = 5$), and ϕ is the Lagrangian refinement factor; $\phi = 0$ enforces constant baryonic mass-per-cell while $\phi < 0$ implies that the mass-per-cell decreases with increasing refinement level. We set $\phi = -0.3$ which results in a baryonic mass-per-cell at the highest refinement level ($l_{\rm max} = 22$) of $\approx 0.1\,M_\odot$.

A hydrodynamical simulation of a self-gravitating fluid must properly resolve the Jeans length to be physically reliable. For grid-based Eulerian codes, this requirement is expressed by the Truelove criterion (Truelove et al. 1997), which states that the Jeans length,

$$L_{\rm J} = \left(\frac{\pi c_{\rm s}^2}{G\rho}\right)^{1/2} \tag{3.3}$$

must be resolved by at least 4 grid cell widths to avoid artificial fragmentation. While this criterion was originally formulated for isothermal gas and does not take into account the effect of Hubble expansion, it is commonly utilized in hydrodynamical cosmological simulations. It would be unnecessary to enforce this criterion across the whole grid, thus we only apply it in the innermost region of the simulation where the most highly refined dark matter particles are present. In this work, we always resolve the Jeans length by at least 12 grid cells and derefine the grid if it is resolved by more than 24. While this is more than sufficient to properly resolve the fragmentation tendencies of gas, it may be insufficient to study the possible small-scale turbulent flow in the gas (see Federrath et al. 2011).

The FLASH code allows for no explicit force softening beyond local (e.g., one cell wide) cloud-in-cell smearing of the dark matter particle mass density on the computational grid. In our simulation, because of AMR, the grid spacing can become many orders of magnitude smaller than interparticle separation. When this happens, the dark matter particle discreteness can introduce severe artifacts into the calculation of the gravitational potential and cause gas on the computational grid to feel the gravity of individual dark matter particles. To achieve sufficient smoothness in the dark matter particle mass distribution, we have developed an algorithm that spatially smears the dark matter density before it is passed to the Poisson solver.

For each dark matter particle we compute a smoothing Kernel radius r_s over which the mass of the particle is to be distributed,

$$r_\mathrm{s} = 0.3\,(M_\mathrm{DM}/\rho_\mathrm{b})^{1/3}\,, \tag{3.4}$$

where M_DM is the dark matter particle mass and ρ_b is the baryonic density of the cell containing the dark matter particle. This choice of smoothing radius ensures that the average dark matter mass per cell contributed by a single dark matter particle inside its smoothing kernel, if multiplied by $\Omega_\mathrm{b}/(\Omega_\mathrm{m}-\Omega_\mathrm{b})$, is not larger than the baryonic mass inside the particle's host cell. Within the smearing radius, we distribute the particle mass following the quadratic (or 'Epanechnikov') kernel $\propto 1-(r/r_\mathrm{s})^2$.

In practice, we achieve the smearing by replacing the dark matter particle with a sufficient number of daughter particles with total mass equal to that of the parent particle and with density approximating the kernel profile. Given the highly parallel nature of this simulation, this algorithm takes advantage of the FLASH code's capability for moving Lagrangian data between structured, Eulerian blocks (see Dubey et al. 2012). The daughter particle spacing is approximately equal to the cell spacing of the parent particle's computational cell. Computation of the gravitational potential is performed from the daughter particle density. Computation of the parent particle's acceleration is then carried out in a momentum conserving fashion by summing up the gravitational force over daughter particles and assigning the result to the parent particle.

3.2.3 Chemistry

Detailed, non-equilibrium chemistry is necessary to properly model the thermodynamic state of cosmological gas flows (for a recent review see Glover 2011). Our chemical model tracks the most relevant chemical species in metal-free gas: H, H^-, H^+, e^-, H_2, H_2^+, He, He^+, He^{++}, D, D^+, and HD. We evolve the species' abundances and the internal energy of the gas by simultaneously integrating $N_{\rm species} + 1$ differential equations with a Bulirsch-Stoer-type, semi-implicit extrapolation mid-point method. We set our chemical timestep, which subcycles within the hydrodynamic timestep, as $\Delta t = 0.1 \times \min\{n_e/|\dot{n}_e|, n_{\rm H_2}/|\dot{n}_{\rm H_2}|, n_{\rm HD}/|\dot{n}_{\rm HD}|\}$, where n_i is the number density of species i.

The initial number density of hydrogen nuclei is given by $n = \bar{\rho}_b(z_i)/[m_{\rm H}(1.0 + 4.0\, x_{\rm He})]$, where $\bar{\rho}_b(z) = (3H_0^2/8\pi G)\,\Omega_{\rm b}(1+z)^3$ is the average, physical baryonic matter density at redshift z, and $x_{\rm He} = 0.08$ is the primordial number fraction of helium. We set $x_{\rm H_2} = 2 \times 10^{-6}$, $x_{\rm H^+} = 3.8 \times 10^{-4}$, and $x_{\rm D} = 4.3 \times 10^{-5}$, where x_i is the number density of species i relative to n, the number density of hydrogen nuclei (henceforth the abundance of that species). The abundance of electrons is calculated by enforcing charge neutrality. The initial gas temperature is set by assuming adiabatic cooling due to Hubble expansion after $z \approx 200$, when gas and the CMB thermally decoupled.

Properly modeling the formation of H_2 and HD is essential since these molecules are the only low temperature ($< 10^4$ K) coolants in metal-free gas. In the absence of dust, H_2 forms primarily through the gas-phase reaction mediated by H^-,

$$\begin{aligned} \mathrm{H} + e^- &\rightarrow \mathrm{H}^- + \gamma, \\ \mathrm{H}^- + \mathrm{H} &\rightarrow \mathrm{H}_2 + e^-, \end{aligned} \tag{3.5}$$

which is feasible in primordial gas owing to the residual ionization fraction present after recombination. At higher densities, $\gtrsim 10^8\,\mathrm{cm}^{-3}$, H_2 can also form directly through 3-body reactions (Palla et al. 1983), though since we do not simulate densities this high, 3-body H_2 formation will not be significant here.

The HD molecule can be a significant coolant at temperatures $< 200\,\mathrm{K}$ that can potentially cool the gas to T_{CMB}. In the absence of a LW background, the HD abundance is primarily determined by its main formation pathway

$$\mathrm{H}_2 + \mathrm{D}^+ \rightleftharpoons \mathrm{HD} + \mathrm{H}^+, \tag{3.6}$$

where the D^+ to H^+ abundance ratio is set by the charge exchange reaction

$$\mathrm{H} + \mathrm{D}^+ \rightleftharpoons \mathrm{D} + \mathrm{H}^+. \tag{3.7}$$

Given equilibrium in reactions (3.6) and (3.7), the HD abundance is (e.g., Omukai et al. 2005)

$$x_{\mathrm{HD}} \approx 2\exp(421\,\mathrm{K}\,/\,T)\,x_{\mathrm{H}_2}\,x_{\mathrm{D}}. \tag{3.8}$$

Therefore with HD in chemical (not photodissociation) equilibrium, the HD to H_2 abundance ratio can exceed the cosmological D to H ratio by a large factor when $T \ll 421\,\mathrm{K}$. This HD to H_2 fractionation, due to the slightly higher binding energy of the HD molecule compared to that of H_2 (Solomon & Woolf 1973), is a reason why HD is thought to be a significant coolant in Pop III.2 star formation where additional cooling from H_2 can induce an elevated HD abundance. As we shall show, even in the presence of a strong LW background, Equation (3.8) describes the HD abundance fairly accurately, although since only a very small fraction of the gas cools down to $T \ll 400\,\mathrm{K}$, significant HD to H_2 fractionation does not occur.

3.2.4 Gas Cooling

Atomic and molecular radiative cooling processes have been well studied in astrophysical settings (e.g., Shapiro & Kang 1987, Cen 1992, Osterbrock & Ferland 2006). For the densities, temperatures, and chemical compositions relevant to this work, the most important cooling mechanisms are $\mathrm{Ly}\alpha$, or more generally atomic, emission from neutral hydrogen, ro-vibrational emission from molecular hydrogen, and emission from hydrogen deuteride. For completeness, we also include Compton heating and cooling due to electron scattering of CMB photons, H and He recombination and collisional ionization cooling, and free-free emission. We do not consider cooling by metals or dust as we specifically focus on primordial gas.

$\mathrm{Ly}\alpha$ cooling becomes significant above $\sim 10^4\,\mathrm{K}$ when the electron fraction and gas temperature become high enough to excite this transition. This extremely efficient cooling channel can cool the gas to $\sim 8000\,\mathrm{K}$. Ro-vibrational emission from molecular hydrogen can potentially cool the gas further. Being a symmetric molecule, however, H_2 lacks a permanent electric dipole moment and consequently cannot cool the gas below $\sim 200\,\mathrm{K}$. HD, if present, can cool gas to even lower temperatures, $\lesssim 100\,\mathrm{K}$, as it does possess an intrinsic dipole moment and more closely spaced energy levels. Nevertheless, an elevated electron fraction is still required for it to form in significant quantities (e.g., Johnson & Bromm 2006). We adopt the H_2 cooling rate from Galli & Palla (1998) and the HD cooling rate from Flower et al. (2000).

Finally, as the CMB imposes a lower limit on the temperature to which gas can radiatively cool, we adopt an effective cooling rate of the form $\Lambda_{\text{eff}}(T) = \Lambda(T) - \Lambda(T_{\mathrm{CMB}})$, where $T_{\mathrm{CMB}} = 2.7\,\mathrm{K}\,(1+z)$ and $\Lambda(T)$ is the total volumetric cooling rate not taking into account the CMB. This formulation ensures the gas temperature will not fall below T_{CMB} unless it does so via adiabatic expansion.

3.2.5 Sink Particles

We utilize sink particles to follow the global evolution of the gas after the first baryon dominated region inside a halo undergoes runaway gravitational collapse. Without sink particles, the first collapse would drive the computational mesh to arbitrarily high refinement, which would impose a prohibitively short Courant-Friedrichs-Lewy (CFL) timestep on the entire simulation. Sink particles allow us to self-consistently simulate the formation of multiple gravitationally bound collapsed structures over many free-fall times by accreting mass from the grid and putting an upper limit on the gas density. This computational method was originally introduced in Bate et al. (1995) and has been used extensively in numerical simulations, both in AMR (e.g., Krumholz et al. 2004, Wang et al. 2010, Federrath et al. 2010a, Padoan & Nordlund 2011, Girichidis et al. 2011) and smoothed particle hydrodynamics (SPH; e.g., Bromm et al. 2002, Bate et al. 2003, Stacy et al. 2010, Greif et al. 2011, Clark et al. 2011b).

Our sink particle implementation is identical to the method introduced in Federrath et al. (2010a). Special care is taken to avoid the spurious creation of sink particles that may not represent gravitationally collapsing regions. To this end, we utilize additional checks for the creation of a sink particle in addition to requiring that the gas density in a cell be greater than some threshold ρ_{thresh}. This includes enforcing that the local velocity divergence is negative and that the region of collapse is both gravitationally bound and Jeans unstable.

Once formed, sink particles are capable of accreting mass directly from the computational grid. Cells with centers within a constant distance, the accretion radius r_{acc}, from a sink particle and with a density $\rho > \rho_{\mathrm{thresh}}$ are examined. For these cells, the mass increment $\Delta M = (\rho - \rho_{\rm thresh})\Delta V$ is calculated, where ΔV is the cell volume. Provided that the cell velocity is radially directed towards the sink particle and that the mass increment ΔM is gravitationally bound to the sink particle and the gas within $r_{\rm acc}$, the increment is deducted from the grid and added to the sink particle.

The gravitational interaction between sink particles and gas is computed by direct summation. To avoid extremely large accelerations, we employ cubic spline softening (e.g., Price & Monaghan 2007) which decreases the gravitational attraction of gas-sink and sink-sink interactions within $r < r_{\rm soft}$, where r is the separation between a cell center and a sink particle or between two sink particles.

In the simulation here, we set the sink particle accretion and softening radii to be equal, $r_{\rm acc} = r_{\rm soft} = 0.01\,{\rm pc} \approx 2000\,{\rm AU}$, which is 2.5 times the grid spacing at the highest level of refinement. Additionally, we set the sink particle creation density threshold to $\rho_{\rm thresh} = 2.2 \times 10^{-16}\,{\rm g\,cm^{-3}}$ corresponding to $n = 10^8\,{\rm cm^{-3}}$.

3.2.6 Transport of $\mathrm{H_2}$-Dissociating Radiation

The occurrence of a metal-free atomic cooling halo requires previous suppression of Pop III.1 star formation in minihalos that could have polluted the atomic cooling halo with metals. As previously discussed, this suppression could have been produced by a molecule-dissociating radiative background produced by neighboring star-forming galaxies. From the initial redshift, we impose a constant LW background incident flux with intensity $J_{21} = 100$ (corresponding to $J_{\rm LW,21} = 90$) onto each of the six faces of the computational box. This ignores periodicity of the domain, which is acceptable given that our target halo is located near the centre of the box. Due to absorption by neutral hydrogen in the IGM, we set $J_\nu = 0$ shortward of the Lyman limit. We assume the spectral shape of this source is a

10^5 K blackbody, representative of massive, metal-free stars (Bromm et al. 2001, Schaerer 2002). While it has been suggested that the photodissociation of H^- can be crucial in regulating the H_2 abundance, we neglect it as it has been shown to have minimal importance for 10^5 K blackbody sources (e.g., Omukai et al. 2008). However, if Pop III stars were not extremely massive ($\sim 100\,M_\odot$) but had more moderate masses ($\sim 10\,M_\odot$), the appropriate radiation source temperature would be somewhat lower. We note, though, that the primary consequence of including H^- photodissociation in this context would be a shift in the density at which H_2 cooling becomes effective, and would not significantly alter our overall results.

The photodissociation of H_2 occurs through Solomon process (Stecher & Williams 1967) in which a photon with an energy coinciding with either the Lyman or the Werner (LW) bands of H_2 places the molecule in an excited electronic state. The subsequent radiative decay has a $\sim 15\%$ chance of reaching the ground state continuum, which results in molecular dissociation. Accurately modeling this process requires detailed modeling of hundreds of LW lines which is computationally unfeasible in 3D hydrodynamic simulations. Fortunately, the photodissociation rate of molecular hydrogen can be expressed as (e.g., Abel et al. 1997)

$$k_{\mathrm{H}_2} = 1.38 \times 10^{-12} J_{\mathrm{LW},21} f_{\mathrm{shield},\mathrm{H}_2} \ \mathrm{s}^{-1} \ , \tag{3.9}$$

where the dimensionless factor $f_{\mathrm{shield},\mathrm{H}_2} \leq 1$ accounts for H_2 self-shielding with $f_{\mathrm{shield},\mathrm{H}_2} = 1$ corresponding to no shielding and $f_{\mathrm{shield},\mathrm{H}_2} = 0$ to complete shielding. For a static, cold medium, $f_{\mathrm{shield},\mathrm{H}_2}$ can be written solely as a function of the H_2 column density N_{H_2} (Draine & Bertoldi 1996),

$$f_{\mathrm{shield},\mathrm{H}_2} = \min\left[1.0,\ \left(\frac{N_{\mathrm{H}_2}}{10^{14}\,\mathrm{cm}^{-2}}\right)^{-0.75}\right] . \tag{3.10}$$

To more accurately model a dynamic medium, Draine & Bertoldi (1996) also pro-

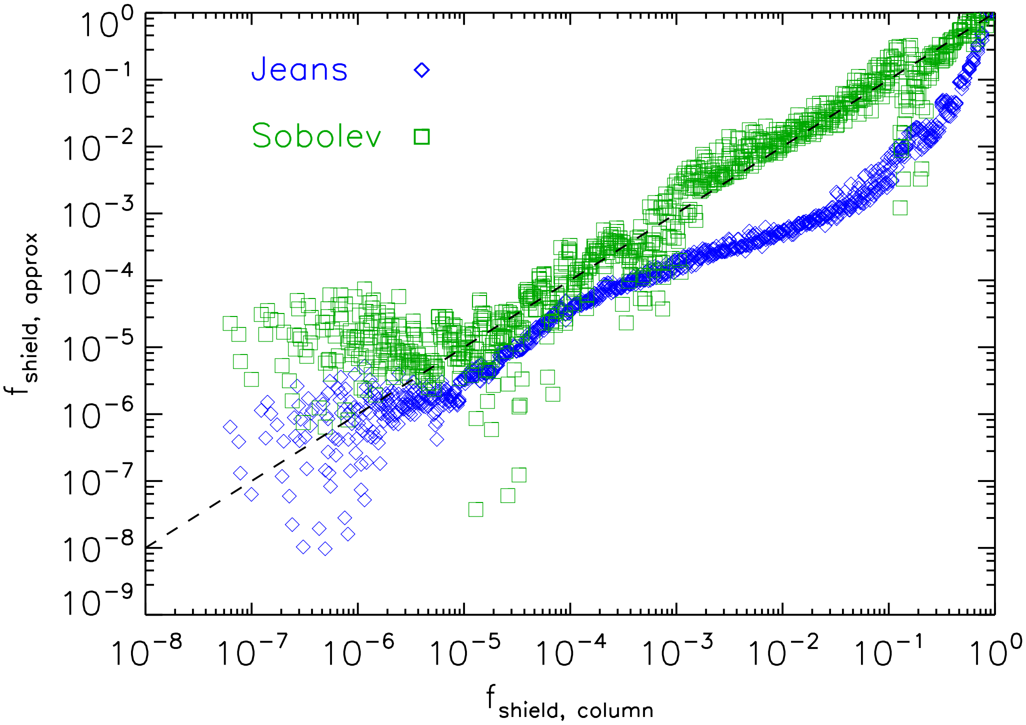

Figure 3.1 Comparison of the H_2 self-shielding factor, Equation (3.11), between approaches where the H_2 column density N_{H_2} is calculated via our column density method ($f_{\mathrm{shield,\ column}}$) and two common approximations ($f_{\mathrm{shield,\ approx}}$). In these approximations, N_{H_2} is calculated locally with a Sobolev (green squares) and a Jeans length approach (blue diamonds). The dashed line represents a one-to-one mapping. The Sobolev approximation for N_{H_2} produces an H_2 self-shielding factor in close agreement with our method, except for a few cases of disagreement, likely due to small velocity gradients. A hybrid of these two approaches may be useful in future work (see Clark et al. 2011b).

vided a fit for $f_{\mathrm{shield,H_2}}$ which takes thermal gas motion into account,

$$\begin{aligned} f_{\mathrm{shield,H_2}} &= \frac{0.965}{(1+x/b_5)^{\alpha}} \\ &\quad + \frac{0.035}{(1+x)^{0.5}} \times \exp[-8.5\times10^{-4}(1+x)^{0.5}]\,, \end{aligned} \tag{3.11}$$

where $x = N_{\mathrm{H_2}}/5{\times}10^{14}\,\mathrm{cm^{-2}}$, $b_5 = b/10^5\,\mathrm{cm\,s^{-1}}$, $\alpha = 2$, and $b = 9.12\,\mathrm{km\,s^{-1}}\,(T/10^4\,\mathrm{K})^{1/2}$ is the velocity spread parameter for H_2 (e.g., Ahn & Shapiro 2007). Unless otherwise noted, we will use Equation (3.11) with $\alpha = 1.1$, a modification suggested by Wolcott-Green et al. (2011), to calculate the self-shielding factor for H_2 from LW radiation.

Hydrogen deuteride can also be destroyed by LW radiation at a rate similar to that given in Equation (3.9),

$$k_{\mathrm{HD}} = 1.5\times10^{-12} J_{\mathrm{LW,21}} f_{\mathrm{shield,HD}} f_{\mathrm{shield,H_2,HD}}\ \mathrm{s^{-1}}\,, \tag{3.12}$$

which includes both a factor due to HD self-shielding and a factor accounting for the shielding of HD by H_2. The HD self-shielding factor is equivalent to that in Equation (3.11) with the HD column density N_{HD} replacing $N_{\mathrm{H_2}}$. Due to slight energy differences between the H_2 and HD LW line centers, the shielding of HD by H_2 does not effectively occur until there is a large H_2 column density, $N_{\mathrm{H_2}} \gtrsim 10^{20}\,\mathrm{cm^{-2}}$. Wolcott-Green et al. (2011) provided a fit for the HD shielding factor due to H_2,

$$f_{\mathrm{shield,H_2,HD}} = \frac{1}{(1+x)^{0.238}} \exp(-5.2\times10^{-3}\,x)\,, \tag{3.13}$$

where $x = N_{\mathrm{H_2}}/2.34\times10^{19}\,\mathrm{cm^{-2}}$. Both H_2 and HD can also be shielded from LW radiation by neutral hydrogen, however we neglect this effect as self-shielding is always the dominant effect. In fact, HD photodissociation is never significant in determining the HD abundance. Instead, as we will argue, it is primarily the

H_2 photodissociation and self-shielding that determine both the H_2 and HD abundances.

We compute the molecular column densities, $N_{\mathrm{H_2}}$ and N_{HD}, using an on-the-fly, non-local approach very similar to the 'six-ray' approximation (e.g., Nelson & Langer 1997, Glover et al. 2010). Specifically we compute the column density at each point in our box as

$$N_{\mathrm{H_2}}(\mathbf{r}) = \min_j\{N_{\mathrm{H_2},j}(\mathbf{r})\}\ , \tag{3.14}$$

where $j = \pm x, \pm y, \pm z$, and $N_{\mathrm{H_2},j}$ is the column density from point **r** to the edge of the box along direction j. The same approach is used for calculating the HD column density. The presence of bulk velocity gradients, which our approach does not account for, may act to decrease the importance of self-shielding by Doppler shifting absorption line centres (e.g., Draine & Bertoldi 1996, Glover & Brand 2001), although Wolcott-Green et al. (2011) argue that this effect is minimal in radially coherent gas flows.

While we self-consistently compute the column densities to each point in our simulation, a commonly used (e.g., Bromm & Loeb 2003a, Shang et al. 2010), and less computationally expensive, approximation is $N_{\mathrm{H_2}} \approx n_{\mathrm{H_2}}\, L_{\mathrm{char}}$, where L_{char} is a local characteristic length scale and $n_{\mathrm{H_2}}$ is the number density of molecular hydrogen. In Figure 3.1, we compare $f_{\mathrm{shield,H_2}}$ computed using $N_{\mathrm{H_2}}$ calculated with our six-ray approach to $f_{\mathrm{shield,H_2}}$ computed with $N_{\mathrm{H_2}}$ based on two local characteristic lengths L_{char} at the time when the gas density first reaches $10^8\ \mathrm{cm^{-3}}$. The first is the Jeans length, $L_{\mathrm{char}} = L_{\mathrm{J}}$, which is motivated by the assumption that the majority of shielding occurs in a region of size similar to the local Jeans length. The second approximation is a close analogue to the Sobolev length (Yoshida et al. 2006, Clark et al. 2011b), $L_{\mathrm{char}} = c_{\mathrm{s}}/|\nabla \cdot \mathbf{v}|$, which, assuming a constant velocity gradient, is the distance at which absorption line centres are Doppler-shifted by approximately one thermal line width. As is evident in Figure 3.1, both approximations agree reasonably well with the more accurate, non-local approach, with the Sobolev approach yielding slightly better overall agreement. While this agreement is likely coincidental given the disparate physics involved in all three approaches, it is still reassuring that they are all of similar magnitude. At least in this regime, a combination of the two local approaches could be useful in future work (e.g., Clark et al. 2011b).

3.3 Results

The LW radiation field of intensity $J_{21} = 100$ prevents the H_2 abundance from reaching the level that would permit efficient gas cooling in any halo not capable of atomic line cooling.[1] Hydrostatic collapse still occurs in these halos, but only along an adiabat. At a redshift $z \sim 13$, our target halo can be classified as an atomic cooling halo, with an average gas temperature of $8000\,\mathrm{K}$ and most of gas within the virial radius lying between $2000\,\mathrm{K} < T < 1.2 \times 10^4\,\mathrm{K}$. With gas now able to radiate its internal energy, collapse proceeds isothermally at $T \approx 8000\,\mathrm{K}$ resulting in an $n \propto r^{-2}$ density profile within the virial radius — see Figure 3.2.

When the maximum gas density near the halo centre reaches $\sim 200\,\mathrm{cm}^{-3}$ at $z = 12.1$, the virial mass of the surrounding halo is $3 \times 10^7\,M_\odot$ with a virial radius $\approx 750\,\mathrm{pc}$, just nominally fulfilling the standard analytic atomic cooling criterion, Equation (3.1). At this point, the H_2 cooling rate first exceeds the rate of adiabatic heating, resulting in rapid gas cooling to $T \sim 400\,\mathrm{K}$. It should be noted that H_2 self-shielding is not the determining factor in setting the density at which H_2 cooling becomes effective. Once that happens, however, the self-shielding fac-

---

[1] If we included no radiation background, the first minihalo in our box would have collapsed at $z \sim 19$; see Ritter et al. (2012), who used identical cosmological initial conditions.

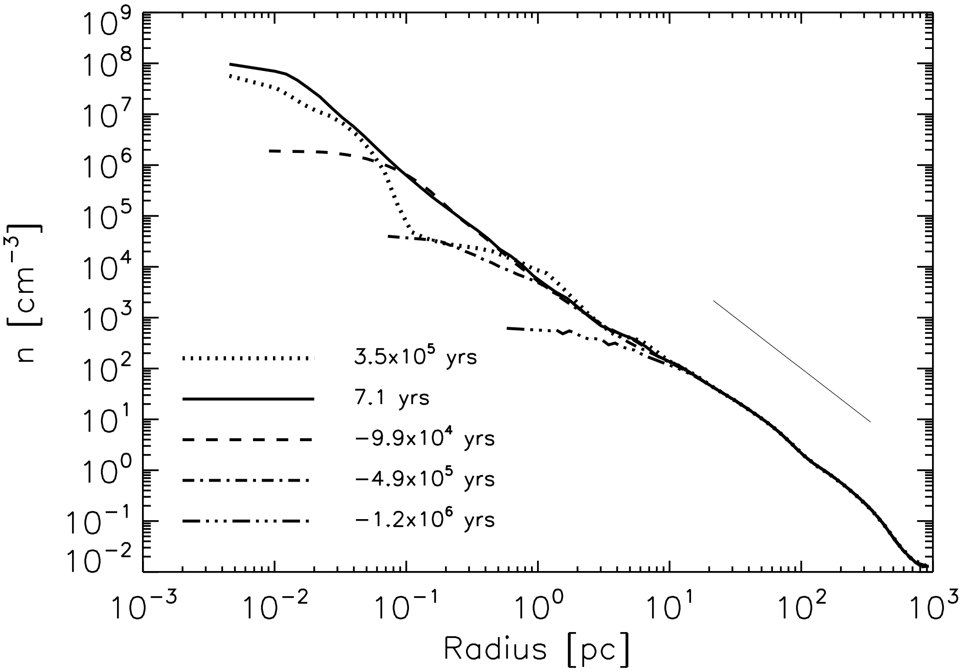

Figure 3.2 Radial profiles of average gas density centered around the point of maximum density with time measured from the point of sink particle formation which occurs shortly after the gas first reaches $n = 10^8\,\mathrm{cm}^{-3}$. The gas density always maintains a roughly $\rho \propto r^{-2}$ density profile (shown by the straight line) with departures from the formation of the core and the gravitational influence of the sink particle at the final time shown.

tor rapidly drops below unity indicating strong shielding. Indeed, the inclusion of self-shielding is essential for the cooling instability to continue and for the H_2 abundance to eventually reach the asymptotic abundance of $\sim 10^{-3}$ (Oh & Haiman 2002).

In a suite of cosmological simulation exploring the effect of LW radiation on the fraction of cool gas in halos, Machacek et al. (2001) determined the threshold halo virial mass for metal-free gaseous collapse as a function of radiation intensity to be

$$M_{\mathrm{TH}} = \{1.25 \times 10^5 + 2.9 \times 10^6 [J_{\mathrm{LW},21}]^{0.47}\}\, M_\odot \,, \tag{3.15}$$

where we have converted their F_{LW} into $J_{\mathrm{LW},21}$. Extrapolating beyond the intensity range, $J_{\mathrm{LW},21} < 0.080$, explored by Machacek et al. (2001), Equation (3.15) still yields an accurate prediction for the halo mass $M \approx 3 \times 10^7\, M_\odot$ where self-shielding and collapse first occur in the simulation here. Since Machacek et al. (2001) did not run simulations with stronger radiation fields, their simulations did not produce any halos in which atomic line cooling was effective. Indeed, once an atomic cooling halo forms, Lyα cooling permits rapid isothermal collapse provided that the halo mass exceeds a minimum that depends very weakly on the LW radiation intensity.

We will denote the density at which the H_2 cooling rate becomes larger than the rate of adiabatic heating and the gas evolution leaves the atomic isothermal track with n_{cool}. We show a representative density-temperature phase diagram in Figure 3.3 which shows this density is $n_{\mathrm{cool}} \approx 200\,\mathrm{cm}^{-3}$ and this density is found within a radius of $\sim 10\,\mathrm{pc}$. This is a larger density than $n_{\mathrm{cool}} \approx 10\,\mathrm{cm}^{-3}$ found by Shang et al. (2010) in a similar simulation with an identical radiation background. We attribute this discrepancy to our different treatments of H_2 self-shielding, in particular the method for computing N_{H_2}. Shang et al. (2010) utilized a local approximation $N_{\mathrm{H}_2} = n_{\mathrm{H}_2} L_{\mathrm{J}}$, while here we computed N_{H_2} more accurately as described in Section 3.2.6. To further understand the source of this discrepancy, we can equate the H_2 gas cooling time $t_{\mathrm{cool,H}_2}$ and the free-fall time t_{ff} to obtain a rough estimate of n_{cool},

$$n_{\mathrm{cool}} \approx 180\,\mathrm{cm}^{-3} \left(\frac{x_{\mathrm{H}_2}}{3 \times 10^{-7}}\right)^{-2} \,, \tag{3.16}$$

where x_{H_2} is the H_2 abundance at n_{cool}, $t_{\mathrm{ff}} = [3\pi/(32G\rho)]^{1/2}$ is the free-fall time, $t_{\mathrm{cool,H}_2} = 3nk_{\mathrm{B}}T/2\Lambda_{\mathrm{H}_2}$ is the H_2 cooling time, and Λ_{H_2} is the volumetric H_2 cooling

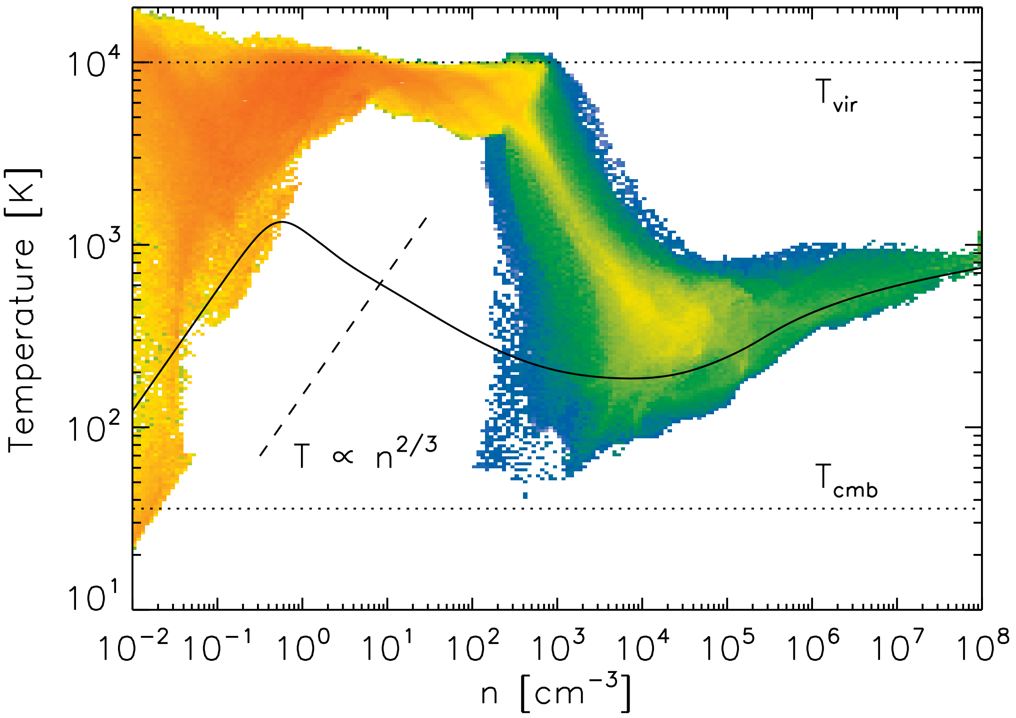

Figure 3.3 Density-temperature phase plot at the time of sink particle formation at $z = 12.1$ showing gas within $2R_{\rm vir}$ of the halo. The colour corresponds to the mass contained in the phase-space region. The solid black curve is a one-zone calculation of a thermodynamic evolution of metal-free gas undergoing free-fall collapse with no radiation background (Pop III.1 track). After the gas in the simulation is able to cool via $\rm H_2$ cooling starting around $n \sim 2\times10^2\,\rm cm^{-3}$, most of the cooled gas reaches minimum temperature at $T \sim 400\,\rm K$ and $n \sim 10^4\,\rm cm^{-3}$. The gas that continues to collapse converges towards the standard Pop III.1 molecular track. Adiabatic gas cooling due to expansion in a turbulent medium is apparent around $n \sim 10^3\,\rm cm^{-3}$, permitting some gas to reach temperatures $T < 100\,\rm K$.

rate (e.g., Galli & Palla 1998) which we evaluate at $8000\,\mathrm{K}$. Equation (3.16) is simply $n_{\rm cool}$ in terms of the required $\mathrm{H_2}$ abundance for the molecular cooling rate to exceed the rate of adiabatic heating, where 3×10^{-7} is the $\mathrm{H_2}$ abundance at which the transition to efficient molecular cooling takes place in our simulation. We can simplify this further by reasonably assuming that the $\mathrm{H_2}$ abundance is determined by its photoequilibrium value,

$$x_{\rm H_2,photo} = \frac{k_{\rm f,H^-}\, x_{\rm e}}{k_{\rm H_2}} n \,, \tag{3.17}$$

where $k_{\rm f,H^-}$ is the formation rate of $\mathrm{H^-}$, $k_{\rm H_2}$ is the photodissociation rate of $\mathrm{H_2}$ given by Equation (3.9), and $\mathrm{H^-}$ photodestruction is considered negligible. Inserting Equation (3.17) into Equation (3.16) and assuming $f_{\rm shield,H_2} = 1$ results in

$$n_{\rm cool} \approx 210\,\mathrm{cm^{-3}} \left(\frac{J_{21}}{100}\right)^{2/3} \left(\frac{x_{\rm e}}{5\times10^{-5}}\right)^{-2/3} \,, \tag{3.18}$$

where J_{21} is the unattenuated radiation intensity and $x_{\rm e}$ is the free electron abundance at $n_{\rm cool}$. Equation (3.18) is in excellent agreement with the density at which $\mathrm{H_2}$ cooling becomes effective in the simulation, suggesting that self-shielding is not necessary for the onset of $\mathrm{H_2}$ cooling. Allowing for self-shielding, $f_{\rm shield,H_2} \leq 1$, and adopting the prescription of Shang et al. (2010) with Equation (3.10) and $N_{\rm H_2} = n_{\rm H_2}\, L_{\rm J}$ gives us

$$n_{\rm cool} \approx 10\,\mathrm{cm^{-3}} \left(\frac{J_{21}}{100}\right)^{2/3} \left(\frac{x_{\rm e}}{10^{-4}}\right)^{-2/3} \,, \tag{3.19}$$

where we have now normalized to a slightly higher value of the electron abundance found in the simulation at lower densities. Equations (3.18) and (3.19) separately agree reasonably well with our simulation and with that of Shang et al. (2010), respectively, suggesting that the $\mathrm{H_2}$ column density computed with the local Jeans length is an overestimate compared to that computed with the more detailed radiative transfer described in Section 3.2.6. As we shall argue in Section 3.7.3, this may have an impact on the star formation efficiencies and observability of these systems.

The onset of effective H_2 cooling at $n_{\rm cool}$ leads to the rapid emergence of a cold $< 10^3\,{\rm K}$, dense $n \sim 10^4\,{\rm cm}^{-3}$ core, similar to that forming in the process of Pop III.1 star formation (e.g., Bromm et al. 2002). While we have argued that self-shielding is not important in determining $n_{\rm cool}$, the H_2 self-shielding factor does begin to drop below unity as the gas cools, reaching as low as $f_{\rm shield,H_2} \approx 10^{-6}$ at the highest densities. Proper treatment of self-shielding is therefore essential for accurately computing the chemical state of high density gas. To discriminate cold, molecule-rich, self-shielding gas from the warmer outer halo, we will generally utilize a simple criterion where we select the cells that have an H_2 shielding factor $f_{\rm shield,H_2} < 10^{-2}$. Some of our results may be sensitive to how we decide which gas belongs to the self-shielding core, although we have verified that alternative criteria, such as only selecting gas with temperatures $< 2 \times 10^3\,{\rm K}$ or densities $> 10^3\,{\rm cm}^{-3}$, would yield similar conclusions.

After effective cooling begins when the gas density reaches $n_{\rm cool}$, gas collapses at close to the free-fall rate and reaches $n = 10^8\,{\rm cm}^{-3}$ in $\sim 3\,{\rm Myr}$. As the collapse progresses, we can estimate the mass of the first gravitationally unstable clump by comparing the enclosed gas mass to the Bonnor-Ebert mass (Ebert 1955, Bonnor 1956) at different radii. The Bonnor-Ebert mass can be written as

$$M_{\rm BE} = \frac{m_1 a_T^4}{P_0^{1/2} G^{3/2}}\,, \tag{3.20}$$

where $a_T = (k_{\rm B}T/\mu m_{\rm H})^{1/2}$ is the isothermal sound speed, P_0 is the ambient pressure, and $m_1 = 1.18$ is the maximum dimensionless mass in the solution to the Lane-Emden equation (e.g., Stahler & Palla 2005). In Figure 3.6 we show the enclosed gas mass (solid line) and the Bonnor-Ebert mass (dashed line) both as a

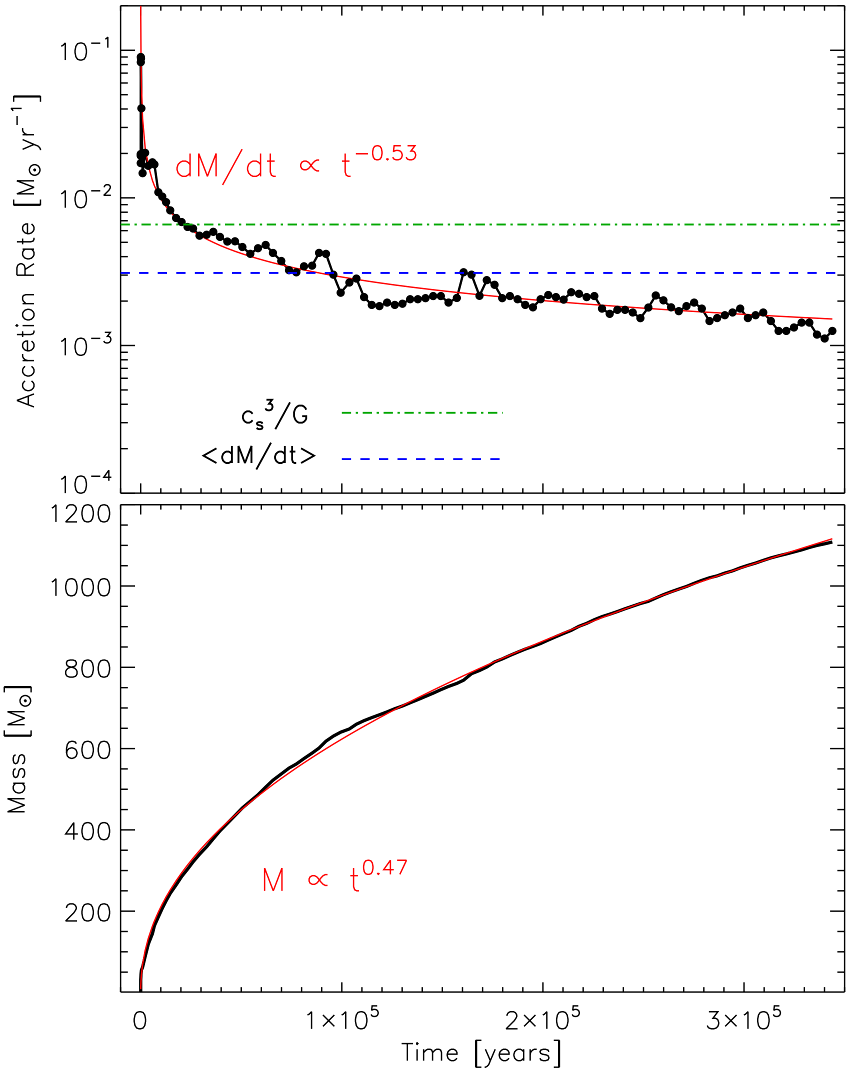

Figure 3.4 Accretion rate (top panel) and mass (bottom panel) of the sink particle as a function of time. Power law fits to the accretion rate and mass in the first 10^5 years are shown in red. The time-averaged accretion rate (blue dashed line) of the sink particle is $3 \times 10^{-3} M_\odot\,\mathrm{yr}^{-1}$, which we take to be an upper limit on the star formation rate that occurred in this time period. The late time accretion rate approaches $10^{-3} M_\odot\,\mathrm{yr}^{-1}$. We also show the characteristic accretion rate c_s^3/G (green dot-dashed line) with the adiabatic sound speed c_s evaluated at $T = 800\,\mathrm{K}$.

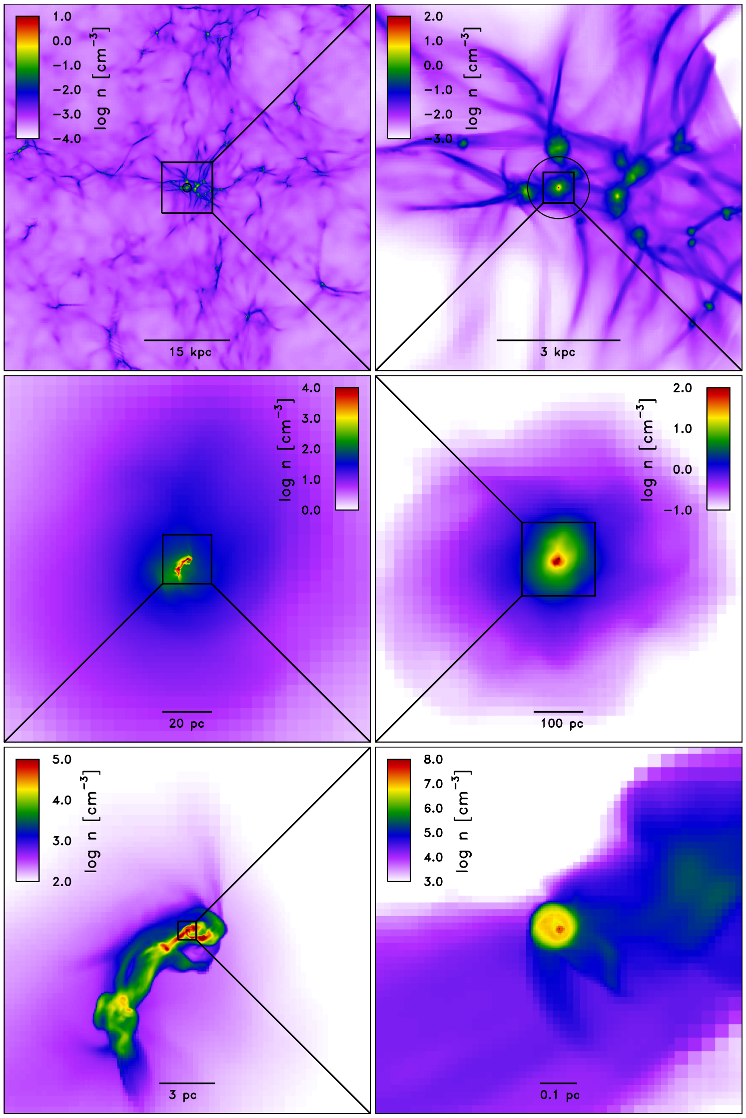

Figure 3.5 Mass-weighted line-of-sight gas density projections 3.5×10^5 years after the sink particle formation ($z = 12.1$). The six panels show progressively smaller fields of view. The black dot marks the location of the sink particle while the black circle in the top panels is the virial radius ($\sim 750\,\mathrm{pc}$) of the target halo. The spatial scale, in physical units, is shown at the bottom of each panel. The upper-left panel shows neighboring halos and the clustered cosmological environment where our target halo formed. Self-shielding, cold gas is seen in the bottom-left panel and the filamentary, irregular nature of this gas is apparent. The high density disc which forms around the sink particle is visible in the bottom-right panel, approximately face-on.

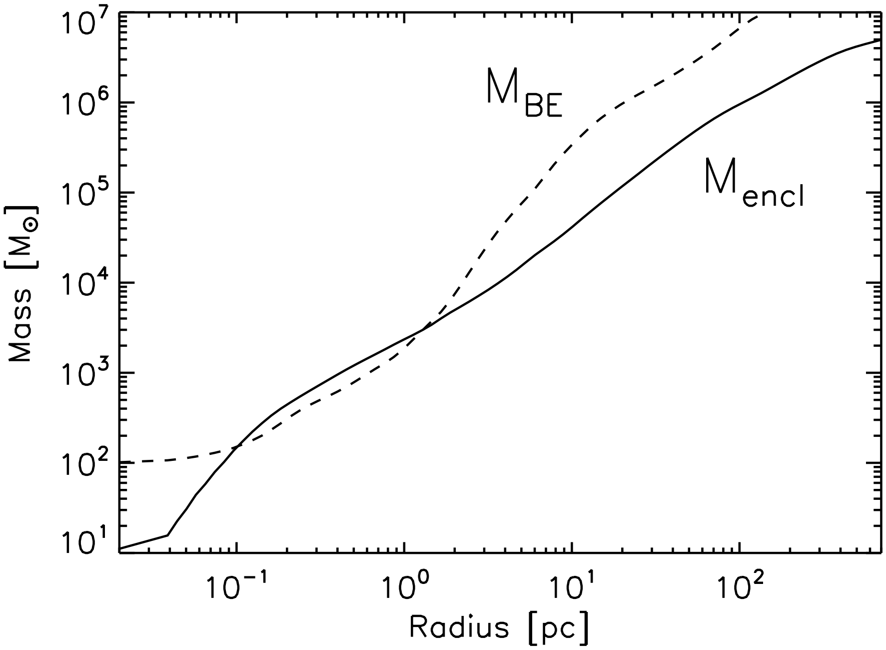

Figure 3.6 Enclosed gas mass (solid line) and Bonnor-Ebert mass (dashed line) as a function of distance from the point of maximum density roughly 10^5 years before sink particle formation. The maximum radius where the enclosed gas mass exceeds the Bonnor-Ebert mass provides a rough measure of the mass of the first gravitationally unstable clump. We see the onset of gravitationally instability occurring inside a radius of $\sim 1\,\mathrm{pc}$ when the enclosed gas mass is $10^3\,M_\odot$.

function of distance from the point of maximum gas density, approximately 10^5 years before sink particle formation. To evaluate the Bonnor-Ebert mass as a function of radius, $M_{\mathrm{BE}}(r)$, we take P_0 to be the pressure at radius r and a_T to be the mass-weighted isothermal sound speed interior to r. The enclosed gas mass first exceeds the Bonnor-Ebert mass at a radius of $\sim 1\,\mathrm{pc}$, corresponding to a mass of $\sim 10^3\,M_\odot$. We thus expect the first gravitationally unstable fragment to have roughly this mass, though there remains the possibility that additional fragmentation may occur on unresolved scales or at later times.

Sink particles are allowed to form at a density of $n = 10^8\,\mathrm{cm}^{-3}$ to follow the gas evolution for multiple free-fall times (see Section 3.2.5). We run the simulation for $3.5 \times 10^5\,\mathrm{yrs}$ after the formation of the sink particle. At this point, the self-shielding core has an average density $\approx 8 \times 10^3\,\mathrm{cm}^{-3}$, total mass $\approx 1.7 \times 10^4\,M_\odot$, mass-weighted root-mean-square (rms) velocity $v_{\mathrm{rms}} \approx 7.1\,\mathrm{km\,s}^{-1}$, average temperature $\approx 480\,\mathrm{K}$, and rms Mach number $\mathcal{M} = v_{\mathrm{rms}}/c_{\mathrm{s}} \approx 3.3$. Additionally, the sink particle has increased in mass to $\approx 1100\,M_\odot$, which is $\approx 6\%$ of the total mass of the self-shielding gas. No additional sink particles form, meaning that additional gravitational fragmentation, if any, would have been confined to occur on unresolved scales inside the sink particle.

In Figure 3.4, we plot the accretion rate and mass of the sink particle as a function of time. Initially, the sink particle accretion rate is $\dot{M}_{\mathrm{sink}} \sim 0.1\,M_\odot\,\mathrm{yr}^{-1}$ which drops to $0.01\,M_\odot\,\mathrm{yr}^{-1}$ within $10^4\,\mathrm{yrs}$. The time averaged accretion rate over the whole simulation is $0.003\,M_\odot\,\mathrm{yr}^{-1}$. Given the average density and mass of self-shielding gas at the end of the simulation, $n \approx 10^4\,\mathrm{cm}^{-3}$ and $\approx 2 \times 10^4\,M_\odot$, respectively, the average rate of accretion onto the sink particle is roughly a factor of 10 lower than what would be expected if the gas had been undergoing free-fall collapse. We discuss this inefficiency of gaseous collapse further in Section 3.5.

In Figure 3.5 we show mass-weighted line-of-sight gas density projections on six different spatial scales $3.5 \times 10^5\,\mathrm{yrs}$ after the formation of the sink particle. The upper-right panel shows neighboring halos and demonstrates the clustered cosmological environment where the target halo formed. The bottom-left panel displays the extent of self-shielding gas and its irregular, filamentary density structure. The self-shielding core is small, $\sim 5 - 10\,\mathrm{pc}$, compared to the virial radius of the halo, $R_{\mathrm{vir}} \approx 750\,\mathrm{pc}$. The bottom-right panel shows that a rotationally supported disc, $\sim 0.1\,\mathrm{pc}$ in diameter, forms around the sink particle approximately 10^5 years after the sink's formation. The disc is seen approximately face-on.

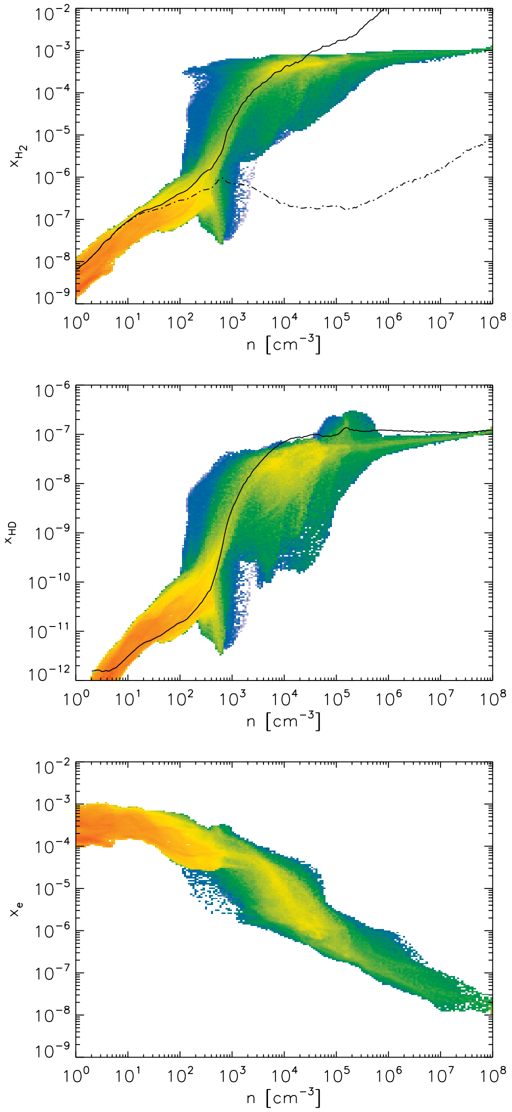

Figure 3.7 Abundance of H_2 (top-left), HD (top-right), and free electrons (bottom) as a function of density at the time when the sink particle formed. In the top panel, the dash-dotted line is the photo-equilibrium H_2 abundance not considering self-shielding ($f_{\mathrm{shield},H_2} = 1$) while the solid line includes self-shielding. As is shown, self-shielding is essential for H_2 abundances larger than $\sim 10^{-6}$. In the middle panel, the black line is the equilibrium abundance of HD only assuming reactions involving H_2 (see Equation 3.8) and excluding HD photodissociation. The three equilibrium curves were computed with data extracted directly from the simulation and represent mass-weighted averages as a function of density.

In Figure 3.7 we show the abundances of H_2, HD, and free electrons as a function of density at the time of sink particle formation. In gas with a density of $n = 10^4\,\mathrm{cm^{-3}}$, the H_2 abundance reaches $\sim$ few $\times\ 10^{-4}$ while the HD abundance is $\sim$ few $\times\ 10^{-8}$. Both of these values approximately match equilibrium abundances, assuming that H_2 is in direct photo-dissociation equilibrium with the self-shielding-attenuated LW radiation field and HD is close to equilibrium with H_2 via the reaction in Equation (3.6). We show the equilibrium abundance expectations for H_2 and HD with solid black lines. Above this density, H_2 approaches the non-equilibrium asymptotic abundance of $x_{\mathrm{H_2}} \approx 10^{-3}$ (e.g., Oh & Haiman 2002) while HD remains in approximate equilibrium with H_2. We observe only minor fractionation of HD over H_2, which is to be expected given the relatively high temperature of the gas $\sim 400\,\mathrm{K}$ compared to what is needed for the $x_{\mathrm{HD}}/x_{\mathrm{H_2}}$ ratio to exceed the cosmological $x_{\mathrm{D}}/x_{\mathrm{H}}$ ratio. In fact, the HD abundance is generally just below its equilibrium value at densities $10^4\,\mathrm{cm^{-3}} \lesssim n \lesssim 10^8\,\mathrm{cm^{-3}}$. The electron abundance shows the expected behavior — when efficient H_2 cooling begins at $n \sim 10^2\,\mathrm{cm^{-3}}$, the abundance is below the residual recombination value even though there is significant collisional ionization, $x_{\mathrm{e}} \sim 10^{-2}$, at lower densities (not shown in Figure 3.7). We propose this as one explanation for the lack of significant HD cooling and discuss this further in Section 3.6.

3.3.1 Kinematical State and Evolution

To gain further insight into the properties of the gas flow we proceed to analyze the gas kinematics at different stages of the collapse. Before the onset of effective H_2 cooling, Lyα cooling acts as a thermostat that keeps gas inside the halo at a temperature $\sim 8000\,\mathrm{K}$. Towards the centre of the halo, isothermal collapse proceeds under quasi-hydrostatic conditions. However, with increasing density, the

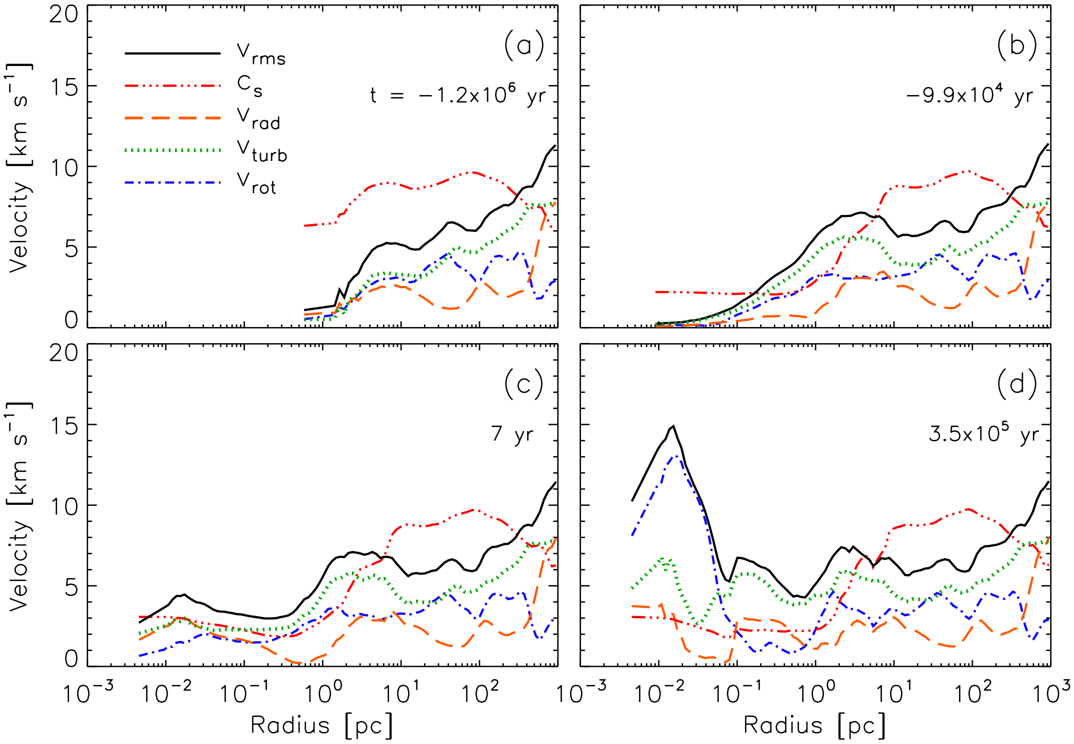

Figure 3.8 Mass-weighted average gas velocities computed in annular shells. Panels (a) through (d) correspond to times -1.2×10^6, -9.9×10^4, 7, and $+3.5 \times 10^5$ yrs from the formation of the sink particle. We show the rms velocity minus the centre of mass motion of the halo (black solid line), sound speed (red triple-dot dashed line), radial velocity (orange dashed line), rms turbulent velocity (green dotted line), and rms rotational velocity (blue dot-dashed line). See text for additional details.

cooling time decreases faster than the free-fall time, eventually reaching a point at which $\mathrm{H_2}$ cooling is so rapid as to effectively remove pressure support and set the gas into free-fall collapse. This also marks the onset of self-shielding which allows the $\mathrm{H_2}$ abundance and cooling-rate to increase further. This thermal instability proceeds until the gas temperature is roughly $400\,\mathrm{K}$. The collapse is also responsible for exciting some bulk turbulent motions and increasing the Mach number of the flow. At the time of sink particle formation, the self-shielding gas has an rms velocity $v_{\mathrm{rms}} \approx 7\,\mathrm{km\,s^{-1}}$ corresponding to a Mach number $\mathcal{M} \approx 3$.

In Figure 3.8 we show different components of the gas velocity computed in annular shells at four times: (a) just before the onset of effective $\mathrm{H_2}$ cooling, (b) after the onset of $\mathrm{H_2}$ cooling but before the maximum gas density reached $10^8\,\mathrm{cm^{-3}}$ and a sink particle formed, (c) at the moment of formation of the sink particle, and (d) at the end of our simulation, 3.5×10^5 years after sink formation. We consider five components of velocity, each computed via mass-weighting in annular shells centered on the sink particle location, except in panel (a) where it is centered on the point of maximum gas density:

1. The rms velocity
$$v_{\mathrm{rms}} = \left(\frac{\sum_i m_i |\mathbf{v}_i|^2}{\sum_i m_i} \right)^{1/2} , \tag{3.21}$$
where the sum ranges over all cells with centres inside the annular shell, m is the cell mass, and **v** is the gas velocity minus the centre-of-mass motion of the particular annular shell.

2. The adiabatic sound speed $c_{\mathrm{s}} = (\gamma k_{\mathrm{B}} T / \mu m_{\mathrm{H}})^{1/2}$, where T is the mass-weighted temperature inside the shell.

3. The rms rotational velocity of the mean rotation inside the shell

$$v_{\rm rot} = \left(\frac{\sum_i m_i |\mathbf{v}_{{\rm rot},i}|^2}{\sum_i m_i} \right)^{1/2} , \tag{3.22}$$

where $\mathbf{v}_{{\rm rot},i} = \mathbf{r}_i \times \mathbf{\Omega}$ is the azimuthal rotational velocity of the mean flow in cell i, $\mathbf{\Omega} = \mathbf{L}/I$ is the mean angular velocity inside the shell, $\mathbf{L} = \sum_i m_i \mathbf{r}_i \times \mathbf{v}_i$ is the total angular momentum inside the shell, and $I = \sum_i m_i |\mathbf{r}_i \times \hat{\mathbf{L}}|^2$ is the moment of inertia of the shell in the direction defined by the total angular momentum.

4. The radial velocity of the bulk motion inside the shell

$$v_{\rm rad} = \frac{\sum_i m_i \hat{\mathbf{r}}_i \cdot \mathbf{v}_i}{\sum_i m_i} \, . \tag{3.23}$$

5. The rms turbulent velocity relative to the mean flow, quantifying unordered gas motions

$$v_{\rm turb} = \left(\frac{\sum_i m_i |\mathbf{v}_i - \mathbf{v}_{{\rm rot},i} - \mathbf{v}_{{\rm rad},i}|^2}{\sum_i m_i} \right)^{1/2} , \tag{3.24}$$

where $\mathbf{v}_{{\rm rad},i} = v_{\rm rad} \, \hat{\mathbf{r}}_i$ is the radial velocity of cell i.

As shown in Figure 3.8, before the onset of significant H_2 cooling (panel a), typical rms gas velocities in the halo are $\sim 10\,{\rm km\,s^{-1}}$ near the virial radius and drop to $\sim 5\,{\rm km\,s^{-1}}$ in the inner $\sim 10\,{\rm pc}$. The sound speed is greater than the rms velocity inside $300\,{\rm pc}$, somewhat smaller than half of the virial radius. Inside the virial radius bulk gas motions are dominated by turbulent and rotational motions, as radial infall motions greatly decrease after the virial shock. Gas kinematics inside the halo can be described as a turbulent, subsonic flow. Within 1 Myr after the onset of H_2 cooling (panel b), and shortly before sink particle formation, the mass of self-shielding gas is $\approx 10^4\,M_\odot$. The temperature has dropped to $\approx 400\,{\rm K}$ in the inner $\sim 1\,\mathrm{pc}$. The rms velocities have increased within $r \approx 10\,\mathrm{pc}$ where the gas flow is transonic, $\mathcal{M} \sim 1$. At the time of sink particle formation (panel c), turbulent motions still dominate within $\sim 10\,\mathrm{pc}$, although towards smaller radii the contributions of rotational and radial motions increase. The Mach number is on the order of 2. Panel (d) shows the kinematical state of the gas $3.5 \times 10^5\,\mathrm{yrs}$ later at the end of the simulation. Turbulent motion is still the dominant form of gas motion, particularly in the range $0.1\,\mathrm{pc} \lesssim r \lesssim 10\,\mathrm{pc}$. Within $r \sim 0.1\,\mathrm{pc}$ there is kinematical evidence of a disc with ordered rotational velocities approaching $\sim 15\,\mathrm{km\,s^{-1}}$. The Mach number of the flow has also increased within the self-shielding core to $\mathcal{M} \sim 2-4$. We will proceed to analyze the impact of these supersonic gas motions on the collapse of gas in the following section.

3.4 Supersonic Turbulence

Supersonic turbulence is believed to play a key role in present-day star formation as it compresses gas to densities at which it can be susceptible to gravitational fragmentation and collapse. It additionally can act as a source of pressure support against gravitational collapse on larger scales (e.g., Mac Low & Klessen 2004). Minihalos, the sites of Pop III.1 star formation, are not thought to contain fully developed supersonic turbulence (e.g., Yoshida et al. 2006). The virialization process, gravitational inflow, and larger virial velocities of atomic cooling halos are believed to give rise to supersonically turbulent flows, likely influencing star formation (Wise & Abel 2007a, Greif et al. 2008, Prieto et al. 2012). The turbulence which develops in the self-shielding core in our simulation is also generated by gravitational infall (see Federrath et al. 2011, for a study of general properties of gravity-driven turbulence), but on a smaller spatial scale defined by thermal instability (e.g., Kritsuk & Norman 2002).

The classical theory of Kolmogorov (Kolmogorov 1941, Frisch 1995) describes turbulence as a chaotic fluid motion in which energy progressively cascades to smaller length scales through a series of eddies. These eddies eventually reach a small enough scale where viscous forces effectively dissipate the turbulence. Typical gas in the interstellar medium is highly compressible and compressible turbulence is known to result in a self-similar network of interacting shocks, large density contrasts, and a filamentary morphology (e.g., Kritsuk et al. 2007).

Many simulations have shown that driven, isothermal, supersonic turbulence results in a gas density probability distribution function (PDF) that is accurately described by a log-normal distribution (e.g., Vazquez-Semadeni 1994, Passot & Vázquez-Semadeni 1998, Scalo et al. 1998, Ostriker et al. 2001). This log-normal shape is understood to be the result of multiple, independent shocks altering the logarithmic gas density contrast in random walk fashion, thus driving the density PDF towards a log-normal form. The addition of self-gravity, magnetic fields, or a realistic equation of state can alter this general shape. We write the lognormal distribution as

$$p(s)\,ds = \frac{1}{(2\pi\sigma^2)^{1/2}} \exp\left[-\frac{1}{2}\left(\frac{s-\bar{s}}{\sigma}\right)^2\right] ds\ , \tag{3.25}$$

where $p(s)$ is the probability that a parcel of gas has s in the range $[s, s+ds]$, $s \equiv \ln(n/n_0)$ is the logarithmic density contrast, σ is the standard deviation, and n_0 is the average density. Additionally, by considering the normalization of the log-normal distribution, it can be shown that $\bar{s} = -\sigma^2/2$. Unless otherwise noted, we consider *volume*-weighted quantities when discussing density PDFs.

In Figure 3.9 we show the volume-weighted density PDF of self-shielding gas, defined such that $f_{\rm shield,H_2} < 10^{-2}$, at five different times. As expected, the peaks of the density PDFs lie just below the average density as most of the volume is underdense, typical of compressive turbulence (the peak of a *mass*-weighted density PDF would lie just above the average density). The black line is a log-normal fit to the final density PDF at $t = 1.2 \times 10^5\,\mathrm{yrs}$, although such a fit to the PDF at any time would look approximately the same in this view. For this particular log-normal fit, $\sigma = 0.93$.

As time progresses, the gas density PDF develops a power-law tail towards higher density contrasts. These power-law tails are understood as a consequence of the self-gravity of the gas and have been seen in both numerical simulations of turbulence (e.g., Scalo et al. 1998, Klessen & Burkert 2000, Federrath et al. 2008a, Collins et al. 2011, Kritsuk et al. 2011, Cho & Kim 2011) and observations of active star forming complexes (e.g., Kainulainen et al. 2009, Schneider et al. 2012b). It can be shown that the slope of the density PDF for a spherical $\rho \propto r^{-n}$ density profile is $-3/n$ (e.g., Kritsuk et al. 2011, Federrath et al. 2011). Thus, for an isothermal, $n = 2$, profile one would expect a power-law PDF with a slope of -1.5; this slope is shown in Figure 3.9 as a dashed black line. The slope of the power-law tail just after sink particle formation matches this expectation quite well, while approximately $10^5\,\mathrm{yrs}$ later the gravity of the sink particle has altered the gas dynamics thus perturbing the shape of the PDF.

Numerous studies (e.g., Padoan et al. 1997, Passot & Vázquez-Semadeni 1998, Price et al. 2011, Molina et al. 2012) have shown the rms Mach number $\mathcal{M}$ and gas density PDF width σ of a supersonically turbulent flow are related by

$$\sigma^2 = \ln(1 + b^2\mathcal{M}^2)\,, \tag{3.26}$$

where b is a constant, found numerically to lie between $\sim 0.2 - 1.1$ (see Federrath et al. 2008b). Since ordered rotational and radial motions do not directly produce density fluctuations, it is the turbulent Mach number, $\mathcal{M}_{\mathrm{turb}} = v_{\mathrm{turb}}/c_{\mathrm{s}}$ with v_{turb}

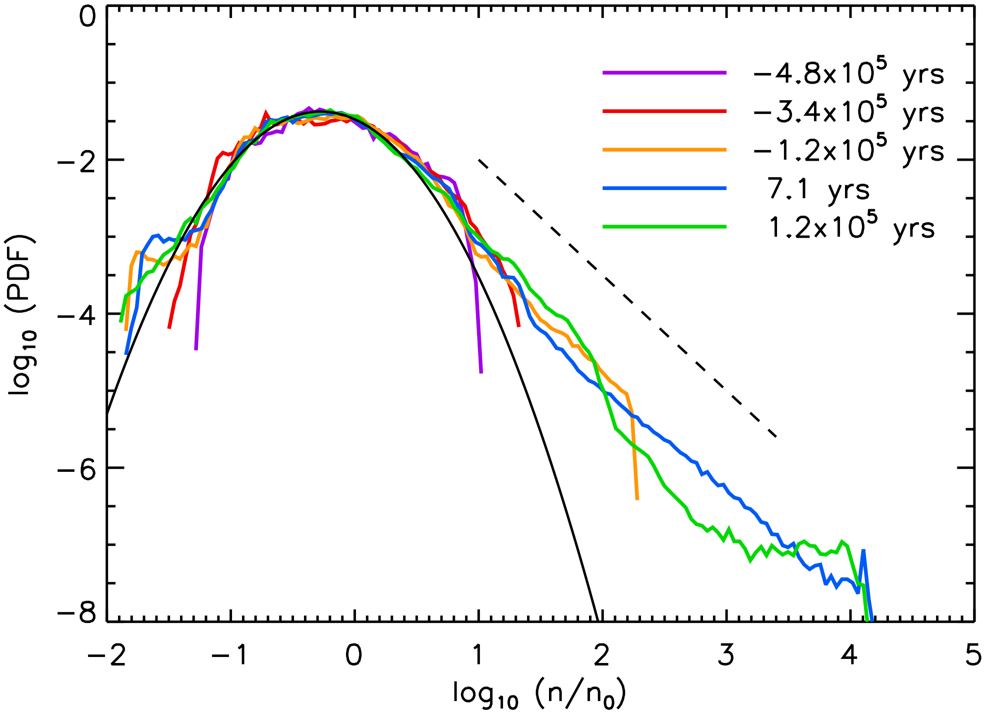

Figure 3.9 Volume-weighted density PDFs of self-shielding gas ($f_{\mathrm{shield,H_2}} < 10^{-2}$) at various times from the creation of the sink particle. We show a log-normal fit to the final density PDF (black curve) which has a standard deviation $\sigma = 0.93$. The PDF populates higher density contrast as gas collapses and at high densities shows a marked departure from the initial log-normal like distribution which can be attributed to the self-gravity of the gas. The dashed black line indicates a power law of slope -1.5, the expected PDF slope of an $\rho \propto r^{-2}$ density profile.

defined as in Equation (3.24), that should be present in Equation (3.26). Since the gas is dominated by turbulent motions after H_2 cooling becomes effective (see Figure 3.8), especially in low-temperature, self-shielding regions, v_{rms} and v_{turb} are very similar here. We can compare the parameters of the density PDF of the self-shielding gas in the simulation with expectations derived from the independently measured turbulent Mach number of the gas flow. Roughly 10^5 yrs after sink particle formation, the width of the density PDF is $\sigma = 0.93$, corresponding to the green curve in Figure 3.9, and the turbulent Mach number in the self-shielding core is $\mathcal{M}_{\mathrm{turb}} \approx 2.7$. Equation (3.26) would then require $b \approx 0.43$, in excellent agreement with previous numerical experiments of idealized turbulence in which turbulence is driven by a combination of solenoidal (divergence-free) and compressive (curl-free) modes, i.e., mixed-mode forcing (Federrath et al. 2010b). This seems to suggest that the gravitational infall which is driving supersonic turbulent motions in the cold, self-shielding core, is exciting a combination of solenoidal and compressive modes, and that turbulence has modified the density structure of the gas in close accord with theoretical expectations.

We stress that log-normal density PDFs have been found in extremely idealized simulations where supersonic turbulence is driven by random forcing. In the simulation presented here, however, the turbulence is driven by gravitational infall and thermal instability. Thus, it is interesting, though not surprising, that the parameters of the gas density PDF in our cosmological simulation so closely match the idealized, theoretical expectations.

3.5 Gas Fragmentation and Star Formation Rate

In this section we discuss trends towards gravitational fragmentation in our simulation. We also attempt to predict properties of the expected sub-grid star formation in the sink particle, including whether fragmentation on scales smaller than the sink particle accretion radius is expected. Our analysis is the first step towards learning about the mass spectrum of the stellar objects produced and the overall efficiency in which this system converts gas into stars.

3.5.1 Star Formation Rate and Global Fragmentation

For 3×10^5 years after sink particle creation, the extent of our simulation, no additional sink particles form. At the end of the simulation the lone sink particle has a mass of $\approx 1100\, M_\odot$, which is $\sim 6\%$ of the mass of the self-shielding, cold gas. To understand this lack of fragmentation and gain insight into the expected rate of star formation, we define the dimensionless star formation rate per free-fall time as

$$\mathrm{SFR_{ff}} = \frac{\dot{M}_\mathrm{sink}}{(M/t_\mathrm{ff})}\,, \tag{3.27}$$

where M and t_ff are the total mass and characteristic free-fall time of the self-shielding region, and $\dot{M}_\mathrm{sink}$ is the sink particle accretion rate (see Figure 3.4). $\mathrm{SFR_{ff}}$ is a measure of the actual rate of star formation compared to the rate if gas is collapsing on the free-fall timescale. Even though $\dot{M}_\mathrm{sink}$ is the sink accretion rate, not the star formation rate, it can be interpreted as the rate at which gas collapses to high densities where it can fuel star formation. Given that we do not attempt to model any feedback effects from the sink particles, such as protostellar outflows and radiation, $\dot{M}_\mathrm{sink}$ is a firm upper limit to the actual star formation rate.

Taking fiducial values for the self-shielding core, namely the average sink particle accretion rate, characteristic self-shielding cloud density, and its mass Equation (4.17) becomes

$$\begin{aligned}\mathrm{SFR}_{\mathrm{ff}} &\approx 0.1\left(\frac{\dot{M}_{\mathrm{sink}}}{3\times10^{-3}\,M_{\odot}\,\mathrm{yr}^{-1}}\right)\\ &\quad\times\left(\frac{t_{\mathrm{ff}}}{10^{6}\,\mathrm{yr}}\right)\left(\frac{M}{10^{4}\,M_{\odot}}\right)^{-1}\,, \end{aligned}\tag{3.28}$$

which suggests that star formation in our system is at least 10 times slower than it would be if all the gas in the self-shielding core gas had been collapsing at the free-fall rate. We will argue this retardation stems from the supersonic turbulence and a centrifugally supported disc around the sink particle.

One way to understand how supersonic turbulence suppresses the rate of gaseous collapse is by considering it an additional source of pressure support. The Jeans mass, M_{J}, scales with sound speed and density like $M_{\mathrm{J}} \propto \rho^{-1/2} c_{\mathrm{s,eff}}^{3}$. The presence of supersonic turbulent motions enhances the effective sound speed, $c_{\mathrm{s,eff}}^{2} = c_{\mathrm{s}}^{2} + v_{\mathrm{rms}}^{2}/3$. Additionally, strong isothermal shocks impart density fluctuations scaling as $\rho \propto \mathcal{M}^{2} \propto v_{\mathrm{rms}}^{2}$. These two effects lead to a scaling of $M_{\mathrm{J}} \propto v_{\mathrm{rms}}^{2}$ in supersonic gas, implying turbulence does indeed impede collapse by increasing the effective Jeans mass (e.g., Chandrasekhar 1951, Bonazzola et al. 1987). It should be noted, however, that this analysis assumes that the highly anisotropic turbulent velocity field is isotropic; thus treating supersonic turbulence as an additional source of pressure is not necessarily justified.

It has long been known that the global $\mathrm{SFR}_{\mathrm{ff}}$ in the Galactic giant molecular clouds (GMCs) is on the order of ~ 0.01 (e.g., Zuckerman & Evans 1974). This low rate of star formation extends to more compact star-forming systems as well, such as infrared dark clouds (IRDCs) and higher density clumps embedded within (see Krumholz et al. 2007, and references therein). Equation (3.28) suggests a global $\mathrm{SFR}_{\mathrm{ff}}$ of ~ 0.1 for self-shielding, cold gas seen in our simulation, ten times that of the Galactic norm. Perhaps this is not surprising, though, given we neither include any sort of stellar feedback nor magnetic fields, both of which would likely reduce the star formation rate. Additionally, the rms Mach number in the self-shielding gas here, $\mathcal{M} \sim 3$, is much less than typical Mach numbers in Galactic molecular clouds, $\mathcal{M} \sim 10 - 20$ (e.g., Bergin & Tafalla 2007) implying a relatively smaller contribution of turbulent pressure support in the simulation compared to molecular clouds. Indeed, Krumholz & McKee (2005) showed that the density threshold for star formation, understood as the density where thermal pressure equals turbulent pressure, in a supersonically turbulent medium is $\rho_{\rm crit} \sim \rho_0 \, \mathcal{M}^2$.

3.5.2 Disc Fragmentation

The idea that supersonic turbulence suppresses star formation and fragmentation does not apply in the $\sim 1\,{\rm pc}$ vicinity of the sink particle where the densities exceed $\sim 10^6\,{\rm cm^{-3}}$. In Figure 3.5 we show that a disc of size $\sim 0.1\,{\rm pc}$ forms around the sink particle with rotational velocities approaching $\sim 15\,{\rm km\,s^{-1}}$ at $r \sim 10^{-2}\,{\rm pc}$. It is interesting why this disc does not become unstable and fragment into multiple sink particles, given that disc fragmentation has been seen in recent simulations of Pop III.1 star formation (e.g., Stacy et al. 2010, Clark et al. 2011b, Greif et al. 2011), though at much higher densities and smaller spatial scales than probed here.

In general, two conditions must be met for a disc to fragment. The disc must be gravitationally unstable which requires that the Toomre Q parameter, $Q = c_{\rm s}\Omega/\pi G\Sigma$, be less than unity (Toomre 1964, Goldreich & Lynden-Bell 1965), where $c_{\rm s}$ is the sound speed in the disc, $\Omega = v_{\rm rot}/R$ is the angular velocity, and Σ is the gas surface density. Additionally, even if a disc is gravitationally unstable, a number of effects can prevent fragmentation into gravitationally bound collapsing

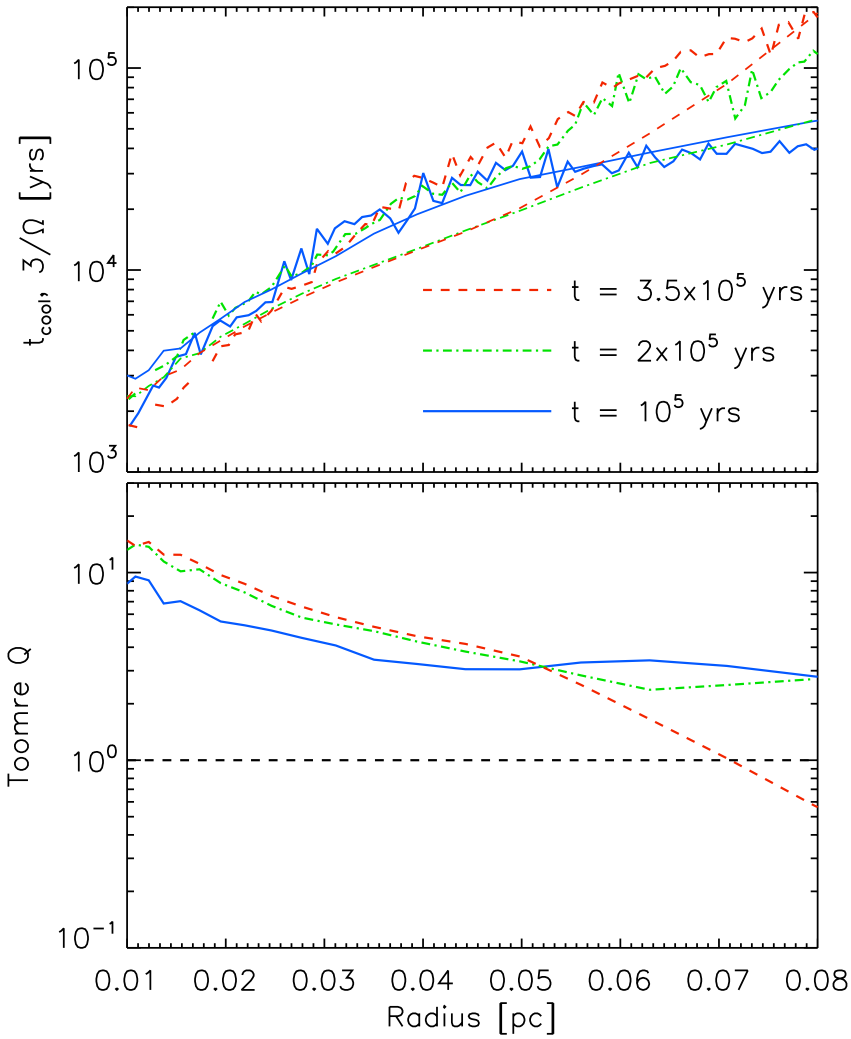

Figure 3.10 Cooling timescale $t_{\rm cool}$ and $3/\Omega$ (top panel) and the Toomre Q parameter (bottom panel) plotted as a function of distance from the sink particle for gas with $n > 10^6\,{\rm cm}^{-3}$ which roughly selects gas in the sink particle's disc. In the top panel, thick lines are the cooling time while the thin lines represent $3/\Omega$. Both panels suggest that the disc is stable against fragmentation. Specifically, in the top panel, $3/\Omega$ is generally below $t_{\rm cool}$ (the Gammie criterion), while in the bottom panel, $Q \gtrsim 1$ throughout the disc's extent. For reference, the disc radius is approximately $\sim 0.05 - 0.07\,{\rm pc}$.

clumps (e.g., Kratter & Murray-Clay 2011). In particular, Gammie (2001) argued that a key effect influencing the fragmentation behavior of a disc is the balance between cooling and the dissipation of turbulence, which is a source of heating. Quantitatively, Gammie found that if $t_{\rm cool} < 3/\Omega$ then discs tend to fragment into clumps.

In the top panel of Figure 3.10 we show the mass-weighted average of the cooling time as a function of distance from the sink particle for gas with density $n > 10^6\,{\rm cm^{-3}}$ at three different times (thick lines). We also show the mass-weighted average of $3/\Omega$ (thin lines). As is shown, $3/\Omega$ and $t_{\rm cool}$ trace each other in the inner disc ($r \lesssim 0.03\,{\rm pc}$), while $3/\Omega$ is a factor of ~ 2 lower than $t_{\rm cool}$ at larger radii and particularly in the last two times shown. According to the results of Gammie (2001), this disc is stable to fragmentation given its inefficient cooling and relatively rapid rotational velocity. For reference, the radius of the disc is sharp and is approximately $\sim 0.05 - 0.07\,{\rm pc}$.

In the bottom panel of Figure 3.10, we show the Toomre Q parameter as a function of distance from the sink particle. To calculate $Q(r)$, we rewrite the gas surface density as $\Sigma(r) = \rho(r)H$, where H is the characteristic vertical thickness of the disc. We have verified that for the disc here, $H \approx 0.05\,{\rm pc}$ is approximately constant both in radius and time, and that a more detailed calculation of $\Sigma(r)$ would come within a factor of two of this estimate. Thus, $Q(r)$ provides an additional reason for the absence of disc fragmentation since $Q \gtrsim 1$ within the disc's extent and actually increases slightly with time.

3.6 HD Cooling and Pop III.2 Star Formation

Elevated electron abundances created by the ionizing radiation emitted by the first stars, or in our case, by collisional ionization in $T_{\rm vir} > 10^4\,{\rm K}$ halos, are thought to result in an increase of the HD abundance (see Section 3.2.3). HD is an agent that can act as a coolant in metal-free gas below $200\,\mathrm{K}$. These lower temperatures reduce the Jeans mass and may result in stars with lower characteristic masses, the so-called Pop III.2. However, as discussed in Section 3.3, HD is never a significant coolant. Some gas does cool to temperatures $< 100\,\mathrm{K}$ as seen in Figure 3.3, but this is the result of adiabatic expansion, not HD cooling.

In Figure 3.11 we show a phase plot of the HD cooling time, $t_{\mathrm{cool,HD}}$ as a function of density at the time when the sink particle formed. We also show the free-fall time t_{ff}. For HD cooling to be significant, it is necessary that $t_{\mathrm{cool,HD}} < t_{\mathrm{ff}}$. This criterion is never met.

Many studies have explored the HD cooling mode in Pop III.2 star formation. Johnson & Bromm (2006) calculated that an HD abundance of $x_{\mathrm{HD}} \sim 10^{-8}$ is needed for HD emission to cool gas to T_{CMB} in a Hubble time. They suggested that this sets a firm lower limit on the HD abundance needed for its cooling to have a thermodynamic impact. Using one-zone thermodynamic models, they also found that this HD abundance is realized in the downstream of $T \sim 10^4\,\mathrm{K}$ virialization shocks, in supernova remnant cooling, and in the collapse of relic Pop III.1 HII regions. In a cosmological setting, Greif et al. (2008) detected gas with temperatures $\sim T_{\mathrm{CMB}}$, which they attribute to efficient HD cooling, in an atomic cooling halo of similar mass to the one we analyze. Yoshida et al. (2007) found that HD cooling was responsible for gas cooling to the CMB temperature after the collapse of a Pop III.1 relic HII region and argued this was responsible for reducing the mass of the clump which eventually will undergo runaway collapse. There has even been a suggestion, by McGreer & Bryan (2008), that in Pop III.1 star formation HD cooling may play a thermodynamically significant role. In contrast, other studies that have examined the collapse of metal-free gas in a similar context to the one explored here are in agreement that HD never plays a major thermodynamic role (Omukai 2001, O'Shea & Norman 2008, Shang et al. 2010).

We propose two related reasons for the lack of significant HD cooling in our simulation. First, as found by Wolcott-Green et al. (2011) using one-zone models, the LW flux necessary to suppress HD cooling is $J_{\rm crit,HD} \approx 10^{-22}\,{\rm erg\,s^{-1}\,cm^{-2}\,Hz^{-1}\,sr^{-1}}$. This is far smaller than the flux required to completely suppress $\rm H_2$ formation and cooling, $J_{\rm crit,H_2} \approx 10^{-20} - 10^{-16}\,{\rm erg\,s^{-1}\,cm^{-2}\,Hz^{-1}\,sr^{-1}}$ (Shang et al. 2010). This critical HD flux is not the result of direct HD photodissociation, but is instead due to the partial photodissociation of $\rm H_2$ which never permits a significant fraction of gas to cool below $\sim 300\,\rm K$ where significant HD fractionation can occur. Second, at $n_{\rm cool} \approx 200\,{\rm cm^{-3}}$ where $\rm H_2$ cooling becomes effective, the free electron abundance is not high enough to drive up the $\rm H_2$ abundance. Gas heated to high temperatures in virialization shocks can have a free electron abundance of $x_{\rm e} \sim 10^{-2}$, but only at low densities, $10^{-2} - 10^{-1}\,{\rm cm^{-3}}$. At larger densities around $n_{\rm cool}$ the electron abundance drops to $\sim 10^{-4}$ (see Figure 3.7), below the residual abundance after recombination, simply because the electron recombination time is inversely proportional to density. This would seem to suggest that Pop III.2 star formation is very similar to Pop III.1, at least in the scenario explored here.

3.7 Discussion

3.7.1 Lyman-Werner Radiation Field

A key physical parameter in this study is the intensity of the constant LW radiation background. Given the large mean free path of photons with energies below $13.6\,\rm eV$, the formation of the first stars should have established a LW background well before the completion of reionization (e.g., Haiman et al. 2000).

In terms of the cosmic star formation rate, we can estimate $J_{\rm LW,21}$ as (e.g.,

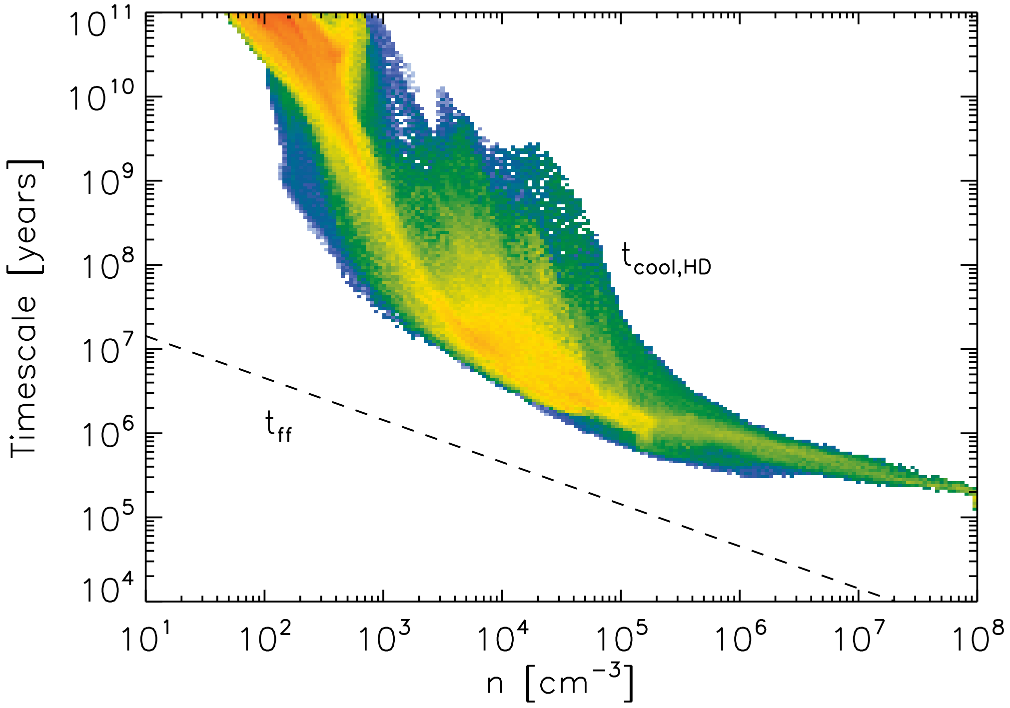

Figure 3.11 HD cooling time and the free-fall time as a function of density when the sink particle forms. For HD cooling to be thermodynamically significant, the HD cooling time must be shorter than the free-fall time, which is never realized. This is a result of many factors, including the reduction in the free electron fraction when $\mathrm{H_2}$ cooling becomes significant at $n \approx 200\,\mathrm{cm^{-3}}$ and the reduction in the HD cooling rate when it thermalizes at $n \approx 10^5\,\mathrm{cm^{-3}}$.

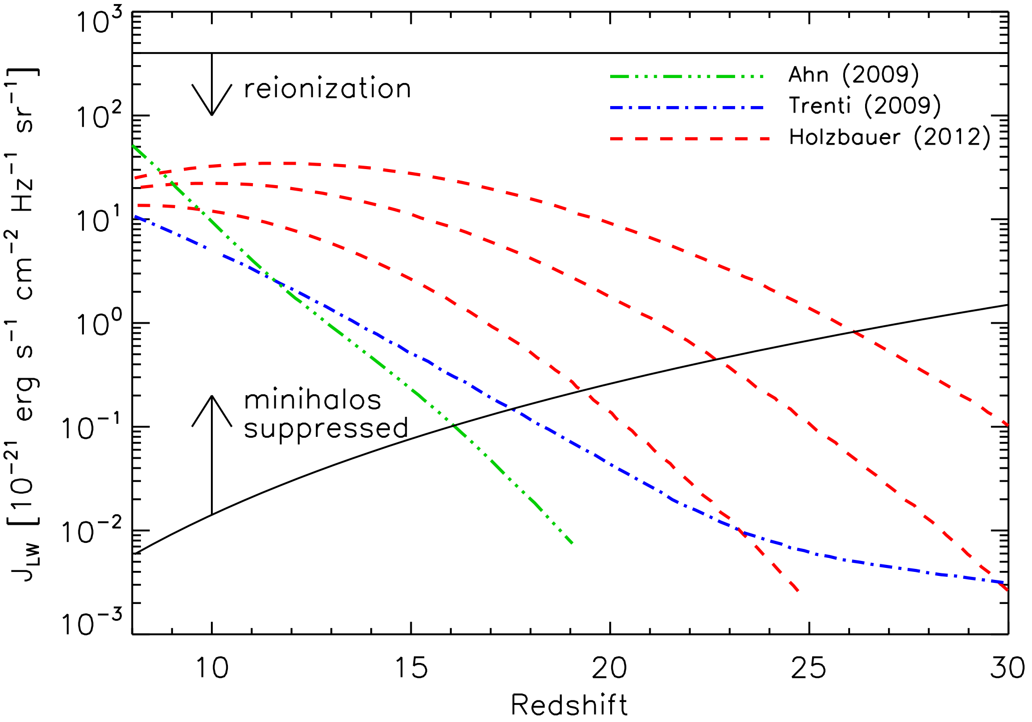

Figure 3.12 Theoretical estimates of the redshift evolution of the average radiation intensity in the LW bands ($J_{\mathrm{LW},21}$) compiled from the literature. The curves show the results of Ahn et al. (2009) (*green triple-dot dashed lined*), Trenti et al. (2009) (*blue dashed-dot line*), and Holzbauer & Furlanetto (2012) (*red dashed lines*). The three curves of Holzbauer & Furlanetto (2012) correspond to different choices for the minimum virial mass of a halo capable of forming stars, which they take, from top to bottom, as $10^6, 10^7$, and $10^8\,M_\odot$. The top black line denotes the LW radiation background which accompanies reionization of the IGM at $z = 9$, assuming an escape fraction of ionizing radiation of $f_{\mathrm{esc}} = 0.1$ and 10 ionizing photons-per-baryon required for reionization. The bottom black line is an estimate of the LW background needed to suppress cooling in halos which rely exclusively on H_2. See the text for further details.

Johnson 2013)

$$J_{\mathrm{LW},21} \approx 2\left(\frac{\eta_{\mathrm{LW}}}{10^4}\right)\left(\frac{\dot{\rho}_*}{10^{-2}\,M_\odot\,\mathrm{yr}^{-1}\,\mathrm{Mpc}^{-3}}\right)\left(\frac{1+z}{10}\right)^3, \tag{3.29}$$

where η_{LW} is the number of LW photons produced per stellar baryon, $\dot{\rho}_*$ is the star formation rate per comoving volume, and the lifetime of stars producing the LW radiation is implicitly assumed to be $5 \times 10^6\,\mathrm{yrs}$. The star formation rate is normalized with a reasonable value around $z = 10$ (e.g., Trenti et al. 2009).

Another estimate of $J_{\mathrm{LW},21}$ can be obtained by considering the ionizing background needed to reionize the Universe. Assuming that reionization was driven by photons with energies just above the Lyman limit, it is straightforward to estimate the value of the UV background just below the limit, $J_{21}^{-} \approx J_{\mathrm{LW},21}$ (e.g., Bromm & Loeb 2003a),

$$J_{21}^{-} \approx 400\left(\frac{N_\gamma}{10}\right)\left(\frac{f_{\mathrm{esc}}}{0.1}\right)^{-1}\left(\frac{1+z}{10}\right)^3, \tag{3.30}$$

where N_γ is the number of ionizing photons-per-baryon required to reionize the Universe and f_{esc} is the ionizing photon escape fraction from high-redshift star forming galaxies. Both of the above estimates suggest that before reionization was complete, radiation intensities as high as $J_{\mathrm{LW},21} \sim 100$, the value we adopt here, were realized in the Universe. Depending on the scenario for reionization, these may overestimate the mean background intensity, but Dijkstra et al. (2008) showed that, due to dark matter halo clustering, a small fraction of halos can experience LW intensities greatly above the global mean value.

Even though the UV background intensity around the time of reionization is very uncertain, the above estimates suggest it was likely far above the threshold, $J_{\mathrm{LW},21} \sim 10^{-1}$, that would have suppressed the formation of H_2 in small-mass $\sim 10^5 - 10^6\,M_\odot$ halos, thus delaying cooling and star formation until the assembly of atomic cooling halos. As we shall discuss in Section 3.7.3, the precise value of $J_{\rm LW,21}$ may significantly change the results of our simulation, particularly the star formation efficiency.

For more accurate estimates of $J_{\rm LW,21}$ we can look to other studies which have undertaken detailed modeling of the redshift evolution of the LW background intensity. In Figure 3.12, we show three such estimates in the literature. We also show the LW intensity which would have accompanied reionization at $z = 9$ (top solid line) assuming the fiducial values in Equation (3.30). Additionally, we plot the redshift-dependent LW radiation intensity $J_{\rm LW,crit}(z)$ needed to completely suppress H_2 formation in halos with $T_{\rm vir} < 10^4\,{\rm K}$ (bottom solid line). We compute $J_{\rm LW,crit}(z)$ by equating the $J_{\rm LW,21}$-dependent minimum halo mass needed for H_2 cooling with the halo mass at which the virial temperature equals $10^4\,{\rm K}$ (equations 12 and 14 from Trenti et al. 2009, respectively) to obtain

$$J_{\rm LW,crit}(z) = 1.5\left(\frac{1+z}{31}\right)^{4.5}. \tag{3.31}$$

We refer the reader to the original references for the details of the models, but briefly summarize the critical components. Trenti et al. (2009) and Holzbauer & Furlanetto (2012) model $J_{\rm LW,21}(z)$ in a semi-analytic fashion, using the formalism of Press & Schechter (1974) modified for ellipsoidal collapse by Sheth & Tormen (2002) to estimate the mass function of collapsed halos, which they combine with a prescription for star formation in these halos. Trenti et al. (2009) self-consistently utilize their calculated LW background to estimate the minimum mass of a star-forming halo. The three curves in Figure 3.12 from Holzbauer & Furlanetto (2012) correspond to different choices for the minimum mass of a star-forming halo; $M_{\rm min} = 10^6$, 10^7, and $10^8\,M_\odot$ from top to bottom, respectively, each with a fixed star formation efficiency of 0.1. Ahn et al. (2009) do not rely on a semi-analytic approach, but instead carry out transfer of ionizing and LW radiation in a large, cosmological, N-body simulation. Their resolution, however, is limited to $10^8\ M_\odot$, which may be responsible for their $J_{\rm LW,21}$ estimate being the lowest at high redshifts, as can be seen in Figure 3.12.

There are numerous uncertainties in these estimates of $J_{\rm LW,21}(z)$, particularly in the choice of star formation efficiency (which is likely to depend on $J_{\rm LW,21}$ itself, as well as the redshift, halo mass, and metallicity), LW escape fraction of radiation, mass and multiplicity of Pop III sources, and different prescriptions for star formation feedback. We note that all these models assume that Pop III sources have an extremely top-heavy IMF with a characteristic mass $\sim 100\,M_\odot$. In spite of these uncertainties, most of these estimates seem to converge around $z = 10$, but they still underpredict the LW intensity that would have accompanied reionization by $z = 9$. Additionally, all models suggest that at $z \lesssim 15 - 20$, the average LW radiation field is large enough to completely suppress cooling and star formation in halos with $T_{\rm vir} < 10^4\,{\rm K}$.

Furthermore, as discussed in Ahn et al. (2009) and Holzbauer & Furlanetto (2012) (see also Dijkstra et al. 2008), the LW radiation field is expected to be very spatially uniform around the time of reionization, in the sense that isolated regions with $J_{\rm LW,21}$ significantly above or below the mean were extremely rare. This homogeneity increases with decreasing redshift and increasing spatial scale. Compared to this spatially homogenous LW radiation feedback, chemical enrichment of the IGM by galactic outflows has been suggested to be extremely inhomogeneous (e.g., Scannapieco et al. 2002, Tornatore et al. 2007, Trenti et al. 2009). This suggests that the scenario we explore in this work, a chemically pristine atomic cooling halo subjected to a strong LW background, is a physically plausible scenario for the formation of metal-free stellar clusters.

3.7.2 Internal Feedback

This work focused on the impact of an external LW radiation background and its effect on star formation in metal-free atomic cooling halos. However, once a starburst begins, LW and photoionizing radiation feedback from internal sources will likely impact subsequent star formation. Glover & Brand (2001) explored the conditions under which a metal-free gaseous clump exposed to LW radiation can continue to collapse and form stars. They argue that star formation in gas clumps will be suppressed if the H_2 photodissociation time, $t_{\rm dis}$, is shorter than the free-fall time of the clump. Glover & Brand (2001) derived that $t_{\rm dis}$ for a spherical, homogeneous cloud of density n, mass M, and distance D from a source which produces $\dot{N}_{\rm dis}$ LW photons per second is given by

$$t_{\rm dis} = 20 x_{\rm H_2} n^{2/3} M_{\rm solar}^{1/3} D_{\rm pc}^2 f_{\rm dis}^{-1} f_{\rm abs}^{-1} \left(\frac{\dot{N}_{\rm dis}}{10^{48}\,{\rm s}^{-1}} \right)^{-1} \ {\rm yrs} \tag{3.32}$$

where $f_{\rm abs}$ is the fraction of incident photons which are actually absorbed by the cloud, $f_{\rm dis}$ is the fraction of H_2 excitations by a LW photon which result in a successful dissociation, and $M_{\rm solar}$ and $D_{\rm pc}$ are measured in units of $M_\odot$ and parsecs, respectively. Considering the simulation here, a clump at a distance of $\sim 1\,{\rm pc}$ from the source of LW photons (which we take to be the sink particle) has a characteristic mass on order of the Jeans mass $\sim 3000\,M_\odot$, density $\sim 10^5\,{\rm cm}^{-3}$, and an H_2 abundance $\sim 10^{-3}$. If we reasonably assume that the central sink particle forms roughly ten $10\,M_\odot$ stars (see Section 3.5) the LW photon production rate is $\dot{N}_{\rm dis} \approx 10^{48}\,{\rm s}^{-1}$. The resulting H_2 photodissociation time $t_{\rm dis} \approx 6 \times 10^4\,{\rm yrs}$ assuming that $f_{\rm dis} = f_{\rm abs} = 0.1$. The free-fall time is $t_{\rm ff}(10^5\,{\rm cm}^{-3}) \approx 1.5 \times 10^5\,{\rm yrs}$, therefore this clump will have its primary cooling agent, H_2, photodissociated and thus its further collapse suppressed.

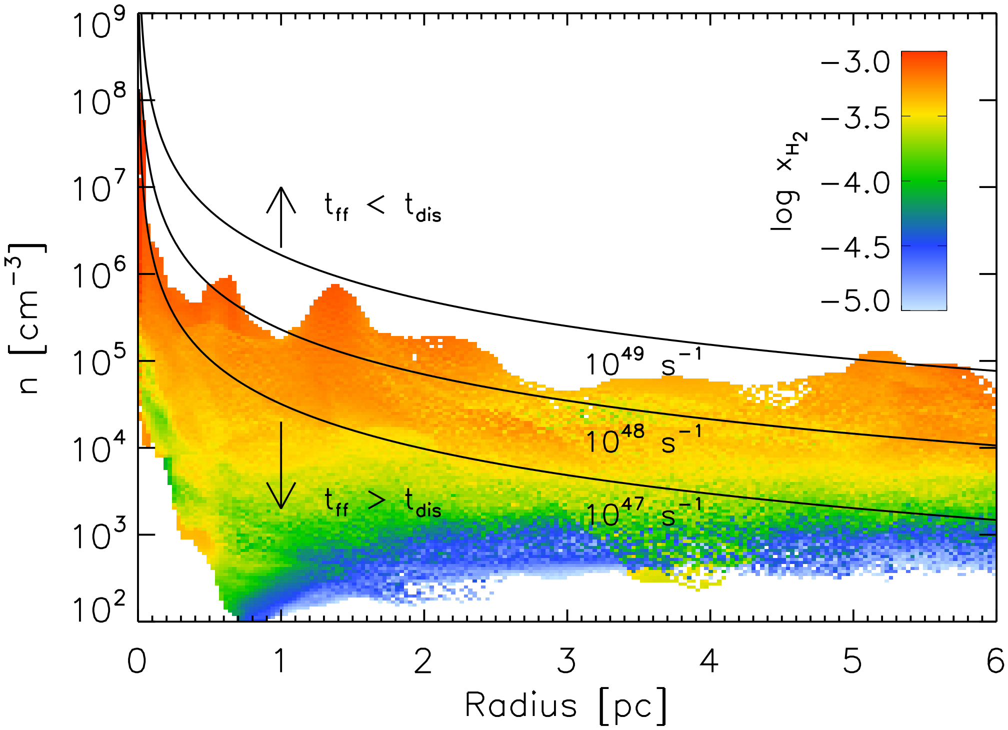

Figure 3.13 Gas density as a function of distance from the sink particle 10^5 years after sink particle formation colour coded by the mass-weighted H_2 abundance. The required density for a given clump's free-fall time to equal its H_2 dissociation time is also shown by the solid lines, that were computed assuming all clumps have a mass of $3000\,M_\odot \approx M_{\rm J}$ and and H_2 abundance of $x_{\rm H_2} = 10^{-3}$. The different solid lines correspond to three different choices for the LW photon production rate $\dot{N}_{\rm dis}$: $10^{49}\,{\rm s}^{-1}$ (top) is appropriate for a single $100\,M_\odot$ star, $10^{48}\,{\rm s}^{-1}$ (middle) for ten $10\,M_\odot$ stars, while $10^{47}\,{\rm s}^{-1}$ (bottom) would be the rate from ten $5\,M_\odot$ stars. Assuming a homogeneous clump, its density must lie above a solid line for its collapse to occur before its supply of H_2 is exhausted by photodissociation.

In reality, the effect of LW feedback on nearby collapsing clumps will depend strongly on their distances from the radiation source and on the level of precondensation in the gas, i.e., how dense the clump is when the neighboring LW source turns on. In Figure 3.13 we show the radius and density dependence of the H_2 abundance in cells with $x_{H_2} > 10^{-5}$ at a time 10^5 years after sink particle formation, roughly the Kelvin-Helmholtz time of massive stars that would be the primary producers of LW photons. The cells are colour coded by their H_2 abundance. We also show the density where $t_{ff} = t_{dis}$ for three different choices of the LW photon production rate. To derive this density, we assume that collapsing clumps have a total mass of $3000\,M_\odot$,[1] H_2 abundance of 10^{-3}, and that $f_{dis} = f_{abs} = 0.1$. Evidently the effect of LW radiative feedback on subsequent star formation is a strong function of $\dot{N}_{dis}$ and the source distance. If star formation which occurs in the sink particle results in a LW photon production rate of $\dot{N}_{dis} \approx 10^{48}\,s^{-1}$, it is clear from Figure 3.13 that further collapse and star formation will be strongly suppressed in the uncollapsed fraction of the self-shielding core, even given the large simplifications we have made in this analysis. This may have an adverse effect on the overall star formation efficiency and detectability of these systems.

3.7.3 Direct JWST Observations of a Metal-Free Stellar Population

Since the basic characteristics and formation mechanisms of the first cosmic structures are very uncertain, one of the main goals of future observations with the JWST is to observe light from the first stars and galaxies. By modeling metal-free synthetic stellar spectra, Zackrisson et al. (2011) determined JWST exposure limits and colour criteria for high-redshift, metal-free galaxies. Given the uncertainties

---

[1] We note that the clumps visible in Figure 3.13 at $\sim 0.5\,pc$ and $\sim 1.5\,pc$ are in fact not Jeans unstable and have masses well below $3000\,M_\odot$. This downward mass revision will decrease their H_2 photodissociation time which depends weakly on mass, $t_{dis} \propto M^{1/3}$.

of these sources, Zackrisson et al. (2011) explored a large parameter space defined by the shape of the stellar IMF, nebular emission strength, stellar population age, stellar mass, and formation redshift. Their most optimistic scenario involves a 3 Myr old stellar population with an extremely top-heavy IMF ($dn/dM \propto M^{-2.35}$ for $50 < M/M_{\odot} < 500$) and maximal nebular emission, requiring a vanishing escape fraction of ionizing radiation, $f_{\rm esc} = 0$. At $z = 10$, a cluster with stellar mass $M_{*} \approx 10^5\,M_{\odot}$ and the above characteristics would just be detectable (at 10σ) with JWST in ultra-deep (100 hr) broadband exposures.

Given our finding that $\approx 1.5 \times 10^4\,M_{\odot}$ of cold gas becomes available for star formation in an atomic cooling halo at $z \approx 12.1$ exposed to a LW intensity of $J_{21} = 100$, it seems extremely unlikely this starburst could be detected by JWST, even if 100% of the mass turns into stars with an extremely top-heavy IMF. It is conceivable, however, that a weaker UV background could still have suppressed star formation until the assembly of an atomic cooling halo, but could have allowed for a larger global star formation efficiency. An inspection of Figure 3.12 suggests that a background LW intensity $J_{\rm LW,21} \gtrsim 1$, at least for $z \lesssim 30$, would have fully suppressed star formation in halos not capable of atomic cooling.

To get a sense of how the mass of cold gas depends on J_{21}, we proceed as follows. First, recall Equation (3.18) which expresses the density at which $\rm H_2$ cooling becomes effective, $n_{\rm cool}$, as a function of J_{21} and $x_{\rm e}$. This cooling density partially determines the mass of cold $T \lesssim 10^3\,{\rm K}$ gas, $M_{\rm cold}$, available for the first burst of star formation. Once a halo reaches the atomic cooling limit, the accretion rate of gas onto the self-shielding core, $\dot{M}_{\rm cold}$, will not a strong function of J_{21}. With this, we can estimate the cold gas mass as $M_{\rm cold} \approx \dot{M}_{\rm cold}\, t_{\rm ff}(n_{\rm cool}) \propto J_{21}^{-1/3}\, x_{\rm e}^{1/3}$. The abundance of free electrons would be higher at lower densities, but by how much is difficult to determine given the highly non-equilibrium electron abundance. For example, if $x_{\rm e}$ is 10 times higher than in our simulation at $n_{\rm cool}$ and if $J_{21} = 10$, the mass of cold gas would be $M_{\rm cold} \sim 10^{2/3} \times 1.5 \times 10^4\,M_{\odot} \approx 7 \times 10^4\,M_{\odot}$. If we furthermore assume a relatively high star formation efficiency, $f_* = 0.1$, which represents the fraction of cold gas that will eventually turn into stars, we find a total stellar mass of $M_* \sim f_*\,M_{\rm cold} \sim 7000\,M_{\odot}$. Even if these stars form with an extremely top-heavy IMF, a possibility recent simulations suggest is unlikely (e.g., Stacy et al. 2010, Clark et al. 2011b, Greif et al. 2011), the analysis of Zackrisson et al. (2011) implies this cluster will not be detectable with the JWST.

One effect, however, which may render these targets within the JWST detection limit is gravitational lensing. Low-redshift galaxy clusters are capable of magnifying high-redshift sources by factors of $\mu \sim 10 - 100$. Indeed, the recently discovered $z \approx 9.6$ galaxy MACS 1149-JD1 (Zheng et al. 2012) is gravitationally lensed by a foreground galaxy cluster with a magnification factor of $\mu \approx 14$, though lensing was not strictly required for its detection. To this end, Zackrisson et al. (2012) estimated the conditions under which the JWST could detect gravitationally lensed, metal-free stellar populations behind the $z \approx 0.546$ galaxy cluster MACS J0717.5+3745, an ideal gravitational lens for high-redshift stellar sources. Mock halo catalogs of metal-free galaxies, generated with the methodology of Trenti et al. (2009), were simulated to lie beyond this particular galaxy cluster and the expected number of metal-free stellar populations as a function of limiting magnitude was generated. The primary source of uncertainty in these estimates is ϵ, the efficiency of Pop III.2 star formation, defined as $M_{*,{\rm popIII.2}} = \epsilon M_{\rm halo}(\Omega_{\rm b}/\Omega_{\rm m})$. This efficiency could be broken down as $\epsilon = f_* f_{\rm cold}$, where $f_{\rm cold}$ is the fraction of a halo's baryonic mass which is cold and available for star formation and f_* is, as before, the fraction of cold gas that will eventually become incorporated into stars.

Zackrisson et al. (2012) find that with efficiencies as low as $\epsilon \approx 10^{-3}$, clusters of metal-free stars with moderately top-heavy IMFs, $M_{\rm char} = 10\,M_\odot$, will be visible in deep JWST lensing surveys around MACS J0717.5+3745. Our optimistic $J_{21} = 10$ scenario, described above, results in an efficiency $\epsilon \approx (7000\,M_\odot/3 \times 10^7 M_\odot)(\Omega_{\rm m}/\Omega_{\rm b}) \approx 10^{-2.9}$. Thus, according to the estimates of Zackrisson et al. (2012) and our relatively crude estimate for the Pop III.2 star formation efficiency, it appears that JWST will marginally detect metal-free stellar populations in deep, foreground cluster lensing enhanced surveys. This conclusion, though, is very approximate and more detailed studies are needed to fully assess the observational prospects for detecting these primitive, low luminosity stellar clusters.

3.8 Summary and Conclusions

We have performed a high-resolution cosmological simulation focused on the collapse of metal-free gas in a region of the Universe subjected to a strong molecule-dissociating Lyman-Werner background. We resolved densities up to $10^8\,{\rm cm}^{-3}$ and length scales down to ~ 1000 AU. This simulation utilized a fully non-equilibrium primordial chemistry network coupled with a non-local column density calculation to accurately compute the H_2 and HD photodissociation rates. Additionally, our use of sink particles allowed us to evolve the simulation for many free-fall times past the first gravitational collapse.

Here we summarize the main findings of this work:

- With a LW intensity $J_{21} = 100$ in a $1\,{\rm Mpc}^3$ (comoving) box, effective H_2 cooling first occurs in a $3 \times 10^7\,M_\odot$ halo at $z \approx 12.1$. This cooling results in a thermal instability and a cold, dense core develops in which H_2 shields itself from LW radiation. Upon sink particle creation at $n = 10^8\,{\rm cm}^{-3}$, the central core containing self-shielding, cold gas has a mass of $\sim 10^4\,M_\odot$, characteristic size $\sim 5\,\mathrm{pc}$, temperature $\sim 400\,\mathrm{K}$, mean rms velocity $v_{\mathrm{rms}} \approx 6\,\mathrm{km\,s^{-1}}$, and Mach number ≈ 2. Mach numbers increase to $\approx 2-4$ within 3.5×10^5 years.

- Within the inner $\sim 10\,\mathrm{pc}$ of the halo, the gas flow becomes supersonic only when H_2 cooling becomes effective. The gas density PDF in the cold, self-shielding gas is approximately log-normal and has a width consistent with the turbulent Mach number of the flow given expectations derived from idealized simulations in which turbulence is driven by a mixture of solenoidal and compressive forcing. With time, the density PDF acquires a high density power-law tail as self-gravitating gas decouples from the turbulent flow.
- The rate of gaseous collapse on scales comparable to the size of the self-shielding region is suppressed compared to what would be expected if all the gas in the self-shielding core was collapsing at its free-fall rate. By the time the sink particle grows to $\sim 6\%$ of the total mass of the self-shielding cloud, no other sinks have formed, suggesting any additional sites of fragmentation remain unresolved in the simulation. We find an upper-limit to the star formation rate per free-fall time of $\mathrm{SFR_{ff}} \approx 0.1$ on scales of $\sim 10\,\mathrm{pc}$. We argue this is due to the additional effective pressure provided by infall-driven supersonic turbulence on large scales and centrifugal support on smaller ones.
- HD cooling was found to be thermodynamically insignificant for the entirety of the gas evolution. We attribute this to partial photodissociation of H_2 and the low free electron fraction when H_2 cooling becomes significant. Given the relatively low LW intensity needed for HD formation to be suppressed, $J_{\mathrm{LW,21}} \sim 0.1$, in comparison with the relatively high intensity required to delay gaseous collapse until the formation of atomic cooling halos, $J_{\mathrm{LW,21}} \sim 10$, it seems unlikely that HD cooling is ever significant in Pop III.2 star formation, at least in the scenario explored here.

- Given the similarities between the thermodynamic behavior of Pop III forming halos with and without LW feedback, and the complete absence of significant HD cooling in both cases, we suggest that Pop III.2 star formation delayed by LW radiation is very similar to Pop III.1 star formation. Additionally, the similarities of our results with other simulations that probed higher densities and smaller spatial scales (e.g., Stacy et al. 2010, Clark et al. 2011b, Greif et al. 2011) seem to suggest that Pop III.2 stellar masses in the LW-delayed mode are likely comparable to Pop III.1 masses, $\sim 1 - 40\,M_{\odot}$, possibly even lower.

Chapter 4

Clustered Star Formation and the Influence of Metal Line Cooling[1]

4.1 Introduction

The process of star formation is extremely complex, with gas thermodynamics, supersonic turbulence, self gravity, magnetic fields, and stellar feedback all playing important roles on a variety of spatial and temporal scales. It is observed that the vast majority of present-day stars form as part of small associations or clusters inside supersonically turbulent molecular clouds (e.g., Lada & Lada 2003). The stellar initial mass function (IMF) peaks around $\sim 0.1 - 0.5\,M_{\odot}$ (e.g., Kroupa 2002, Chabrier 2003) and has a power-law tail extending to larger masses (Salpeter 1955). Compared with the free-fall time evaluated at the characteristic density of the parent molecular clouds, star formation is a slow and inefficient process (e.g., Zuckerman & Evans 1974, Evans et al. 2009). Any comprehensive theory of star formation should be able to explain these characteristics in a single unified framework (see McKee & Ostriker 2007).

Supersonic turbulence, along with self-gravity, is believed to be the main process controlling star formation (Mac Low & Klessen 2004). It creates a complex, self-similar network of sheet-like and filamentary shock compressed density fluctuations. When one of these fluctuations becomes Jeans unstable it collapses

---

[1] This chapter has been published as Safranek-Shrader, C., Milosavljevic, M., Bromm, V., 2014, MNRAS, 438, 1669. M. Milosavljevic and V. Bromm supervised the project.

and forms one, or possibly many, protostellar objects (Elmegreen 1993, Padoan & Nordlund 1999, Mac Low & Klessen 2004). This process is known as 'gravoturbulent fragmentation' and is pivotal for understanding how stars and stellar clusters form. The character of turbulence (Klessen et al. 2000, Klessen 2001a, Padoan & Nordlund 2002), cloud geometry (Bonnell & Bastien 1993), rotation level, and magnetic field strength (Heitsch et al. 2001, Vázquez-Semadeni et al. 2005, Padoan & Nordlund 2011, Federrath & Klessen 2012) will all influence gas fragmentation. The thermodynamical behavior of collapsing turbulent gas, set by various heating and cooling processes, is also crucial in moderating fragmentation (e.g., Larson 1985, 2005). In simulations utilizing a polytropic equation of state, $P \propto \rho^{\gamma}$, Li et al. (2003) demonstrated that the degree of fragmentation increases with decreasing polytropic exponent γ (corresponding to an increase in the gas cooling rate). Jappsen et al. (2005) further demonstrated that the characteristic fragmentation mass scale is approximately the Jeans mass at the point where γ first exceeds unity after dipping below unity. Variations in γ have also been shown to have strong effects on gas morphology (e.g., Peters et al. 2012), the gas density probability distribution function (PDF) of supersonically turbulent gas (Scalo et al. 1998, Vázquez-Semadeni et al. 2006), and may also affect the shape of the stellar IMF (Spaans & Silk 2000).

The theory of Galactic star formation is only partially applicable to the formation of the first, so-called Population III (Pop III), stars (reviewed in Bromm 2013). These objects formed in $10^{5-6}\,M_{\odot}$ dark matter 'minihaloes' at redshifts $z \sim 15 - 40$ (Couchman & Rees 1986, Haiman et al. 1996, Tegmark et al. 1997). Given the complete lack of metals, gas cooling was provided by molecular hydrogen (H_2), a relatively inefficient cooling agent. The thermalization and energy spacing of the lowest rotational levels of H_2 set a characteristic density, $n \sim 10^4\,\mathrm{cm}^{-3}$, and temperature, $T \sim 200\,\mathrm{K}$, where primordial gas ends its initial free-fall collapse phase. Simulations have shown the resulting star-forming clumps to have masses $\gtrsim 100\,M_{\odot}$, in accord with the Jeans mass at this point (Abel et al. 2000, Bromm et al. 2002, Yoshida et al. 2006, O'Shea & Norman 2007). The final stellar mass is determined by subsequent accretion onto the initial protostellar hydrostatic core. Recent simulations revise this characteristic mass downwards by showing that the Pop III protostellar disk can fragment at high densities (Machida et al. 2008, Stacy et al. 2010, Greif et al. 2011, 2012, Clark et al. 2011a,b), or that prostostellar radiation can suppress gas accretion (Stacy et al. 2012, Hosokawa et al. 2011, Susa 2013), but still support the general conclusion that Pop III stars were typically more massive than later stellar generations.

What caused the transition from solitary, high-mass Pop III star formation to clustered, low-mass star formation is an important open question in cosmology. The introduction of metals by the first supernovae is generally thought to have driven the transition, given the enhanced cooling and thus fragmentation in metal-enriched gas. This idea was explored in Omukai (2000) who showed an increase in metallicity leads to larger cooling rates and thus lower temperatures during gaseous collapse. Bromm et al. (2001) found that when metallicity is greater than a critical metallicity of $Z \approx 10^{-3.5}\,Z_{\odot}$, gaseous fragmentation occurs due to metal fine-structure line emission. Later studies that explored a metal fine-structure 'line induced' Pop III-II transition (e.g., Bromm & Loeb 2003b, Santoro & Shull 2006, Smith & Sigurdsson 2007, Safranek-Shrader et al. 2010) all found similar values for the metallicity needed for the star formation to transition to an efficiently fragmenting mode.

A separate set of studies suggest that the Pop III-II mode transition is not induced by metal line emission, but instead by the thermal coupling of gas and dust grains (e.g., Omukai et al. 2005, Schneider et al. 2006, Clark et al. 2008, Dopcke et al. 2011, 2013). This 'dust induced' fragmentation occurs at a much higher density, $n \sim 10^{10-12}\,\mathrm{cm}^{-3}$, than line-induced fragmentation when the thermal Jeans mass is of order of $0.1 - 1 M_{\odot}$. Studies have shown that the metallicity needed for dust-gas coupling to significantly affect the gas thermodynamical evolution and induce a star formation transition is $Z \approx 10^{-6}\,Z_{\odot}$, much lower than the metallicity needed for a line-induced transition. This depends, though, on the creation, abundance, and composition of dust at high redshifts (e.g., Dwek & Cherchneff 2011, Schneider et al. 2012a) which remains very uncertain.

More realistic three-dimensional simulations have also addressed the Pop III-II transition. Clark et al. (2008), using a piecewise equation of state, showed dust induced fragmentation does indeed induce solar-mass scale fragmentation at high densities and emphasized the importance of angular momentum in regulating fragmentation. Dopcke et al. (2011, 2013) confirmed this finding utilizing a non-equilibrium chemical network. Starting from cosmological initial conditions, Smith et al. (2009) suggested the interplay of metal fine-structure line cooling and the cosmic microwave background (CMB) temperature floor, $T_{\mathrm{CMB}} = 2.725\,\mathrm{K}(1+z)$, strongly controls gas fragmentation and leads to three distinct modes of metal-enriched star formation at high redshifts. The smoothly decreasing CMB temperature sets a lower limit to which gas can radiatively cool, which may regulate the process of star formation (Clarke & Bromm 2003, Schneider & Omukai 2010) and imprint observational signatures in the chemical abundances of Galactic metal-poor stellar populations (Tumlinson 2007, Bailin et al. 2010b). The CMB may also considerably increase the opacity mass limit for fragmentation given the strong temperature dependance of the mean dust opacity (Low & Lynden-Bell 1976).

Distinguishing between a dust induced and line induced star formation transition can be accomplished by observing chemical abundance patterns in metal-poor stars. Frebel et al. (2007) compiled observations of metal-poor stars and showed that none has oxygen and carbon abundances smaller than the critical value needed for a line induced transition. The recently discovered star of Caffau et al. (2011), though, has such small carbon and oxygen abundances that only dust cooling induced fragmentation could explain its existence (Schneider et al. 2012b, Klessen et al. 2012), though the possibility has been raised that its true metal abundance is higher than observed (MacDonald et al. 2013). Additionally, it should be stressed that disk fragmentation into sub-solar mass clumps can occur even in completely metal-free gas (Greif et al. 2011, Clark et al. 2011a), obviating the need for any sort of metal-enhanced cooling for low mass stellar object production.

Though the level of metal enrichment in gas plays a key thermodynamic role, numerous other factors likely contributed to effecting the transition to Pop II star formation. For example, in a series of papers Jappsen et al. (2007, 2009a,b) argued that there is no metallicity threshold for a Pop III-II transition – instead, the cosmic hydrodynamic context setting the initial conditions for star formation will have the largest effect on how fragmentation proceeds. This may be especially relevant since the first metal-enriched stellar clusters likely formed in atomic cooling haloes, rather than relatively low-mass minihaloes, with potential wells deep enough to sustain supersonic turbulent motions (e.g., Wise & Abel 2007a, Greif et al. 2008), though this is dependent on how exactly Pop III stars ended their lives.

The formation of stellar clusters comprised of low mass stars, rather than solitary massive stars, has profound cosmological implications (Tornatore et al. 2007, Maio et al. 2010, Aykutalp & Spaans 2011, Latif et al. 2012, Wise et al. 2012). These earliest clusters played a key role in cosmic reionization (Bouwens et al. 2011, Finkelstein et al. 2012, Kuhlen & Faucher-Giguère 2012, Robertson et al. 2013) and

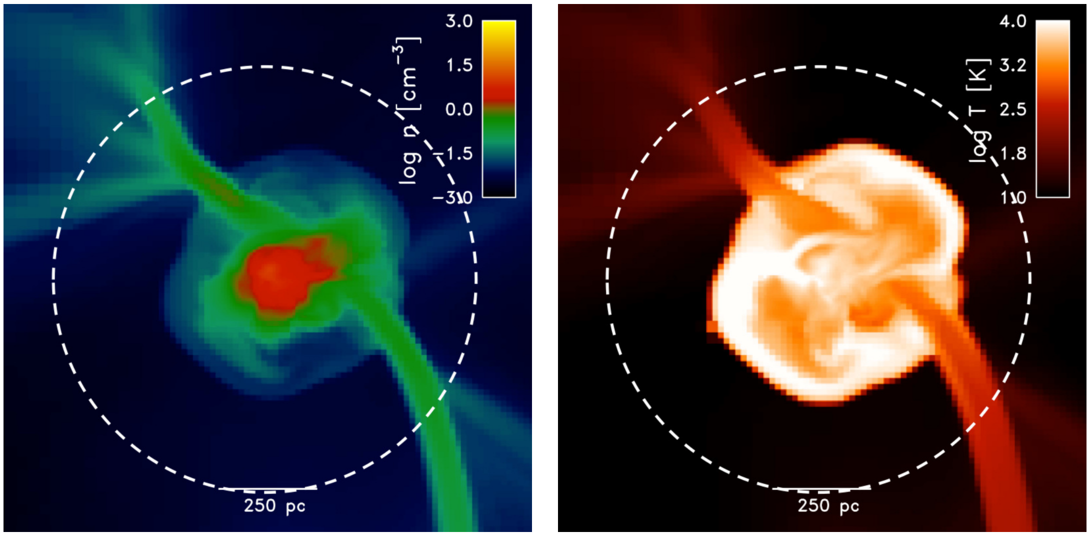

Figure 4.1 Slices of gas density (left) and temperature (right) when the metallicity of the gas was first made non-zero. The dashed circle denotes the region in which the gas metallicity was first set to a non-zero value. Cold accretion streams that penetrate the virial shock of the halo and account for most of gas accretion are readily apparent.

may still survive today in the form of metal-poor globular clusters, as part of the recently discovered ultra-faint dwarf (UDF) Milky Way satellites (e.g., Belokurov et al. 2007, Frebel & Bromm 2012), or individually as metal-poor stars residing in the Galactic halo. If sufficiently luminous they are capable of being detected by upcoming telescopes designed to probe redshifts $\gtrsim 10$, such as the *James Webb Space Telescope* (JWST) (Pawlik et al. 2011, Zackrisson et al. 2011, 2012, Dunlop 2013). Additionally, the long term chemical evolution of a star cluster imprints unique chemical signatures onto its members that will be useful for decoding the enrichment patterns of the first supernovae (e.g., Bland-Hawthorn et al. 2010).

This work is focused on the process of gas fragmentation, and thus star formation, in high-redshift atomic cooling haloes that have been enriched to some non-zero, but sub-solar, metallicity. We present the results of three high-resolution cosmological simulations, achieving a spatial resolution of ~ 0.01 physical parsecs and maximum physical density of $\sim 10^{6-7}\,\mathrm{cm}^{-3}$. We impose a strong Lyman-Werner (LW) radiation field that photodissociates molecular hydrogen across the computational box, delaying gaseous collapse until the assembly of a $M_{\mathrm{vir}} \approx 2 \times 10^7\,M_{\odot}$ halo capable of cooling by $\mathrm{Ly}\alpha$ line emission at $z \approx 16$. When we identify the conditions for runaway gaseous collapse in a halo, we endow the gas in its vicinity with a non-zero metallicity and observe the subsequent metal-cooling induced collapse. At high densities, we introduce sink particles which serve as proxies for stellar associations that would have formed at gas densities not directly resolved in the simulations. We evolve this star formation region for multiple free-fall times to observe the long-term fragmentation process, measure the efficiency with which gas is converted into stars, and study mass spectrum of high-density gaseous clumps. Using this approach we aim to better understand the star formation properties of metal enriched gas and the role that metal fine-structure line cooling plays in the first instances of clustered star formation in the Universe.

We organize this paper as follows. In Section 4.2 we describe our numerical setup and physical ingredients that enter into our study. In Section 4.3 we describe the results and analysis of our simulations. In Section 4.4 we discuss the potential limitations of our simulations. Finally, in Section 4.5 we discuss the implications of our findings and provide our conclusions.

Throughout this paper we assume cosmological parameters consistent with the *Wilkinson Microwave Anisotropy Probe* (WMAP) 7 year results (Komatsu et al. 2011): $\Omega_{\Lambda} = 0.725$, $\Omega_{\mathrm{b}} = 0.0458$, $\Omega_{\mathrm{m}} = 0.275$, $h = 0.704$, $\sigma_8 = 0.810$, and $n_{\mathrm{s}} = 0.967$. Additionally, all quantities will be expressed in physical, rather than comoving, units unless explicitly stated otherwise.

4.2 Numerical Setup

4.2.1 Parameter Choices and Initial Conditions

We run our simulation using the adaptive mesh refinement (AMR) code FLASH (Fryxell et al. 2000), version 4. Our cosmological initial conditions are identical to those used in Safranek-Shrader et al. (2012). Specifically, we use a $1\,\mathrm{Mpc}^3$ (comoving) box initialized at $z = 145$ with a base grid resolution of 128^3 and two nested grids for an effective resolution of 512^3. This results in an effective dark matter particle mass of $230\,M_\odot$.

Our grid refinement/derefinement scheme is also identical to Safranek-Shrader et al. (2012), though now we resolve the Jeans length,

$$L_{\mathrm{J}} = \left(\frac{\pi c_{\mathrm{s}}^2}{G\rho}\right)^{1/2}, \tag{4.1}$$

by at least 24 grid cells. This comfortably satisfies the Truelove criterion (Truelove et al. 1997) for avoiding artificial fragmentation, though it may not be sufficient to resolve the true character of turbulence, particularly small-scale vortical motions ultimately responsible for magnetic field amplification (Sur et al. 2010, Federrath et al. 2011, Turk et al. 2012). We derefine the grid if the Jeans length is resolved by more than 48 grid cells.

When the grid is highly refined, dark matter particles begin to become very coarsely sampled when their mass is mapped onto the grid for the purpose of the gravitational potential calculation. To alleviate this we spatially smooth the gravitational influence of dark matter (in a manner similar to Richardson et al. 2013) above a refinement level of 12, resulting in a dark matter smoothing length of ≈ 60 comoving pc. At the redshift at which we study metal-enchanced fragmentation, this corresponds to 3.7 physical pc, roughly the radial length scale on which baryons begin to dominate the gravitational potential.

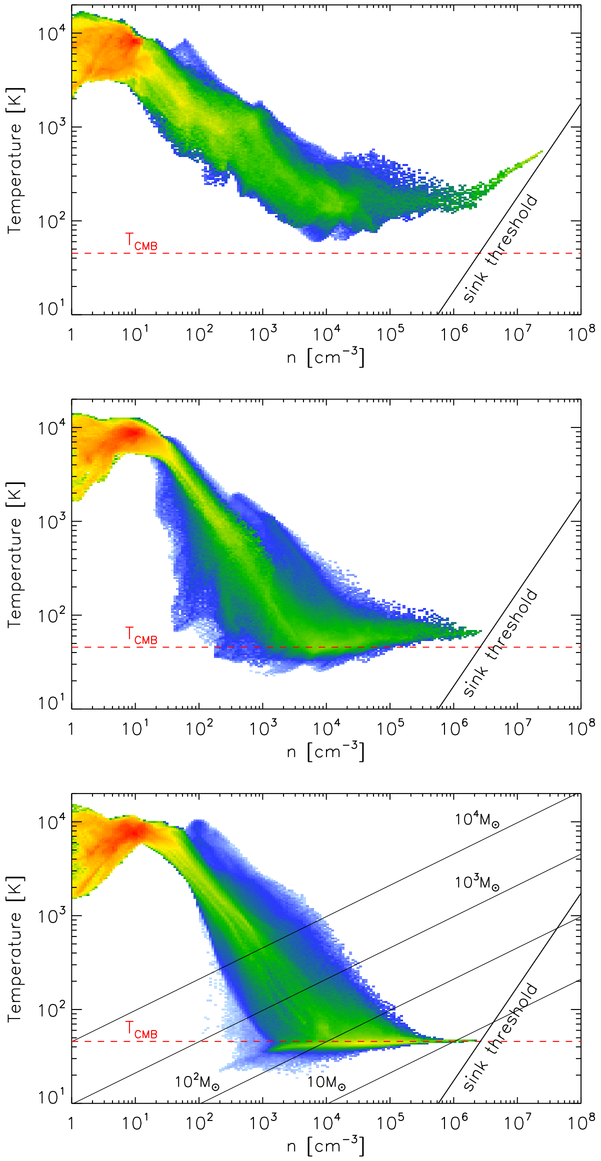

Figure 4.2 Density-temperature phase diagrams for gas within $50\,\mathrm{pc}$ of the densest point as the first sink particle forms for the 10^{-4} (top), 10^{-3} (middle), and $10^{-2}\,Z_\odot$ (bottom) runs. Color corresponds to the gas mass at a given density and temperature. We also show the CMB temperature (red dashed horizontal line) and the temperature-dependent density threshold for sink particle creation (steep solid line; see Equation 4.13). Additionally, in the bottom panel, we show lines of constant Jeans mass. In the higher metallicity simulations gas first reaches T_{CMB} when $M_{\mathrm{J}} \sim 100\,M_\odot$, consistent with the typical sink particle mass forming in these simulations.

Because we focus on haloes capable of $\mathrm{Ly}\alpha$ cooling, we suppress gravitational collapse in minihaloes that relies on molecular hydrogen cooling. We do this by including a background Lyman-Werner (LW) radiation field that is capable of destroying H_2 by the two-step Solomon process (Stecher & Williams 1967). The H_2 photodissociation rate from LW radiation is (e.g., Abel et al. 1997, Glover & Jappsen 2007)

$$k_{\mathrm{H}_2} = 1.38 \times 10^{-12}\, J_{\mathrm{LW},21} f_{\mathrm{shield,H}_2}\, \mathrm{s}^{-1}, \tag{4.2}$$

where $J_{\mathrm{LW},21}$ is the radiation intensity at the centre of the Lyman-Werner bands, $12.4\,\mathrm{eV}$, in units of $10^{-21}\,\mathrm{erg\,s^{-1}\,cm^{-2}\,Hz^{-1}\,sr^{-1}}$ and $f_{\mathrm{shield,H}_2} \leq 1$ is a dimensionless factor which accounts for H_2 self-shielding. By setting $J_{\mathrm{LW},21} = 100$, we effectively guarantee the suppression of cooling in minihaloes at all redshifts of interest (see Safranek-Shrader et al. 2012). We model the effect of H_2 self-shielding in an approximate way by writing the H_2 self-shielding factor as (Draine & Bertoldi 1996)

$$f_{\mathrm{shield,H}_2} = \min\left[1.0, \left(\frac{N_{\mathrm{H}_2}}{10^{14}\,\mathrm{cm}^{-2}}\right)^{-0.75}\right], \tag{4.3}$$

and approximating N_{H_2}, the H_2 column density, as

$$N_{\mathrm{H}_2} = 0.1\, n_{\mathrm{H}_2}\, L_{\mathrm{J}}, \tag{4.4}$$

where n_{H_2} and L_{J} are, respectively, the local H_2 number density and Jeans length. This allows the H_2 abundance to increase once metal cooling has allowed the gas to collapse to high densities (see Wolcott-Green et al. 2011, for a more sophisticated approach).

4.2.2 Metal Enrichment Strategy

The dispersal of metals synthesized in the first stars is a complicated process moderated by the interplay of supernova ejection, gravitational reassembly, and turbulent mixing with primordial gas (e.g., Karlsson et al. 2013). The outcome of primordial metal enrichment is strongly dependent on the mass of the first stars. A non-rotating, metal-free star with a mass between 140 and $260\,M_{\odot}$ is believed to end life as a highly energetic ($E_{\rm kin} \sim 10^{52}\,{\rm ergs}$) pair-instability supernova (PISN) (e.g., Heger et al. 2003), though rotationally induced mixing may bring the lower limit down by nearly a factor of two (Chatzopoulos & Wheeler 2012). Since this explosion completely disrupts the host minihalo, the onset of metal-enriched star formation is delayed until a $\sim 10^{8}\,M_{\odot}$ halo forms around a redshift of ~ 10 (Wise & Abel 2008, Greif et al. 2010, Wise et al. 2012) where the metal ejecta would likely reassemble.

More recent simulations of Pop III star formation, though, have suggested stellar masses exceeding $\sim 50\,M_{\odot}$ are unlikely given radiative feedback that acts to shut off gas accretion (e.g., Hosokawa et al. 2011, Stacy et al. 2012). These more moderate mass Pop III stars end their lives as less energetic core-collapse supernovae that may not completely disrupt the host minhalo. Ritter et al. (2012) simulated the HII region, supernova, and metal transport from a $40\,M_{\odot}$ Pop III star ending its life as an $E_{\rm kin} = 10^{51}\,{\rm erg}$ core collapse supernova. While only about a half metal ejecta expanded beyond the minihalo's virial radius, within $10\,{\rm Myr}$ the ejecta began to fall back into the center of the host minihalo, suggesting the first burst of metal enriched star formation may have followed closely in the wake of the Pop III star formation already in cosmic minihaloes (see also Whalen et al. 2013).

With this in mind, to emulate the complex process of metal ejection and transport in the early Universe, we first run our metal-free cosmological simulation until a halo with a virial temperature of $T_{\rm vir} \sim 10^{4}\,{\rm K}$ capable of cooling by ${\rm Ly}\alpha$ emission has formed in the simulation. At the point at which ${\rm Ly}\alpha$ cooling is effective enough for gas in the centre of the halo to begin to isothermally collapse, we increase the metallicity within $1.5\,R_{\rm vir}$ of the halo to a non-zero value, either 10^{-4}, 10^{-3}, or $10^{-5}\,Z_{\odot}$. Figure 4.1 shows a slice of gas density and temperature through the selected dark matter halo at this point of virialization and denotes the spatial region where we increased the metallicity of the gas with a dashed circle.

This idealized approach is not meant to realistically reproduce the results of simulations that track the injection and transport of metals from the first supernovae, such as Wise & Abel (2008), Greif et al. (2010), and Ritter et al. (2012). These studies have shown there to be significant metal inhomogenities on kiloparsec scales around atomic cooling haloes. Mixing between primordial and metal-enriched gas, though, is much more effective at higher densities near the centers of atomic cooling halos. One should be aware, though, that the transport of passive scalars in grid-based codes is well known to overpredict the diffusion speed and degree of mixing (e.g., Plewa & Müller 1999, Ritter et al. 2012). The goal of the present paper is to isolate the thermodynamic impact of metals on protostellar collapse and star cluster formation. Therefore we opted to perform controlled numerical experiments separating out potential effects of inhomogeneous metal dispersal by introducing metals artificially, assuming perfect mixing. Furthermore, all gaseous fragmentation, the focus of this paper, occurs within a ~ 5 parsec region in the centre of the target halo well after the metals are introduced ($t \sim 4\,{\rm Myr}$) where turbulent motions are expected to homogenize metals on the order of a dynamical time. We discuss the possible implications of this idealized approach in Section 4.4.

4.2.3 Chemical and Radiative Processes

We employ a non-equilibrium chemistry solver that tracks the abundances of the following primordial chemical species: H, H^-, H^+, e^-, H_2, H_2^+, He, He^+, He^{++}, D, D^+, and HD. We additionally include the following gas-phase metal species: C, C^+, Si, Si^+, O, and O^+ with the solar abundance pattern. Even a modest intergalactic ultraviolet (UV) radiation field is effective in keeping species with a first ionization potential less than $13.6\,\mathrm{eV}$, such as carbon and silicon, singly ionized. Above $13.6\,\mathrm{eV}$, it is a reasonable assumption that neutral hydrogen significantly attenuates the radiation field, especially before the epoch of reionization. We include this effect in our chemical network by setting the photoionization rate of neutral carbon and silicon to values corresponding to our choice of the LW background, $J_{\mathrm{LW},21} = 100$, assuming a $T = 10^4\,\mathrm{K}$ blackbody spectral shape. The ionization state of oxygen is determined by collisional processes since its ionization potential is above that of neutral hydrogen's and thus does not experience a significant photoionizing flux.

In low density ($n < 10^8\,\mathrm{cm}^{-3}$) molecule-free gas, the most significant thermodynamic effect from heavy elements is fine-structure line emission from forbidden transitions of carbon, oxygen, and silicon. To model fine structure cooling, we follow the method of Glover & Jappsen (2007), which we briefly review here.

For a given metal fine-structure coolant, the net volumetric energy rate of change due to photon emission and absorption can be written as

$$\dot{e} = \Gamma - \Lambda, \tag{4.5}$$

where Λ and Γ are, respectively, the volumetric cooling and heating rates due to all available electronic transitions, stimulated emission, and absorption. The cooling rate for a single fine-structure coolant can be written as

$$\Lambda = \sum_{i \to j} (A_{ij} + B_{ij} I_{ij}) h\nu_{ij} n_i, \tag{4.6}$$

and the heating rate as

$$\Gamma = \sum_{j \to i} B_{ji} I_{ij} h\nu_{ij} n_j, \tag{4.7}$$

where A_{ij} is the Einstein coefficient for spontaneous emission for the transition from level $i \to j$, B_{ij} is the Einstein coefficient for stimulated emission ($i > j$) or for absorption ($i < j$), $h\nu_{ij}$ is the energy difference between levels i and j, I_{ij} is the radiation intensity at frequency ν_{ij}, and n_i is the number density, or level population, of ions in state i.

We solve for the level populations, n_i, by assuming statistical equilibrium,

$$n_i \sum_{j \neq i} R_{ij} = \sum_{j \neq i} n_j R_{ji}, \tag{4.8}$$

where the sum runs over all possible transitions and

$$R_{ij} = \begin{cases} A_{ij} + C_{ij} + B_{ij} I_{ij} & \text{if } i > j \ , \\ C_{ij} + B_{ij} I_{ij} & \text{if } i < j \ . \end{cases} \tag{4.9}$$

Here, C_{ij} represents the total rate of collisional de-excitations ($i > j$) or excitations ($j > i$). The collisional de-excitation rate is given by

$$C_{ij} = \sum_k \gamma_{ij,k} n_k, \tag{4.10}$$

where $\gamma_{ij,k}$ is the collisional de-excitation rate for collisions with species k and n_k is the number density of the collider. We use the de-excitation rates (and other atomic data) given in Glover & Jappsen (2007) which include collisions with neutral and molecular hydrogen, protons, and electrons as sources of excitations and de-excitations. Finally, the excitation and de-excitation rates are related by (for $i > j$)

$$C_{ji} = C_{ij} \frac{g_i}{g_j} \exp\left(-\frac{h\nu_{ij}}{k_{\rm B}T}\right), \tag{4.11}$$

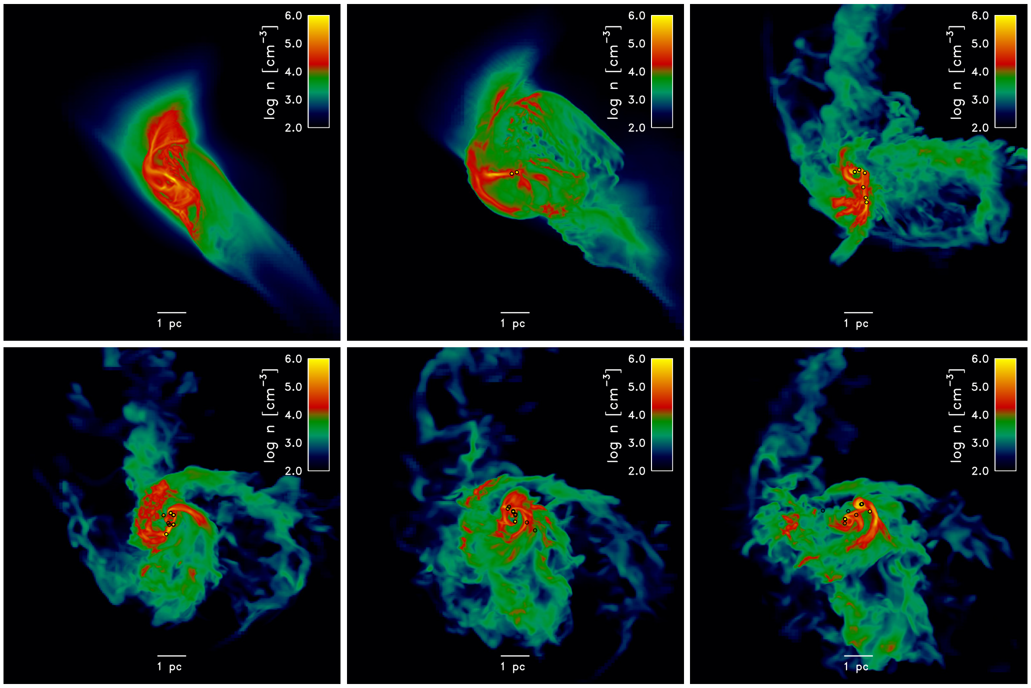

Figure 4.3 Snapshots showing mass-weighted line-of-sight density projections from the $10^{-2}\,Z_{\odot}$ run. Black circles represent sink particles, with the circle radius equal to the particle accretion radius. The top left panel shows the state of the simulation just before sink particle formation. After the gas has reached the CMB temperature, thermal instability and strong, quasi-isothermal shocks produce a sheet-like morphology (seen face-on in the top-left panel) and filamentary striations. These features are transient and within $\sim 2\,\mathrm{Myr}$ the star-forming cloud becomes more disordered and has an apparent net rotation. The consecutive snapshots from left-to-right and top-to-bottom are separated by a time interval of $0.8\,\mathrm{Myr}$.

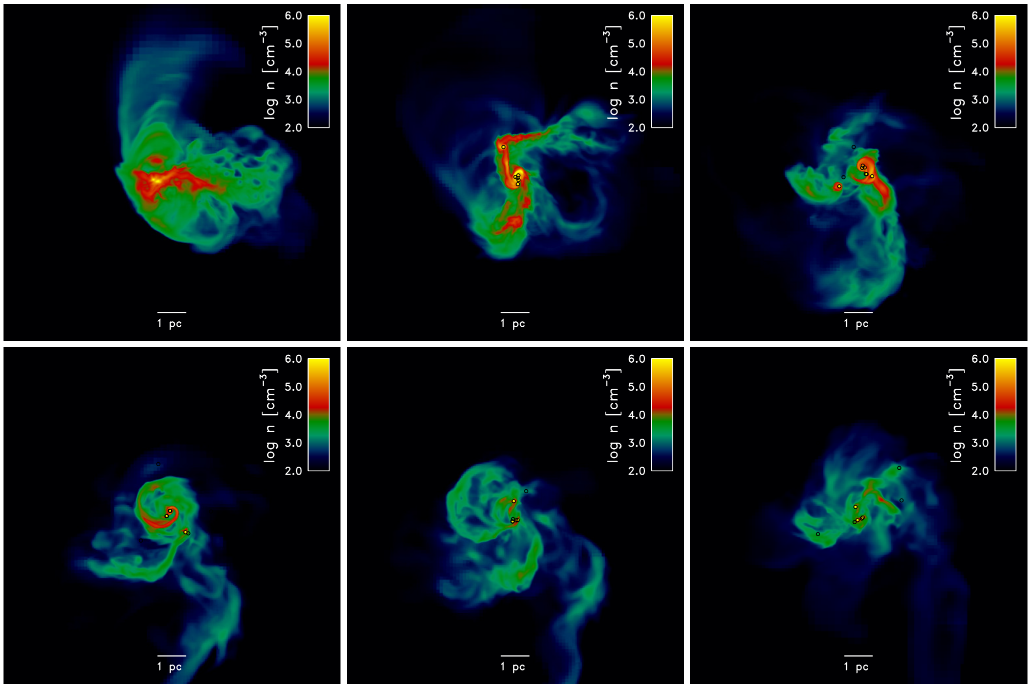

Figure 4.4 Same as Figure 4.3 but for the 10^{-3} $Z_{\odot}$ run.

where g_i is the statistical weight of level i and T is the gas temperature.

This formulation of metal fine-structure line cooling implicitly includes a CMB imposed temperature floor by including photon absorption terms with a radiation intensity $I_\nu = B_\nu(T_{\rm CMB})$. Below $T_{\rm CMB}$, fine-structure cooling becomes heating via CMB photon absorption. For other coolants, notably HD, we use an effective cooling rate of the form

$$\Lambda_{\rm eff}(T) = \Lambda(T) - \Lambda(T_{\rm CMB}) \, , \tag{4.12}$$

which mimics the effect of the CMB temperature floor.

4.2.4 Sink Particles

We utilize sink particles to follow the evolution of gas undergoing gravitational collapse over multiple free-fall times. Sink particles were originally introduced by Bate et al. (1995) in smoothed-particle hydrodynamics (SPH) simulations and were first adapted into a grid-based Eulerian setting by Krumholz et al. (2004). By accreting gas directly from the grid, sink particles effectively impose an upper-limit on gas density and a lower-limit on the simulation timestep. Without sink particles, the timestep would become prohibitively short as gas reached increasingly high densities.

The limitations of the sink particle approach have been discussed extensively in the literature (e.g., Bate et al. 2003, Bate 2009, Bate et al. 2010, Federrath et al. 2010a). According to the original implementation of Bate et al. (1995), when a sink particle forms all SPH particles within its accretion radius are removed and their mass is added to the new sink particle. This results in a sharp pressure discontinuity around the sink particle and can lead to grossly overestimated accretion rates for subsonic gas flow. This problem can be overcome by imposing a boundary pressure at the sink particle accretion radius or by gradually, rather than instantaneously, accreting SPH particle mass (Hubber et al. 2013). This problem is not as severe in Eulerian implementations, like ours, since sink particle formation and the subsequent gas accretion does not result in a sharp pressure discontinuity. Other limitations include the effects of treating sink particles as softened extended objects and issues concerning angular momentum conservation and viscous torques during gas accretion. Finally, it should be stressed that inside the accretion radius of a sink particle all knowledge of the flow is lost and unless sinks form at a density much greater than the opacity limit for fragmentation, which is not the case in the present simulation, there is the possibility of unresolved sub-fragmentation.

We use the sink particle implementation from Safranek-Shrader et al. (2012), which is originally from Federrath et al. (2010a), with slight modifications. Specifically, we no longer use a constant density cutoff for sink particle formation. Instead, we utilize a criterion similar to that in Krumholz et al. (2004) where the sink particle formation is triggered by the failure to properly resolve the Jeans length. By mandating that the Jeans length (Equation 4.1) be resolved by at least N grid cells, we can write the density threshold for sink particle creation as

$$\rho_{\rm J} = \frac{\pi c_{\rm s}^2}{G N^2 \Delta x^2} \,, \tag{4.13}$$

where $c_{\rm s}$ is the sound speed and Δx is the physical grid size at the highest level of refinement ($l_{\rm max} = 20$). In practice, we always resolve the Jeans length by 24 grid cells until the highest level of refinement is reached where we set $N = 4$ for sink particle creation. If a cell has density $\rho > \rho_{\rm J}$ we flag it and perform a series of additional checks for sink particle creation. These include checking for convergence of the gas flow, $\nabla \cdot \mathbf{v} < 0$, that the cell is a local gravitational potential minimum, and that a small control volume around the cell (typically 2 – 3 cells) is gravitationally bound. These checks have been shown to be very important for avoiding the spurious creation of sinks by structures not undergoing runaway free-fall collapse (Federrath et al. 2010a). If all these conditions are fulfilled, a sink particle is created in the cell centre. The sink's initial mass $(\rho-\rho_{\rm J})\Delta x^3$ is deducted from the cell mass, effectively capping the cell density at $\rho_{\rm J}$. Gas accretion onto existing sink particles is handled in a similar way; cells with $\rho > \rho_{\rm J}$ inside a sink particle's accretion radius, $r_{\rm acc}$, have a portion of their mass transferred to the sink particle if the gas is gravitationally bound to the sink particle and the radial component of the cell's velocity is directed towards the sink.

We evolve the systems for $\sim 4\,{\rm Myr}$ past the formation of the first sink particle. It is important to note that sink particles do not represent individual stars. Instead, sink particles are utilized as a computational tool making it possible evolve a self-gravitating, collapsing system for many free-fall times. In physical terms, they are approximately related to a pre-stellar core or clump that is destined to become a small stellar association (e.g., Bergin & Tafalla 2007). The properties of the sink particles, such as spatial distribution, mass, and accretion rates, thus do have physical significance. Higher-resolution studies are in progress that will shed light on the high-density fragmentation behavior of the sinks.

In the simulations here we take the sink accretion radius to be the Jeans length (Equation 4.1) at the highest level of refinement, $r_{\rm acc} = 4\Delta x = 0.06\,{\rm pc} \approx 12,000\,{\rm AU}$, where Δx is the cell spacing at the highest level of refinement. The softening length for the sink-gas gravitational interaction is set to $r_{\rm soft} = r_{\rm acc}/2$ to ensure that the gravitational softening does not interfere with accretion onto the sink. Sink-sink interactions are softened when the distance between the two particles is less than $\Delta x/2 = r_{\rm acc}/8$. While the density threshold $\rho_{\rm J}$ is temperature dependent, we note that at a typical temperature of $50\,{\rm K} \approx T_{\rm CMB}(z = 16)$, the threshold is $\rho_{\rm J} = 6.3 \times 10^{-18}{\rm g\,cm^{-3}}$. Finally, we do not allow merging between sinks, even

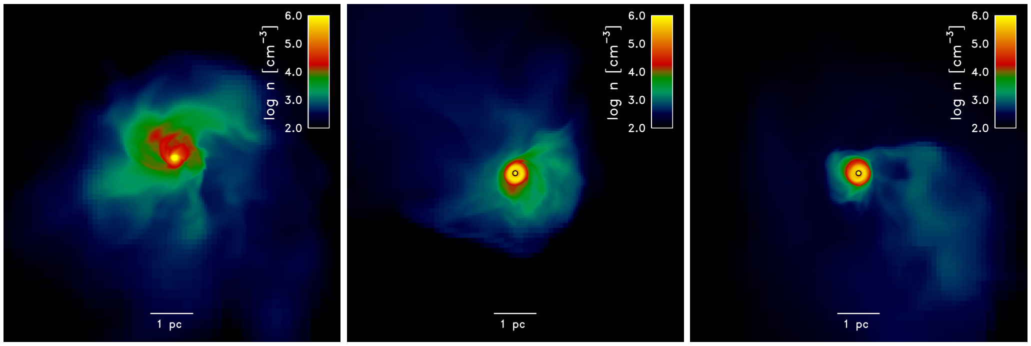

Figure 4.5 Same as Figure 4.3 but for the $10^{-4}\,Z_{\odot}$ run. The snapshots are approximately $2\,\mathrm{Myr}$ apart. Differences between this and the higher metallicity runs (Figures 4.3 and 4.4) are evident. Here, only a single sink forms and is surrounded by a non-fragmenting gas disk of radius $\sim 0.5\,\mathrm{pc}$.

if the sink particles are gravitationally bound to each other. We comment on the validity of this choice in Section 4.4.

4.3 Results

As in Safranek-Shrader et al. (2012), a spatially constant LW background with intensity $J_{\mathrm{LW},21} = 100$ strongly suppresses the formation of H_2 and thus prevents the collapse of gas in haloes unable to cool by atomic Lyα emission. Once a halo grows massive enough so that its virial temperature is $T_{\mathrm{vir}} \approx 10^4\,\mathrm{K}$, gas begins to isothermally collapse at $T \sim 8000\,\mathrm{K}$. When gas reaches a density of $\sim 100\,\mathrm{cm}^{-3}$, we increase the gas metallicity within $\sim 500\,\mathrm{pc}$ of the halo's point of maximum density to a constant, non-zero value. This occurs at a redshift of $z = 15.8$ in a halo with virial mass $M_{\mathrm{vir}} = 1.4 \times 10^7\,M_{\odot}$, maximum circular velocity $v_{\mathrm{circ}} = 12\,\mathrm{km\,s^{-1}}$, and virial radius $r_{\mathrm{vir}} \approx 350\,\mathrm{pc}$. The halo at this point is shown in the top panels of Figure 4.1.

We choose three different values for this metallicity, $Z = 10^{-2}$, 10^{-3}, and

$10^{-4}\,Z_\odot$. The limiting values bracket the metallicity needed for metal fine-structure lines to significantly alter the thermodynamic evolution of gas and promote fragmentation (e.g., Bromm et al. 2001). They are also physically reasonable given the expected generation and dispersal of metals in the first star forming halos (e.g., Wise & Abel 2008, Greif et al. 2010, Ritter et al. 2012), and the metallicities of local, metal-poor ultra-faint dwarf spheroidal galaxies (e.g., Kirby et al. 2011, Frebel & Bromm 2012). The three simulations discussed here are identical except for the value of the metallicity.

4.3.1 Overall Evolution

In all three simulations, the non-zero metallicity greatly enhances the cooling rate. The dominant cooling processes are fine-structure line emission by O and C^+. The onset of enhanced cooling allows the gas in the halo's center to cease its quasi-hydrostatic isothermal contraction and begin a collapse where temperature decreases with increasing density. In the 10^{-2} and $10^{-3}\,Z_\odot$ runs, the metal cooling induced collapse proceeds isobarically, remaining in pressure equilibrium with the surrounding warm halo gas. In the $10^{-4}\,Z_\odot$ run radiative cooling is not as efficient and the collapsing gas is overpressurized with respect to the surrounding gas. Therefore the collapse takes longer, by roughly a factor of two, for sink particles to form in this simulation compared with the higher metallicity runs. Gas in both the 10^{-2} and $10^{-3}\,Z_\odot$ runs reaches the CMB temperature, $T_{\rm CMB} \sim 50\,{\rm K}$, in approximately one local free-fall time, although the larger cooling rate in the $10^{-2}\,Z_\odot$ run leads to much stronger CMB coupling and nearly isothermal evolution for $10^4\,{\rm cm}^{-3} < n < 10^6\,{\rm cm}^{-3}$. In the $10^{-4}\,Z_\odot$ run, the gas temperature remains above $T_{\rm CMB}$, instead reaching a minimum temperature of $T \sim 100\,{\rm K}$. Eventually, gas in all three simulations reaches the density for sink particle formation given

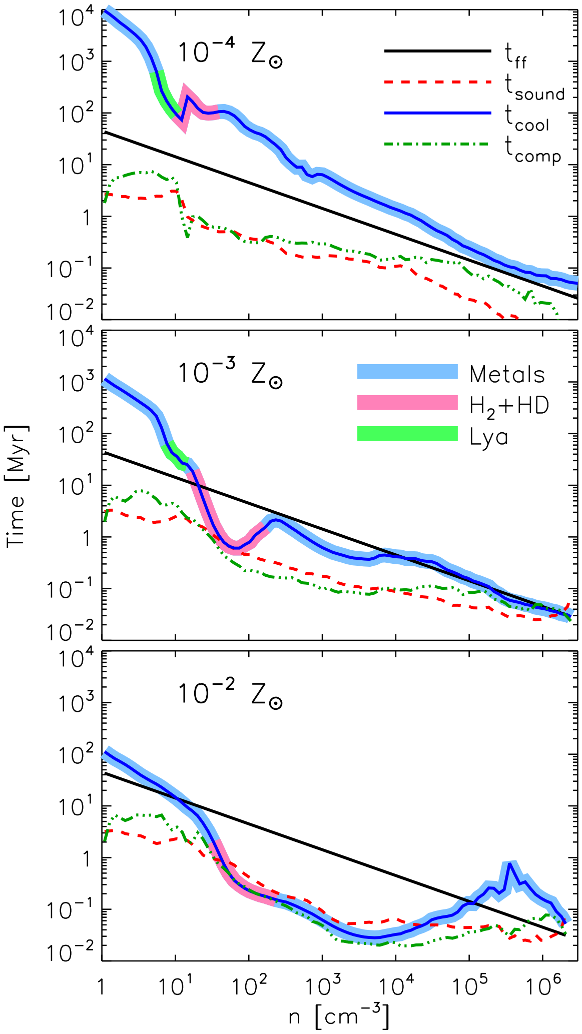

Figure 4.6 Various characteristic time scales as a function of gas density in the 10^{-4} (top), 10^{-3} (middle), and 10^{-2} $Z_\odot$ run (bottom). Shown is the free-fall time (solid black line), the sound crossing time of the pressure scale height (red dashed line — see text), the compression time (green dot-dashed line — see text) and the cooling time $t_{\rm cool} = 3nk_{\rm B}T/2\Lambda$ (blue solid line enclosed by a thicker line). The color of the thicker line enclosing the cooling time indicates the identity of the most effective coolant. Light blue refers to metal line cooling, light red is the cooling by $\rm H_2$ and HD, and green is Lyα cooling.

in Equation 4.13. We show density-temperature phase plots at the time of the first sink particle formation in Figure4.2. Past the formation of the first sink particle we evolve each run for $\approx 4\,\mathrm{Myr}$. Given the characteristic density of the cold, dense regions in each run, $n \sim 10^4\,\mathrm{cm}^{-3}$, this corresponds to roughly eight free-fall times. In this time period, fragmentation was widespread in the 10^{-2} and $10^{-3}\,Z_\odot$ runs which formed 11 and 9 sink particles, respectively. Only one sink particle formed in the $10^{-4}\,Z_\odot$ run.

4.3.1.1 Morphology and Density Evolution

The subsequent collapse in the $10^{-2}\,Z_\odot$ run becomes nearly isothermal at a density of $n \sim 10^3 - 10^4\,\mathrm{cm}^{-3}$ and $T = 45\,\mathrm{K} = T_{\mathrm{CMB}}$. The resulting structure is a cold, dense pocket of gas embedded within the turbulent, hot ($T \sim 10^4\,\mathrm{K}$) gas of the halo. This cold, dense region contains approximately $400\,M_\odot$ in gas and is $\sim 1-2\,\mathrm{pc}$ in physical size. Compression of the cold by the warm medium produces a strong, quasi-isothermal shock with Mach number $\mathcal{M} \equiv v/c_{\mathrm{s}} \sim 3$. The morphology of the cooled region evolves from roughly spherical to sheet-like and is seeded with filamentary density perturbations. These are the well known 'thermal pancakes,' an outcome of nonlinear effects developing in the aftermath of thermal instability (e.g., Kritsuk & Norman 2002). We see this in projection in the top-left panel of Figure 4.3 — in this view the sheet-like compressed region is seen face-on. The filamentary morphology is created entirely by the strong shock and resulting instabilities after the gas hit T_{CMB}. We note this is very similar to the model in which cold atomic and molecular clouds form as a result of supersonic flow convergence and thermal instability in a warm neutral medium (e.g., Hennebelle & Pérault 1999, Koyama & Inutsuka 2000, Hartmann et al. 2001, Heitsch et al. 2005, Vázquez-Semadeni et al. 2006, Hennebelle et al. 2007, Heitsch et al. 2008).

The density enhancement from the isothermal shock elevates the peak gas density to $\sim 10^5\,\mathrm{cm}^{-3}$. At this point, self-gravity becomes dominant in the highest density gas and two nearby sites of fragmentation emerge nearly concurrently, separated by $\sim 0.1\,\mathrm{pc}$. This point in the simulation is shown in the top-middle panel of Figure 4.3. These sites of fragmentation form two sink particles that rapidly create a tight binary pair. One of these sinks remains the most massive for the remainder of the simulation. We consider the onset of star formation to correspond to the time of the first sink particle formation. This occurs $4.8\,\mathrm{Myr}$ after the gas metallicity was assigned a non-zero value and corresponds to one free-fall time when evaluated at the density triggering metal introduction, $n = 100\,\mathrm{cm}^{-3}$.

The morphology of the cold, dense gas changes substantially over the course of the ensuing $\sim 4\,\mathrm{Myr}$ as can be seen in the remaining panels of Figure 4.3. Only the densest regions, $n > 10^4\,\mathrm{cm}^{-3}$ survive this subsequent hydrodynamic bounce. Over the first $3.8\,\mathrm{Myr}$ after the first sink particle formation, approximately $1700\,M_\odot$ of gas becomes incorporated into a total of 11 sink particles, a value that can also be considered a firm upper limit to the mass in stars that would have formed. Most of this mass, $\sim 1000\,M_\odot$, exists in the two most massive sink particles (the first and third to form), with masses of 460 and $510\,M_\odot$, respectively. The average sink particle mass is $\approx 145\,M_\odot$, though this does include two sink particles whose masses are 0.2 and $0.4\,M_\odot$. These sink masses are near the grid mass resolution of the simulation ($\rho\Delta x^3 \sim 0.3 M_\odot$), though we argue in Section 4.3.2 that these are genuine gravitationally collapsed structures and not numerical artifacts. The average accretion rate onto sink particles was $\approx 10^{-4}\,M_\odot\,\mathrm{yr}^{-1}$, consistent with a few times the characteristic accretion rate in gas clumps collapsing after Jeans instability c_s^3/G (e.g., Shu 1977, Larson 2003) evaluated at $T = 50\,\mathrm{K}$. The sink particles are distributed in a region of approximately $1\,\mathrm{pc}$ in size. We stop the simulation $\approx 4\,\mathrm{Myr}$

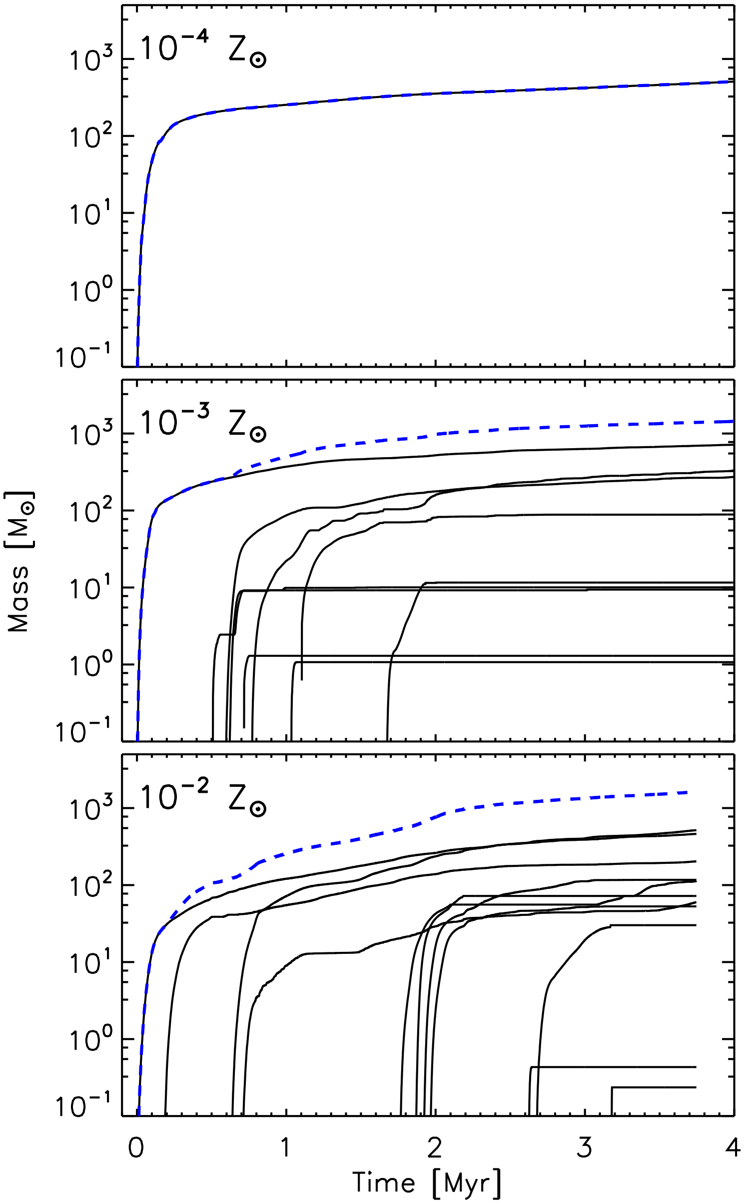

Figure 4.7 Masses of individual sink particles (black lines) and total mass in sink particles (blue dashed line) in the 10^{-4} (top), 10^{-3} (middle), and the 10^{-2} $Z_\odot$ (bottom) runs. Even though the 10^{-2} and 10^{-3} $Z_\odot$ runs formed similar numbers and total masses of sink particles, new sink particle formation in the 10^{-3} $Z_\odot$ run effectively ceased after $\sim 2\,\mathrm{Myr}$.

after the formation of the first sink particle because this is roughly the time scale at which we would expect stellar radiative feedback to significantly affect the subsequent evolution.

The $10^{-3}\,Z_\odot$ run is qualitatively similar to the $10^{-2}\,Z_\odot$ run. We show the density evolution for that run in Figure 4.4 and a representative density-temperature diagram in Figure 4.2(b). At $4\,\mathrm{Myr}$ after the formation of the first sink particle there is a similar number of and amount of mass incorporated in sink particles as in the $10^{-2}\,Z_\odot$ run. The gas, as in the $10^{-2}\,Z_\odot$ run, hits the CMB temperature floor at a density of $n \sim 10^4\,\mathrm{cm}^{-3}$, but, unlike in the higher metallicity run, because of the smaller cooling rate, begins heating up again at still higher densities. It is difficult to assess the impact of the CMB temperature floor — one-zone models would suggest that even in the absence of the CMB, gas at this metallicity would reach a minimum temperature of $T \sim 50\,\mathrm{K}$ (Omukai et al. 2005). Nine sink particles form within the course of $4\,\mathrm{Myr}$ with a total mass of $1450\,M_\odot$. Unlike in the $10^{-2}\,Z_\odot$ run, most of the fragmentation occurred in a disk that assembled around the first sink particle. The disk became locally gravitationally unstable and underwent pervasive fragmentation (seen in the top-middle panel of Figure 4.4). This can be contrasted with fragmentation resulting from the collapse and break up of filamentary features in the $10^{-2}\,Z_\odot$ run.

Another major difference between the 10^{-2} and $10^{-3}\,Z_\odot$ runs is the amount of cold gas available for sink particle accretion. As can be seen in the progression of the panels in Figure 4.4, the dense gas supply is continually diminishing and gas above a density of $n \sim 10^4\,\mathrm{cm}^{-3}$ is virtually non existent in the last panel when sink particles have been accreting for $4\,\mathrm{Myr}$. Quantitatively, after $\approx 4\,\mathrm{Myr}$, there is $5700\,M_\odot$ of cold gas (defined such that $n > 100\,\mathrm{cm}^{-3}$ and $T < 1000\,\mathrm{K}$) in the $10^{-2}\,Z_\odot$ run and only $1500\,M_\odot$ in the $10^{-3}\,Z_\odot$ run. Either the sink particles in this run are much more effective at accreting gas, or more likely the supply of cold, dense gas from the halo is unable to meet the demand of sink particle accretion. We return to this point in Section 4.3.2.

We show the density evolution in the $10^{-4}\,Z_\odot$ run in Figure 4.5. We also show a representative density-temperature diagram in Figure 4.2(a). Gas reaches a minimum temperature of $T \sim 100\,\mathrm{K}$ at $n \sim 10^4\,\mathrm{cm}^{-3}$ where the Jeans mass is $\sim 1000\,M_\odot$. While the initial cooling that prompted the collapse was due to metal fine-structure emission, H_2 did play a significant role due to self-shielding allowing the molecular abundance to increase (see Equation 4.3). This is identical in many respects to the thermodynamical evolution of collapsing metal-free gas and likely leads to a similar outcome (see, e.g., Safranek-Shrader et al. 2012). Given the warmer temperature of the dense gas, the strong shock present in the higher metallicity simulations was absent following the collapse, the subsequent collapse remained relatively spherical, and it did not exhibit sheet-like or filamentary density perturbations. Only a single sink particle formed surrounded by a gravitationally stable, non-fragmenting gaseous disk formed in the simulation. In $4\,\mathrm{Myr}$, the lone sink particle reached a mass of $520\,M_\odot$, had an average accretion rate of $\approx 10^{-4}\,M_\odot\,\mathrm{yr}^{-1}$, and a peak accretion rate of $\approx 10^{-3}\,M_\odot\,\mathrm{yr}^{-1}$. This is a much smaller accretion rate than the peak rate found in collapsing primordial gas (e.g., Abel et al. 2002, Yoshida et al. 2006, O'Shea & Norman 2007), a discrepancy predominantly due to the much higher time and spatial resolution in those studies and their ability to capture the onset of collapse at higher densities. If stellar mass scale fragmentation occurred at higher densities than resolved in the simulation, this would result in an extremely compact stellar association, or cluster, with size less than the sink particle accretion radius, $0.01\,\mathrm{pc}$ — this estimate, however, neglects the internal dynamical evolution of the cluster which could eject stars onto more extended orbits (e.g., Omukai et al. 2008).

The importance of following the evolution for multiple free-fall times, enabled by our use of sink particles, past the first point of collapse becomes evident from an inspection of the morphology evolution plots (Figures 4.3, 4.4, and 4.5). This is most apparent in the 10^{-2} and $10^{-3}\,Z_\odot$ runs where the gas morphology at the point of the first sink particle formation is not at all representative of its longer-term, $\sim 10^6\,\mathrm{yr}$, evolution. The initial isobaric cooling phase and isothermal collapse towards sink particle formation produces a dense, compact region with significant filamentary density perturbations. Within $1\,\mathrm{Myr}$ the region containing cold, dense gas becomes more diffuse. The further evolution, driven by the accretion of gas and sink particle dynamics produces a disordered, intermittent, filamentary flow morphology, typical of supersonic turbulence (e.g., Kritsuk et al. 2007, Federrath et al. 2010b). The majority of the sink particles, and thus stellar objects, form from density fluctuations not present at the point of first collapse. The $10^{-4}\,Z_\odot$ run, though, does not experience any significant morphological evolution after sink particle creation.

4.3.1.2 Characteristic Time Scales

To better understand the differences between the three runs, in Figure 4.6 we show characteristic time scales related to the dynamical and thermal evolution of the gas. We plot the free-fall time, $t_{\mathrm{ff}} = (3\pi/32G\rho)^{1/2}$, the compression time, $t_{\mathrm{comp}} = \rho/|\boldsymbol{\nabla}\cdot(\rho\boldsymbol{v})|$, the sound crossing time, $t_{\mathrm{sound}} = \lambda_P/c_{\mathrm{s}}$, where λ_P is the pressure scale length given by $\lambda_P = P/|\boldsymbol{\nabla}P|$, and the cooling time, $t_{\mathrm{cool}} = 3nk_{\mathrm{B}}T/2\Lambda$. We choose to treat the sound crossing time as a local quantity since sound waves need not propagate across an extended region to maintain isobaricity, only across one pressure scale length. The time scales are computed via mass-weighting in logarithmically-spaced density bins. For the cooling time, we additionally denote the most dominant coolant in the particular density bin (see figure).

Gas is expected to behave quasi-isobarically when $t_{\rm sound} \lesssim t_{\rm ff}, t_{\rm cool}$. This is indeed the case in the 10^{-2} and $10^{-3}\,Z_{\odot}$ runs at densities between $\sim 10\,{\rm cm}^{-3}$ and $\sim 10^{4}\,{\rm cm}^{-3}$. As evident in Figures 4.2(b) and 4.2(c) the gas cooling from $T \approx 10^{4}\,{\rm K}$ to $T_{\rm CMB}$ does indeed proceed quasi-isobarically. In the $10^{-4}\,Z_{\odot}$ run, however, the ordering of time scales is $t_{\rm sound} \ll t_{\rm ff}, t_{\rm cool}$, suggesting that the gas is overpressured with the respect to its surroundings, with gravity, rather than ambient warm gas pressure, driving the compression. This is supported by the density-temperature slopes in Figure 4.2(a), and by the longer time gravitational collapse took after the gas metallicity was increased in the $10^{-4}\,Z_{\odot}$ run as compared to the higher metallicity simulations. The time scales therefore help explain the different outcomes in the $10^{-4}\,Z_{\odot}$ run that exhibited no fragmentation and the higher metallicity runs with pervasive fragmentation.

Figure 4.6 also highlights the relative importance of molecular and metal cooling (see, e.g., Glover & Clark 2013). When the gas is first endowed with a non-zero metallicity, the increased cooling rate pushes the gas past a threshold where it ceases its isothermal collapse and begins an evolution in which temperature decreases with increasing density and the adiabatic index is sub-isothermal, $d\ln P/d\ln\rho < 1$. This increases the $\rm H_2$ self-shielding factor (Equation 4.3), the $\rm H_2$ abundance rapidly increases, and $\rm H_2$ becomes the dominant coolant in each simulation, albeit only over a small range of densities. Once the gas temperature drops below $\sim 200\,{\rm K}$, however, $\rm H_2$ loses its cooling efficacy and metal line-cooling once again dominates. We note that when $\rm H_2$ is the dominant coolant, its cooling rate is never more than a factor of ~ 3 greater than the metal line cooling rate.

The metal abundance, perhaps surprisingly, plays a significant role in reg-

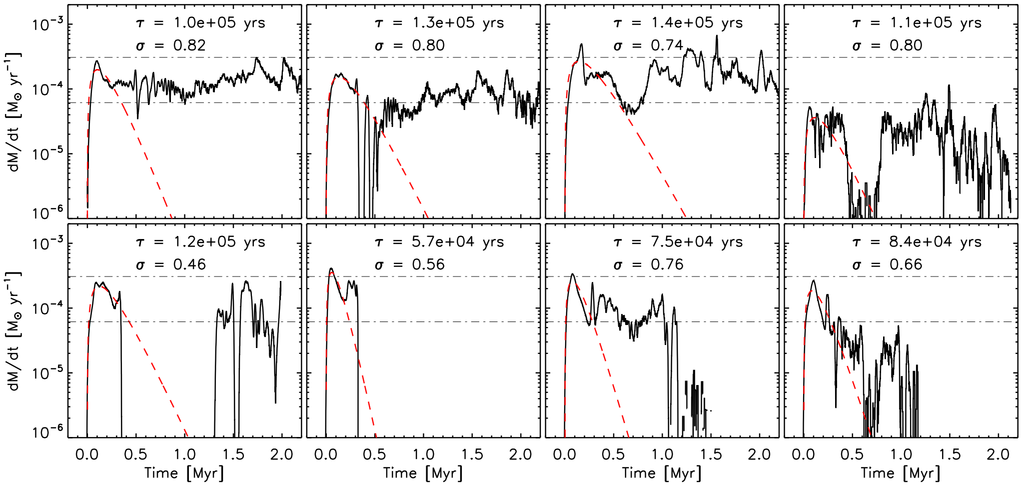

Figure 4.8 Accretion rates of the first eight sink particles to form in the $10^{-2}\,Z_\odot$ run in the first $\sim 2\,\mathrm{Myr}$. The top and bottom horizontal dot-dashed lines show the fiducial accretion rate c_s^3/G evaluated at $T = 100\,\mathrm{K}$ and $T = 50\,\mathrm{K}$, respectively. The dashed red line is a fit to the first $0.5\,\mathrm{Myr}$ of accretion (Equation 4.15) with the value of fitting parameter τ show at the top of each panel.

ulating the H_2 abundance. Our treatment of carbon and silicon as singly ionized significantly elevates the free electron abundance at densities $n > 100\,\mathrm{cm}^{-3}$, an effect more pronounced in the higher metallicity simulations. In the $10^{-2}\,Z_\odot$ run these additional free electrons actually set a lower limit of $x_\mathrm{e} \sim 2 \times 10^{-6}$ on the free electron abundance. Given that the formation of H_2 through the gas phase H^- channel depends sensitively on x_e, it is not surprising that the primordial coolant would depend on the gas metallicity.

4.3.2 Sink Particle Formation, Growth, and Mass Function

We emphasize that the sink particles here do not represent single stars, but instead are small stellar associations. We take the sink particle mass as a proxy for the stellar mass of the association. This mass is a firm upper limit as we do not include any form of stellar feedback that would likely act to reduce the gas-to-star conversion efficiency. The total mass accretion rate onto protostellar objects in one association, which is approximated by the sink particle gas accretion rate, has implications for protostellar evolution (e.g., Omukai & Palla 2003). We calculate the sink particle accretion rates by dividing the mass accreted during a timestep by the length of the timestep. To derive any insight on the nature of individual protostars we would need to probe higher densities up to the opacity limit for fragmentation (Low & Lynden-Bell 1976, Rees 1976).

In Figure 4.7 we show the total mass in sink particles over time in the three simulations. The two higher metallicity runs reach a total sink mass of $\approx 1500\,M_{\odot}$ in $4\,\mathrm{Myr}$. The $10^{-4}\,Z_{\odot}$ run converts roughly a factor of 3 lower gas mass, $500\,M_{\odot}$, into one sink particle $4\,\mathrm{Myr}$ after its formation. In all runs, most of the sink mass is in a few large mass ($> 500\,M_{\odot}$) objects. The average sink accretion rate is $\approx 4 \times 10^{-4}\,M_{\odot}\,\mathrm{yr}^{-1}$ in the two higher metallicity simulations and $\approx 10^{-4}\,M_{\odot}\,\mathrm{yr}^{-1}$ in the lowest metallicity simulation. The general trend is that the first sink particles to form remain the most massive, though there are exceptions.

In the 10^{-2} and $10^{-3}\,Z_{\odot}$ runs, many sink particles appear to permanently stop accreting after less than $\sim 10^{5}$ years of growth — this is most apparent in the middle panel of Figure 4.7. It is possible these ephemerally accreting sink particles do not represent physical gravitationally bound structures but are numerical artifacts; many of their masses lie far below the typical Jeans mass where fragmentation is likely to set in ($M_{\mathrm{J}} \sim 50 - 100\,M_{\odot}$). These sinks, though, did pass a stringent suite of tests for creation (see Section 4.2.4) that includes only forming sink particles from a gravitationally bound converging gas flow. Thus it seems that these objects are collapsed physical structures and that their mass growth was terminated by a physical mechanism, likely strong tidal interactions with more massive sink particles, though higher resolution simulations are needed to establish this conclusively.

We can understand the formation and growth of sink particles further by inspecting their individual accretion rates. In Figures 4.8 and 4.9 we do so for the first eight sink particles formed in each simulation (except for the $10^{-4}\,Z_\odot$ run where only one sink formed). The individual sink particle accretion rates in the $10^{-3}\,Z_\odot$ simulation are qualitatively similar to the $10^{-2}\,Z_\odot$ run and are not shown. We also show a simple fit meant to capture the accretion rate history of protostellar objects forming via gravo-turbulent fragmentation suggested by Schmeja & Klessen (2004),

$$\dot{M}(t) = \dot{M}_0 \frac{e}{\tau}\, t\, e^{-t/\tau}, \tag{4.14}$$

where $\dot{M}_0$ and τ are fitting parameters and t is time measured from sink particle formation. We estimate the quality of the fit similarly to Schmeja & Klessen (2004) by computing the normalized standard deviation

$$\sigma = \sqrt{\frac{1}{n-1}\sum_{i=1}^{n}\left[1 - \frac{\dot{M}(t_i)}{\dot{M}_{\rm fit}(t_i)}\right]^2}, \tag{4.15}$$

where $\dot{M}_{\rm fit}(t)$ is the fit from Equation 4.15, $\dot{M}(t)$ is the accretion rate extracted from our simulations, n is the total number of data points, and we compute σ for a time period of 5τ for each sink particle. In this 5τ time period, we find σ to be typically between $0.5 - 0.8$. Most sinks possess an initial accretion rate peak which lasts for $\sim 5 \times 10^4 - 10^5$ years. This peak accretion rate is typically on the order of $\dot{M}_{\rm J} = M_{\rm J}/t_{\rm ff} \sim c_{\rm s}^3/G$. In this time period, the sink particle accretes the initial Jeans unstable gas clump that triggered its formation. In the 10^{-2} and $10^{-3} Z_\odot$ runs this mass is between $20 - 100\,M_\odot$ depending on the exact temperature and density when fragmentation set in. This evolution of the accretion rate can be understood by considering the initial reservoir of the gas the sink particles accrete as a Bonnor-Ebert sphere or a Plummer-like density profile consisting of a flat plateau at small radii and a power law envelope at larger radii (e.g., Whitworth & Ward-Thompson 2001). This first peak in $\dot{M}(t)$ is the accretion of the flat, inner plateau. For the majority of the sink particles, this early phase lasting $\sim 0.5\,\mathrm{Myr}$ is fit reasonably well by Equation (4.15) as shown by the small standard deviation, but the fit becomes significantly worse as time passes and the accretion rate either stays relatively constant or instantaneously drops to zero.

Almost all the sink particle accretion rates show a similar early time ($\lesssim 0.5$ Myr) behavior — a rapid rise to a peak value followed by a drop to a lower (or zero) accretion rate. It is reasonable to ask whether this general behavior is physical or is instead a numerical artifact from instantaneous gas pressure loss following sink particle formation (e.g., Bate et al. 1995). As discussed in Section 4.2.4, Eulerian sink particle implementations do not suffer from this issue to the same degree that SPH implementations do. Additionally, numerous numerical studies of protostellar collapse have found rapidly peaking accretion rates followed by a decrease (e.g., Hunter 1977, Basu 1997, Whitworth & Ward-Thompson 2001, Motoyama & Yoshida 2003, Schmeja & Klessen 2004). While it is possible the accretion rates we measure are slightly overestimated by the reduction of gas density around sink particles, this general behavior we see is physically expected.

Beyond the first accretion rate peak, many sink particles in the 10^{-2} and $10^{-3}\,Z_{\odot}$ runs, especially the earliest ones formed, show sustained gas accretion over many Myr. Others do not display sustained gas accretion but instead have their accretion terminated within a few 10^{5} years after their formation. This sharp cutoff in the accretion rates is primarily the result of these sinks experiencing a close encounter with a more massive sink particle, also seen in idealized simulations of present-day (e.g., Klessen & Burkert 2000, Klessen 2001b) and Pop III (Clark et al. 2011a) star formation. These strong dynamical encounters tend to eject less massive sinks to the outskirts of the cold gas environment where gas densities are smaller and accretion is thus lowered or completely shut off. Given the density and velocity dependence of the Bondi-Hoyle accretion rate, $\dot{M}_{\rm BH} \propto \rho v^{-3}$, the ejected sinks effectively stop accreting.

Overall, it seems that the mode of gaseous accretion onto sink particles is a hybrid between monolithic collapse (e.g., McKee & Tan 2003), where the stellar mass (and mass function) is ultimately determined by the mass of gravitationally unstable cores, and competitive accretion (e.g., Bonnell et al. 2001), where stellar masses are the result of many cores competing for the same reservoir of gas resulting in more massive (though rarer) objects near the cluster center accreting more such that the 'rich get richer.' The less massive sink particles, typically the latter ones to form, can only accrete a portion of their initial Jeans-unstable gas clumps before dynamical interactions with other sink particles terminate gas accretion. Higher mass sink particles from more massive Jeans-unstable clumps and then continue accreting from the dense gas in the central region of the cluster over many Myr.

The top panel of Figure 5.4 shows the sink particle mass function at the end of each run after star formation has progressed for $\approx 4\,{\rm Myr}$. The higher metallicity simulations show a preferred mass scale around $\sim 50\,M_{\odot}$, roughly consistent with the Jeans mass at the point at which the gas density hits the CMB temperature and fragmentation is expected to be thermodynamically suppressed. While this mass function does not represent the final stellar IMF, observations have shown there to be a connection between the pre-stellar clump mass function and the ultimate stellar IMF (e.g., Motte et al. 1998, Beuther & Schilke 2004, André et al. 2010), suggesting that the power-law slope toward higher masses, only marginally evident in the $10^{-2}\,Z_{\odot}$ run, may translate directly to the slope of the ultimate stellar IMF.

We caution that the inclusion of radiative feedback from accreting protostars has the potential to suppress fragmentation and thus alter the resultant mass function, particularly at the low mass end (e.g., Krumholz et al. 2007, Urban et al. 2010, Bate 2012). The bottom panel of Figure 5.4 shows the mass function in which sink particles located within each others accretion radius are merged in post-processing and are only counted as a single particle. Doing this, four sink particles in the $10^{-2}\,Z_\odot$ run merge into two sinks, while in the $10^{-3}\,Z_\odot$ run only one pair of particles merges. As is clear, this merging procedure has little effect on the resultant mass function. Finally, we emphasize that the mass function is sensitive to the resolution (which determines the sink particle formation density) and the particular choice of sink particle parameters (such as the accretion radius and the sink-gas softening length) as discovered in our initial exploratory simulations.

4.3.3 Density Probability Distribution Function

The gas density probability distribution function (PDF), $p(\rho)$, is defined such that $p(\rho)d\rho$ represents the probability that a given parcel of gas has density within the range $[\rho, \rho + d\rho]$. It is particularly sensitive to the character and strength of turbulence that imprints a specific turbulent signature on the gas density PDF. We show volume-weighted gas density PDFs for the three simulations and two different times in Figure 4.10. We show the PDF for all gas within the virial radius of the halo and only for gas with temperature $T < 200\,\mathrm{K}$ and density $n > 100\,\mathrm{cm}^{-3}$, the latter representing the gas that has cooled and is participating in star formation.

The density PDFs in Figure 4.10 exhibit a number of interesting features. The high density, cold gas PDFs peak at densities roughly 3 orders of magnitude higher than that of the full density PDFs. The cold gas PDFs also represent a significant ‘bump’ in the full density PDF, mainly seen in the bottom panel. This is clearly reminiscent of the density structure in thermally bistable turbulent flows (e.g., Gazol & Kim 2010, Seifried et al. 2011, Saury et al. 2013). The sharp increase in the peak density of the cold gas PDF in the $10^{-4}\,Z_\odot$ run is due to the $T < 200\,\mathrm{K}$ temperature cutoff which was selected with the higher metallicity simulations in mind, meant to cleanly separate the cold and hot phases that are separated by an isobarically unstable cooling phase. In the $10^{-4}\,Z_\odot$ run, is it not possible to cleanly distinguish between the ambient halo gas and the cooling gas.

It is well established that supersonic, isothermal turbulence tends to produce a lognormal gas density PDF (e.g., Vazquez-Semadeni 1994, Scalo et al. 1998, Passot & Vázquez-Semadeni 1998, Ostriker et al. 2001, Federrath et al. 2008b). As in Safranek-Shrader et al. (2012), we write the lognormal distribution as

$$p(s)ds = \frac{1}{(2\pi\sigma^2)^{1/2}}\exp\left[-\frac{1}{2}\left(\frac{s-\bar{s}}{\sigma}\right)^2\right]ds, \tag{4.16}$$

where $s = \ln(n/n_0)$ is the logarithmic density contrast and σ is the lognormal width. The average of the logarithmic density contrast is related to σ via $\bar{s} = -\sigma^2/2$, effectively reducing Equation 4.16 to a one parameter model. Only the cold gas PDFs for the 10^{-2} and $10^{-3}\,Z_\odot$ runs $4\,\mathrm{Myr}$ after sink particle formation are reasonably well fit by the lognormal distribution. We plot a lognormal fit to these two PDFs in the bottom panel of Figure 4.10. The main deviation from the lognormal shape is the power-law tail at high density contrasts, understood to be a result of self-gravity (e.g., Kritsuk et al. 2011) or the peculiar dynamics of bistable turbulent flows (Gazol & Kim 2010, Seifried et al. 2011, Saury et al. 2013, Federrath & Klessen 2013).

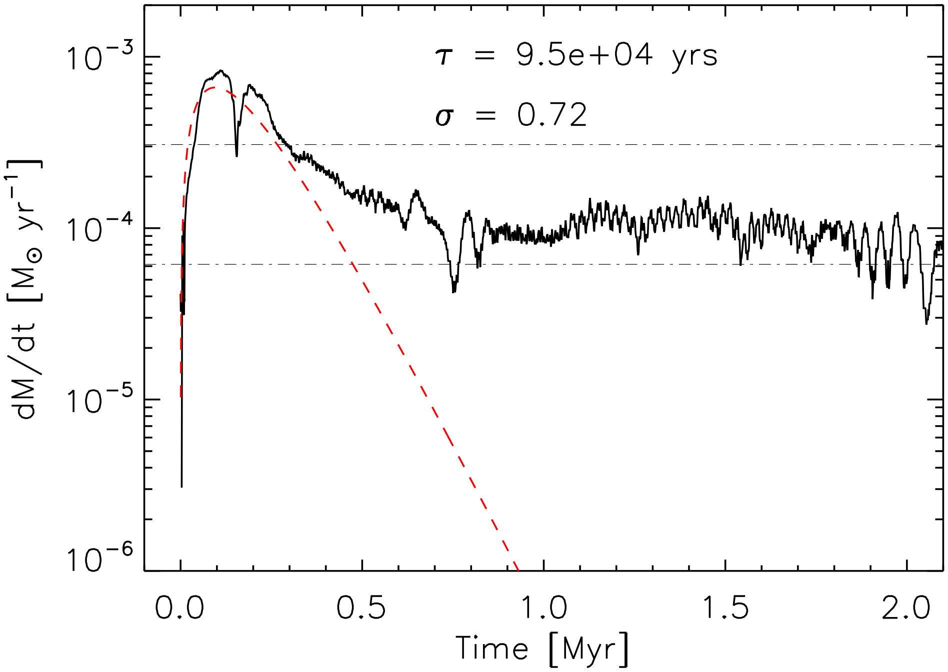

Figure 4.9 Same as Figure 4.8, but for the $10^{-4}\,Z_\odot$ run and smoothed on a 10^4, yr time scale. Only one sink particle formed in the simulation.

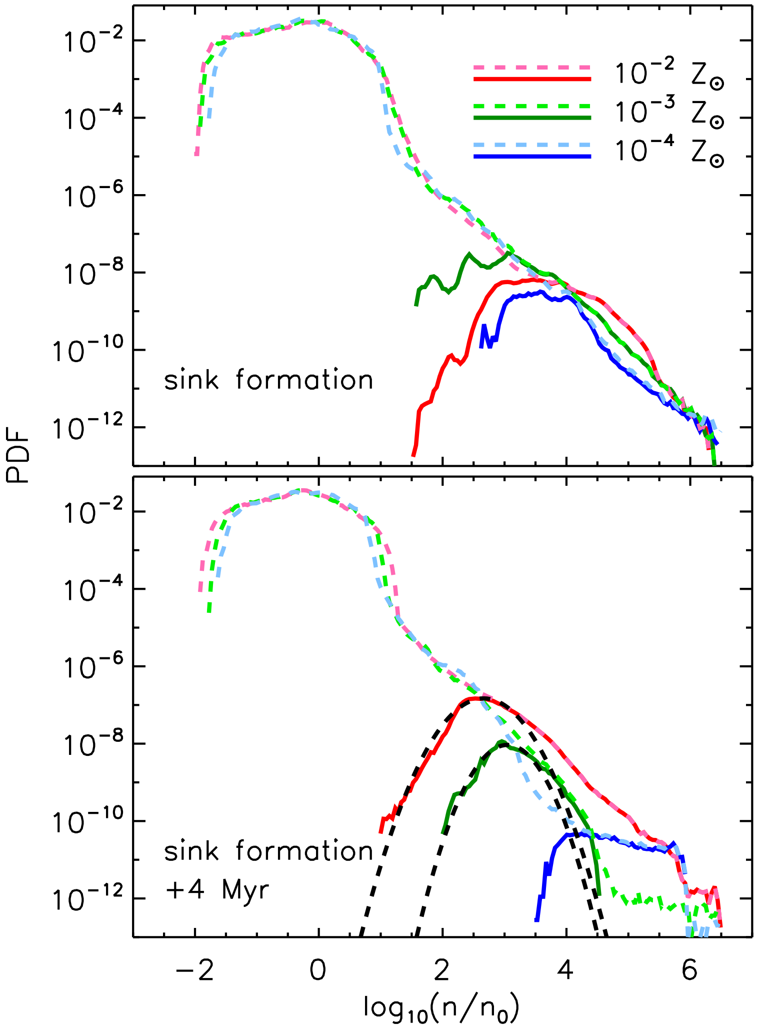

Figure 4.10 Gas density PDFs at the onset of sink particle formation (top panel) and 4 Myr later (bottom panel). We show PDFs from the 10^{-2} (red lines), 10^{-3} (green lines), and $10^{-4}\,Z_\odot$ (blue lines) runs. We separately plot PDFs computed using all gas within the virial radius of the halo (dashed lines) and only gas with $T < 200\,\mathrm{K}$ and $n > 100\,\mathrm{cm}^{-3}$ (solid lines). For the all-gas PDFs, the average density is $n_0 \approx 1\,\mathrm{cm}^{-3}$ at both times. In the bottom panel, we show lognormal fits to the 10^{-2} and $10^{-3}\,Z_\odot$ run cold gas PDFs which have widths of $\sigma = 0.86$ and 0.71, respectively. Power law tails, evident in the top panel and in the $10^{-4}\,Z_\odot$ run in the bottom panel, are an anticipated outcome of self-gravity. In the $10^{-3}\,Z_\odot$ run, however, this power-law tail disappears within $\sim 2\,\mathrm{Myr}$ after the first sink particle formation as the sink particles deplete the cold, dense gas.

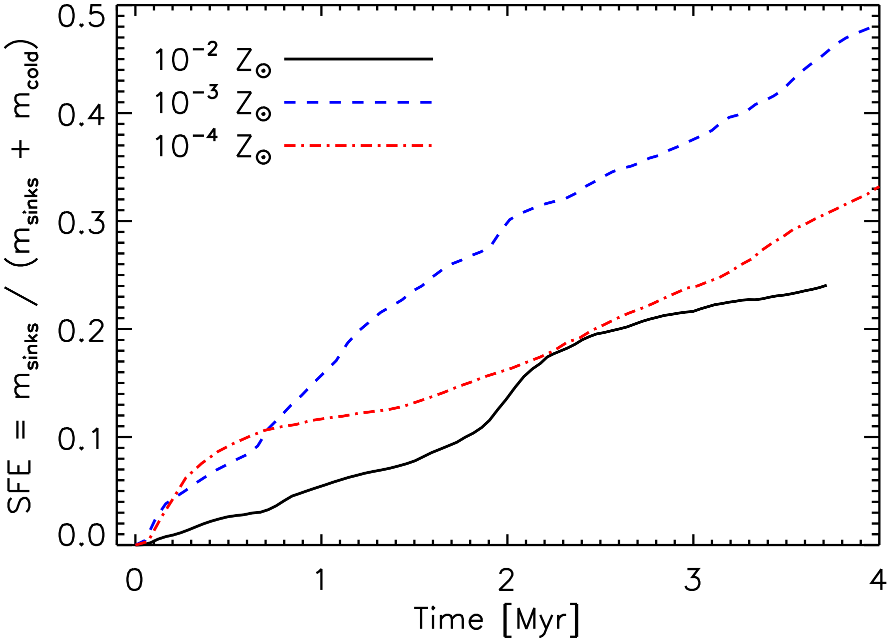

Figure 4.11 Star formation efficiency as a function of time in the three different metallicity runs. We define the star formation efficiency as $\mathrm{SFE}(t) \equiv M_{\mathrm{sinks}}(t)/(M_{\mathrm{gas,cold}}(t) + M_{\mathrm{sinks}}(t))$ where $M_{\mathrm{gas,cold}}$ is the total mass of gas with temperature $T < 1000\,\mathrm{K}$ and density $n > 10\,\mathrm{cm}^{-3}$. This efficiency measures the efficiency with which the cold and dense gas is being incorporated in stars. Since all the curves increase with time, the sink particles are depleting the cold gas supply faster than gas is able to cool, implying that eventually, the star-forming cluster becomes gas-starved.

4.3.4 Star Formation Efficiency

As discussed in Section 4.3.2, the lowest metallicity simulation converts less mass, by roughly a factor of 3, into sink particles than the higher metallicity simulations. Is this smaller mass the result of inefficient accretion of gas that has already cooled and collapsed, or is it instead due to inefficient cooling and collapse starving the sink particle? To answer this, we compute the star formation efficiency (SFE), which we define as

$$\mathrm{SFE} = \frac{M_{\mathrm{sinks}}}{M_{\mathrm{sinks}} + M_{\mathrm{gas,cold}}}, \tag{4.17}$$

where $M_{\mathrm{gas,cold}}$ is the total mass in gas that has cooled and collapsed as a result of metal fine-structure emission, defined to have temperature $T < 1000\,\mathrm{K}$ and density $n > 10\,\mathrm{cm}^{-3}$, and again we are taking sink particle mass as a proxy for the total stellar mass in the stellar association that the sink represents. Given that in our simulations gas both flows from the halo to the star forming region, and from the star forming region into sink particles, Equation 4.17 is better construed as a measure of how effective sink particles accrete gas that has already cooled and collapsed. We show the time evolution of the SFE in Figure 4.11. The similarity in the SFE between the three runs is most striking, differing by no more than a factor of ~ 3 at any time. This suggests that sink particles, regardless of gas metallicity, are equally efficient at accreting cold, dense gas. The primary difference stems from how gas is supplied to the star forming region — in the lowest metallicity simulation, gas cooling is inefficient and accretion onto sinks is modulated by gas cooling. In high metallicity gas ($Z \sim 10^{-2}\,Z_{\odot}$), the total stellar mass is modulated by the hydrodynamics of gas accretion onto prestellar cores, not by the ability of the gas to cool.

4.4 Caveats and Limitations

The most significant approximation used in the simulations is our metal enrichment strategy. Recall that when the target halo has entered the Lyα cooling-enabled isothermal collapse, we endowed gas in the vicinity of the halo with a non-zero metallicity. The metallicity was made spatially uniform, implying that metal mixing acted with perfect efficiency, which is certainly not the case. Realistically, the mixing is not instantaneous and could potentially result in concurrent Pop III and Pop II star formation (e.g., de Avillez & Mac Low 2002, Pan et al. 2011, 2013). The process of metal mixing may begin in hydrodynamic instabilities of supernovae (e.g., Joggerst et al. 2009) and supernova remnants (e.g., Madau et al. 2001, Ritter et al. 2012) and following turbulent transport is ultimately completed on microscopic scales via molecular diffusion. Since molecular diffusion is effective only on microscopic spatial scales (e.g., Oey 2003, Pan & Scalo 2007), turbulence is paramount for efficient mixing of primordial and metal-enriched gas. There is evidence that the process of virialization and the inflow of dark matter directed 'cold accretion' streams in atomic cooling haloes can be effective in driving supersonic turbulent motions (Wise & Abel 2007a, Greif et al. 2008, Prieto et al. 2012, Latif et al. 2013) and thus accelerating the mixing of primordial and metal enriched gas. Frebel & Bromm (2012) suggested that a signature of incomplete mixing can be found in the chemical inhomogeneity of metal-poor stellar populations, particularly those in ultra-faint dwarf galaxies.

The fact that metals were not present during the initial virialization process of the atomic cooling halo may also have consequences. If the high density, cold accretion streams that account for the majority of baryonic accretion into the halo had been metal enriched we would have expected them to have significantly lower temperatures than if the gas was primordial. Given the lower temperatures, the stream termination shocks would be more compressive and this could affect the virialization and star formation processes. Our choice of the time to raise the gas metallicity to a non-zero value may also directly set the characteristic fragmentation mass. In all simulations the metals were introduced when the maximum gas density in the halo reached $100\,\mathrm{cm}^{-3}$. Increasing the metallicity of the gas at a lower (higher) peak density threshold would have let the gas hit the CMB floor at a smaller (larger) density, thus increasing (decreasing) the characteristic fragmentation mass scale. Our main result, though, concerning efficient fragmentation above $Z = 10^{-4}\,Z_{\odot}$ is robust in this respect, as is the typical gas accretion rate and total cluster mass. Additionally, actual protostellar fragments must ultimately emerge at higher densities in the presence of thermal gas-dust coupling and would be unaffected by this caveat.

Our simulations did not include any prescriptions for stellar feedback, processes well known to play significant roles in star formation, allowing us to isolate the process of gas collapse and fragmentation in the presence of metal cooling. We run the simulations for 4 Myr past the formation of the first sink particle, a timescale meant to capture only the initial starburst. In this time we do not expect supernovae, stellar winds, or stellar evolutionary effects to play significant roles given these processes operate on longer timescales ($\sim 3-100$ Myr). Radiative feedback from accreting protostars should influence the outcome of turbulent fragmentation in the first metal-enriched star forming regions. Detailed radiation hydrodynamic simulations (e.g., Krumholz et al. 2007, Bate 2012) have shown that the primary impact of radiative heating is the suppression of fragmentation. This results in fewer low-mass brown dwarf-like objects (e.g., Offner et al. 2009) and may enable the formation of high mass stars in dense star forming regions (e.g., Krumholz et al. 2012). This suppression may be less effective in the present simulations given the much smaller metallicity and dust abundance (though see Myers et al. 2011). Simulations of metal-free star formation that include prescriptions for radiation from accreting protostars (e.g., Smith et al. 2011, Greif et al. 2011) find fragmentation to be delayed by the feedback, but not suppressed. In addition to radiative feedback, accreting protostars are known to posses energetic jets that are capable of driving turbulence and reducing the rate of star formation in actively star forming regions (Li & Nakamura 2006, Matzner 2007, Wang et al. 2010, Cunningham et al. 2011, Krumholz et al. 2012). These jets may be especially significant in the regime considered here since our results suggest these earliest stellar clusters formed in relatively dense environments ($\sim 0.01 - 1\,\mathrm{pc}$) where the effect from these outflows would be more pronounced.

We do not include dust grains in our chemical model. This eliminates dust catalyzed $\mathrm{H_2}$ formation and dust-gas collisional coupling that can act to heat or cool the gas. The neglect of dust-gas coupling is well justified since this does not occur at densities $<\sim 10^8\,\mathrm{cm^{-3}}$ that we resolve (e.g., Omukai et al. 2005). The dust-grain-catalyzed formation of $\mathrm{H_2}$ may have more significant thermal consequences. However, given that much of the star forming gas in our simulations has temperatures below $100\,\mathrm{K}$ where $\mathrm{H_2}$ cooling is ineffective, this would completely eliminate $\mathrm{H_2}$ as an effective coolant even if it did form in much higher abundance. The formation of $\mathrm{H_2}$, though, is an exothermic reaction and thus elevated $\mathrm{H_2}$ formation from dust grains, while not augmenting the cooling rate, may act as a heating source.

Finally, it is worth stressing that the results of the simulations here are resolution dependent. At higher or lower resolutions, resolving higher and lower maximum densities,, different physical processes will dominate the gas thermodynamics. Gas-dust coupling would have a significant thermodynamic effect on the gas at much higher densities ($n \gtrsim 10^{10}\,\mathrm{cm^{-3}}$). At lower densities ($n \lesssim 10^3\,\mathrm{cm^{-3}}$)

there would be almost no difference between the different metallicities considered here (see Figure 4.2). Our resolution was chosen to most effectively study the effect that metal fine-structure cooling has on the fragmentation of collapsing gas concentrations. The results of the simulations are also sensitive to the sink particle parameters we used (such as the accretion radius, softening length, density for sink creation, etc.). In preparation for the production simulations presented here, exploratory simulations were performed that varied the resolution and the sink particle parameters. Modification of the gas-sink softening length and accretion radius had the largest effect on sink particle creation, growth, and dynamics. Overall, the main difference between these initial simulations and the ones presented here was the number of sink particles created, though never by more than a factor of ~ 1.5. The $Z = 10^{-4}\,Z_{\odot}$ simulations always produced only one sink particle independent of the resolution or sink particle parameters.

4.5 Discussion and Summary

In this work, we have focused on the effect that metallic fine-structure line cooling has on the process and outcome of star formation in a high-redshift atomic cooling halo. We have run three high-resolution, zoomed cosmological simulations until the assembly of a $M_{\rm vir} \approx 2 \times 10^{7}\,M_{\odot}$ halo at redshift ~ 16 capable of atomic cooling. At this point, we endowed gas in the halo with a non-zero metallicity and observed the subsequent collapse and progression of star formation. We utilized the sink particle technique, allowing us to follow the process of star formation for many free-fall times past the first point of gravitational runaway collapse.

Theory predicts that below a metallicity of $Z \sim 10^{-3.5}\,Z_{\odot}$, fine-structure metal line cooling is not strong enough to significantly alter the thermodynamic and fragmentation behavior of collapsing gas (e.g., Bromm et al. 2001). We indeed

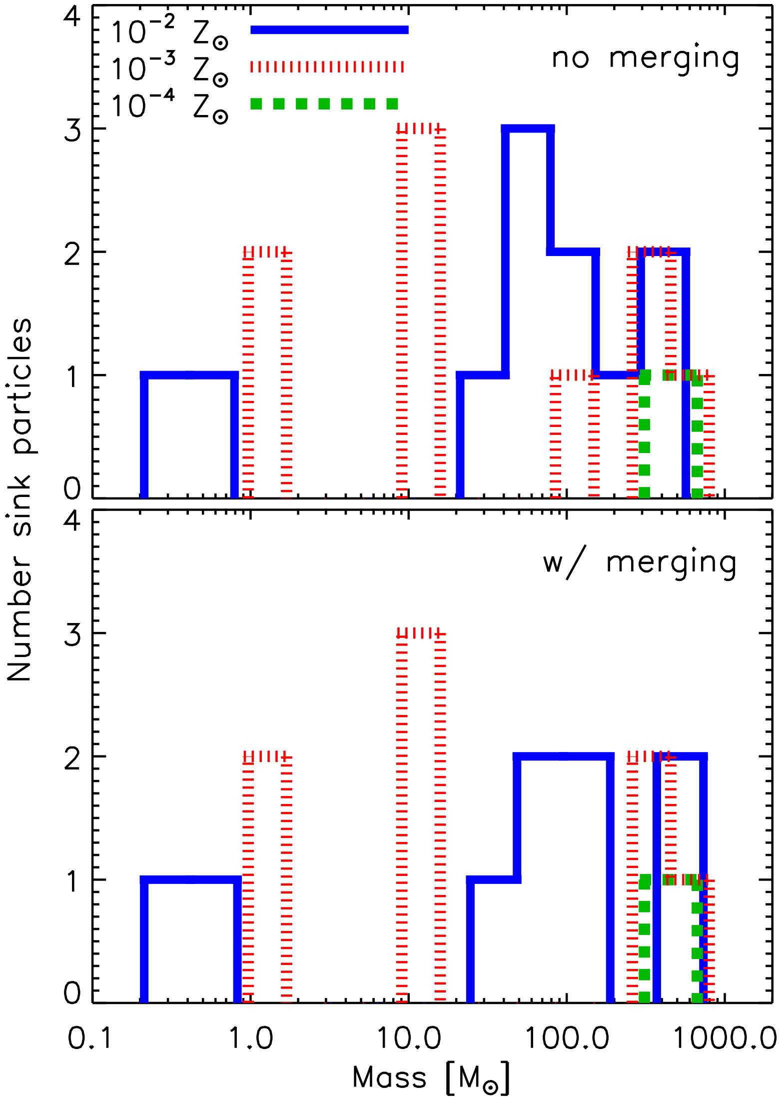

Figure 4.12 Distribution of sink particle masses in the 10^{-2} (blue solid line), 10^{-3} (red short-dashed line), and 10^{-4} $Z_\odot$ (green dotted line) runs $4\,\mathrm{Myr}$ after the first sink particle formation. The top panel is the mass function extracted directly from the simulations. In the bottom panel, in post-processing, we merged any sink particles within each other's accretion radius. Sink merging performed in post-processing does not drastically affect the mass spectrum.

confirm this by finding a marked difference in gas morphology and fragmentation between the 10^{-3} and $10^{-4}\,Z_{\odot}$ runs (as shown in Figures 4.4 and 4.5). In the higher metallicity runs, 10^{-2} and $10^{-3}\,Z_{\odot}$, the gas acquires a disordered, turbulent flow morphology. In the $10^{-4}\,Z_{\odot}$ run, cooling was not effective enough to allow the gas to reach $T_{\rm CMB}$, the thermal Jeans mass stayed relatively high, and no fragmentation occurred. We attribute this to two key reasons. First, the lower cooling rate in the low metallicity simulation produces gas with higher temperatures and a correspondingly higher thermal Jeans mass, decreasing the propensity for fragmentation. Additionally, the higher Mach number in the higher metallicity runs where gas was able to reach $T_{\rm CMB}$ led to larger compressibility and a greater propensity for dynamical instabilities to induce small scale density fluctuations. This was not the case in the $10^{-4}\,Z_{\odot}$ run where the collapse took longer (by roughly a factor of 2), maintained a large degree of spherical symmetry, and underwent no fragmentation.

The accretion rates of individual sink particles are well approximated by $c_{\rm s}^3/G$, potentially over many millions of years. Quite generically, sink particle accretion rates begin low and increase to some maximum value within a few $\times 10^4$ years. This first phase ends when the initial Jeans unstable gas clump is accreted by the sink. Sink particles destined to become the most massive have their accretion rate fall off by only a factor of $2-10$ after this phase, but stay on order of $c_{\rm s}^3/G$ for many Myr. Lower mass sinks have their accretion terminated shortly after consuming all or a portion of the initially Jeans unstable gas clump, mainly through dynamical encounters with larger mass sinks. This suggests protostellar accretion is a combination of relatively quick collapse ($t \sim 10^5\,{\rm yrs}$) and sustained accretion as the stellar association moves throughout the parent gas cloud. Sink particle masses are controlled by both the physical properties of the parent gas cloud, such as the

Jeans mass when the gas hits the $T_{\rm CMB}$, and dynamical encounters that regulate the long-term accretion rate. The creation of stellar mass fragments must predominantly occur at densities above our resolution limit, possibly as a result of dust-gas coupling (Schneider et al. 2006, Dopcke et al. 2013) or through the fragmentation of gravitationally unstable disks (Stacy et al. 2010, Greif et al. 2011). Overall, it seems most appropriate to describe the process of gaseous fragmentation and sink particle growth in the higher metallicity simulations as a hybrid between competitive accretion and monolithic collapse.

We do not detect suppression of fragmentation at high metallicities due to the CMB temperature floor suggested by Smith et al. (2009). Gas in the $10^{-2}\,Z_{\odot}$ run does become more strongly coupled to the CMB temperature than the $10^{-3}\,Z_{\odot}$ run, but continues to fragment. In fact, both runs with metallicities above the critical value for efficient fine-structure cooling, $Z_{\rm crit} \approx 10^{-3.5}\,Z_{\odot}$, exhibited roughly the same fragmentation behavior as discussed in Section 4.3, although the primary cause of the fragmentation was different between the two runs as discussed in Section 4.3.1.1. Given the clump-finding approach of Smith et al. (2009) to characterize the amount of fragmentation, our differing results are unsurprising. Shown in Figure 4.7, fragmentation and sink particle formation is continuous over many Myr, well after the initial runaway gravitational collapse. It is possible that another run with metallicity between 10^{-4} and $10^{-3}\,Z_{\odot}$ would have demonstrated an elevated degree of fragmentation, but even so this would suggest that the 'metallicity regulated' star formation mode of Smith et al. (2009) would exist only under a very narrow range of metallicities and would not be a significant star formation pathway.

We also find disagreement with the simulations of Jappsen et al. (2007, 2009b,a) who find no metallicity threshold that distinguishes Pop III and Pop II star formation, and instead argue it is the initial conditions (e.g., level of rotation, initial temperature, degree of turbulence) that moderate the process of gas fragmentation, whereas we unambiguously identify a metallicity threshold in controlling fragmentation. Jappsen et al. (2007) argues that H_2 cooling is partly responsible for eliminating a Pop III-II metallicity threshold given that it may be a dominant coolant even in the presence of metals. In all three of the simulations presented here, H_2 was a significant coolant even given the strong Lyman-Werner background we included, though there was still a clear metallicity threshold for widespread fragmentation between 10^{-4} and $10^{-3}\,Z_\odot$. The disagreement additionally stems from the differing redshift at which the collapse occurs. In Jappsen et al. (2009b), this redshift was 25 where the CMB temperature is $\sim 70\,\mathrm{K}$, as opposed to a CMB temperature of $T_{\mathrm{CMB}}(z \approx 16) \sim 50\,\mathrm{K}$ in the present work. Given Jeans mass scale fragmentation sets in when gas reaches T_{CMB} and the temperature dependance of the Jeans mass, $M_{\mathrm{J}} \propto T^{3/2}$, this difference in redshift can potentially be significant in suppressing fragmentation (see also Clarke & Bromm 2003).

In previous work, Safranek-Shrader et al. (2010), we presented a semi-analytical, one-zone model for fragmentation in metal-enriched atomic cooling halos with results directly applicable to the present study. The model assumed cold-flow accretion into a $M_{\mathrm{vir}} = 10^8\,M_\odot$ halo at $z = 10$. These cold flows, when shocked in the halo's interior, were heated to a temperature of $T = 10^4\,\mathrm{K}$, compressed to a density $n = 4 \times 10^3\,\mathrm{cm}^{-3}$, and began to isobarically cool. Continued gas accretion resulted in the compressed layer increasing in size until the sound crossing time across the fragment exceeded its free-fall time, our criteria for the onset of fragmentation. While highly simplified, it supported the conclusion, here and elsewhere, that above $10^{-4}\,Z_\odot$ gas will experience fragmentation due to metal line-cooling. Safranek-Shrader et al. (2010) did predict a much smaller fragmentation mass scale than found here. We attribute this discrepancy to an overestimate of the post-shock density and the lower redshift and cooler CMB temperature. We also argued that gas with metallicity $10^{-2}\,Z_{\odot}$ should not evolve isobarically given its short cooling time compared to the sound crossing time across the compressed post-shock layer. We find this is not the case if considering only the sound crossing time of one local pressure scale height. Overall, it is clear that the process of gas fragmentation in high-redshift atomic cooling halos is complex and difficult to analyze using one-zone models.

Extrapolating beyond the results of the simulation here, it seems plausible that two different fragmentation episodes occur in low metallicity gas at high redshifts. The first occurs at relatively low densities, $n \sim 10^{3} - 10^{4}\,\mathrm{cm}^{-3}$, when gas reaches the CMB floor as a result of metal line cooling. As shown in the simulations here, this mode is capable of forming a compact cluster of size $\sim 1\,\mathrm{pc}$ and fragment masses on the order of $50 - 100\,M_{\odot}$. Solar mass fragments, however, are not expected to form as a result of metal-line-induced fragmentation, especially at high redshifts, $z > 10$, since the CMB sets a thermodynamic lower limit on the temperature that gas can reach. The second fragmentation episode occurs at much higher densities, $n \sim 10^{10} - 10^{14}\,\mathrm{cm}^{-3}$, when dust grains and gas thermally couple. This dust-induced fragmentation is capable of producing solar mass scale fragments (e.g., Clark et al. 2008, Dopcke et al. 2013) that have the potential to survive until the present day. Whether these two modes of fragmentation acted in tandem, or were individually responsible for separate stellar populations (e.g., Norris et al. 2013) is yet to be determined. An intriguing possibility, supported by the simulations presented here, is that dust-induced fragmentation is responsible for isolated solar mass Pop II stars, while the formation of a bona-fide stellar cluster requires metal fine-structure line cooling operating at lower densities and larger spatial scales (e.g., Karlsson et al. 2013).

Higher resolution studies will probe densities $n \gtrsim 10^{14}\,\mathrm{cm}^{-3}$ approaching the final opacity limit for fragmentation. These future studies are crucial to fully assess the impact of metallicity and dust on the Pop III to II transition and constrain the resulting stellar IMF. Simulations that focus on the mechanical, radiative, and chemical feedback from this first metal-enriched stellar generation will provide a clearer picture of stellar assembly in the first galaxies and hints to what next generation telescopes, such as the JWST, will observe.

Chapter 5

Formation of the First Low-Mass Stars from Cosmological Initial Conditions[1]

5.1 Introduction

Observations of low-metallicity stars in the stellar halo and satellites of the Milky Way have furnished an expanding window into how the Galaxy's primitive precursors formed and evolved in the ancient Universe. In a pursuit named "stellar archaeology," the chemical abundance patterns of metal-poor stars are used to expose the character of the supernovae that had enriched them and the physical state of their formation environment (e.g., Frebel et al. 2005, Karlsson et al. 2013). In particular, the metallicities and abundance patterns in the faintest and most metal-poor galaxies, the ultra-faint dwarf spheroidal satellites (UFDs), can potentially be used to probe the very first stellar generation forming from metal-free initial conditions and its immediate successors (Brown et al. 2012, Frebel & Bromm 2012, Vargas et al. 2013). Furthermore, there are hints that in the measured mass range, the stellar initial mass function (IMF) is shallower in UFDs than in more metal-rich and evolved galaxies (Geha et al. 2013), a potential challenge to star formation models and an important clue as to the origin of UFDs and of primitive, early stellar systems in general.

Capitalizing on the information provided by the fossils of the first galaxies requires a theoretical understanding of star formation under conditions distinct

---

[1] This chapter has been published as Safranek-Shrader, C., Milosavljevic, M., Bromm, V., 2014, MNRAS, 440, L76. M. Milosavljevic and V. Bromm supervised the project.

from those in the present Milky Way (e.g., Bromm 2013). Typical metallicities in UFDs are only $\sim 1\%$ of the solar value (e.g., Kirby et al. 2011). Current theory suggests that the first metal-enriched stellar generations formed in predominantly atomic gas clouds assembled by dark-matter-driven cosmic infall and thermal instability, and were subject to a temperature floor imposed by the cosmic microwave background (CMB) (e.g., Wise et al. 2012, Safranek-Shrader et al. 2014). In contrast, the bulk of present-day star formation, where recent numerical breakthroughs have focused (e.g., Bate 2012, Krumholz et al. 2012, Federrath & Klessen 2012), occurs in turbulent molecular clouds where the thermodynamics is dominated by dust and its coupling to the interstellar radiation field. Salient aspects of star formation in molecular clouds could apply to all systems with supersonic gas flow velocities, excluding star formation at extremely low or zero metallicities that operates in a distinct, Population III mode (e.g., Yoshida et al. 2006, Clark et al. 2011a, Greif et al. 2011, Dopcke et al. 2013). These aspects include the formation of low-mass stars through turbulent gravitational fragmentation and of more massive stars through the coherent collapse of self-gravitating cores as well as (possibly "competitive") accretion stabilized by local protostellar radiative heating (Bate et al. 2003, Mac Low & Klessen 2004, McKee & Ostriker 2007, Zinnecker & Yorke 2007).

Our goal is to investigate the formation of the first generation of metal-enriched stars from cosmological initial conditions so that we can begin charting out the UFD formation history, relating it to concepts normally used to describe star formation under distinct, molecular-cloud-like conditions. We present highly zoomed adaptive-mesh-refinement (AMR) hydrodynamical simulations extending those in Safranek-Shrader et al. (2014) to much higher resolution, resolving the density and length scales where protostellar masses are imprinted. Namely, gaseous collapse in the presence of dust is now tracked to the densities $\sim 10^{13}\,\mathrm{cm}^{-3}$ where gas becomes optically thick to its cooling radiation and further fragmentation is strongly suppressed. We use Lagrangian sink particles to follow protostellar accretion after the initial collapse.

Importantly, the simulations here are derived from a section of a coarser simulation initialized from a realization of the $\Lambda\mathrm{CDM}$ cosmological model, instead of beginning from an artificially generated turbulent velocity field and spherically symmetric gas configuration. Therefore the gas flow morphology in the simulations here is a self-consistent outcome of turbulent virialization in a dark matter halo, thermal instability, and gravitational collapse.

5.2 Methodology

The simulations were performed with the AMR hydrodynamics code FLASH (Fryxell et al. 2000), version 4. The initial conditions were extracted from the highest metallicity cosmological simulation of Safranek-Shrader et al. (2014). The original cosmological simulation was performed in a $1\,\mathrm{Mpc}$ comoving box with standard ΛCDM metal-free initial conditions and an externally imposed H_2-dissociating UV background that prevented star formation in halos that have not reached the atomic cooling limit. Upon identifying an atomic cooling halo at $z = 13.8$, we endowed gas within its virial radius with a nonzero, uniform metallicity of $10^{-2}\,Z_\odot$, crudely mimicking enrichment by preceding Population III stars. The cooling by metallic fine structure lines induced localized gaseous collapse in the halo. Sink particles (hereafter "sinks") were allowed to form at densities $> 10^6\,\mathrm{cm}^{-3}$ and had accretion radii $\sim 10^4\,\mathrm{AU}$. Since fragmentation at still higher densities is expected on physical grounds, the sinks in Safranek-Shrader et al. (2014) did not represent individual stars, but pre-stellar clumps poised to form small stellar associations or clusters (Bergin & Tafalla 2007).

To study the formation and evolution of *individual* stars, much higher resolution is required to attain conditions at which the gas becomes optically thick to all forms of cooling radiation and further fragmentation is thermodynamically suppressed (unresolved fragmentation may still be possible in rotationally-supported protostellar disks). At the metallicity considered here and in the presence of dust, this occurs at a density $\sim 10^{12}\,\mathrm{cm}^{-3}$. Since achieving the requisite dynamical range in a full cosmological simulation is computationally prohibitive, we opted for the "cut-out" strategy, similar to Greif et al. (2011). When the maximum density in the $10^{-2}\,Z_\odot$ run of Safranek-Shrader et al. (2014) reached $10^{7}\,\mathrm{cm}^{-3}$, we extracted a cubical section of size $0.52\,\mathrm{pc}$ containing a total gas mass of $390\,M_\odot$ centered on the densest cell. The cut-out region contains a single, slightly ellipsoidal pre-stellar clump undergoing supersonic compression along one direction. The compression was produced by a collaboration of gravitational and pressure forces in the aftermath of thermal instability at densities $\sim 10^{2}-10^{4}\,\mathrm{cm}^{-3}$ in the parent simulation.

Since the gravitational potential was strongly gas-dominated we neglected the dark matter. We proceeded to integrate the cut-out simulation with a Jeans length resolution of at least 24 grid cells and subject to reflective hydrodynamical boundary that represented an approximately pressure-confined environment. However, we were careful to run the simulation only for a time much shorter than the sound crossing time from the box center to the boundary ($\approx 0.4\,$Myr at temperature $T = 50\,\mathrm{K}$), rendering the nature of the boundary condition immaterial. The gravitational potential of the gas was obtained with the multigrid solver with isolated gravitational boundary conditions. The simulations did not include magnetic fields, though we plan to explore their significance in future work.

We inserted sinks when the density in a cell exceeded $n_{\mathrm{sink}} = 10^{13}\,\mathrm{cm}^{-3}$, the gas flow was converging $\nabla \cdot \mathbf{v} < 0$, the gravitational potential was a local minimum, and a small control volume around the cell was gravitationally bound. In

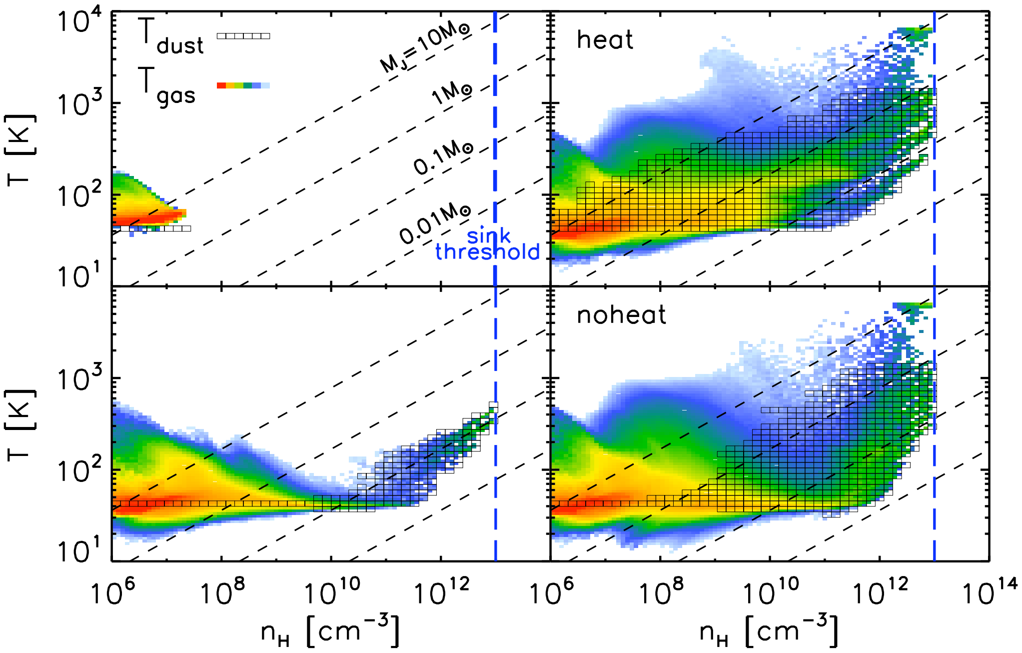

Figure 5.1 Density-temperature distribution of the gas (color from white to red scaling with gas mass) and dust (boxed points). Counterclockwise from top left, the panels show the beginning of the simulation, the onset of sink particle formation, and 7000 yr later in the simulations NOHEAT and HEAT. Dashed diagonals show lines of constant Jeans mass.

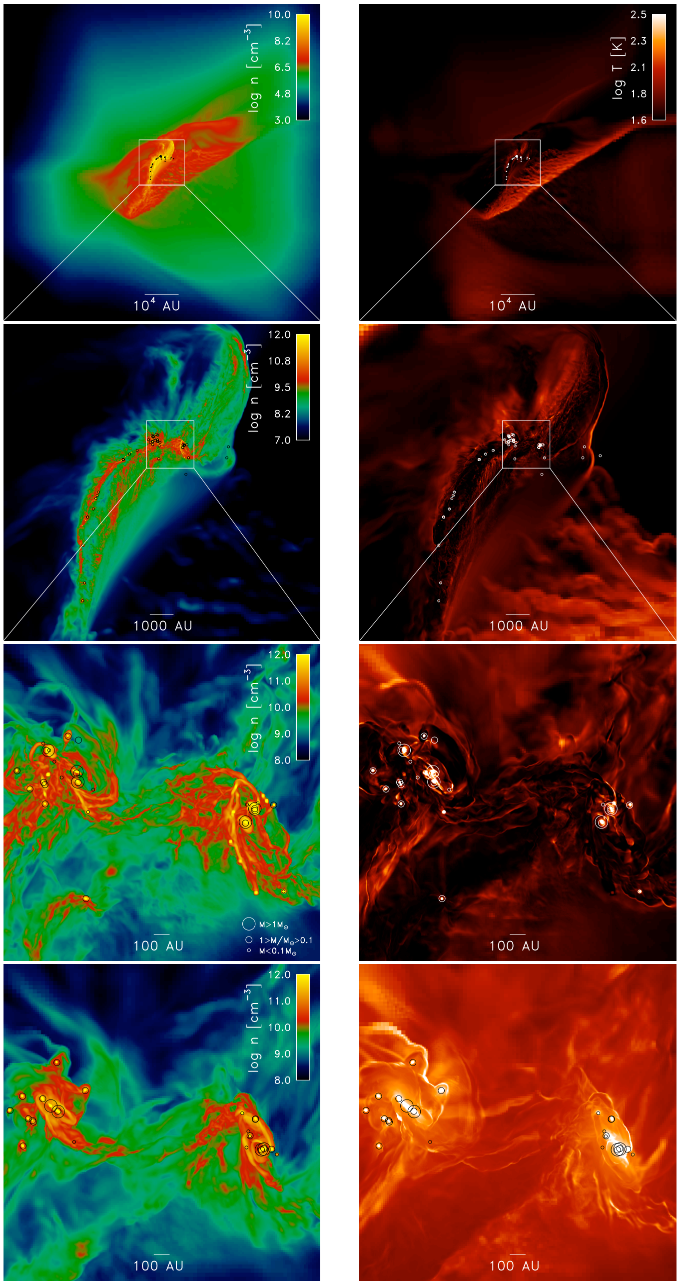

Figure 5.2 Mass-weighted line-of-sight projections of gas density (left column) and temperature (right column) at the end of NOHEAT (top three rows) and at the end of HEAT (bottom row). Circles denote sinks with the size increasing with sink mass. In the lower four panels, the smallest circles are sized with the sink accretion radius, $r_{\rm acc} = 10\,{\rm AU}$.

practice, sink formation is preceded by Jeans instability in this highly compressed gas. Cells within the sink's accretion radius $r_{\rm acc} = 10\,{\rm AU} = 2.5\,\Delta x_{\rm min}$ with hydrogen densities $n_{\rm H} > n_{\rm sink}$ transferred a fraction $(n_{\rm H} - n_{\rm sink})/n_{\rm H}$ of their mass to the sink if the gas was gravitationally bound to the sink and had a radial velocity directed towards it. Here, $\Delta x_{\rm min}$ is the cell size at the highest level of grid refinement. We did not allow sinks to merge with each other. Sink particle motions were sub-cycled with a leapfrog scheme (for further details, see Federrath et al. 2010a and Safranek-Shrader et al. 2014).

We utilized the thermodynamical model and non-equilibrium chemical network described in Safranek-Shrader et al. (2010, 2012, 2014), now augmented with the dust processes in Omukai et al. (2005). The dust temperature, $T_{\rm d}$, was determined by grain thermal balance in the presence of thermal emission, heating by the CMB and protostellar radiation, and thermal coupling to the gas:

$$\begin{aligned} 4\sigma_{\rm SB}(T_{\rm d}^4 - T_{\rm CMB}^4)\kappa_{\rm d}(T_{\rm d})\rho\beta_{\rm esc} = &\frac{2k_{\rm B}(T_{\rm g} - T_{\rm d})n_{\rm d}}{t_{\rm coll}} \\ &+ \sum_i \left(\frac{L_{{\rm acc},i}}{4\pi r_i^2}\right) \kappa_{\rm d}(T_{\rm d})\rho\beta_{\rm esc}, \end{aligned} \tag{5.1}$$

where ρ is the gas density, $n_{\rm d}$ is the number density of dust grains, $T_{\rm g}$ and $T_{\rm CMB}$ are the gas and CMB temperatures, and $k_{\rm B}$ and $\sigma_{\rm SB}$ are the Boltzmann and Stefan-Boltzmann constants. The collision time between gas and dust particles is $t_{\rm coll}^{-1} = n_{\rm H}\sigma_{\rm d}\bar{v}_{\rm H}f$ where $\sigma_{\rm d}$ is the average dust grain cross-section, $\bar{v}_{\rm H}$ is the average speed of hydrogen nuclei, and $f \approx 0.4$ accounts for non-hydrogenic species (Schneider et al. 2006). The Planck mean opacity of dust grains, $\kappa_{\rm d}(T)$, was taken from Semenov et al. (2003) and we assumed linear scaling with metallicity. Thermal dust emission, which is a source of gas cooling through collisional coupling, was attenuated by a factor $\beta_{\rm esc} = \min(1, \tau_{\rm cont}^{-2})$, appropriate for optically-thick radiative diffusion (e.g., Masunaga et al. 1998). The continuum optical depth is given by

$\tau_{\rm cont} = (\kappa_{\rm d} + \kappa_{\rm g})\rho L_{\rm J}$ where $L_{\rm J}$ is the Jeans Length, a local estimate for the physical extent of a gravitationally collapsing core, and $\kappa_{\rm g}$ is the metal-free gas Planck mean opacity (Mayer & Duschl 2005). To determine the metal fine-structure line cooling rates we iteratively calculated consistent line escape probabilities and level populations (e.g., Takahashi et al. 1983, Omukai 2000), using a local estimate of the Sobolev length, $L_{\rm sob} = c_{\rm s}/|\nabla \cdot \mathbf{v}|$, to approximate the size of the shielding region.

The summand in the last term of Equation 5.1 represents the heating by the radiation of the $i{\rm th}$ protostar located at distance r_i producing accretion luminosity $L_{{\rm acc},i} = GM_{*,i}\dot{M}_{*,i}/R_{*,i}$. By treating sinks as the sources of radiation, we took M_* to be the sink mass and $\dot{M}_*$ to be the sink accretion rate smoothed over a 10 yr (~ 30 hydrodynamical timesteps) period. This assumes that the luminosity is dominated by the accretion luminosity and that all mass accreted by a sink is immediately and permanently incorporated into the protostar. We calculated the radius of the protostellar photosphere R_* with an analytic fit from Stahler et al. (1986), valid independent of metallicity for $M_* \lesssim 3\,M_\odot$ (e.g., Hosokawa & Omukai 2009).

5.3 Results

We run a simulation HEAT that includes dust heating by protostellar radiation (via the last term in Eq. 5.1) and a reference simulation NOHEAT without heating. The thermodynamic evolution of gas and dust is shown in Figure 5.1. As the collapse proceeds, efficient fine-structure line cooling by [C II] and [O I] keeps the gas nearly isothermal at $T_{\rm CMB} \approx 40\,{\rm K}$ at densities $\lesssim 10^7\,{\rm cm}^{-3}$. Above this density, the lines become optically thick and the gas heats slightly, but cools back to $T_{\rm CMB}$ after reaching densities $\gtrsim 10^9\,{\rm cm}^{-3}$ where gas and dust collisionally couple. Isothermal collapse then continues until reaching densities $\sim 5 \times 10^{11}\,{\rm cm}^{-3}$. At these densities, marking the opacity limit for fragmentation, the continuum op-

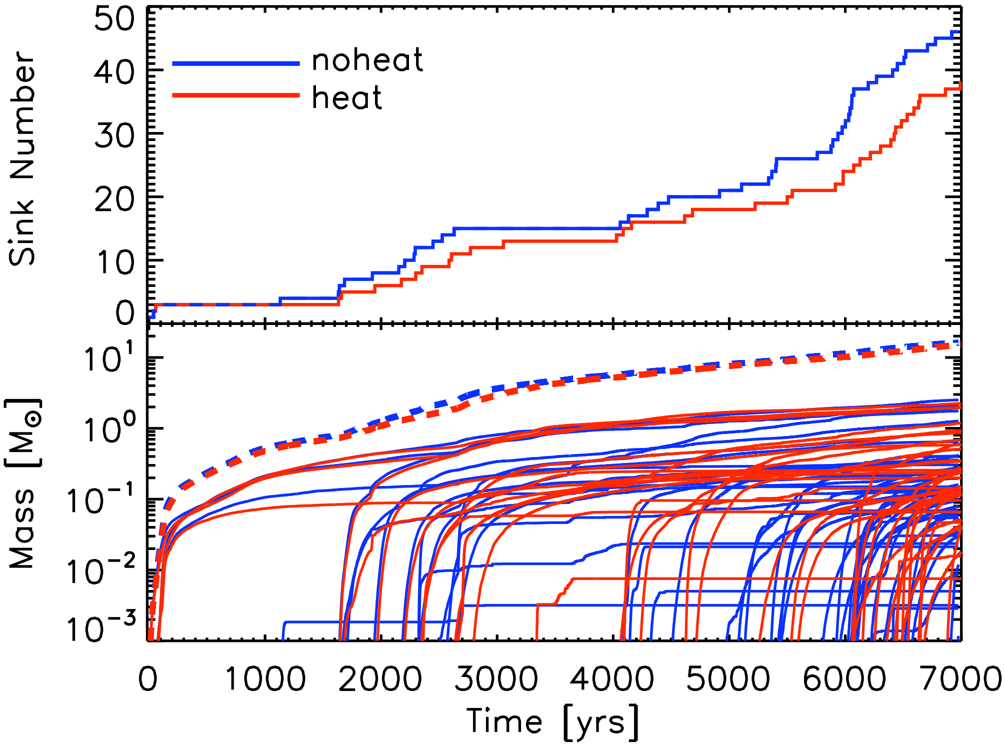

Figure 5.3 Number (upper panel) and masses (lower panel) of sink particles as a function of time since first sink formation in HEAT (red lines) and NOHEAT (blue lines). In the lower panel, solid and dashed lines show individual and total sink masses, respectively.

tical depth due to dust exceeds unity ($\beta_{\rm esc} \lesssim 1$, see Eq. 5.1), dust-cooling loses its efficacy, and the gas begins to evolve adiabatically. The effect of protostellar dust heating is minimal, mainly resulting in higher gas temperatures at densities $\gtrsim 10^8\,{\rm cm}^{-3}$ and a slight suppression of sink formation, consistent with the findings of Omukai et al. (2010).

When the gas reaches densities $\sim 10^{13}\,{\rm cm}^{-3}$ sink formation is possible based on the conditions described in Section 5.2. The first sink forms 4.3×10^4 yr after the beginning of the simulations and both are run for 7000 yr after this point. Figure 5.2 shows mass-weighted density and temperature projections at the end of both simulations. Sinks are forming over an extended $\sim 10^4$ AU-long filamentary structure, with thickness $\sim 1000\,{\rm AU}$ and density $\sim 10^8\,{\rm cm}^{-3}$. The structure is produced by a large-scale, supersonic colliding flow and is undergoing global gravitational collapse. We identify two sites of sink formation: in locally fragmenting filamentary structures, and in rotating, quasi-virialized disky flows produced by progressive global gravitational collapse of the filaments (as seen, respectively, in row 2 and rows 3 and 4 of Fig. 5.2).

Figure 5.3 shows the total number of sinks and their individual masses. In NOHEAT, 46 sinks formed with a total mass of $16\,M_\odot$. In HEAT, 37 sinks formed with a total mass of $15\,M_\odot$. The average sink mass in both simulations is $M_{*,{\rm tot}}/N_{\rm tot} \approx 0.3 - 0.4\,M_\odot$ and median mass is $\approx 0.13\,M_\odot$. Sink binaries form in both simulations and we observe that binary interactions eject a number of low-mass sinks ($< 0.08\,M_\odot$) from the star forming region with velocities $3-7\,{\rm km\,s^{-1}}$. Figure 5.4 shows the average sink accretion rate as a function of mass. Sinks that are not ejected accrete at an average individual accretion rate of $2 \times 10^{-4}\,M_\odot\,{\rm yr}^{-1} \approx {\rm few} \times c_{\rm s}^3/G$ while their mass is in the range $0.01\,M_\odot < M_* < 0.3\,M_\odot$. At higher masses, the accretion rate increases approximately as $\dot{M}_* \propto M_*^{2/3}$ as sinks accrete from within

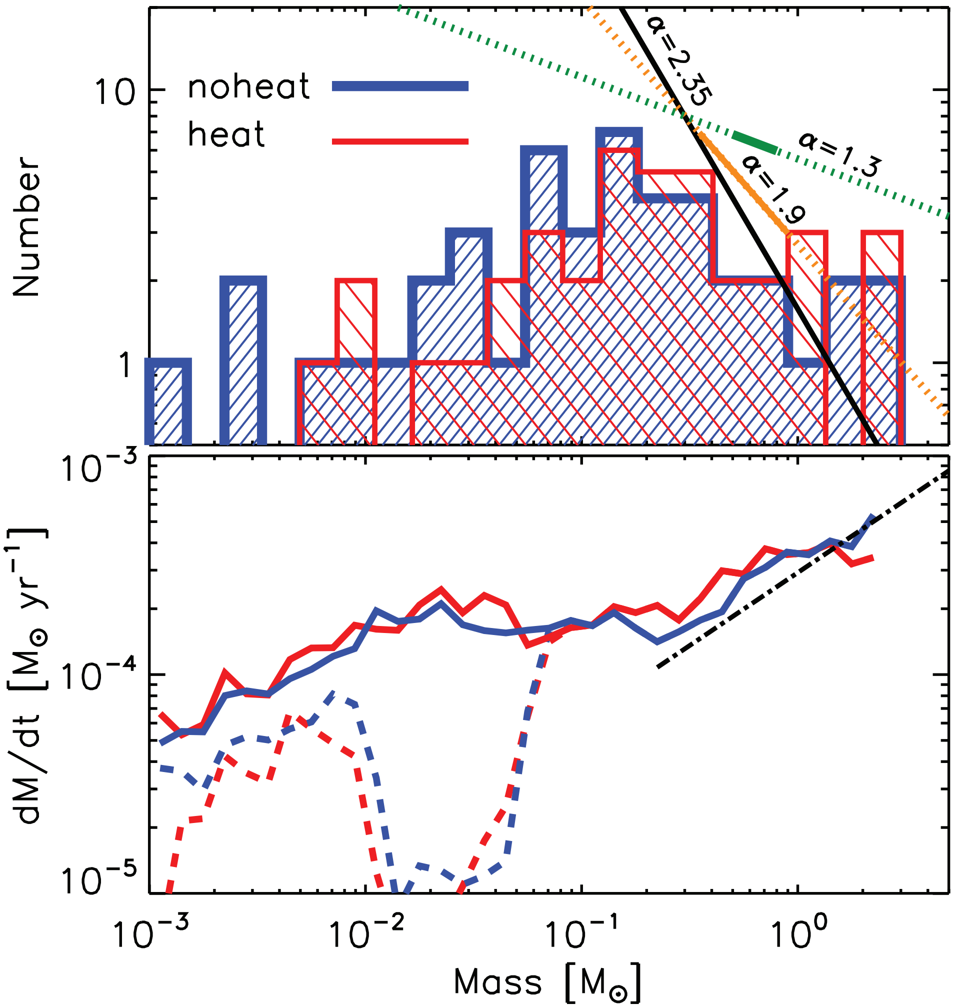

Figure 5.4 Upper panel: Sink particle mass function in HEAT (red line) and NOHEAT (blue line). Dashed lines show power-law IMF slopes $\alpha = 2.35$ (Salpeter), $\alpha = 1.9$ (in the Small Magellanic Cloud; Kalirai et al. 2013), and $\alpha = 1.3$ (the UFD Leo IV; Geha et al. 2013). The mass range over which the power-law slope was measured is indicated with a solid line. Lower panel: average sink accretion rate as a function of sink mass, including all sinks (dashed lines) and only accreting sinks (solid lines). The dot-dashed line shows the scaling $\dot{M}_\star \propto M_*^{2/3}$.

the extended gaseous disks in which they are embedded. This trend continues up to the highest sink mass in NOHEAT, but in HEAT the increase of accretion rate with mass levels above $M_* \sim 0.7\,M_\odot$.

Figure 5.4 also shows the sink mass function at the end of both simulations. Because sinks do not instantaneously accrete their initial gravitationally unstable Jeans mass $\gtrsim 0.01\,M_\odot$, the simulations contain some sinks with very low masses that cannot be interpreted as fully fledged proto- or sub-stellar objects. The mass spectrum $dN/d\ln M_*$ in both simulations exhibits a broad peak at $M_* \sim (0.05 - 0.4)\,M_\odot$. The most massive sinks $M_* \approx 2.5\,M_\odot$ are located close to the centers of the densest disky structures (Fig. 5.2), already indicating hints of primordial segregation in the proto-stellar cluster.

5.4 Discussion and Conclusions

Studies that investigate the control of gravitational fragmentation in collapsing gas clouds using one-zone models, (e.g., Omukai et al. 2005, 2010, Schneider et al. 2006) assume that the fragmentation mass scale is set by the interplay of monolithic gravitational collapse and thermodynamics, neglecting large-scale, multi-dimensional gas motions. They predict that at the metallicity we consider, the characteristic fragmentation mass should be $\sim 0.5\,M_\odot$ as a result of gas-dust coupling at high densities $\gtrsim 10^8\,\mathrm{cm}^{-3}$. Since the Jeans mass $M_\mathrm{J} \propto \rho^{-1/2}$ and the compression at Mach number $\mathcal{M}$ results in a factor of $\mathcal{M}^2$ density enhancement, the characteristic mass should be revised downward by a factor $\sim 1/\mathcal{M}$. With the Mach number of the inflow into the fragmenting structure in the simulations being $\mathcal{M} \sim 3$, this revises the prediction of the one-zone models for the characteristic fragmentation mass to $\sim 0.1\,M_\odot$, consistent with the peak of our sink mass function. Models for gravitational fragmentation that do account for the underlying supersonically turbulent gas flow normally assume fully developed, statistically-homogeneous turbulence, as in molecular clouds, but potentially inapplicable in the present context, and idealized thermodynamic evolution (e.g., Padoan & Nordlund 2002).

A more definitive theoretical point of reference are simulations that resolve fragmentation into individual stars, albeit in a variety of contexts widely different from ours (e.g., Milky Way disk, metal-free or ultra-low-metallicity minihalos, etc.). Clark et al. (2008) and Dopcke et al. (2013) studied the onset of sink formation in clouds initialized with imposed turbulent velocity fluctuations at very low metallicities ($\leq 10^{-4}\,Z_{\odot}$), and followed the evolution of the cluster for only up to few hundred years. They identified gas-dust thermal coupling as the trigger of the conclusive fragmentation episode in this regime. Bate (2012) and Krumholz et al. (2012) carried out longer-duration integrations, also in clouds with imposed turbulent density fluctuations, designed to model the formation of small star clusters at $Z = Z_{\odot}$, both including protostellar radiative feedback. They found that the peak and shape of the resulting IMF are delicate functions of protostellar feedback and of how turbulence is introduced (Krumholz et al. 2012).

An isolated sink will accrete its initial Jeans mass, but a sink interacting with other matter (e.g., being subject to a tidal field, becoming a member of a binary system, or being ejected via a ≥ 3 body interaction) may fail to attain the Jeans mass. The most massive sinks at the end of the simulations owe their status to sustained accretion, at a typical average rate of $\sim 4\times10^{-4}\,M_{\odot}\,\mathrm{yr}^{-1}$. The sites of this sustained accretion are the disky structures, mentioned in Section 5.3 and previously reported by Clark et al. (2008), in which shearing seems as important as turbulence. Various theoretical models for continued accretion after a core has accreted its initial Jeans mass typically predict a dependence of the mass accretion rate on the protostellar mass $\dot{M}_{*} \propto M_{*}^{\xi}$ (e.g., McKee & Tan 2003). Tentatively we find $\xi \approx 2/3$ at least in the range of stellar masses in which our two simulations agree. At higher masses $> 1\,M_\odot$ local protostellar heating in an increasingly crowded environment may be depressing Bondi-Hoyle accretion onto the most massive sinks. If the long-term accretion rate does remain at $\sim 2 \times 10^{-4}\,M_\odot\,\mathrm{yr}^{-1}$, the cluster will form a $\sim 20\,M_\odot$ star in $\sim 10^5\,\mathrm{yr}$ with the potential to produce an H II region that could truncate star formation.

The present simulation resolves small-scale fragmentation in only one of several (9 forming within $\sim 3\,\mathrm{Myr}$) pre-stellar clumps satisfying the conditions for gravitational collapse and star formation in the parent cosmological simulation. The other clumps would likely undergo a similar small scale evolution, implying that the total number of sinks, and thus stars, in a single episode of star formation could be an order of magnitude larger. Moreover, a single clump, like the one followed here for $7000\,\mathrm{yr}$ after initial sink formation, will continue infall on a dynamical time $\sim 3\times 10^4\,\mathrm{yr}$, roughly five times longer than integrated here, producing $\sim 5 \times 40 = 200$ stars in one pre-stellar clump, or ~ 2000 stars in the whole halo. This value is interestingly consistent with the stellar masses of the faintest UFDs, Boötes II, Segue I & II, and Willman I. The surrounding halo at the time of star formation contains $\approx 2 \times 10^5\,M_\odot$ of dark matter within a reference radius of $30\,\mathrm{pc}$, furthermore consistent with the stellar-kinematics-inferred dynamical masses of these UFDs (McConnachie 2012).

The coarse-grained sinks representing pre-stellar clumps in Safranek-Shrader et al. (2014) and the fine-grained ones representing individual stars in the present work occupy a highly compact spatial region ($\sim 1\,\mathrm{pc}$) in which the gravitational potential is strongly baryon-dominated, whereas the stars in UFDs occupy much more extended, dark-matter-dominated regions. Long term evolution will inevitably convert the compact baryon-dominated star cluster into a more diffuse, highly dark-matter-dominated one. We already observe ejections of low-mass sinks by dynamical interactions, similar to Bate (2012). Given the low total number of stars in the cluster ejections will undoubtedly continue, extending to stellar mass objects, as long as the cluster remains baryon-dominated. If the ejected stars do not escape the host dark matter halo they will predominantly reside at large, dark-matter-dominated galactocentric radii. Stellar mass loss will further increase the mass-to-light ratio.

The stellar IMF in two UFDs measured in the mass range $0.5\,M_\odot < M_* < 0.8\,M_\odot$ is shallower, $dN/dM_* \propto M_*^{-\alpha}$ with $\alpha = 1.3 - 1.4$ (Geha et al. 2013), than the IMF of the Milky Way ($\alpha = 2.3$; Kroupa 2001) and the Small Magellanic Cloud ($\alpha = 1.9$; Kalirai et al. 2013) in a similar mass range. While we emphasize that the stellar IMF in our simulations is still evolving at the end of each simulation, we do find that for $M_* > 0.1\,M_\odot$, a truncated Pareto distribution maximum likelihood estimate (Aban et al. 2006) yields $\alpha = 1.26 \pm 0.05$ (HEAT) and $\alpha = 1.41 \pm 0.09$ (NOHEAT), consistent with the Geha et al. (2013) values.

It should be kept in mind that at present it is not clear whether UFDs started forming low-mass stars before reionization, where they were subject only to a non-ionizing H_2-dissociating UV background, or if their first low-mass stars formed only in a patch of the Universe reionized by more massive neighboring halos. In the latter case, we expect a similar outcome in a more massive host halo, though possibly modified due to higher inflow velocities and larger clump accretion rates. Furthermore, an object already forming stars at $z \approx 14$ could have ended up being incorporated into the central part of the Milky Way, rather than remaining an orbiting satellite. One central issue to be resolved is which process terminated star formation in UFDs: internal feedback from star formation, photoevaporation by reionization, or ram pressure stripping during infall into a more massive Milky Way progenitor halo.

We will report on a more comprehensive set of simulations and test cases, including a detailed analysis of the role of turbulence, in forthcoming publications. We are entering a period of rapid discovery, where ever more realistic simulations and comprehensive stellar archaeological surveys promise a deeper understanding of our ancient cosmic origins.

Chapter 6

Outlook

In this dissertation we have presented a numerical study of star formation in the first galaxies. Above all else, it is clear that this process is rich with complexity — metallicity-dependent thermodynamics, self-gravity, and supersonically turbulent gas motions are all intricately coupled and play a significant role in regulating the conversion of gas into stars. Placing these processes in the broader context of early galaxy formation, as we have done, is significant: The first galaxies are fed by dark matter filament driven accretion flows that churn supersonic turbulence and funnel gas inwards, setting the stage for star formation.

We have explored two main scenarios. In the first, gas in an atomic cooling halo remained metal-free due to a molecular hydrogen photodissociating Lyman-Werner radiation field. Once molecular hydrogen began to self-shield from the radiation background does gas cooling, and thus star formation, become possible. This Population III formation path (Pop III.2) is an alternative to Population III star formation in a minihalo. While thermodynamically similar, the collapse in a more massive atomic cooling halo results in larger gas masses and increased infall rates, favorable conditions for the formation of a clusters of metal-free stars that have the potential to be detected directly in deep JWST surveys.

In the second scenario, the addition of heavy-elements to the star forming gas has a significant impact on the thermodynamics. Above metallicities of $Z \approx 10^{-4}\,Z_\odot$, fine-structure line cooling at moderate densities, $n \sim 10^{3-6}\,\mathrm{cm}^{-3}$, induces parsec-scale fragmentation. Within a typical first-galaxy system, we show this likely results in a stellar cluster of mass $\sim 1000\,M_\odot$ forming within $\sim 4\,$Myr. At higher densities, $n \gtrsim 10^8\,\mathrm{cm}^{-3}$, dust grains become the main regulator of thermodynamics, couple the gas to the CMB temperature floor, and allow the formation of solar mass fragments.

Numerically, there is still much to be done. Simulations that begin from *ab initio* first principles are currently bound by computational speed. State-of-the-art cosmological simulations including dark matter, baryons, and stellar feedback processes are resolution limited to $\sim$ parsec scales. Star formation, radiative feedback, supernovae, and other essential physical processes are handled through sub-grid prescriptions that require numerous finely-tuned free parameters. In Chapter 5 we have shown that forming individual stars within a cosmological simulation is within reach, though limits the simulation run time to a few $\times 10^4$ years. Additionally, the resultant stellar cluster is only $\sim 50\,M_\odot$, many of orders-of-magnitude below what could be detected at $z \sim 10$, even with next-generation observatories.

Next generation simulations that will drive this field forward will need to probe sub-parsec scales to reduce the reliance on phenomenological sub-grid prescriptions while concurrently forming systems with stellar masses $\gtrsim 10^6\,M_\odot$. Significantly, this should allow convergence and meaningful comparison between simulations and next-generation observations that are predicted to directly probe similarly luminous systems at $z \sim 10$. Additionally, the ongoing discovery of metal-poor stars in the Galactic halo and local dwarf galaxies, objects believed to be ‘fossils’ from the first galaxies, will benefit from numerical advancements. As one example, future simulations that accurately track the lifecycle of heavy elements made in Population III stars, from supernovae to fallback to second-generation Population II star formation, can be directly compared to the observed chemical abundance patterns in metal-poor stellar populations, such as the recently discovered ultra-faint dwarf satellite galaxies.

The era of the first stars and galaxies is at the frontier of astrophysics and it is the close interplay of theory and observations that will drive this field forward. Next-generation space- and ground-based infrared telescopes are designed in large part to observe the high-redshift Universe. A slew of complementary observational probes, such as high-redshift supernovae, the chemical fingerprints of local metal-poor stars and dwarf galaxies, as well as the redshifted 21 cm line of neutral hydrogen, necessitate increasingly detailed numerical experiments. The preceding chapters in this dissertation represent a small step towards a comprehensive understanding of this uncharted phase in early cosmic history.

Bibliography

Aban, I. B., Meerschaert, M. M., & Panorska, A. K. 2006, J. Am. Stat. Assoc., 101, 270

Abel, T., Anninos, P., Zhang, Y., & Norman, M. L. 1997, New Astronomy, 2, 181

Abel, T., Bryan, G. L., & Norman, M. L. 2000, ApJ, 540, 39

—. 2002, Science, 295, 93

Ahn, K. & Shapiro, P. R. 2007, MNRAS, 375, 881

Ahn, K., Shapiro, P. R., Iliev, I. T., Mellema, G., & Pen, U.-L. 2009, ApJ, 695, 1430

André, P., Men'shchikov, A., Bontemps, S., Könyves, V., Motte, F., Schneider, N., Didelon, P., Minier, V., Saraceno, P., Ward-Thompson, D., di Francesco, J., White, G., Molinari, S., Testi, L., Abergel, A., Griffin, M., Henning, T., Royer, P., Merín, B., Vavrek, R., Attard, M., Arzoumanian, D., Wilson, C. D., Ade, P., Aussel, H., Baluteau, J.-P., Benedettini, M., Bernard, J.-P., Blommaert, J. A. D. L., Cambrésy, L., Cox, P., di Giorgio, A., Hargrave, P., Hennemann, M., Huang, M., Kirk, J., Krause, O., Launhardt, R., Leeks, S., Le Pennec, J., Li, J. Z., Martin, P. G., Maury, A., Olofsson, G., Omont, A., Peretto, N., Pezzuto, S., Prusti, T., Roussel, H., Russeil, D., Sauvage, M., Sibthorpe, B., Sicilia-Aguilar, A., Spinoglio, L., Waelkens, C., Woodcraft, A., & Zavagno, A. 2010, A&A, 518, L102

Aykutalp, A. & Spaans, M. 2011, ApJ, 737, 63

Bailin, J., Stinson, G., Couchman, H., Harris, W. E., Wadsley, J., & Shen, S. 2010a, ApJ, 715, 194

—. 2010b, ApJ, 715, 194

Balbus, S. A. 1986, ApJ, 303, L79

Baldry, I. K., Glazebrook, K., Brinkmann, J., Ivezić, Ž., Lupton, R. H., Nichol, R. C., & Szalay, A. S. 2004, ApJ, 600, 681

Barkana, R. & Loeb, A. 1999, ApJ, 523, 54

—. 2001, Phys. Rep., 349, 125

Basu, S. 1997, ApJ, 485, 240

Bate, M. R. 2009, MNRAS, 392, 590

—. 2012, MNRAS, 419, 3115

Bate, M. R., Bonnell, I. A., & Bromm, V. 2003, MNRAS, 339, 577

Bate, M. R., Bonnell, I. A., & Price, N. M. 1995, MNRAS, 277, 362

Bate, M. R., Lodato, G., & Pringle, J. E. 2010, MNRAS, 401, 1505

Beers, T. C. & Christlieb, N. 2005, ARA&A, 43, 531

Begelman, M. C., Volonteri, M., & Rees, M. J. 2006, MNRAS, 370, 289

Bell, K. L., Berrington, K. A., & Thomas, M. R. J. 1998, MNRAS, 293, L83

Belokurov, V., Zucker, D. B., Evans, N. W., Kleyna, J. T., Koposov, S., Hodgkin, S. T., Irwin, M. J., Gilmore, G., Wilkinson, M. I., Fellhauer, M., Bramich, D. M., Hewett, P. C., Vidrih, S., De Jong, J. T. A., Smith, J. A., Rix, H.-W., Bell, E. F., Wyse, R. F. G., Newberg, H. J., Mayeur, P. A., Yanny, B., Rockosi, C. M., Gnedin, O. Y., Schneider, D. P., Beers, T. C., Barentine, J. C., Brewington, H., Brinkmann, J., Harvanek, M., Kleinman, S. J., Krzesinski, J., Long, D., Nitta, A., & Snedden, S. A. 2007, ApJ, 654, 897

Bergin, E. A. & Tafalla, M. 2007, ARA&A, 45, 339

Bertschinger, E. 2001, ApJS, 137, 1

Beuther, H. & Schilke, P. 2004, Sci, 303, 1167

Binney, J. 2004, MNRAS, 347, 1093

Birnboim, Y. & Dekel, A. 2003, MNRAS, 345, 349

Bland-Hawthorn, J., Karlsson, T., Sharma, S., Krumholz, M., & Silk, J. 2010, ApJ, 721, 582

Bonazzola, S., Heyvaerts, J., Falgarone, E., Perault, M., & Puget, J. L. 1987, A&A, 172, 293

Bonnell, I. & Bastien, P. 1993, ApJ, 406, 614

Bonnell, I. A., Bate, M. R., Clarke, C. J., & Pringle, J. E. 2001, MNRAS, 323, 785

Bonnor, W. B. 1956, MNRAS, 116, 351

Bouwens, R. J., Illingworth, G. D., Oesch, P. A., Labbé, I., Trenti, M., van Dokkum, P., Franx, M., Stiavelli, M., Carollo, C. M., Magee, D., & Gonzalez, V. 2011, ApJ, 737, 90

Bromm, V. 2013, Reports on Progress in Physics, 76, 112901

Bromm, V. & Clarke, C. J. 2002, ApJ, 566, L1

Bromm, V., Coppi, P. S., & Larson, R. B. 2002, ApJ, 564, 23

Bromm, V., Ferrara, A., Coppi, P. S., & Larson, R. B. 2001, MNRAS, 328, 969

Bromm, V. & Larson, R. B. 2004, ARA&A, 42, 79

Bromm, V. & Loeb, A. 2003a, ApJ, 596, 34

—. 2003b, Nature, 425, 812

Bromm, V. & Yoshida, N. 2011, ARA&A, 49, 373

Bromm, V., Yoshida, N., & Hernquist, L. 2003, ApJ, 596, L135

Bromm, V., Yoshida, N., Hernquist, L., & McKee, C. F. 2009, Nature, 459, 49

Brown, T. M., Tumlinson, J., Geha, M., Kirby, E. N., VandenBerg, D. A., Muñoz, R. R., Kalirai, J. S., Simon, J. D., Avila, R. J., Guhathakurta, P., Renzini, A., & Ferguson, H. C. 2012, ApJ, 753, L21

Burton, M. G., Hollenbach, D. J., & Tielens, A. G. G. M. 1990, ApJ, 365, 620

Caffau, E., Bonifacio, P., François, P., Sbordone, L., Monaco, L., Spite, M., Spite, F., Ludwig, H.-G., Cayrel, R., Zaggia, S., Hammer, F., Randich, S., Molaro, P., & Hill, V. 2011, Nature, 477, 67

Cazaux, S. & Spaans, M. 2004, ApJ, 611, 40

—. 2009, A&A, 496, 365

Cazaux, S. & Tielens, A. G. G. M. 2002, ApJ, 575, L29

Cen, R. 1992, ApJS, 78, 341

Chabrier, G. 2003, PASP, 115, 763

Chandrasekhar, S. 1951, Royal Society of London Proceedings Series A, 210, 26

Chatzopoulos, E. & Wheeler, J. C. 2012, ApJ, 748, 42

Cherchneff, I. & Dwek, E. 2010, ApJ, 713, 1

Cho, W. & Kim, J. 2011, MNRAS, 410, L8

Ciardi, B. & Ferrara, A. 2005, Space Sci. Rev., 116, 625

Ciardi, B., Ferrara, A., & Abel, T. 2000, ApJ, 533, 594

Clark, P. C., Glover, S. C. O., & Klessen, R. S. 2008, ApJ, 672, 757

Clark, P. C., Glover, S. C. O., Klessen, R. S., & Bromm, V. 2011a, ApJ, 727, 110

Clark, P. C., Glover, S. C. O., Smith, R. J., Greif, T. H., Klessen, R. S., & Bromm, V. 2011b, Sci, 331, 1040

Clarke, C. J. & Bromm, V. 2003, MNRAS, 343, 1224

Colella, P. & Woodward, P. R. 1984, Journal of Computational Physics, 54, 174

Collins, D. C., Padoan, P., Norman, M. L., & Xu, H. 2011, ApJ, 731, 59

Couchman, H. M. P. & Rees, M. J. 1986, MNRAS, 221, 53

Cunningham, A. J., Klein, R. I., Krumholz, M. R., & McKee, C. F. 2011, ApJ, 740, 107

de Avillez, M. A. & Mac Low, M.-M. 2002, ApJ, 581, 1047

Dekel, A. & Birnboim, Y. 2006, MNRAS, 368, 2

Dekel, A., Birnboim, Y., Engel, G., Freundlich, J., Goerdt, T., Mumcuoglu, M., Neistein, E., Pichon, C., Teyssier, R., & Zinger, E. 2009, Nature, 457, 451

Dijkstra, M., Haiman, Z., Mesinger, A., & Wyithe, J. S. B. 2008, MNRAS, 391, 1961

Dopcke, G., Glover, S. C. O., Clark, P. C., & Klessen, R. S. 2011, ApJ, 729, L3

—. 2013, ApJ, 766, 103

Draine, B. T. & Bertoldi, F. 1996, ApJ, 468, 269

Dubey, A., Daley, C., ZuHone, J., Ricker, P. M., Weide, K., & Graziani, C. 2012, ApJS, 201, 27

Dubey, A., Reid, L. B., Weide, K., Antypas, K., Ganapathy, M. K., Riley, K., Sheeler, D., & Siegal, A. 2009, ArXiv e-prints

Dunlop, J. S. 2013, in Astrophysics and Space Science Library, Vol. 396, Astrophysics and Space Science Library, ed. T. Wiklind, B. Mobasher, & V. Bromm, 223

Dwek, E. & Cherchneff, I. 2011, ApJ, 727, 63

Ebert, R. 1955, ZAp, 37, 217

Eisenstein, D. J. & Hut, P. 1998, ApJ, 498, 137

Elmegreen, B. G. 1993, ApJ, 419, L29

Elmegreen, B. G. & Scalo, J. 2004, ARA&A, 42, 211

Evans, II, N. J., Dunham, M. M., Jørgensen, J. K., Enoch, M. L., Merín, B., van Dishoeck, E. F., Alcalá, J. M., Myers, P. C., Stapelfeldt, K. R., Huard, T. L., Allen, L. E., Harvey, P. M., van Kempen, T., Blake, G. A., Koerner, D. W., Mundy, L. G., Padgett, D. L., & Sargent, A. I. 2009, ApJS, 181, 321

Federrath, C., Banerjee, R., Clark, P. C., & Klessen, R. S. 2010a, ApJ, 713, 269

Federrath, C., Glover, S. C. O., Klessen, R. S., & Schmidt, W. 2008a, Physica Scripta Volume T, 132, 014025

Federrath, C. & Klessen, R. S. 2012, ApJ, 761, 156

—. 2013, ApJ, 763, 51

Federrath, C., Klessen, R. S., & Schmidt, W. 2008b, ApJ, 688, L79

Federrath, C., Roman-Duval, J., Klessen, R. S., Schmidt, W., & Mac Low, M.-M. 2010b, A&A, 512, A81

Federrath, C., Sur, S., Schleicher, D. R. G., Banerjee, R., & Klessen, R. S. 2011, ApJ, 731, 62

Ferrara, A. 1998, ApJ, 499, L17

Field, G. B. 1965, ApJ, 142, 531

Finkelstein, S. L., Papovich, C., Ryan, R. E., Pawlik, A. H., Dickinson, M., Ferguson, H. C., Finlator, K., Koekemoer, A. M., Giavalisco, M., Cooray, A., Dunlop, J. S., Faber, S. M., Grogin, N. A., Kocevski, D. D., & Newman, J. A. 2012, ApJ, 758, 93

Flower, D. R., Le Bourlot, J., Pineau des Forêts, G., & Roueff, E. 2000, MNRAS, 314, 753

Frebel, A. 2010, Astronomische Nachrichten, 331, 474

Frebel, A., Aoki, W., Christlieb, N., Ando, H., Asplund, M., Barklem, P. S., Beers, T. C., Eriksson, K., Fechner, C., Fujimoto, M. Y., Honda, S., Kajino, T., Minezaki, T., Nomoto, K., Norris, J. E., Ryan, S. G., Takada-Hidai, M., Tsangarides, S., & Yoshii, Y. 2005, Nature, 434, 871

Frebel, A. & Bromm, V. 2012, ApJ, 759, 115

Frebel, A., Johnson, J. L., & Bromm, V. 2007, MNRAS, 380, L40

—. 2009, MNRAS, 392, L50

Frisch, U. 1995, Turbulence. The legacy of A. N. Kolmogorov.

Fryxell, B., Olson, K., Ricker, P., Timmes, F. X., Zingale, M., Lamb, D. Q., MacNeice, P., Rosner, R., Truran, J. W., & Tufo, H. 2000, ApJS, 131, 273

Fumagalli, M., O'Meara, J. M., & Prochaska, J. X. 2011, Science, 334, 1245

Furlanetto, S. R. & Loeb, A. 2005, ApJ, 634, 1

Galli, D. & Palla, F. 1998, A&A, 335, 403

—. 2002, Planet. Space Sci., 50, 1197

Gammie, C. F. 2001, ApJ, 553, 174

Gardner, J. P., Mather, J. C., Clampin, M., Doyon, R., Greenhouse, M. A., Hammel, H. B., Hutchings, J. B., Jakobsen, P., Lilly, S. J., Long, K. S., Lunine, J. I., McCaughrean, M. J., Mountain, M., Nella, J., Rieke, G. H., Rieke, M. J., Rix, H.-W., Smith, E. P., Sonneborn, G., Stiavelli, M., Stockman, H. S., Windhorst, R. A., & Wright, G. S. 2006, Space Sci. Rev., 123, 485

Gazol, A. & Kim, J. 2010, ApJ, 723, 482

Geha, M., Brown, T. M., Tumlinson, J., Kalirai, J. S., Simon, J. D., Kirby, E. N., VandenBerg, D. A., Muñoz, R. R., Avila, R. J., Guhathakurta, P., & Ferguson, H. C. 2013, ApJ, 771, 29

Genzel, R., Tacconi, L. J., Eisenhauer, F., Förster Schreiber, N. M., Cimatti, A., Daddi, E., Bouché, N., Davies, R., Lehnert, M. D., Lutz, D., Nesvadba, N., Verma, A., Abuter, R., Shapiro, K., Sternberg, A., Renzini, A., Kong, X., Arimoto, N., & Mignoli, M. 2006, Nature, 442, 786

Girichidis, P., Federrath, C., Banerjee, R., & Klessen, R. S. 2011, MNRAS, 413, 2741

Glover, S. C. O. 2011, in IAU Symposium, Vol. 280, IAU Symposium, ed. J. Cernicharo & R. Bachiller, 313–324

Glover, S. C. O. & Abel, T. 2008, MNRAS, 388, 1627

Glover, S. C. O. & Brand, P. W. J. L. 2001, MNRAS, 321, 385

Glover, S. C. O. & Clark, P. C. 2013, ArXiv e-prints

Glover, S. C. O., Federrath, C., Mac Low, M.-M., & Klessen, R. S. 2010, MNRAS, 404, 2

Glover, S. C. O. & Jappsen, A.-K. 2007, ApJ, 666, 1

Gnat, O. & Sternberg, A. 2007, ApJS, 168, 213

Goldreich, P. & Lynden-Bell, D. 1965, MNRAS, 130, 97

Greif, T. H. & Bromm, V. 2006, MNRAS, 373, 128

Greif, T. H., Bromm, V., Clark, P. C., Glover, S. C. O., Smith, R. J., Klessen, R. S., Yoshida, N., & Springel, V. 2012, MNRAS, 424, 399

Greif, T. H., Glover, S. C. O., Bromm, V., & Klessen, R. S. 2010, ApJ, 716, 510

Greif, T. H., Johnson, J. L., Klessen, R. S., & Bromm, V. 2008, MNRAS, 387, 1021

—. 2009, MNRAS, 399, 639

Greif, T. H., Springel, V., White, S. D. M., Glover, S. C. O., Clark, P. C., Smith, R. J., Klessen, R. S., & Bromm, V. 2011, ApJ, 737, 75

Grevesse, N. & Sauval, A. J. 1998, Space Sci. Rev., 85, 161

Haiman, Z., Abel, T., & Rees, M. J. 2000, ApJ, 534, 11

Haiman, Z. & Bryan, G. L. 2006, ApJ, 650, 7

Haiman, Z., Rees, M. J., & Loeb, A. 1997, ApJ, 476, 458

Haiman, Z., Thoul, A. A., & Loeb, A. 1996, ApJ, 464, 523

Harford, A. G., Hamilton, A. J. S., & Gnedin, N. Y. 2008, MNRAS, 389, 880

Hartmann, L., Ballesteros-Paredes, J., & Bergin, E. A. 2001, ApJ, 562, 852

Heger, A., Fryer, C. L., Woosley, S. E., Langer, N., & Hartmann, D. H. 2003, ApJ, 591, 288

Heger, A. & Woosley, S. E. 2002, ApJ, 567, 532

Heitsch, F., Burkert, A., Hartmann, L. W., Slyz, A. D., & Devriendt, J. E. G. 2005, ApJ, 633, L113

Heitsch, F., Hartmann, L. W., Slyz, A. D., Devriendt, J. E. G., & Burkert, A. 2008, ApJ, 674, 316

Heitsch, F., Mac Low, M.-M., & Klessen, R. S. 2001, ApJ, 547, 280

Hennebelle, P., Audit, E., & Miville-Deschênes, M.-A. 2007, A&A, 465, 445

Hennebelle, P. & Chabrier, G. 2008, ApJ, 684, 395

Hennebelle, P. & Pérault, M. 1999, A&A, 351, 309

Hollenbach, D. & McKee, C. F. 1989, ApJ, 342, 306

Holzbauer, L. N. & Furlanetto, S. R. 2012, MNRAS, 419, 718

Hosokawa, T. & Omukai, K. 2009, ApJ, 691, 823

Hosokawa, T., Omukai, K., Yoshida, N., & Yorke, H. W. 2011, Sci, 334, 1250

Hubber, D. A., Walch, S., & Whitworth, A. P. 2013, MNRAS, 430, 3261

Hummel, J. A., Pawlik, A. H., Milosavljević, M., & Bromm, V. 2012, ApJ, 755, 72

Hunter, C. 1977, ApJ, 218, 834

Inoue, A. K. 2011, MNRAS, 415, 2920

Iwamoto, N., Umeda, H., Tominaga, N., Nomoto, K., & Maeda, K. 2005, Science, 309, 451

Jappsen, A.-K., Glover, S. C. O., Klessen, R. S., & Mac Low, M.-M. 2007, ApJ, 660, 1332

Jappsen, A.-K., Klessen, R. S., Glover, S. C. O., & Mac Low, M.-M. 2009a, ApJ, 696, 1065

Jappsen, A.-K., Klessen, R. S., Larson, R. B., Li, Y., & Mac Low, M.-M. 2005, A&A, 435, 611

Jappsen, A.-K., Mac Low, M.-M., Glover, S. C. O., Klessen, R. S., & Kitsionas, S. 2009b, ApJ, 694, 1161

Jasche, J., Ciardi, B., & Enßlin, T. A. 2007, MNRAS, 380, 417

Joggerst, C. C., Woosley, S. E., & Heger, A. 2009, ApJ, 693, 1780

Johnson, C. T., Burke, P. G., & Kingston, A. E. 1987, Journal of Physics B Atomic Molecular Physics, 20, 2553

Johnson, J. L. 2013, in Astrophysics and Space Science Library, Vol. 396, Astrophysics and Space Science Library, ed. T. Wiklind, B. Mobasher, & V. Bromm, 177

Johnson, J. L. & Bromm, V. 2006, MNRAS, 366, 247

Johnson, J. L., Greif, T. H., & Bromm, V. 2008, MNRAS, 388, 26

Kainulainen, J., Beuther, H., Henning, T., & Plume, R. 2009, A&A, 508, L35

Kalirai, J. S., Anderson, J., Dotter, A., Richer, H. B., Fahlman, G. G., Hansen, B. M. S., Hurley, J., Reid, I. N., Rich, R. M., & Shara, M. M. 2013, ApJ, 763, 110

Karlsson, T., Bromm, V., & Bland-Hawthorn, J. 2013, Rev. Mod. Phys., 85, 809

Kennicutt, R. C. & Evans, N. J. 2012, ARA&A, 50, 531

Kereš, D., Katz, N., Weinberg, D. H., & Davé, R. 2005, MNRAS, 363, 2

Kirby, E. N., Lanfranchi, G. A., Simon, J. D., Cohen, J. G., & Guhathakurta, P. 2011, ApJ, 727, 78

Kitayama, T. & Yoshida, N. 2005, ApJ, 630, 675

Klessen, R. S. 2001a, ApJ, 556, 837

—. 2001b, ApJ, 550, L77

Klessen, R. S. & Burkert, A. 2000, ApJS, 128, 287

Klessen, R. S., Glover, S. C. O., & Clark, P. C. 2012, MNRAS, 421, 3217

Klessen, R. S., Heitsch, F., & Mac Low, M.-M. 2000, ApJ, 535, 887

Klessen, R. S. & Hennebelle, P. 2010, A&A, 520, A17

Kolmogorov, A. 1941, Akademiia Nauk SSSR Doklady, 30, 301

Komatsu, E., Dunkley, J., Nolta, M. R., Bennett, C. L., Gold, B., Hinshaw, G., Jarosik, N., Larson, D., Limon, M., Page, L., Spergel, D. N., Halpern, M., Hill, R. S., Kogut, A., Meyer, S. S., Tucker, G. S., Weiland, J. L., Wollack, E., & Wright, E. L. 2009, ApJS, 180, 330

Komatsu, E., Smith, K. M., Dunkley, J., Bennett, C. L., Gold, B., Hinshaw, G., Jarosik, N., Larson, D., Nolta, M. R., Page, L., Spergel, D. N., Halpern, M., Hill, R. S., Kogut, A., Limon, M., Meyer, S. S., Odegard, N., Tucker, G. S., Weiland, J. L., Wollack, E., & Wright, E. L. 2011, ApJS, 192, 18

Kormendy, J. 1985, ApJ, 295, 73

Koyama, H. & Inutsuka, S.-I. 2000, ApJ, 532, 980

Kratter, K. M. & Murray-Clay, R. A. 2011, ApJ, 740, 1

Kritsuk, A. G. & Norman, M. L. 2002, ApJ, 569, L127

Kritsuk, A. G., Norman, M. L., Padoan, P., & Wagner, R. 2007, ApJ, 665, 416

Kritsuk, A. G., Norman, M. L., & Wagner, R. 2011, ApJ, 727, L20

Kroupa, P. 2001, MNRAS, 322, 231

—. 2002, Sci, 295, 82

Krumholz, M. R., Klein, R. I., & McKee, C. F. 2007, ApJ, 656, 959

—. 2012, ApJ, 754, 71

Krumholz, M. R. & McKee, C. F. 2005, ApJ, 630, 250

Krumholz, M. R., McKee, C. F., & Klein, R. I. 2004, ApJ, 611, 399

Krumholz, M. R., McKee, C. F., & Tumlinson, J. 2008, ApJ, 689, 865

Kuhlen, M. & Faucher-Giguère, C.-A. 2012, MNRAS, 423, 862

Lada, C. J. & Lada, E. A. 2003, ARA&A, 41, 57

Larson, R. B. 1985, MNRAS, 214, 379

—. 1998, MNRAS, 301, 569

—. 2003, Rep. Prog. Phys., 66, 1651

—. 2005, MNRAS, 359, 211

Latif, M. A., Schleicher, D. R. G., Schmidt, W., & Niemeyer, J. 2013, MNRAS, 432, 668

Latif, M. A., Schleicher, D. R. G., & Spaans, M. 2012, A&A, 540, A101

Latif, M. A., Schleicher, D. R. G., Spaans, M., & Zaroubi, S. 2011a, A&A, 532, A66

Latif, M. A., Zaroubi, S., & Spaans, M. 2011b, MNRAS, 411, 1659

Li, Y., Klessen, R. S., & Mac Low, M.-M. 2003, ApJ, 592, 975

Li, Z.-Y. & Nakamura, F. 2006, ApJ, 640, L187

Low, C. & Lynden-Bell, D. 1976, MNRAS, 176, 367

Mac Low, M.-M. & Klessen, R. S. 2004, Rev. Mod. Phys., 76, 125

MacDonald, J., Lawlor, T. M., Anilmis, N., & Rufo, N. F. 2013, MNRAS, 431, 1425

Machacek, M. E., Bryan, G. L., & Abel, T. 2001, ApJ, 548, 509

Machida, M. N., Omukai, K., Matsumoto, T., & Inutsuka, S.-i. 2008, ApJ, 677, 813

Madau, P., Ferrara, A., & Rees, M. J. 2001, ApJ, 555, 92

Maio, U., Ciardi, B., Dolag, K., Tornatore, L., & Khochfar, S. 2010, MNRAS, 407, 1003

Maio, U., Dolag, K., Ciardi, B., & Tornatore, L. 2007, MNRAS, 379, 963

Masunaga, H., Miyama, S. M., & Inutsuka, S.-I. 1998, ApJ, 495, 346

Mateo, M. L. 1998, ARA&A, 36, 435

Matzner, C. D. 2007, ApJ, 659, 1394

Mayer, M. & Duschl, W. J. 2005, MNRAS, 358, 614

McConnachie, A. W. 2012, AJ, 144, 4

McGreer, I. D. & Bryan, G. L. 2008, ApJ, 685, 8

McKee, C. F. & Ostriker, E. C. 2007, ARA&A, 45, 565

McKee, C. F. & Tan, J. C. 2002, Nature, 416, 59

—. 2003, ApJ, 585, 850

—. 2008, ApJ, 681, 771

Mesinger, A., Bryan, G. L., & Haiman, Z. 2006, ApJ, 648, 835

Miralda-Escudé, J. 2003, Science, 300, 1904

Miralda-Escude, J. & Rees, M. J. 1998, ApJ, 497, 21

Molina, F. Z., Glover, S. C. O., Federrath, C., & Klessen, R. S. 2012, MNRAS, 423, 2680

Motoyama, K. & Yoshida, T. 2003, MNRAS, 344, 461

Motte, F., Andre, P., & Neri, R. 1998, A&A, 336, 150

Myers, A. T., Krumholz, M. R., Klein, R. I., & McKee, C. F. 2011, ApJ, 735, 49

Nakamura, F. & Umemura, M. 2001, ApJ, 548, 19

—. 2002, ApJ, 569, 549

Nelson, R. P. & Langer, W. D. 1997, ApJ, 482, 796

Niklaus, M., Schmidt, W., & Niemeyer, J. C. 2009, A&A, 506, 1065

Norris, J. E., Yong, D., Bessell, M. S., Christlieb, N., Asplund, M., Gilmore, G., Wyse, R. F. G., Beers, T. C., Barklem, P. S., Frebel, A., & Ryan, S. G. 2013, ApJ, 762, 28

Nozawa, T., Kozasa, T., Habe, A., Dwek, E., Umeda, H., Tominaga, N., Maeda, K., & Nomoto, K. 2007, ApJ, 666, 955

Nozawa, T., Kozasa, T., Umeda, H., Maeda, K., & Nomoto, K. 2003, ApJ, 598, 785

Oey, M. S. 2003, MNRAS, 339, 849

Offner, S. S. R., Klein, R. I., McKee, C. F., & Krumholz, M. R. 2009, ApJ, 703, 131

Oh, S. P. & Haiman, Z. 2002, ApJ, 569, 558

—. 2003, MNRAS, 346, 456

Omukai, K. 2000, ApJ, 534, 809

—. 2001, ApJ, 546, 635

Omukai, K., Hosokawa, T., & Yoshida, N. 2010, ApJ, 722, 1793

Omukai, K. & Palla, F. 2003, ApJ, 589, 677

Omukai, K., Schneider, R., & Haiman, Z. 2008, ApJ, 686, 801

Omukai, K., Tsuribe, T., Schneider, R., & Ferrara, A. 2005, ApJ, 626, 627

O'Shea, B. W., Abel, T., Whalen, D., & Norman, M. L. 2005, ApJ, 628, L5

O'Shea, B. W. & Norman, M. L. 2007, ApJ, 654, 66

—. 2008, ApJ, 673, 14

Osterbrock, D. E. & Ferland, G. J. 2006, Astrophysics of gaseous nebulae and active galactic nuclei

Ostriker, E. C., Stone, J. M., & Gammie, C. F. 2001, ApJ, 546, 980

Padoan, P. & Nordlund, Å. 1999, ApJ, 526, 279

—. 2002, ApJ, 576, 870

—. 2011, ApJ, 730, 40

Padoan, P., Nordlund, A., & Jones, B. J. T. 1997, MNRAS, 288, 145

Padoan, P., Nordlund, Å., Kritsuk, A. G., Norman, M. L., & Li, P. S. 2007, ApJ, 661, 972

Palla, F., Salpeter, E. E., & Stahler, S. W. 1983, ApJ, 271, 632

Pan, L. & Scalo, J. 2007, ApJ, 654, L29

Pan, L., Scannapieco, E., & Scalo, J. 2011, ArXiv e-prints

—. 2013, ArXiv e-prints

Pan, T., Kasen, D., & Loeb, A. 2012, MNRAS, 422, 2701

Passot, T. & Vázquez-Semadeni, E. 1998, Phys. Rev. E, 58, 4501

Pawlik, A. H., Milosavljević, M., & Bromm, V. 2011, ApJ, 731, 54

Peters, T., Schleicher, D. R. G., Klessen, R. S., Banerjee, R., Federrath, C., Smith, R. J., & Sur, S. 2012, ApJ, 760, L28

Plewa, T. & Müller, E. 1999, A&A, 342, 179

Press, W. H. & Schechter, P. 1974, ApJ, 187, 425

Price, D. J., Federrath, C., & Brunt, C. M. 2011, ApJ, 727, L21

Price, D. J. & Monaghan, J. J. 2007, MNRAS, 374, 1347

Prieto, J., Jimenez, R., & Martí, J. 2012, MNRAS, 419, 3092

Prieto, J., Padoan, P., Jimenez, R., & Infante, L. 2011, ApJ, 731, L38

Prunet, S., Pichon, C., Aubert, D., Pogosyan, D., Teyssier, R., & Gottloeber, S. 2008, ApJS, 178, 179

Razoumov, A. O. & Sommer-Larsen, J. 2010, ApJ, 710, 1239

Read, J. I., Pontzen, A. P., & Viel, M. 2006, MNRAS, 371, 885

Rees, M. J. 1976, MNRAS, 176, 483

Rees, M. J. & Ostriker, J. P. 1977, MNRAS, 179, 541

Regan, J. A. & Haehnelt, M. G. 2009, MNRAS, 396, 343

Richardson, M. L. A., Scannapieco, E., & Gray, W. J. 2013, ApJ, 778, 80

Ricker, P. M. 2008, ApJS, 176, 293

Ricotti, M., Gnedin, N. Y., & Shull, J. M. 2001, ApJ, 560, 580

—. 2002, ApJ, 575, 49

Ritter, J. S., Safranek-Shrader, C., Gnat, O., Milosavljević, M., & Bromm, V. 2012, ApJ, 761, 56

Robertson, B. E., Furlanetto, S. R., Schneider, E., Charlot, S., Ellis, R. S., Stark, D. P., McLure, R. J., Dunlop, J. S., Koekemoer, A., Schenker, M. A., Ouchi, M., Ono, Y., Curtis-Lake, E., Rogers, A. B., Bowler, R. A. A., & Cirasuolo, M. 2013, ApJ, 768, 71

Roueff, E. 1990, A&A, 234, 567

Rydberg, C. E., Zackrisson, E., & Scott, P. 2010, in Cosmic Radiation Fields: Sources in the early Universe (CRF 2010), ed. M. Raue, T. Kneiske, D. Horns, D. Elsaesser, & P. Hauschildt, 26

Safranek-Shrader, C., Agarwal, M., Federrath, C., Dubey, A., Milosavljević, M., & Bromm, V. 2012, MNRAS, 426, 1159

Safranek-Shrader, C., Bromm, V., & Milosavljević, M. 2010, ApJ, 723, 1568

Safranek-Shrader, C., Milosavljević, M., & Bromm, V. 2014, MNRAS, 438, 1669

Salpeter, E. E. 1955, ApJ, 121, 161

Salvaterra, R., Della Valle, M., Campana, S., Chincarini, G., Covino, S., D'Avanzo, P., Fernández-Soto, A., Guidorzi, C., Mannucci, F., Margutti, R., Thöne, C. C., Antonelli, L. A., Barthelmy, S. D., de Pasquale, M., D'Elia, V., Fiore, F., Fugazza, D., Hunt, L. K., Maiorano, E., Marinoni, S., Marshall, F. E., Molinari, E., Nousek, J., Pian, E., Racusin, J. L., Stella, L., Amati, L., Andreuzzi, G., Cusumano, G., Fenimore, E. E., Ferrero, P., Giommi, P., Guetta, D., Holland, S. T., Hurley, K., Israel, G. L., Mao, J., Markwardt, C. B., Masetti, N., Pagani, C., Palazzi, E., Palmer, D. M., Piranomonte, S., Tagliaferri, G., & Testa, V. 2009, Nature, 461, 1258

Santoro, F. & Shull, J. M. 2006, ApJ, 643, 26

Saury, E., Miville-Deschênes, M.-A., Hennebelle, P., Audit, E., & Schmidt, W. 2013, ArXiv e-prints

Scalo, J., Vazquez-Semadeni, E., Chappell, D., & Passot, T. 1998, ApJ, 504, 835

Scannapieco, E., Ferrara, A., & Madau, P. 2002, ApJ, 574, 590

Schaerer, D. 2002, A&A, 382, 28

Schleicher, D. R. G., Spaans, M., & Glover, S. C. O. 2010, ApJ, 712, L69

Schmeja, S. & Klessen, R. S. 2004, A&A, 419, 405

Schneider, R., Ferrara, A., & Salvaterra, R. 2004, MNRAS, 351, 1379

Schneider, R. & Omukai, K. 2010, MNRAS, 402, 429

Schneider, R., Omukai, K., Bianchi, S., & Valiante, R. 2012a, MNRAS, 419, 1566

Schneider, R., Omukai, K., Inoue, A. K., & Ferrara, A. 2006, MNRAS, 369, 1437

Schneider, R., Omukai, K., Limongi, M., Ferrara, A., Salvaterra, R., Chieffi, A., & Bianchi, S. 2012b, MNRAS, 423, L60

Seifried, D., Schmidt, W., & Niemeyer, J. C. 2011, A&A, 526, A14

Semenov, D., Henning, T., Helling, C., Ilgner, M., & Sedlmayr, E. 2003, A&A, 410, 611

Shang, C., Bryan, G. L., & Haiman, Z. 2010, MNRAS, 402, 1249

Shapiro, P. R. & Kang, H. 1987, ApJ, 318, 32

Sheth, R. K. & Tormen, G. 2002, MNRAS, 329, 61

Shu, F. H. 1977, ApJ, 214, 488

Silk, J. 1997, ApJ, 481, 703

Silk, J. & Langer, M. 2006, MNRAS, 371, 444

Smith, B., Sigurdsson, S., & Abel, T. 2008, MNRAS, 385, 1443

Smith, B. D. & Sigurdsson, S. 2007, ApJ, 661, L5

Smith, B. D., Turk, M. J., Sigurdsson, S., O'Shea, B. W., & Norman, M. L. 2009, ApJ, 691, 441

Smith, R. J., Glover, S. C. O., Clark, P. C., Greif, T., & Klessen, R. S. 2011, MNRAS, 414, 3633

Sokasian, A., Yoshida, N., Abel, T., Hernquist, L., & Springel, V. 2004, MNRAS, 350, 47

Solomon, P. M. & Woolf, N. J. 1973, ApJ, 180, L89

Spaans, M. & Silk, J. 2000, ApJ, 538, 115

Stacy, A. & Bromm, V. 2007, MNRAS, 382, 229

Stacy, A., Greif, T. H., & Bromm, V. 2010, MNRAS, 403, 45

—. 2012, MNRAS, 422, 290

Stahler, S. W. & Palla, F. 2005, The Formation of Stars

Stahler, S. W., Palla, F., & Salpeter, E. E. 1986, ApJ, 302, 590

Stecher, T. P. & Williams, D. A. 1967, ApJ, 149, L29

Stiavelli, M. & Trenti, M. 2010, ApJ, 716, L190

Strigari, L. E., Bullock, J. S., Kaplinghat, M., Simon, J. D., Geha, M., Willman, B., & Walker, M. G. 2008, Nature, 454, 1096

Sur, S., Schleicher, D. R. G., Banerjee, R., Federrath, C., & Klessen, R. S. 2010, ApJ, 721, L134

Susa, H. 2013, ArXiv e-prints

Sutherland, R. S. & Dopita, M. A. 1993, ApJS, 88, 253

Takahashi, T., Silk, J., & Hollenbach, D. J. 1983, ApJ, 275, 145

Tanaka, M., Moriya, T. J., Yoshida, N., & Nomoto, K. 2012, MNRAS, 422, 2675

Tanvir, N. R., Fox, D. B., Levan, A. J., Berger, E., Wiersema, K., Fynbo, J. P. U., Cucchiara, A., Krühler, T., Gehrels, N., Bloom, J. S., Greiner, J., Evans, P. A., Rol, E., Olivares, F., Hjorth, J., Jakobsson, P., Farihi, J., Willingale, R., Starling, R. L. C., Cenko, S. B., Perley, D., Maund, J. R., Duke, J., Wijers, R. A. M. J., Adamson, A. J., Allan, A., Bremer, M. N., Burrows, D. N., Castro-Tirado, A. J., Cavanagh, B., de Ugarte Postigo, A., Dopita, M. A., Fatkhullin, T. A., Fruchter, A. S., Foley, R. J., Gorosabel, J., Kennea, J., Kerr, T., Klose, S., Krimm, H. A., Komarova, V. N., Kulkarni, S. R., Moskvitin, A. S., Mundell, C. G., Naylor, T., Page, K., Penprase, B. E., Perri, M., Podsiadlowski, P., Roth, K., Rutledge, R. E., Sakamoto, T., Schady, P., Schmidt, B. P., Soderberg, A. M., Sollerman, J., Stephens, A. W., Stratta, G., Ukwatta, T. N., Watson, D., Westra, E., Wold, T., & Wolf, C. 2009, Nature, 461, 1254

Tegmark, M., Silk, J., Rees, M. J., Blanchard, A., Abel, T., & Palla, F. 1997, ApJ, 474, 1

Tielens, A. G. G. M. & Hollenbach, D. 1985, ApJ, 291, 722

Todini, P. & Ferrara, A. 2001, MNRAS, 325, 726

Toomre, A. 1964, ApJ, 139, 1217

Toomre, A. 1977, in Evolution of Galaxies and Stellar Populations, ed. B. M. Tinsley & R. B. G. Larson, D. Campbell, 401

Tornatore, L., Ferrara, A., & Schneider, R. 2007, MNRAS, 382, 945

Trenti, M., Stiavelli, M., & Michael Shull, J. 2009, ApJ, 700, 1672

Truelove, J. K., Klein, R. I., McKee, C. F., Holliman, II, J. H., Howell, L. H., & Greenough, J. A. 1997, ApJ, 489, L179

Tumlinson, J. 2007, ApJ, 664, L63

Tumlinson, J., Venkatesan, A., & Shull, J. M. 2004, ApJ, 612, 602

Turk, M. J., Abel, T., & O'Shea, B. 2009, Sci, 325, 601

Turk, M. J., Oishi, J. S., Abel, T., & Bryan, G. L. 2012, ApJ, 745, 154

Uehara, H. & Inutsuka, S.-i. 2000, ApJ, 531, L91

Umeda, H. & Nomoto, K. 2002, ApJ, 565, 385

—. 2003, Nature, 422, 871

Urban, A., Martel, H., & Evans, II, N. J. 2010, ApJ, 710, 1343

Vargas, L. C., Geha, M., Kirby, E. N., & Simon, J. D. 2013, ApJ, 767, 134

Vazquez-Semadeni, E. 1994, ApJ, 423, 681

Vázquez-Semadeni, E., Kim, J., & Ballesteros-Paredes, J. 2005, ApJ, 630, L49

Vázquez-Semadeni, E., Ryu, D., Passot, T., González, R. F., & Gazol, A. 2006, ApJ, 643, 245

Verner, D. A., Ferland, G. J., Korista, K. T., & Yakovlev, D. G. 1996, ApJ, 465, 487

Wang, P., Li, Z.-Y., Abel, T., & Nakamura, F. 2010, ApJ, 709, 27

Whalen, D., O'Shea, B. W., Smidt, J., & Norman, M. L. 2008, ApJ, 679, 925

Whalen, D. J., Johnson, J. J., Smidt, J., Meiksin, A., Heger, A., Even, W., & Fryer, C. L. 2013, ArXiv e-prints

White, S. D. M. & Rees, M. J. 1978, MNRAS, 183, 341

Whitworth, A. P. & Ward-Thompson, D. 2001, ApJ, 547, 317

Wilson, N. J. & Bell, K. L. 2002, MNRAS, 337, 1027

Wise, J. H. & Abel, T. 2005, ApJ, 629, 615

—. 2007a, ApJ, 665, 899

—. 2007b, ApJ, 671, 1559

—. 2008, ApJ, 685, 40

Wise, J. H. & Cen, R. 2009, ApJ, 693, 984

Wise, J. H., Turk, M. J., Norman, M. L., & Abel, T. 2012, ApJ, 745, 50

Wolcott-Green, J., Haiman, Z., & Bryan, G. L. 2011, MNRAS, 418, 838

Wood, K. & Loeb, A. 2000, ApJ, 545, 86

Woods, D. T., Shull, J. M., & Sarazin, C. L. 1981, ApJ, 249, 399

Wyithe, J. S. B. & Loeb, A. 2003, ApJ, 588, L69

Yoshida, N., Oh, S. P., Kitayama, T., & Hernquist, L. 2007, ApJ, 663, 687

Yoshida, N., Omukai, K., Hernquist, L., & Abel, T. 2006, ApJ, 652, 6

Zackrisson, E., Rydberg, C.-E., Schaerer, D., Östlin, G., & Tuli, M. 2011, ApJ, 740, 13

Zackrisson, E., Zitrin, A., Trenti, M., Rydberg, C.-E., Guaita, L., Schaerer, D., Broadhurst, T., Östlin, G., & Ström, T. 2012, MNRAS, 427, 2212

Zheng, W., Postman, M., Zitrin, A., Moustakas, J., Shu, X., Jouvel, S., Høst, O., Molino, A., Bradley, L., Coe, D., Moustakas, L. A., Carrasco, M., Ford, H., Benítez, N., Lauer, T. R., Seitz, S., Bouwens, R., Koekemoer, A., Medezinski, E., Bartelmann, M., Broadhurst, T., Donahue, M., Grillo, C., Infante, L., Jha, S. W., Kelson, D. D., Lahav, O., Lemze, D., Melchior, P., Meneghetti, M., Merten, J., Nonino, M., Ogaz, S., Rosati, P., Umetsu, K., & van der Wel, A. 2012, Nature, 489, 406

Zinnecker, H. & Yorke, H. W. 2007, ARA&A, 45, 481

Zuckerman, B. & Evans, II, N. J. 1974, ApJ, 192, L149

Vita

Chalence Safranek-Shrader was born in Santa Monica, California. After four years at Venice High School, Chalence enrolled at the University of California, Los Angeles. There he wrestled between many potential academic concentrations, from anthropology to piano performance, before settling on astronomical sciences. After receiving his B.S. in astrophysics, Chalence strayed from the world of academia and worked for a year as a radiation safety technician for the UCLA department of Environment, Health, and Safety. Missing academia, he then moved to Austin, Texas to pursue a Ph.D. degree in Astronomy at the University of Texas at Austin working with Volker Bromm and Milos Milosavljevic. After graduate school, Chalence will be returning back to California to begin a postdoc at the University of California, Santa Cruz where he will work with Mark Krumholz on various topics in star formation.

Permanent address: csafranek@gmail.com

This dissertation was typeset with LaTeX by the author.